Computational Investigations of a Few Low-dimensional Systems: Effects of Size, Defects and Molecular Adsorption

A Thesis submitted in partial fulfillment

for the degree of

DOCTOR OF PHILOSOPHY

in the Faculty of Science

by

Sharma S. R. K. C. Yamijala

CHEMISTRY AND PHYSICS OF MATERIALS UNIT
JAWAHARLAL NEHRU CENTRE FOR ADVANCED SCIENTIFIC
RESEARCH
Bangalore − 560 064, India

AUGUST 2015

To my grand parents and my guru

Sri. N. R. Mohan Babu and N. Subbalakshmi

Sri. Goparaju Bala Bhaskara Sarma

DECLARATION

I hereby declare that the matter embodied in the thesis entitled "**Computational Investigations of a Few Low-dimensional Systems: Effects of Size, Defects and Molecular Adsorption**" is the result of investigations carried out by me at the Chemistry and Physics of Materials Unit, Jawaharlal Nehru Centre for Advanced Scientific Research, Bangalore, India under the supervision of Prof. Swapan K. Pati and that it has not been submitted elsewhere for the award of any degree or diploma.

In keeping with the general practice in reporting scientific observations, due acknowledgement has been made whenever the work described is based on the findings of other investigators. Any omission that might have occurred by oversight or error of judgement is regretted.

Sharma S. R. K. C. Yamijala

CERTIFICATE

I hereby certify that the matter embodied in this thesis entitled "**Computational Investigations of a Few Low-dimensional Systems: Effects of Size, Defects and Molecular Adsorption**" has been carried out by Mr. Sharma S. R. K. C. Yamijala at the Chemistry and Physics of Materials Unit, Jawaharlal Nehru Centre for Advanced Scientific Research, Bangalore, India under my supervision and that it has not been submitted elsewhere for the award of any degree or diploma.

Prof. Swapan K. Pati

(Research Supervisor)

Acknowledgements

First of all I would like to thank all my Gurus who taught me how to retain my composure in times of anxiety. I owe gratitude to the following people without whose invaluable contribution, this thesis would not be complete.

Firstly, I would like to thank my research supervisor, Prof. Swapan K. Pati for his guidance and support during my research career. His considerable insight and experience in science is inspiring. He has been a source of support in times of difficulty, both in my academic and personal life. In a time of personal tragedy, his words of reassurance gave me much needed relief and comfort. It has been a wonderful experience working with him.

Next, I would like to thank Prof. S. Balasubramanian, for constantly guiding me. I still remember his suggestion to read "Feynmann Lectures on Physics" even before joining JNC. He is always there to support me in various ways throughout my research career, despite his various important responsibilities.

I would also like to thank Dr. Ganga Periyasamy. I am fortunate to have had a chance to work with her on a project. She found time despite of her many commitments to help me in completing a major part of my M.S. thesis. I would also like to express my gratitude towards Dr. Ayan Datta, who has also helped me while writing my M.S. thesis.

I have been fortunate to have a very fruitful collaboration with Prof. C. N. R. Rao, F. R. S and I would like to thank his students Dr. Sandeep Gosh, Dr. Vasu

Synopsis

Low-dimensional systems are of great interest due to their fascinating properties, which arise due to the quantum confinement (less coordination number) in these systems. In recent years, one of the low-dimensional systems which has got tremendous impetus is the graphene. Apart from graphene, its inorganic analogues and low-dimensional counterparts, namely, nanotubes, nanoribbons and quantum dots have found various applications in advanced devices and energy research. They also display interesting properties such as half-metallicity without magnetic atoms, broad range of optical absorption and emission profiles, large surface area for catalytic activities etc. with applications including photodetectors, broadband modulators, spintronics and so on. In this thesis, we have studied structural, electronic, magnetic and optical properties of various low-dimensional systems including nanoribbons of graphene and boron nitride, nanotubes of carbon and molybdenum disulphide, pure and substituted graphene quantum dots (GQDs), polyaromatic hydrocarbons (PAHs) and chlorophylls. As the properties of these systems will be largely dictated by their edge nature and the surrounding environment, we have considered different external stimuli, such as, electric field, substitution, introduction of defects etc. to tune the properties. Throughout the thesis, we have primarily used density functional theory (DFT) and time dependent DFT (TDDFT). However, we also have used semi-empirical methods such as Zerner's intermediate neglect of differential overlap (ZINDO), density functional tight binding (DFTB) etc. when the number of atoms

exceeds thousand and for cases where consideration of configuration interaction (CI) becomes important. Also, we have implemented semi-empirical complete active space configuration interaction (CAS-CI) method to study the optical and ground state spin properties of a few PAH systems within lattice Hubbard and Pariser-Parr-Pople (PPP) Hamiltonians. This thesis is divided into 7 chapters.

In chapter 1, we briefly introduce the materials considered in this thesis along with various methodologies which we have used including DFT, TDDFT, and DFTB. We also give a brief introduction to some of the properties which we explored in the subsequent chapters.

In chapter 2, we gave a microscopic reason for the huge red shift (54 nm) found in the Q_Y band of the chlorophyll-f (Chl f) compared to its structural isomer Chl b, experimentally. Chl f is the latest addition to the list of chlorophylls which can perform oxygenic photosynthesis, however, Chl f can perform photosynthesis even in low-light conditions (IR-region). Based on TDDFT calculations, we show that the red-shift in Chl f is due to the stabilization of its LUMO which in turn is due to the extended conjugation contribution from its -CHO group towards LUMO. Chl b, a structural isomer of Chl f, have a blue shift due to the absence of such extended conjugation contribution to its LUMO. Also, as chlorophylls exists in nature with axial ligands, through our DFT/TDDFT calculations with various axial ligands, we conjecture that Chl f would act as an electron acceptor (donor) upon the axial ligation with CH_3COOH (imidazole).

Hybrid materials of graphene and boron nitride are known to exhibit interesting properties, such as intrinsic half-metallicity, high carrier mobility etc. In chapter 3, we have studied the effect of edge substitutions on the graphene and boron nitride quantum dots. Using both DFT and TDDFT calculations, we demonstrate that partial-edge BN substituted graphene quantum dots (GQDs) with rectangular shape possess interesting properties such as spin-polarized density of states and broad

band absorption spectra. We will prove (by excluding several possibilities) that the observed spin-polarized density of states is mainly due to the spin-polarized charge transfer among B, N and C atoms, and in particular B atom being Lewis-acid. We will also present a method to understand the shifts in the molecular orbital energy levels by plotting the electron density difference maps under the presence of an external electric field. Also, we show that substituting the edges of BNQDs, either partially or fully, will change their electronic nature from insulating to semi-conducting, with gaps reaching the semi-conducting gaps of the corresponding GQDs.

In chapter 4, we have explored the optical and nonlinear optical properties of $\sim$ 400 GQDs (they are actually polyaromatic hydrocarbons (PAHs)) to understand the structure and optical property relationship in these systems. Experiments have shown that modified GQDs have broadband absorption and emission profiles with applications involving broadband modulators, photodetectors, solar cells etc. Based on both semiempirical and *ab initio* calculations, we show that among the random shaped GQDs, those with inequivalent sublattice atoms show quite rich optical and nonlinear optical properties, such as IR absorption and large nonlinear optical coefficients. Among the regular shaped GQDs, zigzag edged GQDs are less stable and have smaller HOMO-LUMO gaps compared to the GQDs with armchair edges. Such less stability of zigzag edged GQDs is explained using Clar's sextet rule. Finally, using Hubbard model calculations, we will show that both Kekulé and non-Kekulé isomers of $C_{28}H_{16}$ obey Lieb's theorem but they don't obey Nagaoka theorem in their charged states.

Through DFT calculations, in chapter 5, we will prove that thermodynamically less stable but catalytically active planar conformer of Au_{20} cluster can be stabilized on a nitrogen-doped graphene quantum dot over the thermodynamically stable but catalytically less active tetrahedral conformer of Au_{20} cluster. Through this result, we will show the non-necessity of the traditional metal-oxide substrates in stabilizing

the planar conformer of Au_{20} cluster. Also, based on the charge transfer plots, we conjecture that due to the availability of more number of corner sites, with low coordination number, planar conformer would more likely be catalytically active than the tetrahedral conformer.

In chapter 6, we have examined the boron nitride nanoribbons with even and odd-line stone-wales defects. Various experiments have shown that the edges of GNRs are reconstructed to form lines of stone-wales defects, to attain stability. Using DFT calculations, we prove that boron-nitride nanoribbons show half-metallic behavior only when both of their edges are non-passivated and zigzag. Necessity of zigzag edges for the observation of half-metallicity will be demonstrated by substituting the edges of zigzag-BNNRs with even-line (retains zigzag edges) and odd-line (creates armchair edges) stone-wales defects. We will also show that passivation destroys the observed half-metallicity.

In the last chapter, based on DFT calculations, we have proposed the unzipping mechanism for both carbon and MoS_2 nanotubes under the laser irradiation in dimethylformamide (DMF) solvent. The proposed mechanism includes the formation of vacancies and the generation of induced dipole-moment across the nanotube under the influence of external electric-field due to the charge accumulation near the vacancies. DMF molecules align themselves along the tube axis near the vacancies with their dipoles being parallel to the induced dipoles to minimize their interaction with the external field. This leads to the accumulation of further charge near the vacancies and supports longitudinal unzipping of nanotubes.

List of publications

1. *Linear and Nonlinear Optical Properties of Graphene Quantum Dots: A Computational Study.*
   Sharma S. R. K. C. Yamijala; Madhuri Mukhopadhyay; Swapan K. Pati
   J. Phys. Chem. C **119** (21), 12079–12087, 2015.

2. *Clean WS_2 and MoS_2 Nanoribbons Generated by Laser-Induced Unzipping of the Nanotubes.*
   K. Vasu; **Sharma S. R. K. C. Yamijala**; Alla Zak; K. Gopalakrishnan; Swapan K. Pati ; C. N. R. Rao
   Small **11** (32), 3916–3920, 2015.

3. *A Hexanuclear Cu(I) Cluster Supported by Cuprophilic Interaction: Effects of Aromatics on Luminescence Properties.*
   Anindita Chakraborty; Krishna K. Ramachandran; **Sharma S. R. K. C. Yamijala**; Swapan K. Pati and Tapas K. Maji
   RSC Adv. **4** (66): 35167–35170, 2014.

4. *Nitrogen Doped Graphene Quantum Dots as Possible Substrates to Stabilize Planar Conformer of Au_{20} Over its Tetrahedral Conformer: A Systematic DFT Study.*
   Sharma S. R. K. C. Yamijala; Arkamita Bandyopadhyay and Swapan K. Pati

J. Phys. Chem. C **118** (31): 17890–17894, 2014.

5. *Effects of Edge Passivations on the Electronic and Magnetic Properties of Zigzag Boron-Nitride Nanoribbons with Even and Odd-Line Stone-Wales (5-7 Pair) Defects.*

   Sharma S. R. K. C. Yamijala; and Swapan K. Pati

   Indian J. Phys. **88** (7), 1–8, 2014.

6. *Electronic Properties of Zigzag, Armchair and their Hybrid Quantum Dots of Graphene and Boron-Nitride with and without Substitution: A DFT Study.*

   Sharma S. R. K. C. Yamijala; Arkamita Bandyopadhyay and Swapan K. Pati

   Chem. Phys. Lett. **603**, 28-32, 2014.

7. *Structural Stability, Electronic, Magnetic and Optical Properties of Rectangular Graphene and Boron-Nitride Quantum Dots: Effects of Size, Substitution and Electric Field.*

   Sharma S. R. K. C. Yamijala; Arkamita Bandyopadhyay and Swapan K. Pati

   J. Phys. Chem. C **117** (44), 23295–23304, 2013.

8. *Tuning the Electronic and Optical Properties of Graphene and Boron-Nitride Quantum Dots by Molecular Charge-Transfer Interactions: A Theoretical Study.*

   Arkamita Bandyopadhyay; **Sharma S. R. K. C. Yamijala** and Swapan K. Pati

   Phys. Chem. Chem. Phys. **15**, 13881–13887, 2013.

9. *Electronic and Magnetic Properties of Zigzag Boron-Nitride Nanoribbons with Even and Odd-Line Stone-Wales (5-7 Pair) Defects.*

   Sharma S. R. K. C. Yamijala; Swapan K. Pati

   J. Phys. Chem. C **117** (7): 3580–3594, 2013.

10. *The Interaction of Halogen Molecules with SWNTS and Graphene.*

    Ghosh, Sandeep; **Sharma S. R. K. C. Yamijala**; Swapan K. Pati; C. N. R. Rao

    RSC Adv. **2** (3): 1181, 2011.

11. *Computational Studies on Structural and Excited-State Properties of Modified Chlorophyll f with Various Axial Ligands.*

    Sharma S. R. K. C. Yamijala; Ganga Periyasamy; Swapan K. Pati

    J. Phys. Chem. A **115** (44): 12298–12306, 2011.

List of Figures

List of Tables

Contents

5 Nitrogen doped graphene quantum dots as possible substrates to stabilize planar conformer of Au$_{20}$ over its tetrahedral conformer: A systematic dft study.   125

6 Electronic and Magnetic Properties of Zigzag Boron–Nitride Nanoribbons with Even and Odd–Line Stone–Wales (5–7 Pair) Defects   139

Chapter 1

Introduction

The term, "low dimensional systems", refers to those materials which are finite along at least one dimension. Due to their low-dimensionality, motion of microscopic degrees of freedom, such as electrons, phonons etc. is constrained in these systems. This constraint to move in three dimensions makes them as hosts for quantum confinement effects. [1–7] Although one would not, traditionally, consider the natural low-dimensional entities such as atoms and molecules as low-dimensional systems, but some of the most exciting recent developments in the field have involved the use of molecules and even biologically important materials, such as DNA, chlorophylls etc. and had blurred the boundaries between the subject and other physical and life sciences. [8]

Mono-layers, thin films, surfaces like graphene, boron-nitride are the examples of two-dimensional systems. One-dimensional systems include nanotubes, and nanorods. Nanaoribbons, due to their finite width, are generally considered as quasi-one-dimensional systems. Also, clusters of atoms, molecules and quantum dots are the examples of zero-dimensional systems. In all these systems, there is a reduction in the coordination number at the surface and the surface to volume ratio becomes very large for these systems which leads to new properties that are different from bulk. A few examples of such exotic quantum phenomena include Klein-paradox, spin-charge

separation, quantum Hall-effect, Luttinger liquid etc. [9–21] Such phenomena arise in these systems out of disorder, strong electron-electron interactions and restricted boundary conditions. Low-dimensional systems do not generally have true long range order unlike the three-dimensional materials. Prominent examples are spin- and charge-density waves in quasi-one-dimensional systems and spontaneous circulating currents in ring systems, for which one sees chemical shift in NMR. [22]

The physics of low-dimensional and bulk systems are often different. A full quantum mechanical treatment of the confined degrees of freedom is required to study these systems. Emergence of experimental techniques such as scanning tunneling microscopy, transmission electron microscopy (TEM), molecular beam epitaxial growth of thin-films, chemical vapor deposition, atomic-force microscopy, ion-beam sputtering, x-ray photoelectron spectroscopy, Auger electron spectroscopy, electron energy loss spectroscopy, magnetic force microscopy, high-resolved TEM, high temperature XRD etc. [23–38] provided the path for characterization and fabrication of several novel low-dimensional materials.

In this chapter, we will discuss briefly about the low-dimensional materials that we have studied in this thesis. Also we will give the computational and theoretical methods which we have used to study these materials. Mainly, we are interested in understanding the electronic, magnetic, optical and charge transfer properties of these materials. These systems have potential applications in future optoelectronic devices and our studies give the mechanism of charge transfer and its consequences in some of these systems. In sections 1.1.1 – 1.1.4., we will first give a brief overview of graphene, nanoribbons of graphene and boron-nitride, carbon nanotubes and graphene quantum dots, which are two-dimensional, quasi one-dimensional, one-dimensional and zero dimensional systems, respectively. In section 1.1.5, we introduce the zero-dimensional chlorophyll molecule, and we will discuss its importance in photosystems. Numerical methods which we have used to perform different calculations are outlined in section

1.2, followed by an outline of this thesis in section 1.3.

1.1 Low-dimensional systems

1.1.1 Graphene

Apart from the well known allotropes of carbon viz., graphite, amorphous carbon and diamond, scientists have discovered, its other exotic allotropes which include zero-dimensional fullerenes (1985), one-dimensional nanotubes (1991) and recently graphene (2004) – the two dimensional allotrope of carbon. Among the exotic allotropes of carbon, the discovery of graphene was unprecedented in that there were established theoretical concepts precluding its existence. Theoretical argument by Landau and Peirels says that, in low-dimensional crystals, thermal fluctuations lead to atomic displacements in the order of inter-atomic distances, and hence, two-dimensional crystals are thermodynamically unstable and could not exist. This argument was latter supported by Mermin and others. [39–43]

Despite of these arguments, there have been several attempts to isolate graphene using chemical exfoliation but they resulted in new 3D materials [44] and there are cases in which scientists have grown single and few-layer graphene [45, 46] but their quality and continuity are not known. For the first time, in 2004, physicists from Manchester university extracted high quality graphene crystallites by the micro mechanical cleavage of bulk graphite, for which they were awarded the 2010 Nobel prize in physics. [47, 48] Experimental discovery of graphene didn't violate the above theoretical arguments and is justified by the observation of the ripples in the so-called 2D graphene, which affect its properties. [49] Indeed, it can be argued that, thermal fluctuations and other crystal defects cannot occur in these 2D-crystals because of their small size ($\ll$ 1 mm) and strong inter-atomic bonds. [40, 41]

Graphene has become a great sensation because of its wonderful properties.

Many groups have been investigating chemically derived graphene as a transparent conductive electrode. [50] For rechargeable lithium batteries, graphene has shown to be a potential candidate with high lithium storage capacity and this capacity can further be increased by adding other nanocarbons like CNTs and C_{60}. [51] Single-layer graphene is theoretically predicted to have a large surface area of 2600 m^2/g, and experimental findings shows an uptake of 3 wt % for H_2 at 100 bar and 300 K and 35 wt % for CO_2 at 1 atm and 195 K for a few-layer graphene. [52] Elastic modulus and hardness of polyvinyl alcohol and poly (methyl methacrylate) composites have been shown to increase significantly when they are reinforced with small quantities of a few-layer graphene. [53]

Interestingly, exotic electronic properties of graphene, reflects its structural flexibility. [54] Single layer graphene is a 2D zero-gap semiconductor with a linear dispersion relation near the K-point of the Brillouin zone resembling the Dirac spectrum for massless fermions. [55, 56] This linear dispersion relation can easily be derived using the tight binding approximation including the nearest neighbors. [57] Graphene also displays several exotic phenomena, like, ballistic electron transport, anomalous integer quantum Hall effect at room temperature and fractional quantum Hall effect at low temperature, [58] Klein-paradox [59] etc.

1.1.2   Graphene Nanoribbons (GNRs)

GNRs are the quasi-one-dimensional materials obtained by the finite termination of graphene along one direction, the other direction being periodic. Depending on their edge geometry, GNRs can be divided into two major classes, namely, zigzag GNRs (ZGNRs) and armchair GNRs (AGNRs) (see Figure 1.1). Because of their contrasting boundary conditions, which in turn arise because of their different edge geometries, these nanoribbons show different electronic structure properties. GNRs can be prepared experimentally either through "top-down approaches", which

includes techniques like etching graphene with a STM tip, lithographic patterning on epitaxially grown graphene, unzipping and unrolling of carbon nanotubes by epoxidation of CNTs etc., or through "bottom-up approaches", which includes combining small organic molecules to build up various graphitic structures using elegant synthetic methods.
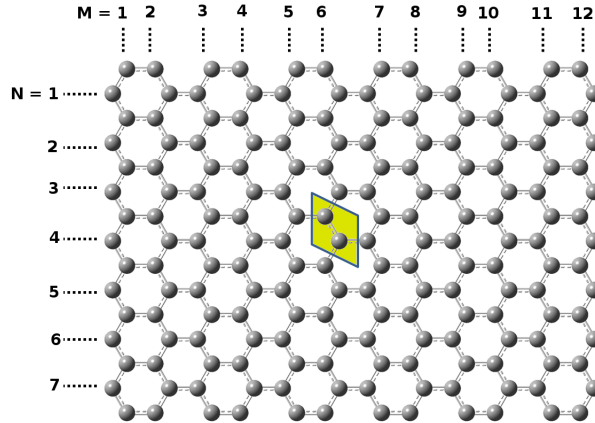
Figure 1.1: GNRs with armchair (zigzag) edges are extended along horizontal (vertical) direction. Shaded area represents the unit cell of graphene. General numbering scheme used to denote the widths of zigzag and armchair nanoribbons are depicted here with M and N indices, respectively.

Among the GNRs, ZGNRs exhibit interesting electronic properties due to the presence of localized electronic states, known as edge states, which are absent in the case of AGNRs. [60] Edge states allow fine tuning of the electronic structure and band-gap of ZGNRs through structural or chemical modifications along with doping and external perturbations. Metal free magnetism can be achieved using semiconducting ZGNRs as they show semi-metallic behavior under external pertur-bations. [60] By selective doping, ZGNRs can be tuned to use as spin filters and spin transistors. [61–63] Similar to ZGNRs, their inorganic and iso-electronic analogues, zigzag boron-nitride nanoribbons (ZBNNRs) have also attracted huge attention because of their intrinsic spin-polarization and also because of their several other interesting applications. [64–70] The exciting electronic and spintronic properties of ZBNNRs are also due to their edge states, [64–70] and mainly, when these edge states

have been tuned by external factors like application of electric-field, [64] doping,[71] passivation etc. [65–67, 70]

Although, majority of the studies have concentrated on GNRs and BNNRs with zigzag edges, it is important to notice that achieving precisely the zigzag edges, experimentally, is hard. [72, 73] General experimental procedures like etching,[74] chemical vapor deposition etc. [72, 73] will generally produce defects in the otherwise perfect ribbons. Among the several kinds of defects, point defects and Stone-Wales defects are found to be ubiquitous in both graphene and boron-nitride sheets. [72–74] In chapter 6, we present our understanding on the effect of Stone-Wales line-defects (also generally called as pentagon-heptagon line-defects) and passivation of edges (both pristine and defect containing) on the electronic and magnetic properties of BNNRs.

1.1.3   Carbon Nanotubes (CNTs)

CNTs are the one-dimensional allotropes of carbon and can be visualized as a graphene sheet rolled into a cylinder. Their discovery [75] marks a major event in the area of carbon materials and more so in one dimensional materials. CNTs are characterized by a pair of chiral indices (n, m), with n and m being two integers, which specify the CNT uniquely. [76] The integers n and m denote the number of unit vectors along two directions in the honeycomb crystal lattice of graphene. Nanotubes are called zigzag if m=0 and are called armchair if n=m. Otherwise, they are called chiral. Their electronic structure is either metallic or semi-conducting depending on (n, m). In general, (n,m) nanotubes are metallic, either when n=m or when n-m is a multiple of 3, and they are semiconducting otherwise and if m=0. [51, 77]

Electronic band structure of SWNTs can be derived easily from a graphene sheet while neglecting hybridization effects due to the finite curvature of the tube

structure. Because of their electronic structure, CNTs act as ideal test beds for studies of quantum confinement effects like ballistic conductance,[78] Kondo effect and spin-injection, [79, 80] Luttinger liquid behavior,[81] and single and double quantum dots states. [82] Electronic and molecular properties of CNTs can be tuned by doping or through molecular charge transfer.

1.1.4   Graphene Quantum Dots (GQDs)

GQDs are the zero-dimensional counterparts of graphene. Reducing the dimensions of graphene is one of the ways to understand the quantum confinement effects on graphene related systems. In this regard, GQDs are the natural successors to GNRs. Unlike graphene, which is a zero band-gap semi-conductor, GNRs and GQDs have finite gap. Because of their band-gap, GNRs and GQDs have applications in semi-conductor industry and in optoelectronic applications. Unlike GNRs, which are confined in two-dimensions, GQDs are confined in all the three dimensions. Thus, GQDs could be considered as the bridge between small polyaromatic hydrocarbon (PAH) molecules and GNRs or they themselves can be considered as the PAHs.

GQDs are found to possess unique electronic, [83, 84] magnetic [84] and optical properties. [85–87] Because of their tunable energy gap, GQDs have been used in solar cells [88] and LEDs. [89] Additionally, GQDs are being emerged as the new carbon based graphitic fluorescent materials, which, depending upon their size and/or passivation can emit light of different wavelengths. [85, 87, 90] Along with their interesting optical properties, GQDs have also been used as bio-markers [91] because of their chemical inertness, bio-compatibility and low toxicity. *In vitro* studies have already been performed using GQDs for bio-imaging cells. [92–94] Furthermore, similar to GNRs, GQDs' properties are also shown to be dependent on their size and shape. [95–100] For example, smaller quantum dots have discrete energy levels, whereas, considerably larger nano-flakes have continuous energy bands

[96] and triangular nano-flakes have finite magnetic moments. [98–100] Similarly, properties of BNQDs have also been shown to vary with their shape and size. [97]

In this thesis, we have studied both GQDs, BNQDs and their hybrids to explore their electronic, magnetic and optical properties. Hybrid BNC sheets have already been prepared experimentally with precise control over (a) the ratio of C:BN [101] and (b) domain shape of BN on C or vice-versa. [102] In addition, recent techniques like nanotomy [103] have shown to produce GQDs of desired geometries from graphite itself. Thus, combining these ideas, hybrid quantum dots of required shape, size and doping ratio could be prepared. In chapter 3, we have studied their properties with a change in size, substitution and electric field and in chapter 4, we have studied their optical and nonlinear optical properties. Additionally, in chapter 5, we have studied the effects of nitrogen doping on these GQDs, while studying the stability of gold clusters over GQD surface.

1.1.5   Chlorophylls

Availability and function

Chlorophyll is an essential and abundant pigment present in the plants, algae and cyanobacteria. [104] Chlorophyll is vital for photosynthesis, a process in which solar energy is converted into chemical energy. Chlorophyll molecules are presented in and around photosystems which in turn are present in the thylakoid membranes of chloroplasts (see Figure 1.2). Chloroplasts are organelles found in plant cells and other eukaryotic organisms. It consists of a material called as "stroma". The sub-organelles, thylakoids, are presented as stacks within the stroma. [105] Empty area inside the thylakoid is called as thylakoid space or "lumen". The membrane separating the stroma from lumen is called as thylakoid membrane and photosynthesis takes place at this membrane. Light harvesting complexes (LHC), also present in thylakoid membranes and each LHC consists of light-absorbing pigments, including

chlorophylls, carotenoids and proteins, which funnel the incident solar energy to reaction center (RC) through resonance energy transfer. In photosystem II (PSII) of higher plants, a special pair of chlorophylls, named as P680, (here P denotes pair of chlorophylls and the number 680 denotes the absorption maximum of the pair), present at the reaction center and receives the funneled energy and utilizes it for charge separation and charge transfer followed by several other processes to finally reduce the absorbed CO_2 from atmosphere to sugars. Thus, *chlorophyll functions in photosystems both as a light harvesting pigment in LHC and as a charge separator at RC.*
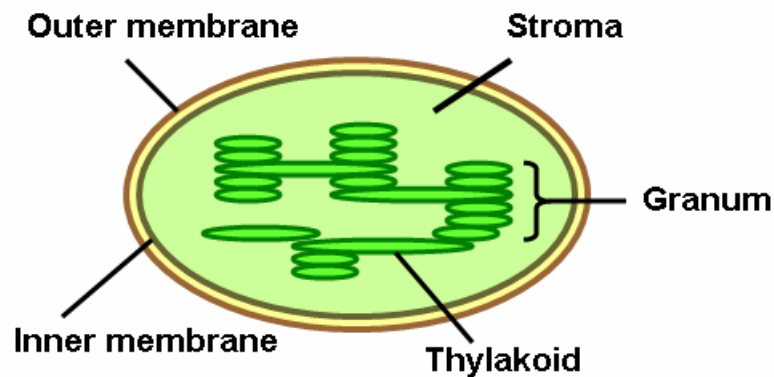
Figure 1.2: Thylakoid (green) inside a chloroplast (source: Wikipedia) [106]

Structural properties

Structure of a chlorophyll mainly consists of a substituted chlorin ring with a Mg atom at the center of the ring and a phytol chain (see Figure 1.3). Chlorin ring is a reduced porphyrin ring, which consists of four pyrrole units connected to each other through methane bridges (see Figure 1.4). If the porphyrin ring is doubly reduced then it is called as bacteriochlorin ring. A chlorophyll molecule without an Mg atom at its center is called as pheophytin.

To date there are 5 kinds of chlorophylls known, which can perform oxygenic photosynthesis, viz. chl a, chl b, chl c, chl d and chl f. Chlorophylls are generally
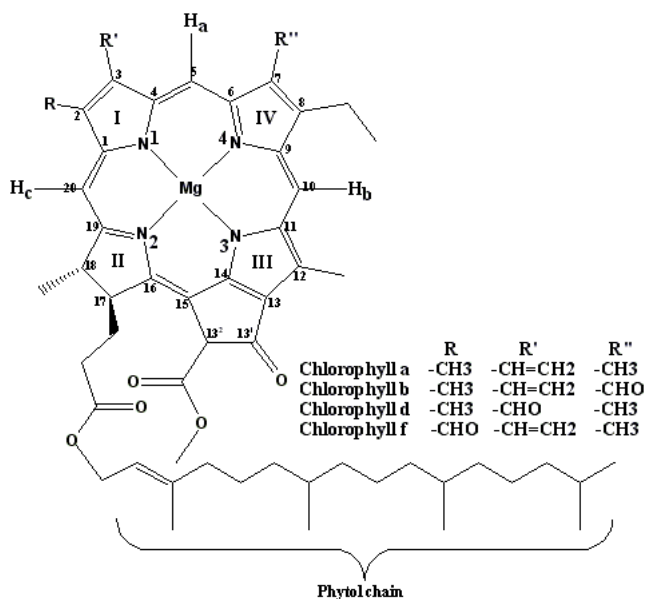
Figure 1.3: Schematic representation of chlorophylls.

penta-coordinated in nature and there is a strong effect of this 5th coordination on the structure and functions of chlorophyll. Major structural changes include Mg-N bond distances and out of plane distance of Mg i.e., distance of Mg from the plane of the chlorin ring. Penta-coordination also affects the redox potential of the chlorophyll molecule. Across the electron transport chain in PSI, the 5th coordination to chlorophylls is arranged in such a manner that overall it maintains a forward electron transfer. [107]
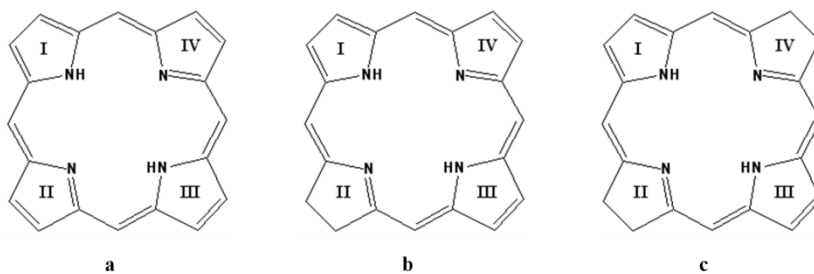
Figure 1.4: Schematic representation of a) Porphyrin (D_{4h}) b) Chlorin (C_{2v}) c) Bacteriochlorin (D_{2h}). Symmetry of the compound is given in braces.

Optical properties

Chlorophylls with different absorption maximum are arranged in an energy hierarchy to transfer the light to the reaction center, as mentioned earlier. Absorption spectrum of a chlorophyll is very sensitive to the changes occurring on the chlorin ring. [108] A typical absorption spectrum of a chlorophyll consists of high energy B(Soret)– bands and low energy Q–bands. Goutermann has proposed his four-orbital model to explain the absorption spectra of porphyrins, substituted porphyrins and its derivatives (chlorin and bacteriochlorin). [109, 110] According to this model, the absorption bands in porphyrin systems arises from the transition between the $a_{1u} \rightarrow e_g$ and $a_{2u} \rightarrow e_g$ (here HOMO and HOMO – 1 orbitals possess a_{1u} and a_{2u} symmetries, respectively and both the orbitals, LUMO and LUMO + 1 possess e_g symmetry). Relative energies of these transitions are affected by the substituents on the ring and the metals present at the center of the ring. It should be emphasized that, four-orbital description is generally accurate for Q-bands but not for B-bands.

In porphyrin, HOMOs with a_{1u} and a_{2u} symmetry are nearly degenerate and LUMOs with e_g symmetry are degenerate. Excitations between these four orbitals will lead to two transitions with y-symmetry (i.e., transition dipole moment in the 'y'–direction) and two transitions with x-symmetry (i.e., transition dipole moment in the 'x'–direction). Among these four transitions, the two transitions with lower energy are termed as Q-bands (Q_y and Q_x) and the transitions with higher energy are termed as B-bands (B_y and B_x). A transition dipole moment which passes through the two opposite pyrrole rings along the y-axis of the porphyrin characterizes a Q_y band. [108] In the case of porphyrin, as both the transitions, $a_{1u} \rightarrow e_g$ and $a_{2u} \rightarrow e_g$ of ^1E_u character are nearly degenerate, mixing of these transitions leads to a lower intense Q-band and a higher intense Soret-band. [108]

In the case of chlorin, reduction in symmetry lifts the degeneracy of the LUMOs which causes a decrement in the mixing of excitations. As excitations are not

mixed much, intensities of both the Q and B-bands remain high. Once there are substitutions on the chlorin ring, symmetries of the ring will be completely destroyed and this leads to an increment in the intensity of Q-band. Increase in the intensity of Q-band reflects the fact that, there is a greater absorption probability and this helps for efficient energy transfer between the component chromophores, which is important for photosynthetic systems. [108]

In chapter 2, we have studied the recently isolated chlorophyll, named as, chlorophyll f. Chl f can perform oxygenic photosynthesis and its Q_y absorption maximum is in the infrared region. This shows that, in low light conditions also chl f can perform oxygenic photosynthesis. As mentioned in reference [111], this ability of chl f can be used for the design of photovoltaic cells. [111] This is because, over half of the light from the sun comes in at infrared wavelengths and the makers of photovoltaic panels have been working on ways to extend the section of the spectrum that solar cells can absorb to beyond red. By the discovery of chl f, now, we can use it to absorb the infrared region of solar spectrum. Chl f can also be used for the artificial photosynthesis technology. [111] Considering these facts, we studied the effects of axial ligation and the reason for the red-shift in the Q_y absorption maximum of chl f.

1.2   Computational methods

1.2.1   Schr*ö*dinger equation for solving electronic structure

One of the main aims of quantum chemical computations is to find approximate solutions for the non-relativistic time-independent Schr*ö*dinger equation (SH-eqn).

$$\hat{H}\Psi = E\Psi \qquad\qquad (1.1)$$

where $\hat{H}$ is the Hamiltonian operator and Ψ is the many-body wave-function, containing all the necessary information about the system. In practice, SH-eqn is exactly solvable only for one electron systems and we employ approximations either in the Hamiltonian or in Ψ to solve SH-eqn for a system of our interest (generally, a molecule or a solid). Approximate methods to solve SH-eqn can mainly be categorized into two forms, namely, wave-function based methods and density based methods. In both of these methods, original complicated many-body problem is replaced with numerically solvable single-particle equations. However, these methods differ from each other in dealing with the level of correlations between electrons.

For a system with N_e electrons and N_n nuclei, the Hamiltonian operator ($\hat{H}$) can be written as: [112–114]

$$\hat{H} = -\sum_{i=1}^{N_e} \frac{\hbar^2}{2m} \nabla_i^2 - \sum_{I=1}^{N_n} \frac{\hbar^2}{2M_I} \nabla_I^2 - \sum_{i=1}^{N_e} \sum_{I=1}^{N_n} \frac{Z_I e^2}{|\mathbf{r}_i - \mathbf{R}_I|}$$
$$+ \sum_{i=1}^{N_e-1} \sum_{j>i}^{N_e} \frac{e^2}{|\mathbf{r}_i - \mathbf{r}_j|} + \sum_{I=1}^{N_n-1} \sum_{J>I}^{N_n} \frac{Z_I Z_J e^2}{|\mathbf{R}_I - \mathbf{R}_J|} \tag{1.2}$$

where, m is the mass of an electron and M_I is the mass of I-th nucleus. The Laplacian operators, ∇_i^2 and ∇_I^2 represent the second order differentiation with respect to the coordinates of i-th electron and I-th nucleus, respectively. e is the charge of an electron and Z_I is the charge of the I-th nucleus. $\mathbf{r}_i$ and $\mathbf{R}_I$ represent the spatial coordinates of i-th electron and I-th nucleus, respectively. In equation 1.2, the first two terms represents the kinetic energy of electrons and nuclei, respectively. The third term represents the Coulomb attraction between electrons and nuclei. The fourth and fifth terms represent the Coulomb repulsion between electron–electron and electron–nuclei, respectively.

1.2.2   Approximations we use while solving the equation

Born-Oppenheimer approximation: Nuclei are heavier than electrons

The first approximation to the above Hamiltonian (equation 1.2) arises by realizing the fact that the nuclei are much heavier than the electrons (for example, carbon atom is $\sim$ 20,000 times heavier than an electron). So, the nuclei kinetic energy will be negligible compared to the electrons kinetic energy. Hence, one can approximate that the nuclei are static and the interactions between the nuclei remain constant. With this approximation, famously known as the *Born-Oppenheimer approximation,* the full Hamiltonian $\hat{H}$ of the equation 1.2 reduces to the electronic Hamiltonian $\hat{H}_{elec}$, given by

$$\hat{H}_{elec} = -\sum_{i=1}^{N_e} \frac{\hbar^2}{2m} \nabla_i^2 - \sum_{i=1}^{N_e} \sum_{I=1}^{N_n} \frac{Z_I e^2}{|\mathbf{r}_i - \mathbf{R}_I|} + \sum_{i=1}^{N_e-1} \sum_{j>i}^{N_e} \frac{e^2}{|\mathbf{r}_i - \mathbf{r}_j|} \tag{1.3}$$

Solution of the above partial differential equation (equation 1.3) gives us the electronic wave-function, ψ_{elec} (hereafter, represented as ψ). Once ψ is known, all interesting properties of the system can be known by operating ψ with the corresponding quantum mechanical operators. For example, Laplacian operator is used to get the kinetic energy of the system. It is important to mention that, although one gets all the properties of a system from ψ, it is not a physical observable. Its modulus square, that is, $|\psi^2|$ $(= \psi^*\psi = |\psi(x_1, x_2, \ldots, x_N)|^2)$ is a physical observable and is interpreted as the simultaneous probability to find electrons 1, 2, ..., N in volumes $dx_1, dx_2, \ldots, dx_N$.

From molecule to molecule, the only changes one need to incorporate in the Hamiltonian (equation 1.3) are the number of electrons N_e, the positions (R_I) and charges (Z_I) of the nuclei. After these changes, all one need to do is to solve $\hat{H}_{elec}$ for ψ. Although, it sounds simple, there is no general strategy to solve $\hat{H}_{elec}$ and one relies on the variational principle to attain the ground state (i.e., the state with

lowest energy), ψ_0, where, variational principle says that the energy of any guess wave-function is greater than the energy of the true ground state wave-function. Thus, the recipe to get ψ_0 is to guess all the wave-functions and choose that wave-function as ψ_0 whose energy is the lowest while solving for $\hat{H}_{elec}$. As it can be noticed, considering all the possible wave-functions is not manageable and one needs suitable subset of wave-functions which can give physically reasonable approximation to the many electron wave-function, ψ_0.

Slater determinant: An approximation to wave-function

Slater determinant is the simplest and widely used approximation to the many body wave-function. It consists of an anti-symmetrized product of N one-electron wave-functions, $\chi_i(x_i)$, as given in the equation 1.4

$$\psi_0(\mathbf{x}_1, \mathbf{x}_2, \ldots, \mathbf{x}_N) \approx \psi_{SD} = \frac{1}{\sqrt{N!}} \begin{vmatrix} \chi_1(\mathbf{x}_1) & \chi_2(\mathbf{x}_1) & \cdots & \chi_N(\mathbf{x}_1) \\ \vdots & \vdots & \ddots & \vdots \\ \chi_1(\mathbf{x}_N) & \chi_2(\mathbf{x}_N) & \cdots & \chi_N(\mathbf{x}_N) \end{vmatrix} \tag{1.4}$$

where, $\chi_i(\mathbf{x}_i)$ are the spin-orbitals formed by the linear combination of the atomic orbitals (such as 1s atomic orbitals of hydrogen which may be either in the slater orbital form or in guassian orbital form). The best Slater determinant, ψ_{SD}, is the one which gives the lowest energy. Different guess wave-functions (here, Slater determinants) can be generated by varying the $\chi_i(\mathbf{x}_i)$'s. Thus, best $\chi_i(\mathbf{x}_i)$'s give the best Slater determinant, and hence, the best approximation for the ψ_0. Flexibility in $\chi_i(\mathbf{x}_i)$'s is offered by the expansion coefficients of the atomic orbitals. So, once we have decided to use ψ_{SD} as an approximation for ψ_0, all we need to do is to determine a set of $\chi_i(\mathbf{x}_i)$'s that gives energy of the system minimum.

However, variation in atomic orbital's coefficients must be carried out in such a way that $\chi_i(\mathbf{x}_i)$'s remain orthonormal. Such constrained optimizations, are generally

handled by means of Lagrange multipliers. Operating, $\hat{H}_{elec}$ on ψ_{SD}, one obtains the Hartree-Fock (HF) equations, solving which gives approximate ground state energy. HF is a mean-field method, where the potential felt by the ith electron due to the left N-1 electrons is only considered in an average manner. Thus, some amount of correlation is neglected in HF method leading to an error in predicted ground state energy. Finally, it is important to notice that, the error in the ground state energy calculated according to HF equations is mainly due to the consideration of single-slater determinant as an approximation to the many body wave-function and the only correlations considered in HF are the exchange and Coulomb interaction between electrons.

Considering HF as starting point, one can include correlations in a system by increasing the number of Slater determinants used to approximate the many body wave-function and all such methods are called as post-HF methods. On the other hand, one may start with a completely different approach, namely, using electron density as the central quantity instead of the wave function and introduce correlation quite significantly. This method, which is known as density functional theory (DFT), is widely used in this thesis.

1.2.3   Density Function Theory

Density functional theory (DFT) is a *ground state* quantum mechanical modeling method used in physics and chemistry for treating a system of interacting electrons. In brief, DFT, in its Kohn-Sham formalism, helps us to map the non-tractable interacting many-body problem into a solvable non-interacting single-body problem. It is one of the most successful methods to investigate the electronic structure of many-body systems, in particular, atoms, molecules and the extended solids, showing satisfactory agreement with the experimental observations. Despite its success, it should always be remembered that DFT is a ground state method and any properties

predicted by DFT related to excited states, for example, using Δ methods (described latter) should be carefully examined. Also, DFT has strong limitations in dealing with strongly correlated systems.

Within DFT, the Hamiltonian ($\hat{H}$) of an N electron system, in the presence of an external field, $V_{ext}(\mathbf{r})$, is expressed as:

$$\hat{H} = \hat{T} + \hat{U} + \hat{V}_{ext} = -\frac{\hbar^2}{2m}\sum_{i=1}^{N}\nabla_i{}^2 + \sum_{i=1}^{N-1}\sum_{j>i}^{N}\frac{e^2}{|\mathbf{r}_i - \mathbf{r}_j|} + \hat{V}_{ext}(\mathbf{r}) \qquad (1.5)$$

Clearly, equations 1.5 and 1.3 are same, except for the fact that, now, apart from electron-nuclei interaction we have also included any external fields (like electric-field etc.) in V_{ext} term and $\hat{T}$, $\hat{U}$ are used to represent the kinetic energy of electrons and the electron-electron repulsion terms. Unlike HF-method, where one starts with an approximate wave-function (typically ψ_{SD}) as a solution to $\hat{H}_{elec}$, in DFT, we rely on the ground state density of the many-body system without any prior approximation. However, in DFT also, one needs to introduce approximations while solving for the many-body ground state density. As will be discussed, in DFT, the major approximation lies in the Hamiltonian (mainly, in exchange-corrleation functional), but not in the density or wave function. Also, DFT is formally an exact theory, unlike HF theory (where, approximation is in wave function).

Formal foundations of DFT lies in the Hohenberg-Kohn (HK) theorems[115–117], where the first theorem proves one to one correspondence between the external potential (V_{ext}) and the ground state density. Thus, if we know the electron density, we uniquely know the Hamiltonian, and hence, all the properties of the system. In other words, as Hamiltonian gives us ψ_0, first theorem proves that ground state wave-function, ψ_0, is a unique functional of density ($\rho_0(\mathbf{r})$), i.e.,

$$\Psi_0(\mathbf{r}) = \Psi_0[\rho_0(\mathbf{r})] \qquad (1.6)$$

Now, because of equation 1.6, expectation value of any observable, $\hat{A}$, in it's ground state will be a functional of ρ_0

$$A[\rho_0] = \langle \Psi_0[\rho_0]|\hat{A}|\Psi_0[\rho_0]\rangle \tag{1.7}$$

Hence, the ground state energy(E_0) will also be a functional of ρ_0.

$$E_0 = E[\rho_0] = \langle \Psi_0[\rho_0]|\hat{T} + \hat{U} + \hat{V}_{ext}|\Psi_0[\rho_0]\rangle \tag{1.8}$$

Thus, through the first HK-theroem, we have shown that any ground state property is a functional of ρ_0, but we didn't establish a way to know whether any arbitrary $\rho(r)$ is indeed ρ_0. Second HK-theorem bridges this gap. It is similar to variational principle and it proves that the energy obtained by any guess density is always greater than or equal (only when it is equal to the ground state density) to the energy obtained by the ground state density. So, the ground state density can be calculated after the minimization of the energy function, $E[\rho]$, with respect to $\rho(\mathbf{r})$ and all other ground-state observables can be calculated from $\rho_0(\mathbf{r})$. The external potential, $\langle \Psi_0[\rho_0]|\hat{V}_{ext}|\Psi_0[\rho_0]\rangle$, in equation 1.8, can be written as,

$$V_{ext} = V_{ext}[\rho_0] = \int \hat{V}_{ext}(\mathbf{r})\rho_0(\mathbf{r})d\mathbf{r} \tag{1.9}$$

More generally, the expectation values of $\hat{T}$, $\hat{U}$ and $\hat{V}_{ext}$ with respect to any arbitrary density, $\rho(\mathbf{r})$, can be written explicitly as:

$$T[\rho] = \langle \Psi[\rho]|\hat{T}|\Psi[\rho]\rangle \tag{1.10}$$

$$U[\rho] = \langle \Psi[\rho]|\hat{U}|\Psi[\rho]\rangle \tag{1.11}$$

$$V_{ext}[\rho] = \langle \Psi[\rho]|\hat{V}_{ext}|\Psi[\rho]\rangle \tag{1.12}$$

$T[\rho]$ and $U[\rho]$ together are called universal functional, as they do not depend on the system of interest. On the other hand, $V_{ext}[\rho]$ depends on systems under study, and hence, it is termed as a non-universal functional of electron density, $\rho_0(\mathbf{r})$. Once the exact form of $T[\rho]$ and $U[\rho]$ are known, we can always get exact results using DFT. Unfortunately, the exact form for the universal functional is not known, and all the approximations in DFT (leading to different exchange correlational functionals) are because of the non-availability of universal functional.

In general, one solves the DFT Hamiltonian, using the Kohn-Sham (KS) formalism. In KS-formalism, energy functional can be considered such that it doesn't have any explicit electron-electron interaction energy term,

$$E_s[\rho] = \langle \Psi_s[\rho] | \hat{T} + \hat{V}_s | \Psi_s[\rho] \rangle \tag{1.13}$$

where, $\hat{V}_s$ is an effective single-particle potential in which particles are moving so that $\rho_s(\mathbf{r}) = \rho(\mathbf{r})$ and V_s can be expanded as:

$$V_s(\mathbf{r}) = V_{ext}(\mathbf{r}) + \int \frac{\rho_s(\mathbf{r}')}{|\mathbf{r} - \mathbf{r}'|} d\mathbf{r}' + V_{xc}(\rho_s(\mathbf{r})) \tag{1.14}$$

The KS equations of this auxiliary non-interacting system are defined as,

$$\left[-\frac{\hbar^2}{2m} \nabla_i^2 + \hat{V}_s \right] \phi_i(\mathbf{r}) = \epsilon_i \phi_i(\mathbf{r}) \tag{1.15}$$

where, $\{\phi_i(\mathbf{r})\}$ are the Kohn-Sham orbitals which reproduce the density of the original many-body system.

$$\rho(\mathbf{r}) = \rho_s(\mathbf{r}) = \sum_{i=1}^{N} |\phi_i(\mathbf{r})|^2 \tag{1.16}$$

Finally, the total energy of the system can be written as:

$$E[\rho(\mathbf{r})] = T_s[\rho(\mathbf{r})] + \frac{1}{2} \int \frac{\rho(\mathbf{r})\rho(\mathbf{r}')}{|\mathbf{r}_i - \mathbf{r}_i'|} d\mathbf{r} d\mathbf{r}' + E_{xc}[\rho(\mathbf{r})]$$
$$+ \int \rho(\mathbf{r}) V_{ext}(\mathbf{r}) d\mathbf{r} \qquad (1.17)$$

where, $T_s[\rho(\mathbf{r})] = -\frac{\hbar^2}{2m} \sum_{i=1}^{N} \int \phi_i^*(\mathbf{r}) \nabla^2 \phi_i(\mathbf{r}) d\mathbf{r}$, is the non-interacting kinetic energy and $V_{xc} = \frac{\delta E_{xc}[\rho(\mathbf{r})]}{\delta \rho(\mathbf{r})}$, is the exchange-correlation potential. There are some important terms in equation 1.17. Firstly, the second and the last terms represents the classical Couloumb interactions between the electron-electron (also, known as the Hartree energy) and electron-nuclei, respectively. Last part of the equation also contains the external fields effects, other than the nuclei potential. Importantly, exact form of these two terms are known, and hence, can be computed in principle. More importantly, the unknown form of the kinetic energy is computed with KS-orbitals of the non-interacting system. Though T_s is not exactly equal to the kinetic energy of the original many-body system, it accounts for a great amount. Cleverly, the rest of the contribution to kinetic energy is added as a part of exchange-corrleation term (E_{xc}). Similarly, several other unknown parts are added to this E_{xc}. Thus, E_{xc}, which may be misleading by its name, not only includes the non-classical exchange and correlation contributions to the potential energy, but also the self-interaction correction and a portion of kinetic energy. As exact functional form of V_{xc} is not known, it has to be approximated to calculate E_{xc}, and hence, $E[\rho(\mathbf{r})]$. The problem of solving the Kohn-Sham equation is done in a self-consistent manner. First, an initial guess for $\rho(\mathbf{r})$ is considered and then the corresponding V_s is calculated. After that, $\{\phi_i(\mathbf{r})\}$ can be calculated by solving the Kohn-Sham equations. From these $\{\phi_i(\mathbf{r})\}$, one can calculate a new density and the process starts all over again. This procedure is then continued until a convergence is reached.

Exchange and Correlation Functionals

There are a variety of approximations for exchange and correlation energy functionals. Some of the E_{xc}'s, which have been used extensively in scientific research are discussed below.

Local Density Approximation (LDA)   The most simplest approximation to the exchange-correlation energy functional, $E_{xc}[\rho(\mathbf{r})]$, is the Local Density Approximation (LDA)[118] which is defined as:

$$E_{xc}^{LDA}[\rho] = \int d\mathbf{r}\epsilon_{xc}(\rho(\mathbf{r})) \cdot \rho(\mathbf{r}) \qquad (1.18)$$

where $\epsilon_{xc}(\rho(\mathbf{r}))$ is the exchange and correlation energy per electron of the homogeneous electron gas with density $\rho(\mathbf{r})$. In this approach, it is considered that the electronic density, $\rho(\mathbf{r})$, is a smooth and homogeneous function in space. Then, any region in space can be treated as a homogeneous electron gas. For spin polarized calculation, the generalization of the LDA is called local spin-density approximation (LSDA) which is defined as,

$$E_{xc}^{LSDA}[\rho_\uparrow, \rho_\downarrow] = \int d\mathbf{r}\epsilon_{xc}(\rho_\uparrow, \rho_\downarrow) \cdot \rho(\mathbf{r}) \qquad (1.19)$$

Generalized Gradient Approximation (GGA)   It is an extended and improved version of LDA functional to systems with inhomogeneous charge densities. For nonuniform charge densities, the exchange-correlation energy can deviate significantly from the uniform result and this deviation can be expressed in terms of the gradient and higher spatial derivatives of the total charge density. As the exchange and correlation energy, in GGA approximation, depend on the gradients of charge density (apart from the local electron densities) it has proved to be an improvement over LDA for systems where the charge density is slowly varying. There are a variety of

formalism for GGA approximation. [119–124]. The exchange and correlation energy is defined as,

$$E_{xc}^{GGA}[\rho, \vec{\nabla}\rho] = \int d\mathbf{r}\epsilon_{xc}(\rho, \vec{\nabla}\rho) \cdot \rho(\mathbf{r}) \tag{1.20}$$

while, for spin polarized systems, the exchange and correlation energy is defined as,

$$E_{xc}^{GSGA}[\rho_\uparrow, \rho_\downarrow, \vec{\nabla}\rho_\uparrow, \vec{\nabla}\rho_\downarrow] = \int d\mathbf{r}\epsilon_{xc}(\rho_\uparrow, \rho_\downarrow, \vec{\nabla}\rho_\uparrow, \vec{\nabla}\rho_\downarrow) \cdot \rho(\mathbf{r}) \tag{1.21}$$

Hybrid Functionals   In hybrid functionals, the exchange and correlation energy includes a mixture of Hartree-Fock exchange with exchange and correlation from different sources, often including various forms of LDA and GGA. For example, for the case of B3LYP (stands for Becke, 3-parameter, Lee-Yang-Parr), [125] one mixes the Hatree-Fock exchange with both LDA (VWN exchange) and GGA (Becke88 exchange) exchange and employs LYP correlation functional. B3LYP exchange-correlation functional is given by:

$$E_{xc}^{B3LYP} = E_x^{LDA} + a_0[E_x^{HF} - E_x^{LDA}] + a_x[E_x^{GGA} - E_x^{LDA}] + \tag{1.22}$$
$$a_c[E_c^{GGA} - E_c^{LDA}] + E_c^{LDA}$$

where, $a_0 = 0.20$, $a_x = 0.72$ and $a_c = 0.81$.

Long range corrected functionals   The non-Coulomb part of exchange functionals typically dies off very rapidly and becomes less accurate at large distances. Therefore, it is not accurate for modeling processes such as electron excitations to higher energy orbitals. Various types of formalisms have been adopted to handle the systems with significant dispersive interactions. Among the many, CAM-B3LYP [126] and ωb97xd [127] are the most commonly used long range corrected functionals.

Pseudopotentials and Numerical Orbitals

In computational physics and chemistry, pseudopotentials are used as an approximation for the simplified description of solving the systems. Pseudopotential approximation is used for (a) reduction of basis set size, (b) reduction of effective number of electrons for explicit consideration and (c) inclusion of relativistic and other effects. Generally it is known that, the core electrons do not participate in chemical bonding and are unaffected by changes in their chemical environment. Therefore, it is a good approximation to consider that all the core electrons of an atom are frozen and an effective external potential is experienced only by valence electrons in the atom. Pseudopotentials are obtained by constructing smoother wave functions in which the oscillations of the valence wave function in the core region are removed. [128, 129] The pseudo wave function and all electron wave function becomes well comparable with each other beyond a particular value of radial distance, which is chosen to be outside of the last node in the all electron wave function; this is called the cutoff radius, r_c. If we can use the same pseudopotential to describe different chemical environments, the pseudopotential is termed as transferable. A good pseudopotential needs to fulfill the following conditions:

- The lowest pseudo wave function generated by the pseudopotential generalization method should not contain any nodes.

- The normalized atomic radial pseudo wave function with an angular momentum l should be equal to the normalized radial all electron (AE) wave function outside a given cut-off radius, r_c (Fig. 1.5):

$$R_i^{PP}(r) = R_i^{AE}(r) \ (r > r_c) \tag{1.23}$$

- Norm conservation: The charge inside of r_c has to be the same for both wave
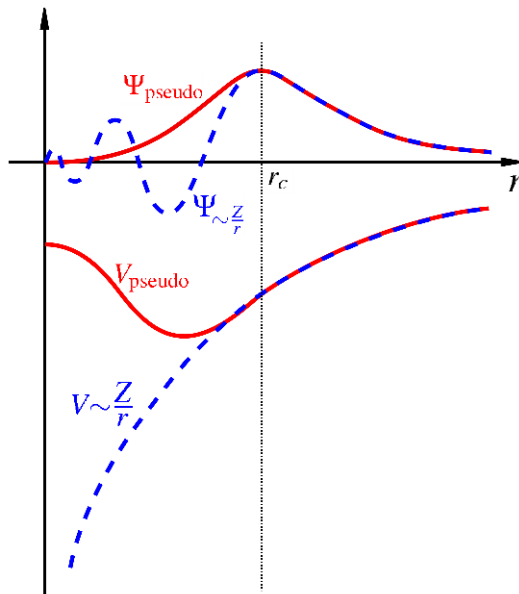
Figure 1.5: Comparison of a wave function in the Coulomb potential of the nucleus (dashed line) to the one in the pseudopotential (continuous line). [130] The real and the pseudo wave function and potentials match above a certain cutoff radius r_c.

functions,

$$\int_0^{r_c} |R_i^{PP}(r)|^2 r^2 dr = \int_0^{r_c} |R_i^{AE}(r)|^2 r^2 dr \tag{1.24}$$

- The eigenvalues of both wave functions should be the same.

There are many packages for the self-consistent calculations of electronic structure using Hartree-Fock and DFT methods. Some of these packages which have been used to study atoms, molecules or nanomaterials are Gaussian, [131] General Atomic and Molecular Electronic Structure System (GAMESS) [132] and Amsterdam Density Functional (ADF) [133] etc. However, since these packages use atom centered basis functions, one cannot handle larger systems. A combination of atom centered basis functions with pseudopotentials make an ideal choice for studying large systems. This has been implemented in the Spanish Initiative for Electronic Simulations with Thousands of Atoms (SIESTA) package, [134] making it an ideal choice for studying realistic systems of large sizes. Other than these, one may adopt CP2K

[135] and Self-Consistent-Charge Density-Functional Tight-Binding (SCC-DFTB) [136] methods to study electronic structure and properties for larger systems. For plane wave basis set, one may use Quantum ESPRESSO [137] or VASP. [138]

1.2.4   Density-Functional Tight-Binding (DFTB)

DFTB is a semi-empirical method based on DFT and it is a very useful method (i) to predict the ground state properties of very large systems (typically, > 1000 atoms) or (ii) to obtain trends from large number of systems belonging to structural families, where calculations with DFT will be quite expensive. Also, DFTB can be used as a supporting tool to run DFT calculations, where one first screen several compounds using DFTB and subsequent calculations will be performed by DFT. DFTB is better than traditional TB, because in DFTB parameters are transferable, though absolute transferability can never be achieved. Because of its tight-binding nature, it yields good results with covalent systems, but not better than DFT. [139]

   Depending on the level of truncation involved in the Taylor series expansion of total energy functional, $E[\rho(r)]$, with respect to a reference density, $\rho_0(r)$, under a small fluctuation, $\delta\rho$, DFTB can be divided into three levels, namely, DFTB (or non-self consistent charge (non-SCC) DFTB), SCC-DFTB and DFTB3. [140, 141] The density $\rho_0(r)$ (generally, composed of atomic densities), doesn't minimize the KS energy functional, $E[\rho(r)]$, but, it is near to the ground state density $\rho(r)$, such that the exact ground state density $\rho(r) = \rho_0(r) + \delta\rho(r)$.

   Following earlier works, [136, 141, 142] one can rewrite the total energy corrected

till the third order in the density fluctuations as below:

$$E[\rho_0(r) + \delta\rho(r)] = \sum_{i=1}^{N} \epsilon_i - E_H[\rho_0(r)] + E_{xc}[\rho_0(r)] - \int V_{xc}[\rho_0(r)]\rho_0(r)dr +$$

$$\frac{1}{2} \int' \int \left(\frac{1}{|r - r'|} + \left.\frac{\delta^2 E_{xc}[\rho]}{\delta\rho\delta\rho'}\right|_{\rho_0} \right) \delta\rho\delta\rho' dr dr' +$$

$$\frac{1}{6} \int'' \int' \int \left.\frac{\delta^3 E_{xc}[\rho]}{\delta\rho\delta\rho'\delta\rho''}\right|_{\rho_0} \delta\rho\delta\rho'\delta\rho'' dr dr' dr'' \quad (1.25)$$

where, the ϵ_i's are the eigenvalues of *non-self consistent* Schrödinger equation, with V(r) being similar to effective KS-potential

$$\hat{H}\psi_i(r) = [-\frac{1}{2}\nabla^2 + V(r)]\psi_i(r) = \epsilon_i\psi_i(r) \quad (1.26)$$

and E_H and E_{xc} are the Hartree and exchange-correlation energies, respectively. Derivation of the equation 1.25 is not straight forward. It mainly depends on the *stationary principle* in DFT. A detailed explanation of stationary principle and the complete derivation of equation 1.25 (till second-order) are given in the section II of Ref. [142].

In the traditional non-SCC DFTB, the last two terms on the right hand side of the Eqn. 1.25 are neglected. This leaves us with the terms which only depend on the reference density ρ_0. So, we enter the non-self consistent scheme i.e., we diagonalize the generalized eigenvalue problem only once. Approximations involved in the DFTB method include: (i) densities and potentials are written as superpositions of atomic densities (so there will not be any charge transfer) and potentials. (ii) terms involving more than two centers (i.e., all the terms other than $\sum_{i=1}^{N} \epsilon_i$ in the first line), together with nuclear repulsion energy terms are written as a sum of pairwise repulsive terms. (iii) Kohn-Sham orbitals are expanded using a minimal basis of optimized atomic orbitals. [143] Thus, non-SCC DFTB will act as a good approximation when the

original many-atom density can be represented as a sum of atom-like densities, but, fails when bonding in the system is dictated by a delicate charge balance between its atoms (as in polar molecules/semiconductors). [136]

In SCC-DFTB, both 1st and 2nd terms of Eqn. 1.25 are considered. Thus, the fluctuations in the charge density are also incorporated while calculating the total energy of the system. Here, the 2nd term is approximated by decomposing the $\delta\rho$ into atomic centered contributions, where, an atom centered contribution is given by

$$\delta\rho_\alpha \approx \Delta q_\alpha F_{00}^\alpha(|\vec{r} - \vec{R}_\alpha|)Y_{00}, \tag{1.27}$$

with F_{ml}^α denoting the normalized radial dependence of density fluctuation on atom α for the corresponding angular momentum and Δq_α is the net charge of atom α. With further approximations, [136] final form of the 2nd term of Eqn. 1.25 is given by:

$$E^{2nd} = \frac{1}{2}\sum_{ab}\Delta q_\alpha\Delta q_\beta\gamma_{\alpha\beta}, \tag{1.28}$$

where, $\gamma_{\alpha\beta}$ accounts for the electron-electron interactions and $\gamma_{\alpha\beta}$ has a dual role: [136, 141] (i) at large inter-atomic distances, XC contributions becomes negligible. Here, E^{2nd} describes pure Coulomb interactions between the two point charges Δq_α and Δq_β. Thus, for large distances, $\gamma_{\alpha\beta} = 1/r_{\alpha\beta}$. (ii) For $\alpha = \beta$, $\gamma_{\alpha\alpha}$ is approximated as the difference between the ionization energy (IE) and electron affinity (EA) of the atom α, similar to the quantum chemistry semi-empirical methods. Thus, at negligible inter-atomic distances, $\gamma_{\alpha\alpha} \approx IA_\alpha$ - $EA_\alpha \approx U_\alpha$ ($\approx$ twice the chemical hardness), describes the Hubbard on-site self-repulsion. U_α is calculated as the second derivative of the total energy of the highest occupied orbital of atom α with respect to its occupation number. As these calculations involve self-consistent DFT, they include the effect of second-order contributions to E_{XC} through $\gamma_{\alpha\beta}$. Analytical form of $\gamma_{\alpha\beta}$, satisfying both of the above roles, is given by the integral over a product

of two normalized Slater-type spherical charge densities [see Ref [136] for further details].

In SCC-DFTB, Hubbard parameter is a constant for an atom irrespective of its charged state and hence, it doesn't distinguish cations/anions from the corresponding neutral species. But, we already know that anions (cations) will have low (high) chemical hardness compared to neutral species. In DFTB3, these shortcomings are addressed by considering all the terms in Eqn. 1.25. Thus, one can use DFTB3 even for highly charged systems [see Ref [141] for further details].

1.2.5   Time Dependent Density-Functional Theory (TDDFT)

Till now, we have gone through the methods, which gives good approximations for the ground state wave-function, energy and related properties. But, these methods are not sufficient enough to tackle the excited states. One may use the ground state methods, like DFT, to calculate the excited state energies in certain scenarios such as when the interested excited state is of different spin-multiplicity (like triplet etc.) or it belongs to a different space group when compared to the ground state. These methods are called Δ methods and their use is very limited. For example, one can't calculate the excited state energy if both the ground and excited states belong to the same symmetry or space-group and this will be the case for general systems of interest. Naturally, one needs a different formalism to explore excited states and, similar to the ground state methods, we do have the wave-function based and density functional based methods to deal with excited states. Wave-function based methods include configuration interaction (CI), time dependent HF etc. and density functional based methods include TD-DFT, TD-DFTB etc. CI and TD-HF are also known as Tamn-Dancoff approximation and random phase approximation (RPA), in nuclear physics literature. [144]

Time-dependent density-functional theory (TDDFT) extends the basic ideas of

ground-state density-functional theory (DFT) to the treatment of excitations or more general time-dependent phenomena. [112] TDDFT can be viewed as an alternative formulation of time-dependent quantum mechanics, but, in contrast to the normal approach that relies on wave-functions and on the many-body Schrödinger equation, its basic variable is the time-dependent electron density, n(r, t). The advantages are clear: The many-body wave-function, a function in a 3N-dimensional space (where N is the number of electrons in the system), is a very complex mathematical object, while the density is a simple function that depends solely on 3 variables, x, y and z. The standard way to obtain n(r, t) is with the help of a fictitious system of non-interacting electrons, the Kohn-Sham system. The final equations are simple to tackle numerically, and are routinely solved for systems with a large number of atoms. These electrons feel an effective potential, the time-dependent Kohn-Sham potential. In the time-dependent case, these Kohn-Sham electrons obey the time-dependent Schrödinger equation

$$i\frac{\partial}{\partial t}\psi_i(\mathbf{r},t) = \left[-\frac{\hbar^2}{2m}\nabla_i^2 + \hat{V}_{KS}(r,t)\right]\psi_i(\mathbf{r},t) \tag{1.29}$$

The density of the interacting system can be obtained from the time-dependent Kohn-Sham orbitals

$$n(r,t) = \sum_i^{occ} \psi_i(\mathbf{r},t) \tag{1.30}$$

1.3 Softwares used

DFT calculations reported in this thesis were carried out using any of Gaussian [131], SIESTA [134] and CP2K[135] packages. DFTB calculations were performed using DFTB+ package. [145] Configuration interaction calculations were done using an in-house code. Xmgrace [146] and gnuplot [147] packages were used for

plotting. Visualizations and graphical analyses were done using GaussView [148], Xcrysden [149], jmol [150] and VMD [151] visualization softwares. Many of the results were analyzed using home developed scripts/codes. The work reported in this thesis required computational calculations which were performed on dedicated home clusters as well as from the resources available in central facilities at Center for Computational Materials Science (CCMS), JNCASR.

1.4   Outline of thesis

Work presented in this thesis is devoted to understand electronic, magnetic and optical properties of a few low-dimensional systems either when they are pristine or when there are defects in these systems or when small molecules/clusters are adsorbed on these low-dimensional systems. All the properties were examined using computer simulations. Different techniques like DFT, TDDFT, CI, ZINDO and DFTB+ were employed to study these properties.

In chapter 2, time-dependent density functional theory (TDDFT) calculations have been used to understand the excited-state properties of modified chlorophyll f (Chlide f), Chlide a, Chlide b, and axial ligated (with imidazole, H_2O, CH_3OH, CH_3COOH, C_6H_5OH) Chlide f molecules. The computed differences among the Q_X, Q_Y, B_X, and B_Y band absorbance wavelengths of Chlide a, b, and f molecules are found to be comparable with experimentally observed shifts for these bands in chlorophyll a (chl a), chl b, and chl f molecules. Our computations provide evidence that the red shift in the Q_Y band of chl f is due to the extended delocalization of macrocycle chlorin ring because of the presence of the –CHO group. The local contribution from the –CHO substituent to the macrocycle chlorin ring stabilizes the corresponding molecular orbitals (lowest unoccupied molecular orbital (LUMO) of the Chlide f and LUMO–1 of the Chlide b). All the absorption bands of Chlide f shift to higher wavelengths on the addition of axial ligands. Computed redox potentials

show that, among the axial ligated Chlide f molecules, Chlide f–imidazole acts as a good electron donor and Chlide f–CH$_3$COOH acts as a good electron acceptor.

In chapter 3, using DFT, we have examined the structural stability, electronic, magnetic, and optical properties of rectangular and cross-shaped quantum dots (QDs) of graphene (G), boron nitride (BN), and their hybrids. Different hybrid QDs have been considered by substituting a GQD (BNQD) with BN-pairs (carbon atoms) at different positions. Several parameters, like size, amount of substitution, and so forth, have been varied for all these QDs to monitor the corresponding changes in their properties. Among the considered parameters, we find that substitution can act as a powerful tool to attain interesting properties with these QDs. For example, a broad range of absorption ($\sim$2000 nm) in the near-infrared (NIR) region, spin-polarized HOMO–LUMO gaps without the application of any external-bias, and so forth, which are highly required in the preparation of opto-electronic and electronic/spintronic devices, among others.

Based on both semiempirical and *ab initio calculations*, in chapter 4, we find that GQDs with inequivalent sublattice atoms can have rich optical and nonlinear optical properties. Based on configuration interaction calculations, with in the Hubbard model, we have predicted the ground state of both Kekulé and non–Kekulé PAHs and we have shown that both these PAHs obey Lieb's theorem in their neutral states.

In chapter 5, utilizing the strengths of nitrogen-doped graphene quantum dot (N-GQD) as a substrate, we have shown that one can stabilize the catalytically more active planar Au$_{20}$ (P-Au$_{20}$) compared with the thermodynamically more stable tetrahedral structure (T-Au$_{20}$) on N-GQDs.

In chapter 6, we have presented our spin-polarized DFT calculations on zigzag boron-nitride nanoribbons (z-BNNRs) with lines of alternating fused pentagon (P) and heptagon (H) rings (pentagon-heptagon (PH) line defect) at a single edge as well as at both edges. Among the different spin-configurations that we have

studied, we find that the spin-configuration with ferromagnetic ordering at each edge and antiferromagnetic ordering across the edges is quite interesting. For this spin-configuration, we find that, if the introduced PH line defect is odd-numbered, the systems behave as spin-polarized semiconductors, but, for even-numbered, all the systems show interesting antiferromagnetic half-metallic behavior. Robustness of these results has been cross checked by the variation of line-defect position and also by the variation of width [from ~ 1.1 nm (6-zBNNR) to ~ 3.3 nm (16-zBNNR)] of the ribbon. The main reason for many of the observed changes was traced back to the change in edge nature of the BNNR, which indeed dictates the properties of the systems.

In the last chapter, based on DFT calculations, we have proposed the unzipping mechanism for both carbon and MoS_2 nanotubes under the laser irradiation in liquid dimethylformamide (DMF). Proposed mechanism includes the formation of vacancies and the generation of induced dipole–moment across the nanotube under the influence of external electric–field due to the charge accumulation near the vacancies. DMF molecules align themselves along the tube axis near the vacancies with their dipoles being parallel to the induced dipoles to minimize their interaction with external field. This leads to the accumulation of further charge near the vacancies and supports longitudinal unzipping of nanotubes.

Bibliography

[1] G. W. Bryant, Phys. Rev. B **37**, 8763 (1988).

[2] M. F. Crommie, C. P. Lutz, and D. M. Eigler, Science **262**, 218 (1993).

[3] B. Delley and E. F. Steigmeier, Phys. Rev. B **47**, 1397 (1993).

[4] G. T. Einevoll, Phys. Rev. B **45**, 3410 (1992).

[5] M. V. R. Krishna and R. A. Friesner, J. Chem. Phys. **95**, 8309 (1991).

[6] G. D. Stucky and J. E. Mac Dougall, Science **247**, 669 (1990).

[7] T. Takagahara and K. Takeda, Phys. Rev. B **46**, 15578 (1992).

[8] M. R. Geller, arXiv preprint cond-mat/0106256 (2001).

[9] K. Y. Arutyunov, D. S. Golubev, and A. D. Zaikin, Physics Reports **464**, 1 (2008).

[10] O. M. Auslaender, H. Steinberg, A. Yacoby, Y. Tserkovnyak, B. I. Halperin, K. W. Baldwin, L. N. Pfeiffer, and K. W. West, Science **308**, 88 (2005).

[11] P. A. Bares and G. Blatter, Phys. Rev. Lett. **64**, 2567 (1990).

[12] G. Binnig, H. Rohrer, G. Ch, and E. Weibel, Appl. Phys. Lett. **40**, 178 (1982).

[13] D. Degiorgi and L., *Strong interactions in low dimensional materials, Introduction* (kluwer academic publishers, 2004).

[14] G. A. Fiete, Reviews of Modern Physics **79**, 801 (2007).

[15] T. Giamarchi and A. J. Millis, Phys. Rev. B **46**, 9325 (1992).

[16] N. Giodano, Physica B: Condensed Matter **203**, 460 (1994).

[17] C. L. Kane and M. P. A. Fisher, Phys. Rev. Lett. **76**, 3192 (1996).

[18] N. Kawakami and Y. Sung-Kil, J. Phys.: Condens. Matter **3**, 5983 (1991).

[19] M. Kohmoto and . . M. Sato, Europhys. Lett. 56, Europhys. Lett. **56** (2001), (2001).

[20] M. G. Zacher, E. Arrigoni, W. Hanke, and J. R. Schrieffer, Phys. Rev. B **57**, 6370 (1998).

[21] M. G. P. W. Y. B. J. V. B. Dardel, D. Malterre and D. Jerome, Europhys. Lett. **24** (1993).

[22] I.-W. Lyo and P. Avouris, Science **253**, 173 (1991).

[23] N. P. Armitage, F. Ronning, D. H. Lu, C. Kim, A. Damascelli, K. M. Shen, D. L. Feng, H. Eisaki, Z. X. Shen, P. K. Mang, et al., Phys. Rev. Lett. **88**, 257001 (2002).

[24] G. Binnig, C. F. Quate, and C. Gerber, Phys. Rev. Lett. **56**, 930 (1986).

[25] R. W. Carpick and M. Salmeron, Chem. Rev. **97**, 1163 (1997).

[26] W. Coene, G. Janssen, M. Op de Beeck, and D. Van Dyck, Phys. Rev. Lett. **69**, 3743 (1992).

[27] A.-A. Dhirani, R. W. Zehner, R. P. Hsung, P. Guyot-Sionnest, and L. R. Sita, J. Amer. Chem. Soc. **118**, 3319 (1996).

[28] M. Gerhard and M. A. Nabil, Appl. Phys. Lett. **53**, 1045 (1988).

[29] F. J. Giessibl, Science **267**, 68 (1995).

[30] D. R. Hansma. and P., Phys.Today **43** (1990).

[31] T. Kondo, A. F. Santander-Syro, O. Copie, C. Liu, M. E. Tillman, E. D. Mun, J. Schmalian, S. L. Bud'ko, M. A. Tanatar, P. C. Canfield, et al., Phys. Rev. Lett. **101**, 147003 (2008).

[32] T. Ohta, A. Bostwick, J. L. McChesney, T. Seyller, K. Horn, and E. Rotenberg, Phys. Rev. Lett. **98**, 206802 (2007).

[33] C. G. Olson, R. Liu, A. B. Yang, D. W. Lynch, A. J. Arko, R. S. List, B. W. Veal, Y. C. Chang, P. Z. Jiang, and A. P. Paulikas, Science **245**, 731 (1989).

[34] M. T. Reetz, W. Helbig, S. A. Quaiser, U. Stimming, N. Breuer, and R. Vogel, Science **267**, 367 (1995).

[35] M. Rief, F. Oesterhelt, B. Heymann, and H. E. Gaub, Science **275**, 1295 (1997).

[36] J. R. Schrieffer and A. P. Kampf, J. Phys. Chem. Solids **56**, 1673 (1995).

[37] Z. L. Wang, J. Phys. Chem. B **104** (2000).

[38] R. R. S. T. A. Jung and . J. K. Gimzewski, Nature 386, Nature **386** (1997), (1997).

[39] L. D. Landau, Phys. Z. Sowjetunion **11** (1937).

[40] L. D. Landau and E. M. Lifshitz, *Statistical Physics*, vol. Part I (Pergamon Press, Oxford, 1980).

[41] N. D. Mermin, Phys. Rev. **176**, 250 (1968).

[42] R. E. Peierls, .Ann. I. H. Poincare **5** (1935).

[43] J. A. Venables and et al., Rep. Prog. Phys. **47**, 399 (1984).

[44] M. S. Dresselhaus and G. Dresselhaus, Advances in Physics **30**, 139 (1981).

[45] T. A. Land, T. Michely, R. J. Behm, J. C. Hemminger, and G. Comsa, Surf. Sci. **264**, 261 (1992).

[46] M. Terai, N. Hasegawa, M. Okusawa, S. Otani, and C. Oshima, Appl. Surf. Sci. **130-132**, 876 (1998).

[47] K. S. Novoselov, A. K. Geim, S. V. Morozov, D. Jiang, M. I. Katsnelson, I. V. Grigorieva, S. V. Dubonos, and A. A. Firsov, Nature **438**, 197 (2005).

[48] K. S. Novoselov, A. K. Geim, S. V. Morozov, D. Jiang, Y. Zhang, S. V. Dubonos, I. V. Grigorieva, and A. A. Firsov, Science **306**, 666 (2004).

[49] S. V. Morozov, K. S. Novoselov, M. I. Katsnelson, F. Schedin, L. A. Pono-marenko, D. Jiang, and A. K. Geim, Phys. Rev. Lett. **97**, 016801 (2006).

[50] M. J. Allen, V. C. Tung, and R. B. Kaner, Chem. Rev. **110**, 132 (2009).

[51] C. N. Rao, A. Sood, K. . Subrahmanyam, and A. Govindaraj, Angew. Chem. Int. Ed. **48**, 7752 (2009).

[52] A. Ghosh, K. S. Subrahmanyam, K. S. Krishna, S. Datta, A. Govindaraj, S. K. Pati, and C. N. R. Rao, J. Phys. Chem. C **112**, 15704 (2008).

[53] D. Barun and et al., Nanotechnology **20**, 125705 (2009).

[54] A. H. Castro Neto, F. Guinea, N. M. R. Peres, K. S. Novoselov, and A. K. Geim, Reviews of Modern Physics **81**, 109 (2009).

[55] F. D. M. Haldane, Phys. Rev. Lett. **61**, 2015 (1988).

[56] G. W. Semenoff, Phys. Rev. Lett. **53**, 2449 (1984).

[57] P. R. Wallace, Phys. Rev. **71**, 622 (1947).

[58] A. K. Geim and K. S. Novoselov, Nat. Mater. **6**, 183 (2007).

[59] M. I. Katsnelson, K. S. Novoselov, and A. K. Geim, Nat Phys **2**, 620 (2006).

[60] S. Dutta and S. K. Pati, J. Mater. Chem. **20**, 8207 (2010).

[61] H. Bing, Y. Qimin, Z. Gang, W. Jian, G. Bing-Lin, D. Wenhui, and L. Feng, Appl. Phys. Lett. **91**, 253122 (2007).

[62] G. Jing, D. Gunlycke, and C. T. White, Appl. Phys. Lett. **92**, 163109 (2008).

[63] H. Scedilahin and R. T. Senger, Phys. Rev. B **78**, 205423 (2008).

[64] V. Barone and J. E. Peralta, Nano Lett. **8**, 2210 (2008).

[65] W. Chen, Y. Li, G. Yu, Z. Zhou, and Z. Chen, J. Chem. Theory Comput. **5**, 3088 (2009).

[66] E. Kan, F. Wu, H. Xiang, J. Yang, and M.-H. Whangbo, J. Phys. Chem. C **115**, 17252 (2011).

[67] L. Lai, J. Lu, L. Wang, G. Luo, J. Zhou, R. Qin, Z. Gao, and W. N. Mei, J. Phys. Chem. C **113**, 2273 (2009).

[68] R. Mukherjee and S. Bhowmick, J. Chem. Theory Comput. **7**, 720 (2011).

[69] S. S. Yamijala and S. K. Pati, J. Phys. Chem. C **117**, 3580 (2013).

[70] F. Zheng, G. Zhou, Z. Liu, J. Wu, W. Duan, B.-L. Gu, and S. B. Zhang, Phys. Rev. B **78**, 205415 (2008).

[71] E. A. Basheer, P. Parida, and S. K. Pati, New J. Phys. **13**, 053008 (2011).

[72] P. Y. Huang, C. S. Ruiz-Vargas, A. M. van der Zande, W. S. Whitney, M. P. Levendorf, J. W. Kevek, S. Garg, J. S. Alden, C. J. Hustedt, and Y. Zhu, Nature **469**, 389 (2011).

[73] M. Pan, E. C. Giro, X. Jia, S. Bhaviripudi, Q. Li, J. Kong, V. Meunier, and M. S. Dresselhaus, Nano Lett. (2012).

[74] H. Zeng, C. Zhi, Z. Zhang, X. Wei, X. Wang, W. Guo, Y. Bando, and D. Golberg, Nano Lett. (2010).

[75] S. Iijima, Nature **354**, 56 (1991).

[76] J. W. Mintmire, B. I. Dunlap, and C. T. White, Phys. Rev. Lett. **68**, 631 (1992).

[77] R. Saito, G. Dresselhaus, and M. Dresselhaus, *Physical Properties of Carbon Nanotubes* (Imperial College Press, 1998), ISBN 9781860942235.

[78] S. Datta, *Electronic Transport in Mesoscopic Systems*, Cambridge Studies in Semiconductor Physics and Microelectronic Engineering (Cambridge University Press, 1997), ISBN 9780521599436.

[79] M. Bockrath, D. H. Cobden, P. L. McEuen, N. G. Chopra, A. Zettl, A. Thess, and R. E. Smalley, Science **275**, 1922 (1997).

[80] S. Hill, Phys. Rev. B **55**, 4931 (1997).

[81] A. Bezryadin, A. R. M. Verschueren, S. J. Tans, and C. Dekker, Phys. Rev. Lett. **80**, 4036 (1998).

[82] A. Thess, R. Lee, P. Nikolaev, H. Dai, P. Petit, J. Robert, C. Xu, Y. H. Lee, S. G. Kim, A. G. Rinzler, et al., Science **273**, 483 (1996).

[83] O. Hod, V. Barone, and G. E. Scuseria, Phys. Rev. B **77**, 035411 (2008).

[84] P. Potasz, A. D. Gl, O. Voznyy, J. A. Folk, and P. Hawrylak, Phys. Rev. B **83**, 174441 (2011).

[85] D. Pan, J. Zhang, Z. Li, and M. Wu, Adv. Mater. **22**, 734 (2010).

[86] Z. Z. Zhang, K. Chang, and F. M. Peeters, Phys. Rev. B **77**, 235411 (2008).

[87] S. Zhu, J. Zhang, C. Qiao, S. Tang, Y. Li, W. Yuan, B. Li, L. Tian, F. Liu, R. Hu, et al., Chem. Commun. **47**, 6858 (2011).

[88] M. Dutta, S. Sarkar, T. Ghosh, and D. Basak, J. Phys. Chem. C **116**, 20127 (2012).

[89] D. Son, B. Kwon, D. Park, W. Seo, Y. Yi, B. Angadi, C. Lee, and W. Choi, Nat. Nanotechnol. **7**, 465 (2012).

[90] S. Baker and G. Baker, Angew. Chem. Int. Ed. **49**, 6726 (2010).

[91] J. Shen, Y. Zhu, X. Yang, and C. Li, Chem. Commun. **48**, 3686 (2012).

[92] Y. Dong, C. Chen, X. Zheng, L. Gao, Z. Cui, H. Yang, C. Guo, Y. Chi, and C. Li, J. Mater. Chem. **22**, 8764 (2012).

[93] D. Ma, W. Ju, X. Chu, Z. Lu, and Z. Fu, Phys. Lett. A (2013).

[94] M. Zhang, L. Bai, W. Shang, W. Xie, H. Ma, Y. Fu, D. Fang, H. Sun, L. Fan, and M. Han, J. Mater. Chem. **22**, 7461 (2012).

[95] A. Bandyopadhyay, S. R. K. C. S. Yamijala, and S. K. Pati, Phys. Chem. Chem. Phys **15**, 13881 (2013).

[96] F. Chen and N. Tao, Acc. Chem. Res. **42**, 429 (2009).

[97] A. Du, Y. Chen, Z. Zhu, R. Amal, G. Q. Lu, and S. C. Smith, J. Amer. Chem. Soc. **131**, 17354 (2009).

[98] W. Sheng, Z. Y. Ning, Z. Q. Yang, and H. Guo, Nanotechnology **21**, 385201 (2010).

[99] Q. Tang, Z. Zhou, and Z. Chen, J. Phys. Chem. C **115**, 18531 (2011).

[100] W. L. Wang, S. Meng, and E. Kaxiras, Nano Lett. **8**, 241 (2007).

[101] L. Ci, L. Song, C. Jin, D. Jariwala, D. Wu, Y. Li, A. Srivastava, Z. F. Wang, K. Storr, L. Balicas, et al., Nat. Mater. **9**, 430 (2010).

[102] Z. Liu, L. Ma, G. Shi, W. Zhou, Y. Gong, S. Lei, X. Yang, J. Zhang, J. Yu, and K. P. Hackenberg, Nat. Nanotechnol. **8**, 119 (2013).

[103] N. Mohanty, D. Moore, Z. Xu, T. Sreeprasad, A. Nagaraja, A. Rodriguez, and V. Berry, Nat. Commun. **3**, 844 (2012).

[104] D. L. Nelson and M. M. Cox, *Lehninger principles of biochemistry*, vol. 5 (WH Freeman New York, 2008).

[105] N. A. Campbell, B. Williamson, and R. J. Heyden, *Biology: Exploring Life* (Massachusetts: Pearson Prentice Hall., Boston, 2006).

[106] Wikipedia, *Thylakoid — wikipedia, the free encyclopedia* (2015), [Online; accessed 9-August-2015].

[107] J. Heimdal, K. Jensen, A. Devarajan, and U. Ryde, J. Biol. Inorg. Chem. **12**, 49 (2007).

[108] M. G. Cory, M. C. Zerner, X. C. Xu, and K. Shulten, J. Phys. Chem. B **102**, 7640 (1998).

[109] M. Gouterman, J. Mol. Spectrosc **6** (1961).

[110] M. Gouterman, G. H. Wagniere, and L. C. Snyder, J. Mol. Spectrosc **11** (1963).

[111] K. McAlpine, *Infrared chlorophyll could boost solar cells* (2010).

[112] F. Jensen, *Introduction to computational chemistry* (John Wiley & Sons, 2013).

[113] W. Koch and M. C. Holthausen, *A chemist's guide to density functional theory*, vol. 2 (2001).

[114] A. Szabo and N. S. Ostlund, *Modern quantum chemistry: introduction to advanced electronic structure theory* (Dover Publications, 1996).

[115] P. Hohenberg and W. Kohn, Phys. Rev. **136**, B864 (1964).

[116] W. Kohn and L. J. Sham, Phys. Rev. **140**, A1133 (1965).

[117] W. Kohn, Rev. Mod. Phys. **71**, 1253 (1999).

[118] D. Ceperley and B. Alder, Phys. Rev. Lett **45**, 566 (1980).

[119] J. P. Perdew, K. Burke, and M. Ernzerhof, Phys. Rev. Lett. **77**, 3865 (1996).

[120] J. P. Perdew and Y. Wang, Phys. Rev. B **45**, 13244 (1992).

[121] J. P. Perdew, J. Chevary, S. Vosko, K. A. Jackson, M. R. Pederson, D. Singh, and C. Fiolhais, Phys. Rev. B **46**, 6671 (1992).

[122] A. D. Becke, Phys. Rev. A **38**, 3098 (1988).

[123] F. A. Hamprecht, A. J. Cohen, D. J. Tozer, and N. C. Handy, J. Chem. Phys. **109**, 6264 (1998).

[124] A. D. Boese, N. L. Doltsinis, N. C. Handy, and M. Sprik, J. Chem. Phys. **112**, 1670 (2000).

[125] A. D. Becke, J. Chem. Phys. **98**, 5648 (1993).

[126] T. Yanai, D. P. Tew, and N. C. Handy, Chem. Phys. Lett. **393**, 51 (2004).

[127] J.-D. Chai and M. Head-Gordon, Phys. Chem. Chem. Phys **10**, 6615 (2008).

[128] G. Bachelet, D. Hamann, and M. Schlüter, Phys. Rev. B **26**, 4199 (1982).

[129] D. Vanderbilt, Phys. Rev. B **41**, 7892 (1990).

[130] Wikipedia, *Pseudopotential — wikipedia, the free encyclopedia* (2015), [Online; accessed 9-August-2015].

[131] M. Frisch, G. Trucks, H. B. Schlegel, G. Scuseria, M. Robb, J. Cheeseman, G. Scalmani, V. Barone, B. Mennucci, G. Petersson, et al., Gaussian Inc., Wallingford (2009).

[132] M. W. Schmidt, K. K. Baldridge, J. A. Boatz, S. T. Elbert, M. S. Gordon, J. H. Jensen, S. Koseki, N. Matsunaga, K. A. Nguyen, S. Su, et al., J. Comput. Chem. **14**, 1347 (1993).

[133] G. Te Velde, F. M. Bickelhaupt, E. J. Baerends, C. Fonseca Guerra, S. J. van Gisbergen, J. G. Snijders, and T. Ziegler, J. Comput. Chem. **22**, 931 (2001).

[134] J. M. Soler, E. Artacho, J. D. Gale, A. García, J. Junquera, P. Ordejón, and D. Sánchez-Portal, J. Phys.: Condens. Matter. **14**, 2745 (2002).

[135] J. Hutter, M. Iannuzzi, F. Schiffmann, and J. VandeVondele, WIREs Comput Mol Sci **4**, 15 (2014).

[136] M. Elstner, D. Porezag, G. Jungnickel, J. Elsner, M. Haugk, T. Frauenheim, S. Suhai, and G. Seifert, Phys. Rev. B **58**, 7260 (1998).

[137] P. Giannozzi, S. Baroni, N. Bonini, M. Calandra, R. Car, C. Cavazzoni, D. Ceresoli, G. L. Chiarotti, M. Cococcioni, I. Dabo, et al., J. Phys.: Condens. Matter. **21**, 395502 (2009).

[138] http://www.vasp.at/.

[139] P. Koskinen and V. Mäkinen, Computational Materials Science **47**, 237 (2009).

[140] M. Elstner and G. Seifert, Philosophical Transactions of the Royal Society of London A: Mathematical, Physical and Engineering Sciences **372**, 20120483 (2014).

[141] M. Gaus, Q. Cui, and M. Elstner, J. Chem. Theory Comput **7**, 931 (2011).

[142] W. M. C. Foulkes and R. Haydock, Phys. Rev. B **39**, 12520 (1989).

[143] G. Seifert and J.-O. Joswig, WIREs Comput Mol Sci **2**, 456 (2012), ISSN 1759-0884.

[144] A. Dreuw and M. Head-Gordon, Chem. Rev. **105**, 4009 (2005).

[145] B. Aradi, B. Hourahine, and T. Frauenheim, The Journal of Physical Chemistry A **111**, 5678 (2007).

[146] GRaphing, Advanced Computation and Exploration of data, http://plasma-gate.weizmann.ac.il/Grace/ (2015).

[147] T. Williams, C. Kelley, et al., Official gnuplot documentation, http://sourceforge. net/projects/gnuplot (2010).

[148] R. Dennington, T. Keith, and J. Millam, Semichem Inc.: Shawnee Mission, KS (2009).

[149] A. Kokalj, J. Mol. Graphics Modell. **17**, 176 (1999).

[150] Jmol: an open-source Java viewer for chemical structures in 3D. http://www.jmol.org/ (2015).

[151] W. Humphrey, A. Dalke, and K. Schulten, J. Mol. Graph. **14**, 33 (1996).

Chapter 2

Computational Studies on Structural and Excited State Properties of Modified Chlorophyll f with Various Axial Ligands *

2.1   Introduction

Chlorophylls (chls) are the essential light harvesting pigments of photosystems present in the thylakoid membrane of plants, algae and cyanobacteria. [1, 2] Five chemically distinct chls, namely, chl a, chl b, chl c, chl d and chl f (see Fig. 1.3) are known to perform oxygenic photosynthesis and all of them absorb solar radiation at different wavelengths. [3, 4] All chls contain a chlorin (reduced porphyrin) ring with Mg at its center (bonded to the nitrogens of the four pyrrole units present in the chlorin ring),

but they differ from each other by their substituents R, R', R", as shown in Fig. 1.3. These substituents affect the π–electron conjugation of the chlorin ring, and thus lead to different absorption spectra. [5]

Spectral properties of chls (except chl f) or their models have been studied by several researchers [4, 6, 7] for many years at different levels of theory, like ZINDO/S-CIS, [8] SAC-CI, [9] *ab initio* methods, [10] TDDFT, [11–13] and CASPT2. [14] In all these studies, four important peaks were observed in the absorption spectra of chls, which include two low energy bands, namely, Q_X and Q_Y and two high energy bands B_X and B_Y. The Q_Y absorption wavelengths of the chls are: chl a (662 nm), chl b (644 nm), chl d (688 nm) and chl f (706 nm). [3, 10, 15, 16] Among all the chls, the Q_Y absorption maximum of chl f is red–shifted and it is in the near infrared (NIR)–region. Chen et. al., [15] discovered chl f from cyanobacteria and reported preliminary structural and spectroscopic studies. However, the reason behind the huge red–shift in the Q_Y band in chl f, when compared with other chls has not been understood. In the present study, we focus our attention on the microscopic understanding behind the unusual spectroscopic signatures of chl f, and to compare and contrast various properties of chl f with other chls.

Although all chls are interesting, our study only focuses on chl f and its structural isomer, chl b. Chl b and chl f structurally differs from each other only by the position of –CHO group (see Fig. 1.3). This makes these systems interesting to study for their optical properties, because just by changing the position of a functional group, there is a huge red-shift in the Q_Y band ($\sim$ 54 nm) of chl f. [15] For a proper microscopic understanding of the structural and spectroscopic properties of these systems, we have employed the *ab initio* methods, density functional theory (DFT) and the time dependent version of it (TDDFT).

To determine the structure of a chl within the complex protein environment is quite challenging. In many chl proteins, the Mg–atom exhibits penta-coordination,
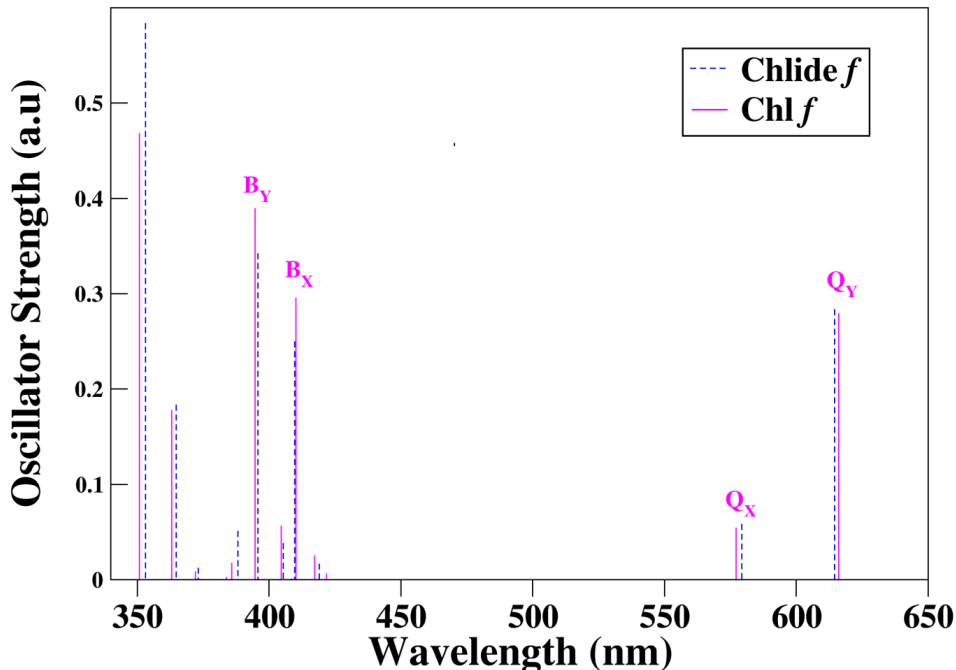
Figure 2.1: TDDFT computed electronic transitions of chl f and Chlide f molecules. Bands are assigned. Observe the minute changes in the position of bands.

[17, 18] where the fifth coordination will generally be with an amino acid residue or with a water molecule. There are a few theoretical papers which considered the effects of axial ligation in chl a. [6, 8, 10, 19–22] The present chapter focuses on the structural and excited state properties of Chlide f in the presence and absence of axial ligands (such as imidazole, CH_3COOH, CH_3OH, C_6H_5OH and H_2O). The calculated structural changes are well supported by the computed NMR results. We also have studied the redox properties of these molecules, since chls in photosystem are involved in electron transfer.

2.2   Computational Details

Initial structures of chl f and chl b are created from the XRD structure of chl a found at 2.5 Å resolution (1JBO.pdb). [23] The substituent at the 17th carbon of the chlorin ring (pyrrole ring II) is modeled as –CH3 group in order to reduce

Table 2.1: Q and B bands of Chl *f* and Chlide *f*. Here 'H' stands for HOMO and 'L' stands for LUMO. Observe the minute changes in the position and nature of bands.

Molecules	Nature	Excitation Wavelength (nm)	Major molecular orbital contributions
Chl *f*	Q_y	616	H to L (0.72)
	Q_x	577	H-1 $\rightarrow$ L (0.72) and H $\rightarrow$ L + 1 (0.20)
	B_y	395	H–1 $\rightarrow$ L+1 (0.62)
	B_x	351	H $\rightarrow$ L+1 (0.50)
Chlide *f*	Q_y	615	H $\rightarrow$ L (0.72)
	Q_x	579	H-1 $\rightarrow$ L (0.73) and H $\rightarrow$ L + 1 (0.19)
	B_y	396	H–1 $\rightarrow$ L+1 (0.61)
	B_x	409	H $\rightarrow$ L+1 (0.51)

the computational cost (see Fig. 1.3). Removal of phytol chain is considered as a reasonable approximation from several previous computational studies on chlorophyll a, which shows negligible changes in the absorption and redox properties of the chl molecules in the absence of phytol chain. [6, 7, 20–22, 22, 24] We refer this modified chlorophyll structure (a chlorophyll whose substituent at 17th carbon of the chlorin ring is modeled with methyl group) as "Chlide". We also have performed calculations considering the complete structure of chlorophylls to know the affects of the substituent at the 17th carbon on the absorption properties of chlorophylls and, as expected, we find little changes in the absorption spectra (see Fig. 2.1 and Table 2.1 for comparison).

As there are two conformers possible with respect to the –CHO group for Chlide *f* and Chlide *b*, geometry optimizations were performed to find the conformer with minimum energy and this minimum energy conformer is considered for further calculations. Five neutral axial ligands are considered in our study. 'Histidine' is modeled as "imidazole", 'Aspartate' as "CH_3COOH", 'Serine' as "CH_3OH", 'Tyrosine as "Phenol" and 'water' as "H_2O". Considering functional groups instead of complete amino acids has been proved to mimic the role of amino acids in various axial ligated chl *a* molecules. [20, 22] The above mentioned axial ligands occur frequently in photosystems of cyanobacterium. [20]

All the geometry optimizations and energy calculations were performed with the

Density Functional Theory (DFT). The three–parameter hybrid functional B3LYP (Beke exchange with Lee, Yang and Parr correlation) [25–27] with 6–31+G (d) basis set is used for all the atoms as implemented in the Gaussian 03 program package. [28] We choose the B3LYP functional, because, it is found to be one of the appropriate functional [7, 10, 12, 13, 19, 20, 24, 29] for the prediction of electronic structure for the various oxidation states of chls. We are aware that this functional is not fully adequate to describe the long–range dispersion forces or stacking interactions, but, we do not expect them to play an important role in the single unit Chlide molecules investigated here. The computed energies have been corrected for basis set superposition error (BSSE) using the counterpoise method. [30, 31] All the molecular properties were calculated at the same level of theory and using the Gaussian 03 program package. ^{1}H–NMR chemical shielding values were calculated using Gauge Including Atomic Orbital (GIAO) method. [32–36] Time Dependent DFT (TDDFT) [37, 38] is used to calculate the absorption properties of the optimized geometries.

In this work, we did not include the implicit solvent effect, since it is already proved that in the continuum model, solvent effect on the neutral ligated chl a molecules are negligible [20] and the initial molecular structures are obtained from 1JBO.pdb crystal structure, where all environmental effects have implicitly been included. In addition, it is known that in protein environment, the inter–molecular H–bonding interaction between axial ligands and the surrounding environment will be dominant, which cannot be mimicked using implicit solvent model. To use an explicit solvent will be expensive and hence, in this work we report only the gas phase results.

2.3 Results and Discussions

In what follows, we have reported the initial structural differences among Chlide f, Chlide b and Chlide a along with the structural changes upon axial ligation,

in section 2.3.1. Bond dissociation energies of axial ligated Chlide *f* molecules are
reported in section 2.3.2. Redox properties are discussed in section 2.3.3. Section 2.3.4
is devoted to the changes in the absorption spectra among different Chlide molecules,
in particular, the reasons for the red–shift in Chlide *f*.
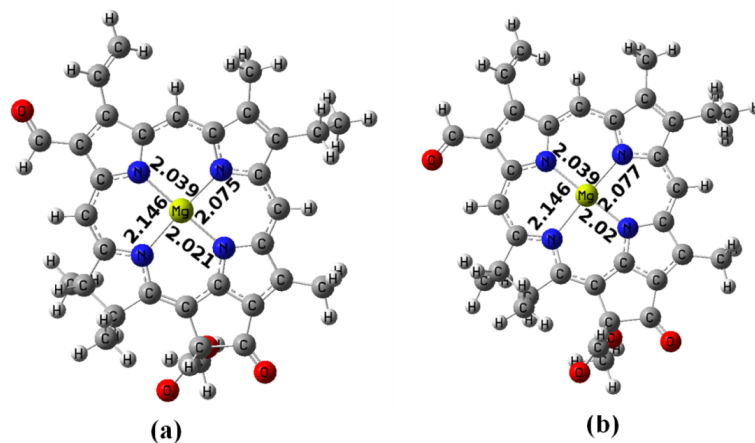
Figure 2.2: Optimized geometry of two stable conformers of Chlide *f* (a) S–cis Chlide *f* (b) S–trans
Chlide *f*. Important bond distances are shown in Å. Note that the Mg is present in the plane of
macrocycle.

2.3.1   Structural changes

In this section, we discuss the structural differences among Chlide *f*, Chlide *a* and
Chlide *b* along with the structural comparison between the two conformers of Chlide
f. In addition, structural changes due to axial ligation are also discussed.

Among the many conformers of chl *b*, the two conformers, S–cis chl *b* (chl *b'*)
and S–trans–chl *b* (chl *b*) are reported to be more stable and with close ground state
energies. [7] We also found the same, where the S–trans conformer turns out to be
more stable than the S–cis conformer. However, the difference in the energies is only
5 kcal mol^{-1}, and hence, both the conformers can be present in gas phase. On the
other hand, one of the conformer might be stabilized in the protein environment due
to the presence of an inter–molecular hydrogen bonding interaction. In order to find
the conformer present in the nature, the chemical shift values of 'formyl hydrogen'

Table 2.2: Computed ^{1}H NMR chemical shift values (ppm) for the H_a, H_b, H_c and formyl hydrogen atoms of various Chlides studied in this paper and the corresponding shifts in the experimentally studied chls. Hydrogen labelling schemes are shown in the Fig. 1.3. Tetramethylsilane (TMS) is used as a reference.

Molecule	Method	H_a	H_b	H_c	Formyl hydrogen
Chlide a	DFT	9.28	9.67	8.51	
Chl a	Exp [39]	9.29	9.54	8.32	
Chlide b	DFT	10.93	9.48	8.17	11.35
Chl b	Exp [40]	10.04	9.64	8.20	11.22
Chlide f	DFT	9.60	9.57	10.17	11.51
Chl f	Exp [15]	9.79	9.86	9.77	11.35
Chlide b'	DFT	9.73	9.71	8.31	11.83
Chlide f'	DFT	9.84	9.64	8.95	11.71
H_2O	DFT	9.57	9.54	10.20	11.55
imidazole	DFT	9.60	9.48	10.15	11.49
CH_3OH	DFT	9.59	9.63	10.09	11.45
CH_3COOH	DFT	9.44	9.66	10.21	11.16
C_6H_5OH	DFT	9.43	9.77	10.15	11.17

for both conformers are computed. Chemical shift value of S–trans Chlide b (11.35 ppm) is comparable with experimental value of chl b (11.25 ppm) (see Table 2.2), than the S–cis Chlide b (11.85 ppm). In addition, our computed values are also in good agreement with the already reported values using CAM–B3LYP functional [15] which validates the functional and basis set used in this study.

Similarly, S–trans conformer of Chlide f is found to be stable by 1 kcal mol^{-1} than the S–cis conformer and the chemical shift value of formyl group for S–cis (11.71 ppm) and S–trans (11.51 ppm) conformers of Chlide f (see Table 2.2) shows that the S–trans conformer chemical shift value is more comparable with experimental value, which is 11.35 ppm. [15] Thus, earlier works and our results on Chlides suggests that chl b and chl f might be present in the S–trans conformation in protein environment, and we have considered only these conformers for further studies reported in this chapter.

In the optimized structure of Chlide f, Mg is in the plane of the chlorin macrocycle, and is coordinated asymmetrically to the four pyrrole nitrogens. The order of the

Table 2.3: Computed important bond distances (Å) and Mülliken partial atomic charges (e) for Chlide a, Chlide b, Chlide b', Chlide f, Chlide f, neutral ligand ligated Chlide f and negative charge ligand ligated Chlide f (Mülliken partial atomic charge on ligated atom in bare ligand are given in italics within brackets).

Molecules	Mg–N1	Mg–N2	Mg–N3	Mg–N4	Mg–ligand	d_{OOP}	Mülliken partial atomic charge (in e)	
							Mg	Ligated atom
Chlide a	2.03	2.15	2.02	2.07	–	0.02	0.84	–
Chlide b	2.03	2.15	2.02	2.08	–	0.03	0.86	–
Chlide b'	2.03	2.15	2.02	2.08	–	0.02	0.82	–
Chlide f	2.04	2.15	2.02	2.08	–	0.02	0.82	–
Chlide f	2.04	2.15	2.02	2.08	–	0.02	0.80	–
H_2O	2.06	2.17	2.04	2.11	2.17	0.24	0.42	-0.84 (-0.93)
imidazole	2.08	2.20	2.06	2.12	2.19	0.37	-2.04	-0.27 (-0.31)
CH_3OH	2.07	2.18	2.04	2.10	2.14	0.27	-0.51	-0.47 (-0.65)
CH_3COOH	2.06	2.17	2.03	2.09	2.25	0.22	-1.23	-0.43 (-0.57)
C_6H_5OH	2.07	2.17	2.04	2.10	2.19	0.26	-1.39	-0.47 (-0.69)
Negative ligands								
CH_3O^-	2.11	2.24	2.08	2.14	1.95	0.54	-0.24	-0.08 (-0.82)
CH_3COO^-	2.12	2.33	2.08	2.16	1.96	0.62	-0.27	-0.22 (-0.63)
$C_6H_5O^-$	2.09	2.21	2.07	2.13	2.02	0.48	-1.44	-0.08 (-0.73)

Mg–N distances are Mg–N2 (2.15 Å) > Mg–N4 (2.08 Å) > Mg–N1 (2.04 Å) > Mg–N3 (2.02 Å), (see Table 2.3) which is similar to the order found for other chls obtained using B3LYP [6, 7, 19–21, 24] and also comparable with the experimental Mg-N bond distance order obtained for ethyl chlorophyllidine a (where the differences in the experimental and calculated bond distances are within 0.02 Å). [41] Longer distance of Mg–N2 is because of the saturation of the corresponding pyrrole ring (ring II).

The effect of the functional groups (R, R' and R") on chlorin ring can further be understood by comparing the structure of Chlide f with those of Chlide a and Chlide b (see Fig. 1.3). Also, changes in the functional groups have a clear impact on the Mg–N1, Mg–N4 bond distances and ^{1}H–NMR chemical shift values of H_a and H_c as shown in the Tables 2.2 and 2.3. The Mg–N1 bond in Chlide f (2.04 Å) is longer than the Mg–N1 bond in Chlide a (2.03 Å) and Chlide b (2.03 Å), due to the presence of the electron withdrawing –CHO substituent at the corresponding pyrrole ring (ring I) of Chlide f (see Table 2.3). Presence of the –CHO substituent at ring I in Chlide f is also the reason for the down-field shift of H_c by 1.66 (2.00) ppm when compared to Chlide a (Chlide b). Similarly, the presence of –CHO group
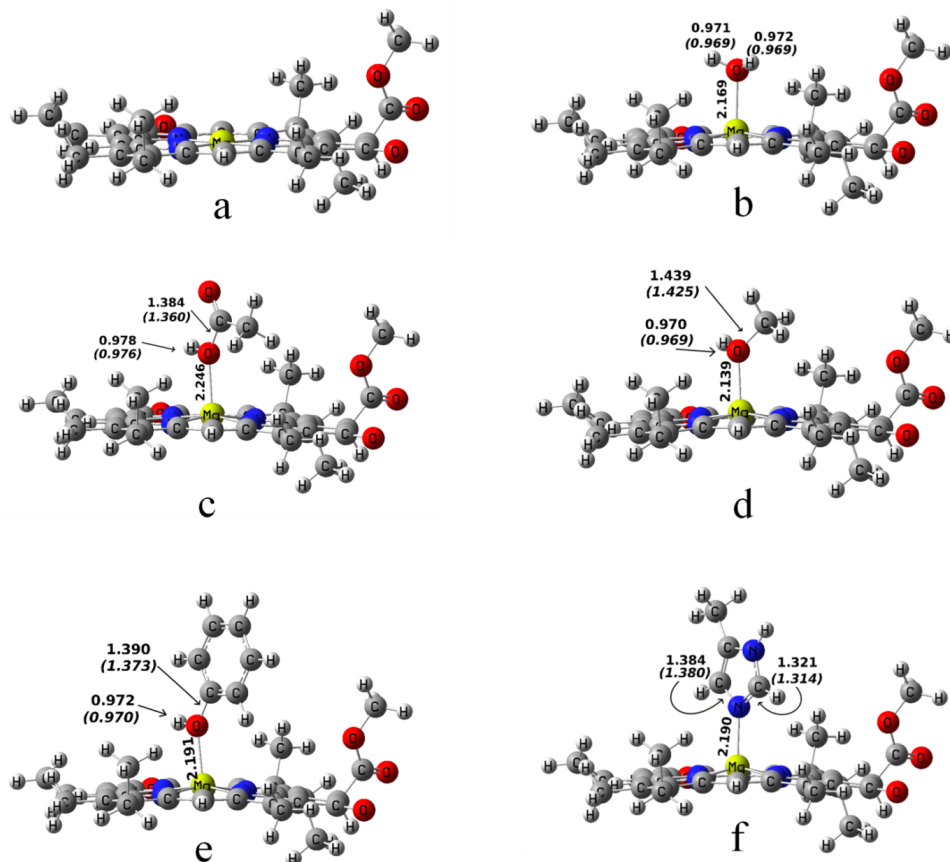
Figure 2.3: Optimized geometry of (a) Chlide f, axial ligated, (b) H_2O, (c) CH_3COOH, (d) CH_3OH, (e) C_6H_5OH and (f) imidazole Chlide f molecules. Important bond distances are shown in Å. Distances of the respective bonds in the bare ligands are written in italics within brackets. The displacement of Mg from the plane can be seen for axial ligated Chlide f molecules and the corresponding distances (d_{OOP}) are shown in the Table 2.3.

at ring IV in Chlide b results in longer Mg–N4 bond (2.08 Å) than Chlide f (2.08 Å) and Chlide a (2.07 Å) (see Table 2.3). In addition, ^{1}H–NMR chemical shielding value of the H_a of Chlide b is shifted down-field by 1.33 (1.65) ppm when compared to the H_a hydrogen of the Chlide f (Chlide a) (see Table 2.2). These results provide an evidence for the most possible chl f conformer in the gas phase. However, the Mg atom of chl f could be penta–coordinated in protein environment, as observed and studied earlier in chl a and chl b. [6, 7, 19–21, 24, 42] As mentioned in the computational details section, we have considered five neutral ligands for our studies.

Coordination of Mg with neutral ligands does not change the order of Mg–N bond distances: Mg–N2 > Mg–N4 > Mg–N1 > Mg–N3 (see Table 2.3). However,

with ligation Mg–N bonds are elongated by 0.01–0.04 Å and Mg atom is displaced from the plane of the macrocycle by 0.2–0.4 Å (see Fig. 2.3). The amount of the displacement of Mg atom is shown by computing out of plane distance (d_{OOP}) (see Table 2.3) by,

$$d_{OOP} = \frac{\left(cos(\frac{\theta}{2})\right) \times (d_1 + d_3)}{2} \qquad (2.1)$$

where, θ is the N1–Mg–N3 bond angle; d_1 = Mg–N1 bond distance; and d_3 = Mg–N3 bond distance.

d_{OOP} distances of Mg are in the order: Mg–imidazole [Mg–N] (0.37 Å) > Mg–CH_3OH [Mg–O] (0.27 Å) > Mg–C_6H_5OH [Mg–O] (0.26 Å) ≈ Mg–CH_3COOH [Mg–O] (0.25 Å) > Mg–H_2O [Mg–O] (0.24 Å). The calculated d_{OOP} of Mg in Mg-H_2O is comparable with the experimentally estimated d_{OOP} (0.385 Å) of Mg in ethyl chlorophyllide a dihydrate. [41] d_{OOP} distance highly depends on the steric class of interactions of the ligated groups (see Table 2.3). There is one exception from the trend, CH_3OH, for which d_{OOP} distance is larger than C_6H_5OH and CH_3COOH. This is due to orientation of CH_3 group of CH_3OH, which is very close to the macrocycle (see Fig. 2.3d).

The computed Mülliken partial atomic charges on Mg atom (of the Chlides) and the ligating atom (of the ligands) clearly shows a ligand to metal charge transfer. Compared with Chlide f Mg atom (0.82 e), the axial ligated Chlide f Mg gains a negative charge of 0.40 e, 2.86 e, 1.33 e, 2.05 e and 2.21 e from H_2O, imidazole, CH_3OH, CH_3COOH and C_6H_5OH, respectively. Among the five neutral ligands, imidazole donates more charge to the metal atom because of the direct coordination of the aromatic ring to the Mg-atom of chlorophyll.

Mg–axial ligand distances are in the order: Mg–CH_3COOH [Mg–O] (2.244 Å) > Mg–imidazole [Mg–N] (2.190 Å) ≈ Mg–C_6H_5OH [Mg–O] (2.190 Å) > Mg–H_2O [Mg–O] (2.168 Å) > Mg–CH_3OH [Mg–O] (2.139 Å). The experimental Mg-H_2O distance in ethyl chlorophyllide a dihydrate 46 is 2.035 Å, which is quite comparable with our

calculated Mg-H_2O bond distance of 2.168 Å. The ligated oxygen atoms of CH_3COOH, C_6H_5OH molecules are attached to the acidic hydrogen, which increases Mg–O bond distances compared with Mg–H_2O distance. However, the larger electrostatic repulsion between the axial -OCH_3 hydrogen and chlorin macrocycle decreases the Mg–O bond distance in Chlide f–CH_3OH (see Fig. 2.3) by distorting Mg atom from its plane. The effect of the presence of acidic hydrogen can further be explained by calculating the Mg–O bond distances for negatively charged $C_6H_5O^-$, CH_3COO^-, CH_3O^- ligands. The Mg–O bond distances are in the order: Mg–$C_6H_5O^-$ (2.02 Å)> Mg–CH_3COO^- (1.96 Å) > Mg–CH_3O^- (1.95 Å) (see Table 2.3), which are smaller than the Mg–H_2O (2.17 Å) bond distance.

Computed Mg–N, d_{OOP}, Mg–Ligand bond distances of axial ligated Chlide f follow the same trend as chl a molecules computed at the B3LYP level of theory, [20] except that these bond distances are shorter in Chlide f by 0.01–0.03 Å. Thus, these results show that, axial ligation to Chlide f affects the macrocycle unit similar to that in chl a.

Additionally, axial ligation to Chlide f follow the similar trend of the chemical shielding values as in Chlide f, i.e., the formyl hydrogen is always in down-field when compared to the H_a, H_b and H_c. But, there are small changes in the chemical shielding values depending upon the orientation of the axial ligands. The presence of electron donating neutral axial ligands shift the chemical shielding values of H_a, H_c, formyl hydrogens by 0.02–0.35 ppm towards upfield (see Table 2.2) and H_b by 0.03–0.20 ppm towards down-field. There are three exceptions from this trend (see Table 2.2).

1. The inter–molecular hydrogen bonding interaction between axial H_2O and substituent formyl group is the reason for the down-field shift in formyl, H_c and the upfield shift in H_b proton.

2. The orientation of imidazole shifts the H_b chemical shielding value towards

Table 2.4: Computed reduction potential (RP1, RP2 in eV) and BSSE corrected Mg–ligand bond dissociation energies (E_{BDE}, KJ mol–1) for Chlide f and axial ligated Chlide f.

Molecules	RP1 = E (N − 1) − E (N) − 4.43 (eV)	RP2 = E (N) − E (N + 1) − 4.43 (eV)	BSSE corrected E_{BDE} (KJ mol^{-1})
Chlide f	2.073	−2.199	0.000
H$_2$O	1.910	−2.253	−45.263
imidazole	1.665	−2.471	−70.704
CH$_3$OH	1.856	−2.308	−48.624
CH$_3$COOH	2.019	−2.144	−25.654
C$_6$H$_5$OH	1.883	−2.253	−34.184

upfield and

3. The H-bonding interaction between the acidic hydrogen of CH$_3$COOH and –CHO is the reason for the down-field shift in the H$_c$.

2.3.2   Bond Dissociation Energy of axial ligated Chlide f

Mg–ligand bond dissociation energy (E_{BDE}) is a measure of its bond strength, which is calculated as,

$$E_{BDE} = E_{[Chlidef-Ligand]} - E_{[Chlidef]} - E_{[Ligand]} \tag{2.2}$$

where, $E_{[Chlidef-Ligand]}$, $E_{[Chlidef]}$ and $E_{[Ligand]}$ are the BSSE corrected energies of the corresponding molecules. These are tabulated in Table 2.4. Negative E_{BDE} values of axial ligated Chlide f molecules, shows their stability. The stability order of ligands (containing oxygen as ligating atom) bonding to Chlide f is: CH$_3$OH > H$_2$O > C$_6$H$_5$OH > CH$_3$COOH (see Table 2.4). E_{BDE} values reflect the Mg-ligand bond distance (see Table 2.3), the shorter the bond, larger is the E_{BDE}. The E_{BDE} values are in the same order as the Mg–ligand bond distances (see Table 2.3), as expected.

Imidazole (Histidine model) has large E_{BDE} value despite of its longer bond distance. The similar larger E_{BDE} value was observed earlier also for imidazole

ligated chl *a*. [20] Interestingly, the reason for strong binding energy of imidazole is traced back due to the direct coordination between aromatic ring and Mg. This direct coordination between imidazole and Mg lead to the large charge transfer (-2.86 e) from imidazole to Mg, which is reflected in the M*ü*lliken partial atomic charge (see Table 2.3) at the Mg center.

2.3.3 Redox properties of Chlide *f* and axial ligated Chlide *f* molecules

One of the major roles of chls in photosystem is that they are involved in electron transfer process, which can be defined by computing reduction potentials (RPs). The reduction potential (RP) is a measure of the ability of a compound to acquire electrons and get reduced. As a chl can accept/donate an electron during the electron transfer process in photosystem, herein, we have considered a redox reaction with three oxidation states, where, N is the number of electrons; RP1 and RP2 are the

$$\text{chls} \atop (\text{N-1}) \quad \underset{\text{-e}}{\overset{\text{+e}}{\rightleftharpoons}} \quad \text{chls} \atop (\text{N}) \quad \underset{\text{-e}}{\overset{\text{+e}}{\rightleftharpoons}} \quad \text{chls} \atop (\text{N+1})$$
$$\qquad\quad\;\text{RP1}\qquad\quad\text{RP2}$$
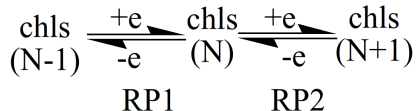
Figure 2.4: Schematic definition of redox potentials RP1 and RP2.

reduction potentials for chls (N-1)/chls (N) and chls (N)/chls (N+1) redox pairs, respectively. RP1 and RP2 values are computed for relaxed geometries of Chlides using the equations

$$RP1 = E(N - 1) - E(N) - 4.43 \tag{2.3}$$

$$RP2 = E(N) - E(N + 1) - 4.43 \tag{2.4}$$

where, the factor 4.43 eV is an estimate of the reduction potential of the standard hydrogen electrode [43] and E is the BSSE corrected energy of the corresponding

oxidation state. RP1 and RP2 values are tabulated in Table 2.4. In general, all the highest occupied and lowest unoccupied molecular orbitals of the Chlide f and axial ligated Chlide f have localized π molecular orbital (see Figs. 2.5 and 2.6) which shows that the redox process has major contributions from the macrocycle ring rather than from the axial ligands. However, addition of axial ligands to Chlide f decreases the RP1 and RP2 values by $\sim$ 0.05–0.4 eV. Thus, electron donating axial ligands brings stabilization to oxidized state (see Table 2.4) except CH_3COOH, which stabilizes the corresponding reduced (N+1) state (see RP2 value of CH_3COOH).

If one compares two compounds, the compound with more positive RP1 or RP2 would acquire the electrons from the other compound and thus acting as an oxidizing agent to the other. Our results provide us an evidence that the CH_3COOH with more positive RP1 and RP2 values can act as an electron acceptor and imidazole with less positive RP1 and RP2 values can act as an electron donor, when compared with other ligands. In addition, it is clear that the order of RPs is in exactly reverse to the order of E_{BDE}s in terms of magnitude. The order of magnitudes of RPs are: $CH_3COOH > H_2O > C_6H_5OH > CH_3OH >$ imidazole.

2.3.4 Absorption properties

There exist a large number of computational studies on chl a, chl b and the related model structures to understand their absorption properties. [10, 44–46] The effect of substituents (on the chlorin macrocycle) on the absorption properties of the chls have also been studied. [8, 10, 21] TDDFT computed absorption spectra of Chlide a, Chlide b and Chlide f are shown in Fig. 2.7. The main peaks of the spectrum are the low energy Q_X and Q_Y band (600–700 nm), the high energy B_X and B_Y bands (350–500 nm). In addition to these bands, we also find a few higher energy bands near the soret region. However, the main emphasis of this work is to understand the underlying reason for the red–shift of experimentally observed Q_Y band of chl
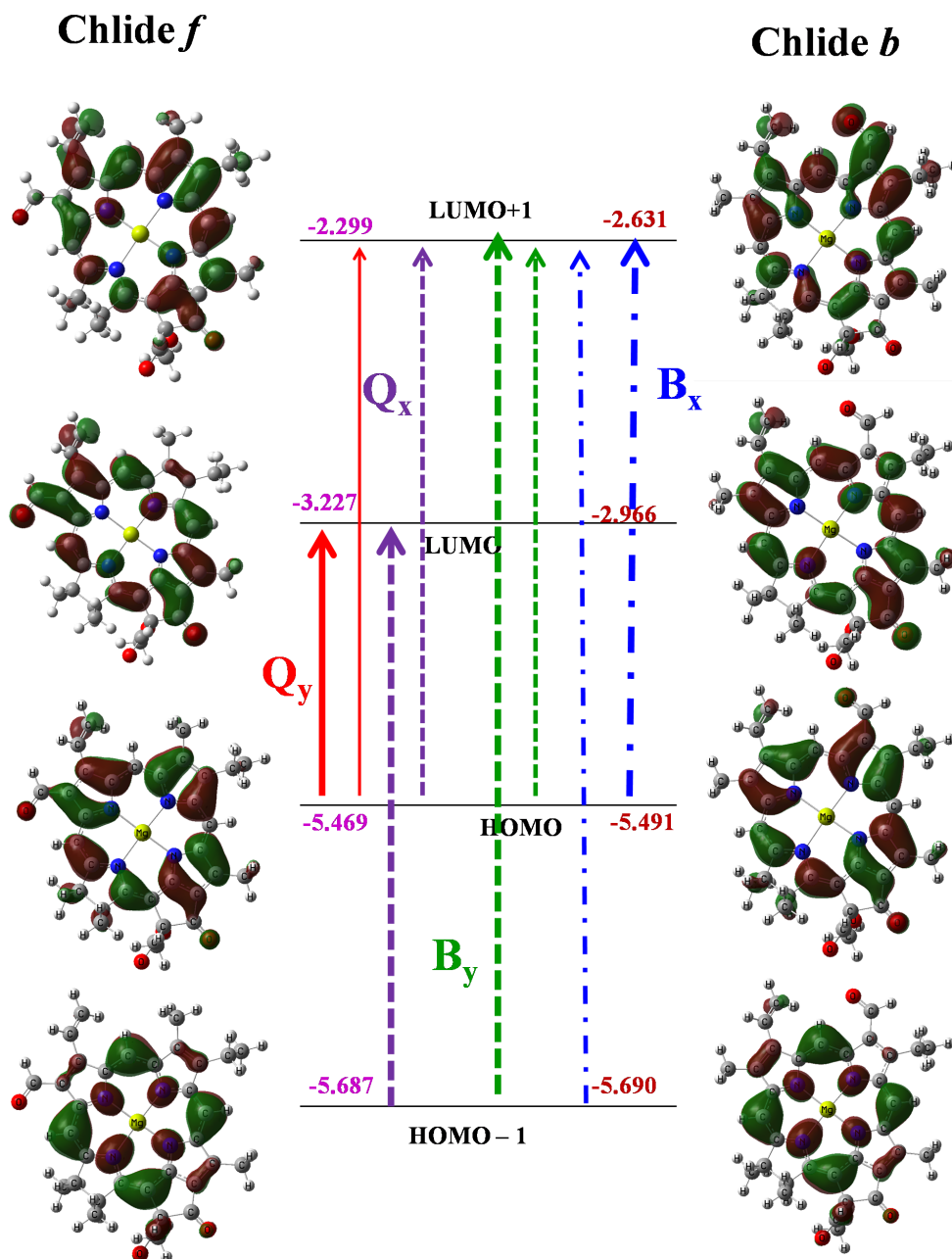
Figure 2.5: Orbital excitation plots of Chlide f and Chlide b. Corresponding MO pictures and MO energies (eV) are shown. The strength of the excitation line reflects its contribution for that absorbance band. Iso-contour values used for molecular orbital plots is $= 0.02$ e $(Bohr)^{-3}$
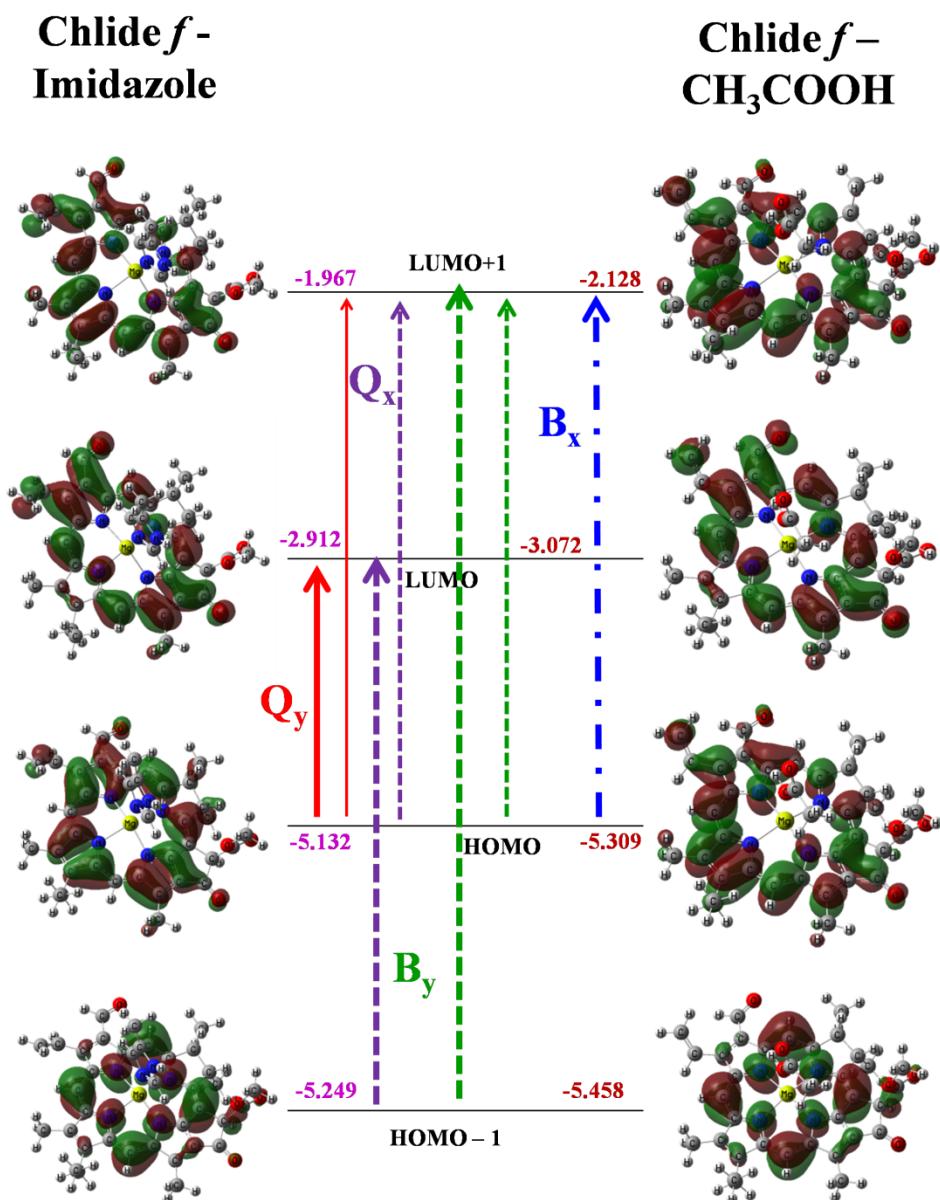
Figure 2.6: Orbital excitation plots of Chlide *f*-imidazole and Chlide *f*-CH$_3$COOH. Corresponding MO pictures and MO energies (eV) are shown. The strength of the excitation line reflects its contribution for that absorbance band. Iso-contour values used for molecular orbital plots is = 0.02 e (Bohr)$^{-3}$
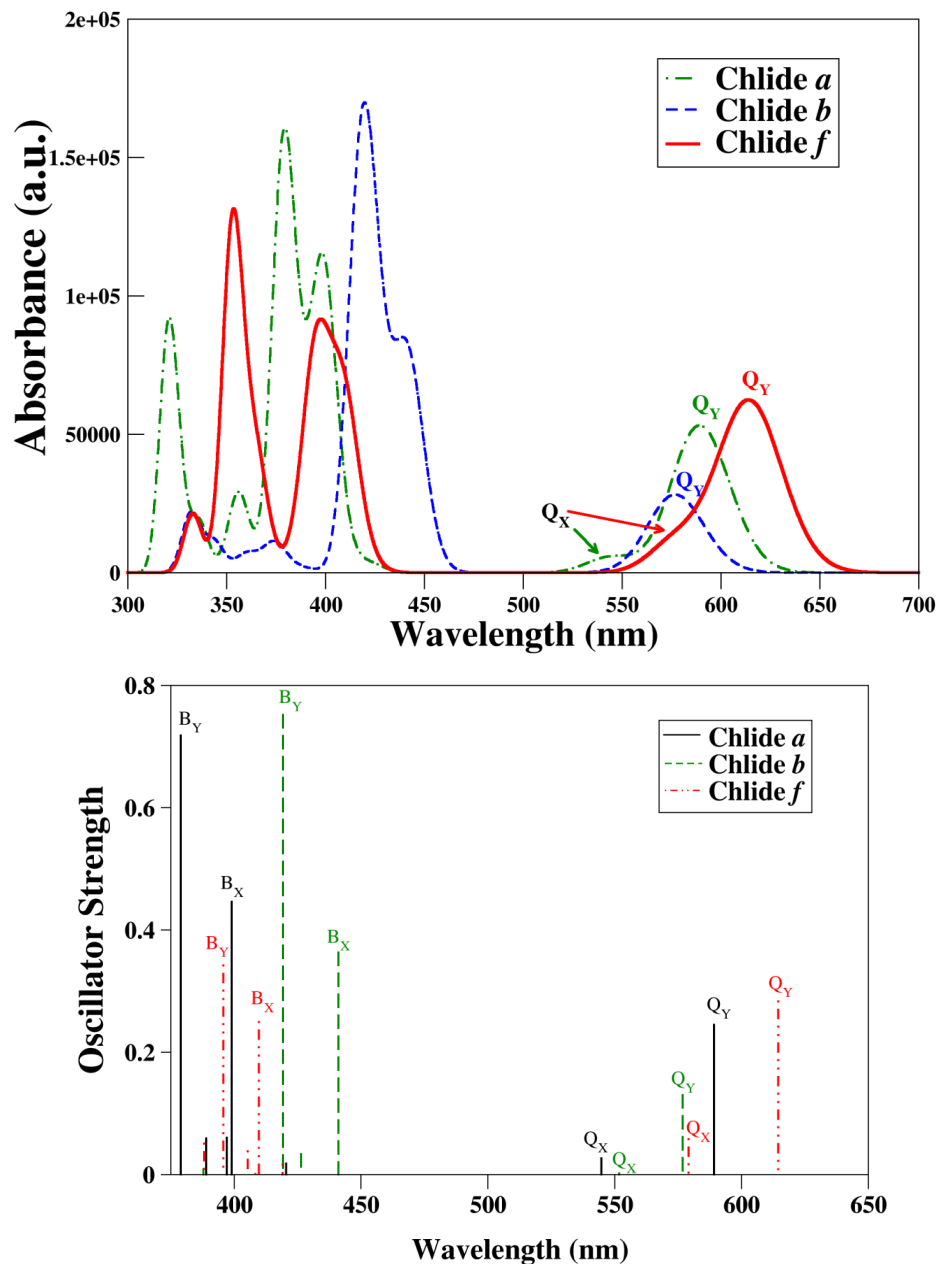
Figure 2.7: (a) Computed absorption spectra of Chlides a, b and f, where Full Width Half Maximum, FWHM= 1000 cm-1. (b) Computed absorption spectra of Chlides *a, b* and *f*. Transitions Q_Y, Q_X, B_X, B_Y are assigned.

f compared to chl *a* and chl *b*. This can be explained by computing molecular orbital (MO) energies and the MO contributions to each excitation as shown in the Table 2.5 and Figs. 2.8 and 2.5. Our computed results for Q_Y bands in Chlide a (589 nm), Chlide *b* (577 nm) and Chlide *f* (615 nm) are lower by $\sim$ 79-91 nm than the experimental transition energies of chl *a* (657 nm), chl *b* (662 nm) and chl *f* (706
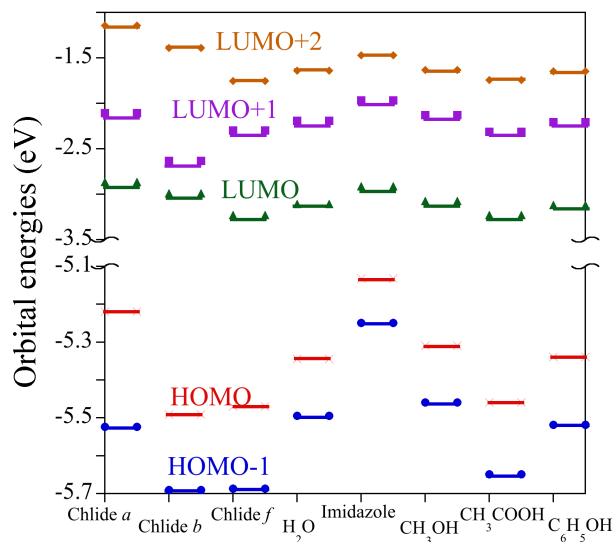
Figure 2.8: HOMO–LUMO energy plots of Chlide a, Chlide b, Chlide f, Chlide f-H_2O (H_2O), Chlide f-imidazole (imidazole), Chlide f-CH_3OH (CH_3OH), Chlide f-CH_3COOH (CH_3COOH) and Chlide f-C_6H_5OH (C_6H_5OH) in eV.

nm) due to the absence of protein environment. However, the transition energies follow the same trend as in the experiment i.e., Chlide b < Chlide a < Chlide f. Also, the shift in the Q_Y bands of Chlide b and Chlide f with respect to the Q_Y bands of Chlide a is –12 nm and +26 nm, which are comparable with the experimental shifts of –13 nm and +41 nm, respectively. [3, 15] The small differences might be due to the absence of protein environment in our studies. Inclusion of the substituent at C17 to Chlide f is found to change the absorption peak values by only 1-2 nm. This can be understood from the molecular orbital plots which show almost no contribution (not shown here) from the phytol chain to the low energy molecular orbitals (see Fig. 2.1 and Table 2.1)

Table 2.5: Computed excitation wavelength (nm) for the Chlide a, Chlide b, Chlide f and axial ligated Chlide f molecules. Major orbital contributions for the corresponding excitations are also given. In this table 'H' denotes HOMO and 'L' denotes LUMO.

Molecules	Nature	Excitation Wave-length (nm)	Major molecular orbital contributions
Chlide a	Q_Y	589	H to L (0.71)
	Q_X	545	H-1 to L (0.65) and H to L + 1 (0.31)
	B_Y	379	H–1 to L+1 (0.57)
	B_X	399	H to L+1 (0.39) and H-3 to L (0.13)
Chlide b	Q_Y	577	H–1 to L+1 (0.27) and H to L (0.65)
	Q_X	552	H-1 to L (0.56) and H to L + 1 (0.40)
	B_Y	419	H–1 to L+1 (0.20) and H to L+1 (0.24)
	B_X	441	H–1 to L+1 (0.36) and H to L+1 (0.16)
Chlide f	Q_Y	615	H to L (0.72)
	Q_X	579	H-1 to L (0.73) and H to L + 1 (0.19)
	B_Y	396	H–1 to L+1 (0.61)
	B_X	409	H to L+1 (0.51)
H_2O	Q_Y	618	H to L (0.71)
	Q_X	596	H-1 to L (0.74) and H to L + 1 (0.16)
	B_Y	408	H–1 to L+1 (0.53)
	B_X	416	H-2 to L (0.31) and H to L+1 (0.33)
imidazole	Q_Y	622	H to L (0.71)
	Q_X	609	H-1 to L (0.74) and H to L + 1 (0.13)
	B_Y	413	H–1 to L+1 (0.42) and H to L+1 (0.24)

	B$_X$	421	H to L+1 (0.38) and H-1 to L+1 (0.22)
CH$_3$OH	Q$_Y$	617	H to L (0.72)
	Q$_X$	596	H-1 to L (0.74) and H to L + 1 (0.15)
	B$_Y$	406	H–1 to L+1 (0.50)
	B$_X$	414	H–1 to L+2 (0.15) and H to L+1 (0.52)
CH$_3$COOH	Q$_Y$	619	H to L (0.71)
	Q$_X$	588	H-1 to L (0.74) and H to L + 1 (0.13)
	B$_Y$	407	H–1 to L+1 (0.33) and H-4 to L (0.39)
	B$_X$	418	H–3 to L (0.28) and H to L+1 (0.23)
C$_6$H$_5$OH	Q$_Y$	620	H to L (0.72)
	Q$_X$	593	H-1 to L (0.73) and H to L + 1 (0.17)
	B$_Y$	403	H–1 to L+1 (0.32) and H-4 to L (0.39)
	B$_X$	359	H–3 to L (0.17) and H to L+1 (0.44)

From the TDDFT results one can see that the major contributions to the Q$_Y$ band of all chls involves the excitations from HOMO → LUMO (coefficient value ∼ 0.65) and HOMO–1 → LUMO+1 (coefficient value ∼ 0.2). Among these two, the HOMO → LUMO excitation has major contribution (coefficient value ∼ 0.7) in the Q$_Y$ band rather than the HOMO–1 → LUMO+1 (coefficient value ∼ 0.2). We find that orbital energy differences among these frontier orbitals (see Fig. 2.8) can explain the position of Q$_Y$ bands in Chlides *a*, *b* and *f*. For the case of Chlide *a*, it is clear that due to the absence of electron withdrawing –CHO group, there is a larger HOMO–LUMO gap leading to larger excitation energy.

Presence of electron withdrawing –CHO group stabilizes the orbital energy of LUMO for Chlide *f* and LUMO+1 for Chlide *b* (see Fig. 2.5). HOMO and HOMO–1 of both Chlide *f* and Chlide *b* have the same amount of contribution from the –CHO
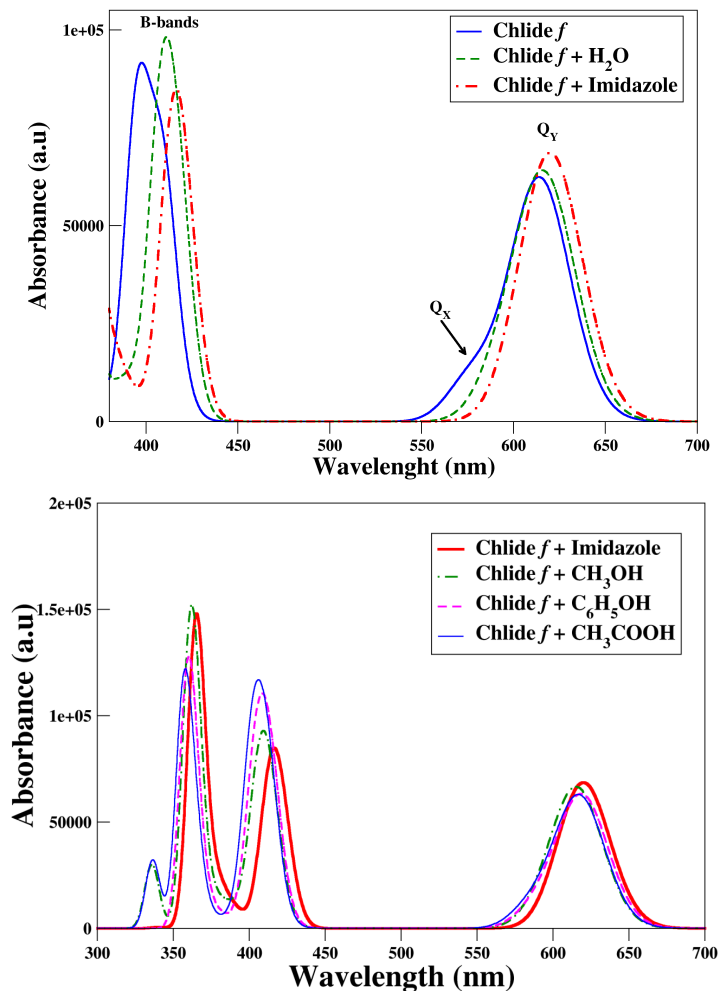
Figure 2.9: Computed absorption spectra of Chlide *f* with and without axial ligation. Name of the axial ligand is given in the legend.

group 15–16 % and 3–4 % respectively, and also, they have similar energy values. However, the LUMO of Chlide *f* has 31 % contribution from –CHO group, which stabilizes the LUMO level by 0.3 eV than its corresponding Chlide *b* LUMO orbital which has only 3 % –CHO group contribution (see Fig. 2.5). Similarly, LUMO+1 of Chlide *f* with smaller –CHO contribution (13 %) destabilizes the orbital energy by 0.1 eV compared to the LUMO+1 of Chlide *b*, which has larger (46 %) –CHO contribution. This shows that the MO with more (less) contribution from –CHO group stabilizes (destabilizes) the corresponding level.

Now, as HOMO $\rightarrow$ LUMO excitation has major contribution to the Q_Y band

and as HOMO energy is almost same in both Chlide b and Chlide f, the deciding factor is the LUMO energy. As LUMO is most stabilized in Chlide f, it is the most red-shifted chlorophyll (when compared to Chlide b). In addition to the Q_Y band, the Q_X bands were observed at 545 nm, 552 nm and 579 nm with lower intensity as shown in Fig. 2.7 for Chlides a, b and f, respectively. The Q_X band in all the Chlides has a major contribution from the HOMO-1 $\rightarrow$ LUMO transition. The red shift in Q_X band in Chlide f is due to the same reason as found in Q_Y band. The changes in the band position due to the change in the –CHO local contribution to a specific molecular orbital can also be observed in the higher energy B_X (370-400 nm) and B_Y (300-350 nm) bands, which have the major contributions from the excitations HOMO $\rightarrow$ LUMO+1 and HOMO–1 $\rightarrow$ LUMO+1, respectively (see Table 2.5 and Fig. 2.5). As the LUMO + 1 orbital is more stablilized in Chlide b than in Chlide f (due to the extra contribution of –CHO in Chlide b), B_X (32 nm) and B_Y (23 nm) bands of Chlide b are red-shifted compared to Chlide f. Thus, the specific coordination between the π orbital of macrocycle ring and the –CHO unit is the primary reason for the red/blue shift of any band in Chlide f when compared with Chlide b.

Note that, all four excitation bands have major contribution from the π orbital of macrocycle chlorin ring, and are not affected by axial ligation (see Fig. 2.6). However, all bands of Chlide f are red–shifted on axial ligation (see Fig. 2.9). Our calculations show a shift of about 5–10 nm in the Q_Y band and 9–30 nm in the Q_X band depending on the nature of the fifth ligand, which can be understood, again, by observing the changes in the energies of HOMOs and LUMOs up on addition of axial ligand (Table 2.5). All the occupied MOs of axial ligated Chlide f are destabilized with the addition of axial ligands, which is the reason for a red shift in Q_X, Q_Y, B_X and B_Y bands (see Table 2.5 and Fig. 2.8).

2.4 Conclusions

Density functional theory and time dependent density functional theory computations have been carried out to understand the different electronic excited state properties of Chlide f, compared to its structural isomer Chlide b. For Chlide f and Chlide b, computed ^{1}H-NMR chemical shielding values show a down-field chemical shift for formyl hydrogen than H_a, H_b and H_c, which compares well with the experimental values. Axial ligation to Chlide f distorts Mg atom from its plane, however, it follows the similar trend of the chemical shielding values as in Chlide f, where the formyl hydrogen is always in down-field when compared to the H_a, H_b and H_c.

In general, low energy Q_X, Q_Y and high energy B_X and B_Y bands are observed for all chls, which have a major contribution from π-type molecular orbitals (HOMO, HOMO-1, LUMO and LUMO+1) localized on the macrocycle chlorin ring. Computed B_X, B_Y, Q_X and Q_Y bands' excitation energies of Chlide a, Chlide b and Chlide f are in good agreement with available experimental, and in certain cases, with earlier theoretical reports. We have found that the LUMO of Chlide f is stabilized due to the larger contribution of –CHO substituent, which is the reason for its red shift of Q_X and Q_Y bands of Chlide f when compared with Chlide b. Even in the presence of axial ligation, the macrocycle chlorin ring plays a major role in the excitation and the redox processes. Axial ligation shows red–shift in the all bands. Our results provide the evidence that Chlide f–CH$_3$COOH with more positive reduction potential values acts as electron acceptor and Chlide f–imidazole with less positive reduction potential values acts as an electron donor, when compared with other possible ligands.

Bibliography

[1] X. Hu, T. Ritz, A. Damjanovic, F. Autenrieth, and K. Schulten, Q. Rev. Biophys. **35**, 62 (2002).

[2] D. L. Nelson and M. M. Cox, *Lehninger principles of biochemistry*, vol. 5 (WH Freeman New York, 2008).

[3] R. J. Porra, *Recent advances and re-assessments in chlorophyll extraction and assay procedures for terrestrial, aquatic, and marine organisms, including recalcitrant algae. In: Chlorophylls* (Boca Raton, FL, Raton, 1991).

[4] H. Scheer, *Chlorophylls and Bacteriochlorophyll* (Springer, Dordrecht, Netherlands., 2006).

[5] M. G. Cory, M. C. Zerner, X. C. Xu, and K. Shulten, J. Phys. Chem. B **102**, 7640 (1998).

[6] A. Ben Fredj, Z. Ben Lakhdar, and M. F. Ruiz-Lpez, Chem. Phys. Lett. **472**, 243 (2009).

[7] Z. Vokácová and J. Burda, J. Phys. Chem. A **111**, 5864 (2007).

[8] J. Linnanto and J. Korppi-Tommola, J. Comput. Chem. **25**, 123 (2004).

[9] J. Hasegawa, Y. Ozeki, K. Ohkawa, M. Hada, and H. Nakatsuji, J. Phys. Chem. B **102**, 1320 (1998).

[10] J. Linnanto and J. Korppi-Tommola, Phys. Chem. Chem. Phys **8**, 663 (2006).

[11] D. Sundholm, Chem. Phys. Lett. **317**, 545 (2000).

[12] D. Sundholm, Chem. Phys. Lett. **317**, 392 (2000).

[13] D. Sundholm, Chem. Phys. Lett. **302**, 480 (1999).

[14] Z.-L. Cai, M. J. Crossley, J. R. Reimers, R. Kobayashi, and R. D. Amos, J. Phys. Chem. B **110**, 15624 (2006).

[15] M. Chen, M. Schliep, R. D. Willows, Z. L. Cai, B. A. Neilan, and H. Scheer, Science **329**, 1318 (2010).

[16] L. L. Shipman, T. M. Cotton, J. R. Norris, and J. J. Katz, J. Amer. Chem. Soc. **98**, 8222 (1976).

[17] T. S. Balaban, P. Braun, C. Hättig, A. Hellweg, J. Kern, W. Saenger, and A. Zouni, Biochimica et Biophysica Acta (BBA)-Bioenergetics **1787**, 1254 (2009).

[18] T. Oba and H. Tamiaki, Photosynth. Res. **74**, 1 (2002).

[19] A. B. Fredj and M. F. Ruiz-Lopez, J. Phys. Chem. B **114**, 6 (2010).

[20] J. Heimdal, K. Jensen, A. Devarajan, and U. Ryde, J. Biol. Inorg. Chem. **12**, 49 (2007).

[21] J. Linnanto and J. Korppi-Tommola, Phys. Chem. Chem. Phys **2**, 4962 (2000).

[22] Y. Sun, H. Wang, F. Zhao, and J. Sun, Chem. Phys. Lett. **387**, 12 (2004).

[23] I. Grotjohann and P. Fromme, Photosynth. Res. **85**, 51 (2006).

[24] P. J. O'Malley and S. J. Collins, J. Amer. Chem. Soc. **123**, 11042 (2001).

[25] A. D. Becke, J. Chem. Phys. **98**, 5648 (1993).

[26] C. Lee, W. Yang, and R. G. Parr, Phys. Rev. B **37**, 785 (1988).

[27] R. G. Parr and W. Wang, *Density-Functional Theory of Atoms and Molecules* (Oxford University Press, New York, 1989), ISBN 0195092767.

[28] M. J. Frisch, G. W. Trucks, H. B. Schlegel, G. E. Scuseria, M. A. Robb, J. R. Cheeseman, J. J. A. Montgomery, T. Vreven, K. N. Kudin, J. C. Burant, et al., *Gaussian 03, Revision C.02*, Gaussian, Inc., Pittsburgh PA (2003).

[29] D. Frolov, M. Marsh, L. I. Crouch, P. K. Fyfe, B. Robert, R. v. Grondelle, A. Hadfield, and M. R. Jones, Biochemistry (Mosc.) **49**, 10 (2010).

[30] S. F. Boys and F. Bernardi, Mol. Phys **19**, 553 (1970).

[31] S. Simon, M. Duran, and J. Dannenberg, J. Chem. Phys. **105** (1996).

[32] J. R. Cheeseman, G. W. Trucks, T. A. Keith, and M. J. Frisch, J. Chem. Phys. **104**, 5497 (1996).

[33] R. Ditchfield, Mol. Phys **27**, 789 (1974).

[34] F. London, J. Phys. Radium **8**, 397 (1937).

[35] R. McWeeny, Phys. Rev. **126** (1962).

[36] K. Wolinski, J. F. Hilton, and P. Pulay, J. Amer. Chem. Soc. **112**, 8251 (1990).

[37] C. V. Caillie and R. D. Amos, Chem. Phys. Lett. **317**, 159 (2000).

[38] R. E. Stratmann, G. E. Scuseria, and M. J. Frisch, J. Chem. Phys. **109**, 8218 (1998).

[39] K. M. Smith, D. A. Goff, and R. J. Abraham, Org. Magn. Reson **22**, 779 (1984).

[40] S. M. Wu and C. A. Rebeiz, J. Biol. Chem. **260**, 3632 (1985).

[41] H.-C. Chow, R. Serlin, and C. E. Strouse, J. Amer. Chem. Soc. **97**, 7230 (1975).

[42] M. Chen, L. L. Eggink, J. K. Hoober, and A. W. D. Larkum, J. Amer. Chem. Soc. **127**, 2052 (2005).

[43] H. Reiss and A. Heller, J. Phys. Chem. **89**, 4207 (1985).

[44] M. G. Dahlbom and J. R. Reimers, Molecular Physics **103**, 1057 (2005).

[45] M. Gouterman, J. Mol. Spectrosc. **6**, 138 (1961).

[46] M. Gouterman, G. H. Wagnière, and L. C. Snyder, J. Mol. Spectrosc. **11**, 108 (1963).

Chapter 3

Electronic properties of zigzag, armchair and their hybrid quanutm dots of graphene and boron-nitride with and without substitution: A first principles study *

3.1 Introduction

Complex devices based on graphene nanoribbons (GNRs), like, GNR-FETs, [1] p-n junctions,[2] spin-filters, [3] etc. have been studied theoretically and some of them have already been realized experimentally. [4] Recently, researchers have

---

started focusing on various shaped nanoribbon junctions which could be the plausible building blocks for 2D-nano-networks. Several shaped nanoribbon junctions, namely, L-shaped, [5] T-shaped, [6] cross-shaped, [7–9] S-shaped, [10] and Z-shaped [11] have been studied and most of these studies have concentrated on the conduction properties of these junctions.

A Z-shaped GNR junction has been shown as a promising candidate to confine the electronic states completely i.e., a quantum dot (QD) can be realized at the junction. [11] Also, conductance through a Z-shaped nanoribbon junction is highly dependent on the angle and width of the junction. [12] Not only GNR, but also boron-nitride nanoribbon (BNNR) junctions have been studied and Z-shaped BNNR junctions were shown to exhibit spin-filtering as well as rectifying effects at the nano-junction depending on the nature of the edge passivation. [13] L-shaped GNRs show low reflectance to the electrons for a large included angle and high reflectance for low included angle when the L-shaped-junction is made of an armchair GNR (AGNR) and a zigzag GNR (ZGNR), and, an opposite effect has been observed when the L-shaped-junction is made of two ZGNRs. [5] Similar spin-polarized calculations on the in-plane conductance of the GNR-cross points at different angles have shown large-scattering for quantum transport, except when two ZGNR ribbons meet at 60° angle. [14] Studies on the T-shaped junctions showed that, these systems are metallic and their conduction properties are sensitive to the height of the stem and the doping position, i.e., whether the doping is on the stem or on the shoulder. [6] Similar results were reported for the cross-shaped ribbons. [8, 9] Spin-polarized-conductance calculations on a cross-shaped junction showed a transverse spin current with zero charge-current. [8]

Motivated by the above mentioned interesting spin-polarized conducting properties of cross-shaped ribbon networks obtained from the theoretical calculations [7–9] and by the recent experimental realization of the various QDs,[15] we have performed

the spin-polarized density functional theory (DFT) calculations to understand the electronic and magnetic properties of the cross-shaped (+ shaped) graphene (G) and boron-nitride (BN) QDs. These QDs can be considered as the low-dimensional siblings of GNRs and can be visualized as the QDs formed by the intersection of a zigzag GQD (ZGQD) and an armchair GQD (AGQD). Apart from the shape, several studies have shown that the electronic and magnetic properties of GNRs can be tuned either by substituting the GNRs' carbon atoms with B, N or by doping the GNRs with B/N atoms. [16–18] Inspired by these findings, we have also studied the substitutional effects on the electronic and magnetic properties of the cross-shaped GQDs and BNQDs. Also, experimentally hybrid BNC sheets have already been prepared, where the ratio of C:BN [19] and the shape or size of BN domain on C or vice versa can be controlled precisely. [20] Thus, these substituted QDs can easily be prepared experimentally either using the conventional lithography [21–23] or the more recent nanotomy techniques. [24]

As cross-shaped graphene (G) and boron-nitride (BN) quantum dots (QDs) can be seen as a hybrid (or combination) of zigzag QDs (ZQDs) and armchair QDs (AQDs) of equal length and width, first we have performed a series of calculations on both substituted and pristine zigzag (ZQDs) and armchair QDs (AQDs). Such calculations are important to understand the electronic properties of cross-shaped (hybrid) QDs (HQDs). It is already known that, the electronic and magnetic properties of these types of QDs are highly dependent on the nature of the edges, [16, 17, 25] and hence, we have considered the substitution of these pristine QDs only at the edges. For a GQD, edges are substituted with boron and nitrogen (BN) pairs and for a BNQD, edges are substituted with carbon. Thus, the systems are iso-electronic before and after the substitution. We have passivated all the systems with H-atoms, because several previous studies,[26, 27] have shown that H passivation makes the systems more stable compared to the corresponding pristine QDs. Depending on whether

all the edge atoms are substituted or only half of them are substituted, we named these QDs as complete-ed-QDs or partial-ed-QDs, respectively, as shown in the Figure 3.1. The remaining chapter is arranged as follows. In section 2, we have given the computational details and in section 3, we have first presented the electronic and magnetic properties of ZQDs and AQDs followed by the results of HQDs of various sizes and different levels of substitution. In the last section, we have summarized the main results of this chapter.

3.2   Computational Details

Spin polarized first-principles calculations have been performed, to obtain all the electronic and magnetic properties of the systems, using the density unctional theory (DFT) method as implemented in the SIESTA package. [28] Generalized gradient approximation (GGA) in the Perdew–Burke–Ernzerhof (PBE) [29] form has been considered for accounting the exchange-correlation functional. Double–ζ polarized (DZP) numerical atomic-orbital basis sets have been used for H, B, C, and N atoms. Norm-conserving pseudopotentials have been considered in Kleinman-Bylander form [30] with 1, 3, 4 and 5 valence electrons for H, B, C, and N, respectively. A reasonable mesh cut-off of 400 Ry for the grid integration has been used to represent the charge density and a vacuum of 20 Å has been maintained, around the quantum-dots, in all directions to avoid any spurious interactions. Systems are considered to be optimized if the magnitude of the forces acting on all atoms is less than 0.04 eV/Å. As the systems are zero-dimensional, all the calculations are performed only at the gamma (Γ) point of the Brillouin zone. For all the DOS and pDOS plots, a broadening parameter of 0.025 eV has been used. All the results below have been obtained using PBE functional. However, for validation, we have cross checked some of our results with HSE06 functional [31] and found that both the methods predict same trends, particularly in band gap.

3.3   Results and Discussions

In this section, first we will present the results of the individual QDs (i.e., both ZQDs and AQDs of which HQDs are made of) and then we will present the results of HQDs. As our aim is to study cross-shaped HQDs, our Z/AQDs will be of rectangular shape.

3.3.1   Zigzag QDs

Systems under consideration

To simulate the ZQDs, we have considered rectangular quantum-dots (QDs) of graphene (G) and boron-nitride (BN) with a zigzag edge along the direction of the length and an armchair edge along the width direction. Following the convention of the graphene nanoribbons, [32] we have assigned an ordered pair (n, m) to represent the length and width of the QDs. Here 'n' represents the number of atoms along the zigzag-edge (length) and 'm' represents the number of atoms along the armchair-edge (width), as shown in Figure 3.1. In the present study, we have considered two values viz., 21 ($\sim$ 2.2 nm) and 33 ($\sim$ 4.2 nm) for 'n' and three values viz., 4 ($\sim$ 1 nm), 6 ($\sim$ 1.4 nm) and 8 (1.8 nm) for 'm'. Thus, for each type of ZQD (i.e., either a GQD or a BNQD or their substituional derivatives) we have considered six different systems, each of which can be distinguished by the difference in their length $\times$ width.

As noted earlier, edge atoms of all the systems have been passivated with hydrogen atoms and substitution is mainly considered in two ways viz., full-edge substitution (full-ed) and partial-edge substitution (partial-ed), as shown in figures Figure 3.1b and 3.1c, respectively. Information of the substitution has been given first, followed by the name of the system. For example, a GQD (BNQD) whose edges are completely (partially) substituted with B and N atoms (C atoms) has been denoted as BN-full-ed-GQD (C-partial-ed-BNQD).
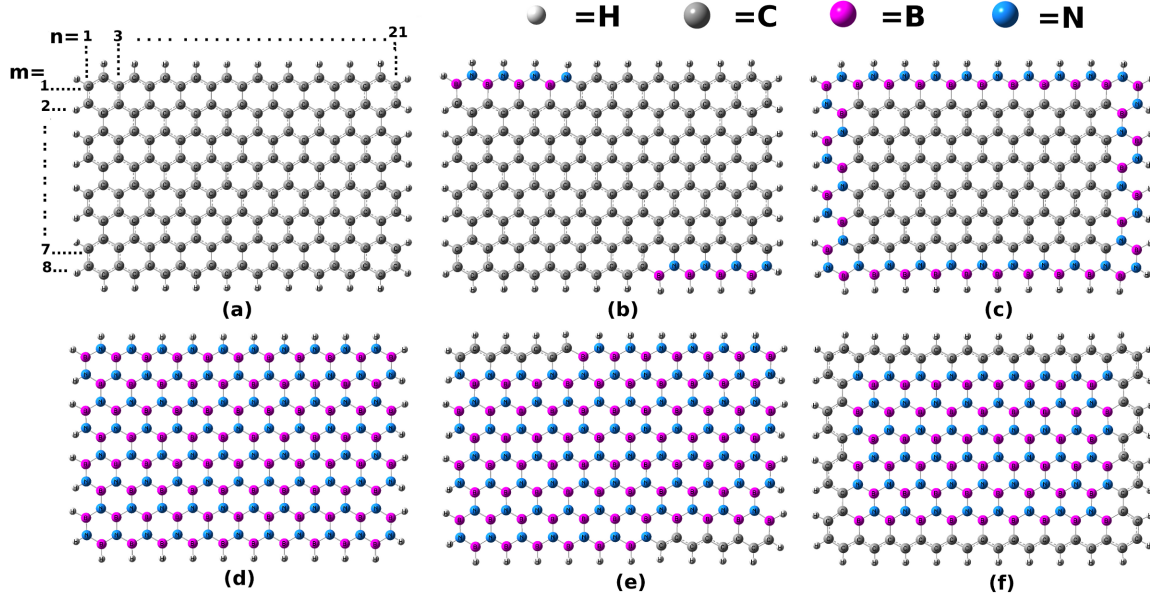
Figure 3.1: Structures of all the (21, 8) QDs. (a) GQD, (b) BN-partial-ed-GQD (c) BN-full-ed-GQD (d) BNQD (e) C-partial-ed-BNQD and (f) C-full-ed-BNQD.

Stability

Based on the previous studies on systems containing BCN, [33, 34] we have calculated the stability of a system by its formation energy per atom (E_{Form}), where E_{Form} is defined as

$$E_{Form} = [E_{tot} - (n_{CC} * \mu_{CC}) - (n_{BN} * \mu_{BN}) - (n_H * \mu_H)]/n_{tot} \qquad (3.1)$$

Here, E_{tot} is the total energy of the system, μ_H, μ_{BN} and μ_{CC} are the chemical potentials of a H atom (calculated from a hydrogen molecule), BN pair (calculated from an 8 × 8 h-BN supercell), and a CC pair (calculated from an 8 × 8 graphene super-cell), respectively and n_H, n_{BN}, n_{CC} and n_{tot} are the number of H atoms, BN pairs, CC pairs and total number of atoms present in the system, respectively. We have considered the formation energies of graphene and BN-sheets to be zero (i.e., they are our reference states). More details of the calculations can be found here. [33, 34] E_{Form} of the systems (21, 4), (21, 6), (21, 8), (33, 4), (33, 6) and (33, 8) are listed in Table 3.1. Formation energies of all the systems are negative indicating

Table 3.1: Formation energies (eV/atom) of all the ZQDs considered in this study.

SystemName	(21,4)	(21,6)	(21,8)	(33,4)	(33,6)	(33,8)
GQD	-0.545	-0.442	-0.386	-0.503	-0.393	-0.333
BN-partial-ed-GQD	-0.472	-0.389	-0.345	-0.428	-0.339	-0.291
BN-full-ed-GQD	-0.386	-0.301	-0.261	-0.349	-0.262	-0.221
C-full-ed-BNQD	-0.453	-0.364	-0.315	-0.412	-0.321	-0.268
C-partial-ed-BNQD	-0.474	-0.388	-0.340	-0.436	-0.343	-0.292
BNQD	-0.502	-0.408	-0.356	-0.466	-0.365	-0.309

that all these systems are energetically feasible. It is important to mention that all the values reported in Table 3.1 are for the ground state spin-configurations of the respective ZQDs, which is found to be anti-ferromagnetic, based on our spin-polarized calculations.

Electronic and magnetic properties

In this section, we will present the electronic (density of states (DOS), projected DOS (pDOS), HOMO–LUMO gap (H–L gap), charge-transfer and wave-functions) and magnetic properties of ZQDs. We will first explain the changes in these properties with the size, then with the substitution, and finally with the application of an external electric-field.

Effect of Size: Similar to GNRs, [35] GQDs also show a finite H–L gap because of the quantum confinement effect (here, in all the directions). As shown in the Table 3.2, for all the QDs, there is a decrement in the H–L gap with an increment in the length and/or width of the QDs. For example, (21, 4) GQD has a H–L gap of 0.71 eV for both the spin-channels, but, once the system size has been increased to (21, 6) and (21, 8), there is a decrement in the H–L gap (from 0.71 eV) to 0.68 and to 0.54 eV, respectively. Lesser H–L gap for greater sizes is due to the (a) decrement in the energy-level spacing, (b) increment in the delocalization of the π electrons (due to the increased conjugation length) in the larger QDs. The H–L gap of 0.54 eV for the (21, 8) or (33, 8) is comparable with the calculated

Table 3.2: HOMO–LUMO gap (eV) of each system is given in both the spin-configurations (here after, we call one spin-configuration as spin-α and the other as spin-β).

System Name	(21, 4)		(21, 6)		(21, 8)		(33, 4)		(33, 6)		(33, 8)	
	spin-α	spin-β	spin-α	spin-β	spin-α	spin-β	spin-α	spin-β	spin-α	spin-β	spin-α	spin-β
GQD	0.71	0.71	0.68	0.68	0.54	0.54	0.70	0.70	0.60	0.60	0.54	0.54
BN-partial-ed-GQD	0.81	0.16	0.04	0.54	0.04	0.43	0.05	0.51	0.32	0.04	0.01	0.19
BN-full-ed-GQD	0.71	0.71	0.41	0.11	0.09	0.34	0.62	0.62	0.32	0.06	0.22	0.03
C-full-ed-BNQD	0.28	0.28	0.44	0.44	0.48	0.48	0.05	0.23	0.16	0.16	0.19	0.19
C-partial-ed-BNQD	1.35	1.35	1.08	1.08	0.91	0.91	0.79	0.79	0.52	0.52	0.36	0.36
BNQD	4.32	4.32	4.16	4.16	4.03	4.03	4.32	4.32	4.16	4.16	4.06	4.06

band-gap of 0.51 eV for the 8-ZGNR obtained within the LDA-approximation. [25] Comparable results have also been obtained previously by Philip Shemella *et al.,* [36] and Oded Hod *et al.* [37] Similar to GQDs, all the other QDs (considered in this study) have shown a decrement in the H–L gap with an increment in their size, except for the C-full-ed-BNQD. This is because as the width of the ribbon increases, in C-full-ed-BNQD, the number of carbon atoms present at the edge increases, which in-turn increases the delocalization of electrons (because B, N atoms are replaced with carbon-atoms). This delocalization brings in stability mainly to the HOMO (leaving the LUMO almost unchanged, see Figure 3.2), and hence, the increment in the H–L gap with an increment in the width of this QD.
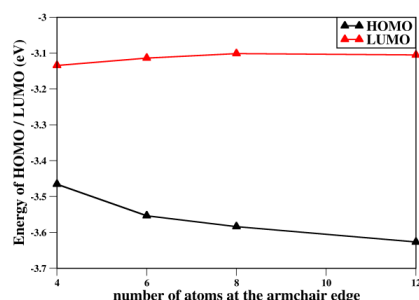
Figure 3.2: HOMO and LUMO energies of C-full-ed-BNQDs with different widths.

Figure 3.3(a) shows the density of states (DOS) and projected-DOS (pDOS) of (21, 8) GQD. Clearly, DOS (green color) near the Fermi-level has a major contribution from the zigzag-edge atoms (orange colour), and also, both the HOMO and LUMO of (21, 8) GQD shows that the wave-functions are localized at the zigzag-edges

(see Figure 3.4(a)). One notable point is HOMO and LUMO are localized at two different edges for each spin, and also, the edge where the wave-function is localized for the spin-α's HOMO is the same as the spin-β's LUMO and vice-a-versa. Similar localization behaviour of wave-function has been previously observed in ZGNRs studied by Zheng *et al.* [38] When we changed the widths and lengths of GQDs, we find similar localization behaviour except that the degree of localization of the wave-function at a particular edge increases with a decrement in the width of the GQD. This result is in contradiction to Shi *et al.*,[39] although their findings are mainly for non-passivated GQDs, $\star$ but our result compares fairly well with the Hod *et al.* [37] As the DOS near the Fermi-level is mainly contributed by the zigzag edges and as substitution at the zigzag edges (with a similar kind of localization behaviour of wave-function [38] which we find for GQDs) has proven to be useful to attain several interesting properties like half-metallicity in ZGNRs, [16, 18, 40] we have substituted these edges with the isoelectronic BN-pairs.
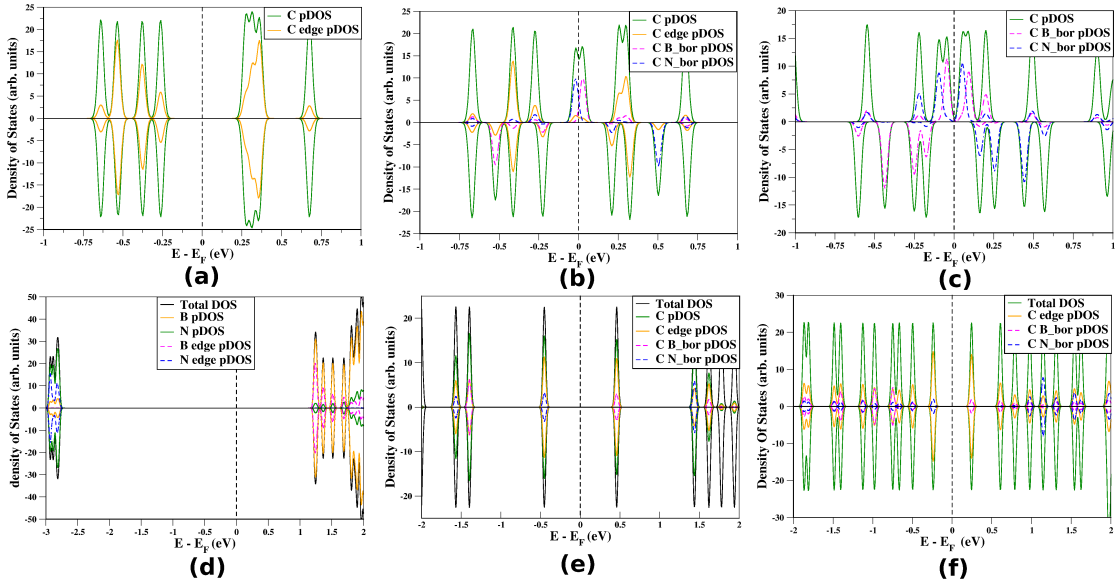
Figure 3.3: pDOS plots of all (21, 8) QDs. (a) GQD, (b) BN-partial-ed-GQD (c) BN-full-ed-GQD (d) BNQD (e) C-partial-ed-BNQD and (f) C-full-ed-BNQD.

$\star$where, they found that the HOMO of small quantum dots is different to that of the larger QDs (also referred to as 'nano-flakes')
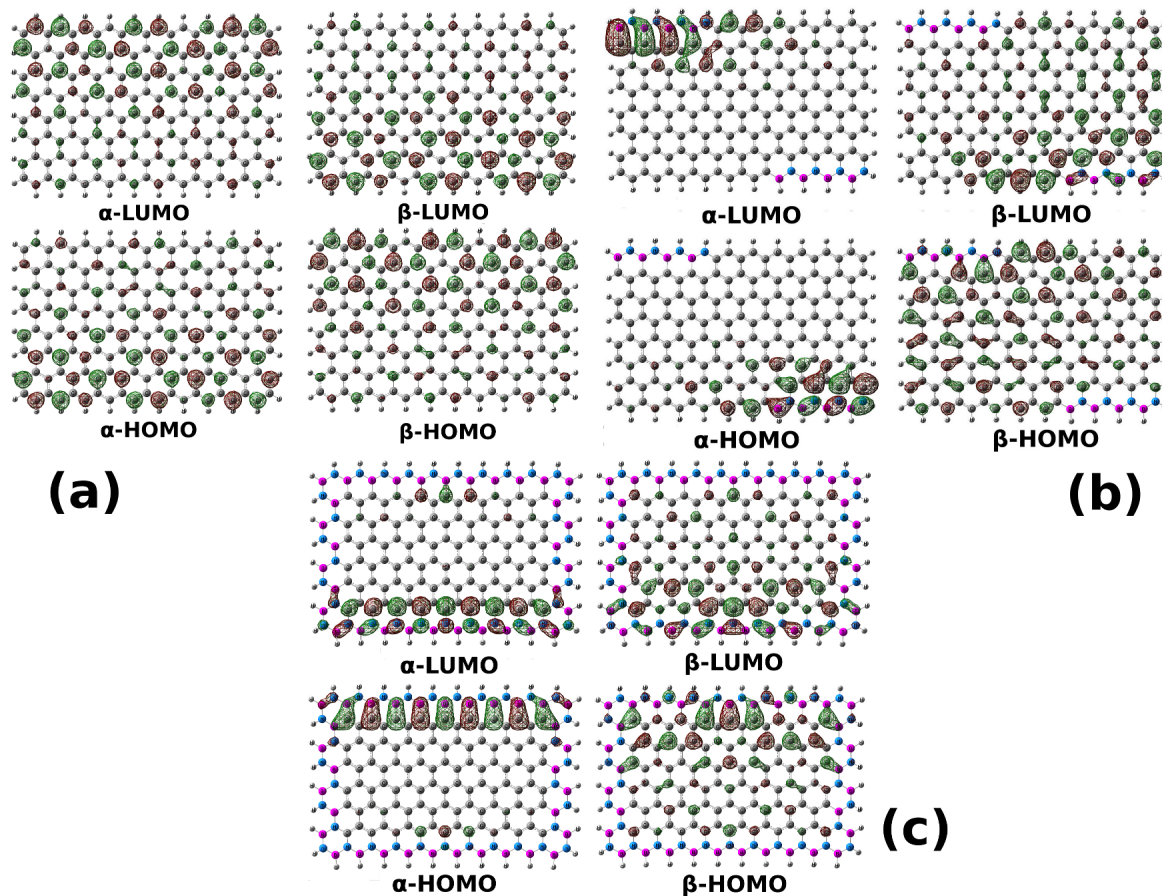
Figure 3.4: HOMO-LUMO plots of (21, 8) QDs. (a) GQD, (b) BN-partial-ed-GQD and (c) BN-full-ed-GQD.

Effect of Substitution   When GQD's edges were substituted completely with BN, H–L gap of these system decreases. Interestingly, when the width of the QD is greater than 4, we find a spin-dependent H–L gap (see Table 3.2 and Figures 3.5(d)-(f)). The spin-dependency of the H–L gap is because of the intrinsic electric-field present in the system. In fact, due to the presence of B and N-atoms at two different zigzag-edges and as B is a Lewis acid, there would be a charge-transfer which generates the potential gradient across the ribbon. [40] The reason for the spin-independency of the H–L gap of the BN-full-ed-GQDs with width 4 is solely because of their smaller width. With a decrease in the width of the QD, the strength of the field which is required to lift the degeneracy between the two configurations of the spins will also

increase. Similar explanation regarding the width dependency of the critical electric-field to break the degeneracy of the two spin configurations for the case of GNRs has been discussed by Son *et al.* [25] Additionally, partial BN substitution on GQDs also produces a spin-dependent H–L gap (see table 1 and Figures 3.5(a)-(c), similar to complete edge substitution, but, the *spin-dependency is there for all the widths.* This result is quite interesting and by bringing the analogy from the previous studies on the ZGNRs, [25, 38] ZBNNRs [41, 42] and their hybrids, [18] we find that there are several possible ways to explain the spin-polarization in BN-partial-ed-GQDs, namely, presence of localized edge-states due to edge carbon-atoms, presence of an intrinsic electric-field along the diagonal direction, presence of border carbon atoms which can strongly contribute to the states near the Fermi-level etc.
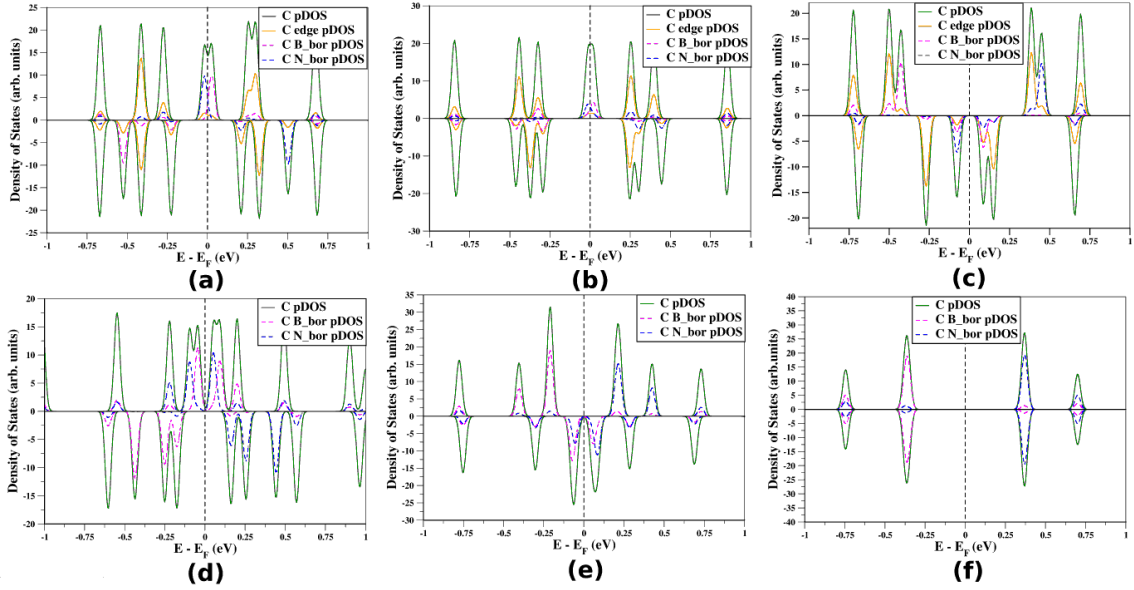
Figure 3.5: pDOS plots of (a) (21, 8) BN-partial-ed-GQD, (b) (21, 6) BN-partial-ed-GQD, (c) (21, 4) BN-partial-ed-GQD, (d) (21, 8) BN-full-ed-GQD, (e) (21, 6) BN-full-ed-GQD, (f) (21, 4) BN-full-ed-GQD.

Among the above, through our calculations, first we find that intrinsic electric-field is not the reason for the spin-polarization in partial edge substituted GQDs, unlike full edge substituted GQDs. To prove this, first we have applied an external electric-field *along the diagonal direction* of pure (15, 4) and (21, 4) GQDs (see

the next subsection). From these calculatins, we find that electric-field induces
spin-polarization in GQDs only above a critical width (see Figure 3.6). Based on this
result, we have discarded the intrinsic electric-field as a reason because we observed
spin-polarized pDOS in BN-partial-ed-GQDs irrespective of the width as shown in
Figure 3.7
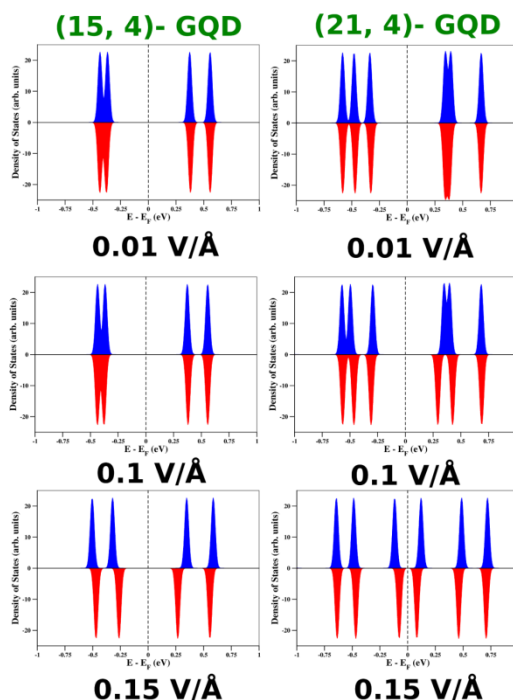
Figure 3.6: DOS plots of (15, 4) and (21, 4) GQDs at different electric-field strengths.

By omitting other possibilities, we find that the main reason for the spin-dependent
H–L gap is due to the presence of both border and edge carbon atoms in BN-partial-
ed-GQDs. To prove this, we have gradually increased the amount of substitution at
both the zigzag edges of (21, 4)-GQDs, as shown in the top panel of Figure 3.8. From
this, we find that the H–L gap of (21, 4)–GQD is spin-dependent for all substitutions
except for the complete edge substitution (see middle panel of Figure 3.8). To
further prove that this spin-dependency in H–L gap is occurring solely because of the
edge and border carbon atoms, we have also plotted the spin-distributions in these
systems and are shown in the bottom panel of Figure 3.8. These spin-distributions
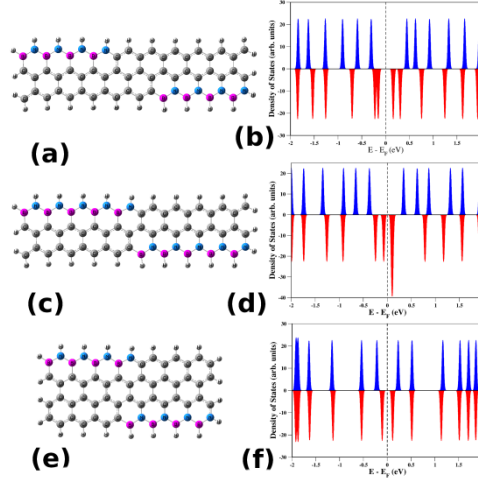
Figure 3.7: Structures of the systems with (a) width less than that of, (c) substitution more than that of and (e) width and length less than that of (21, 4)-BN-partial-ed-GQD. (b), (d), (f) represents the corresponding DOS plots manifesting the spin-polarized H-L gaps.

show that there is a high spin-non-degeneracy at the border and the edge-carbon atoms. Also, to show the effect of width dependency, we have plotted the pDOS of BN-partial-ed-GQDs at different widths (see Figure 3.5(a)-(c)). From these figures, it is clear that the DOS near the Fermi-level always has a major contribution from the border and edge carbon atoms.

To further understand the origin of this spin-dependency, we have performed the Mülliken population analysis and the results for (21, 4)-GQDs (for both pristine and substituted) are tabulated in Table 3.3. Clearly, the average amounts of charge (total charge at each edge, for each spin, divided by 2) present at the edge and at the 2nd zigzag line of a GQD are same for both the spins, and hence, the H–L gap is spin-degenerate. [In a GQD, the charge present at each edge is not same for both the spins but the amount of the charge in up-spin at one-edge will be equal to the amount of charge in down-spin for the other-edge, very similar to ZGNRs. Same rule applies for 2nd zigzag line also]. In BN-full-ed-GQD, although the amount of charge transfer to the border carbon atoms at B-border is different to that of N-border, there is no difference in amount of the charge transferred through each spin, and
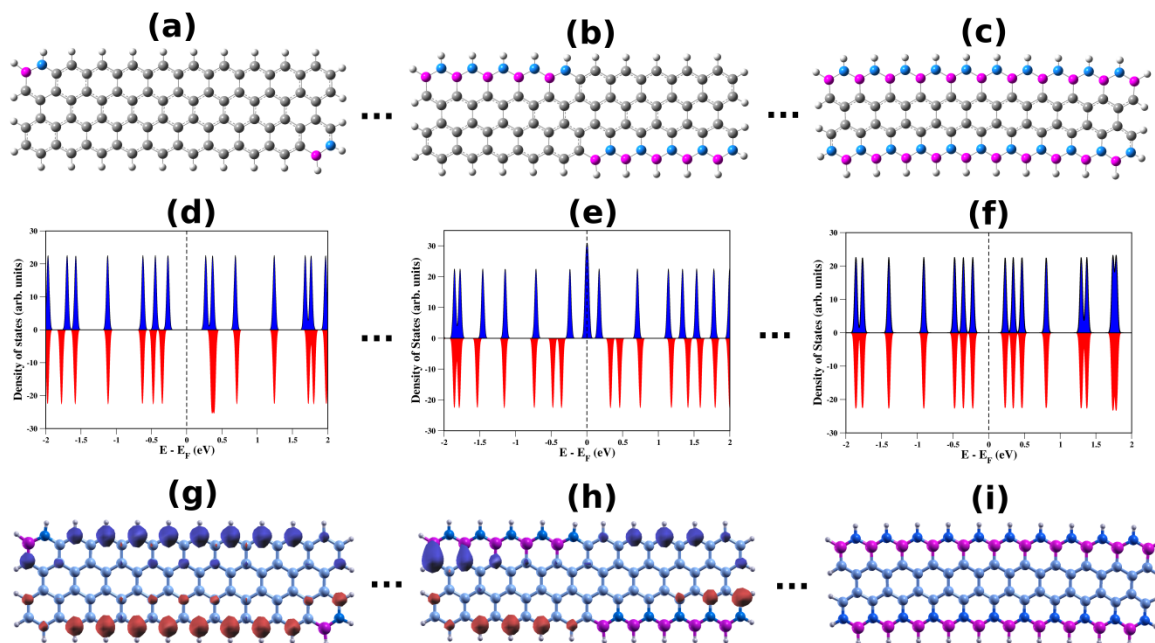
Figure 3.8: Variation in the spin-dependency of the H–L gap with a variation in the amount of substitution at the zigzag edges of (21, 4)-GQDs. (a-c) shows structures with different amount of substitution; (d-f) shows their corresponding DOS and (g-i) are their corresponding spin-distributions. Structures, DOS plots and spin-distributions for all the other substitution levels considered in this study were given in figures S6, S7 and S8, respectively.

hence, again the H–L gap is spin-degenerate. But, when it comes to the BN-partial-ed-GQD, there is an apparent difference also in the amount of the charge-transferred through each spin at each border. In other words, "In a BN-partial-ed-GQD, there is an inherent difference in the amount of charge transferred through spin-α to that of spin-β, whenever there is a charge transfer from a Boron/Nitrogen atom to a border-carbon atom". Similar charge transfer behaviour has been observed for other sizes of BN-partial-ed-GQDs. Thus, the origin of the spin-dependent H–L gap lies in the spin-dependent charge-transfer to the border carbon atoms and is manifested in the DOS and pDOS plots. Finally, it is important to mention that in all the above substitution studies, we have placed boron atoms at one edge and nitrogen atoms at the other, which leads to two different kinds of edge carbon atoms, and hence, also to two different kinds of border carbon atoms. This is another important reason for the observation of the spin-dependent H–L gap in BN-parital-ed-GQDs even for

Table 3.3: M*ü*lliken population analysis of (21, 4)-GQDs (both pristine and substituted). Amount of the charge-transfer from (to) the edge or border carbon atoms to (from) the substituted nitrogen or boron atoms is given in the last row, for each spin, separately.

GQD				BN-zigzag-ed-GQD				BN-partial-ed-GQD							
Avg. edge		Avg. 2nd zigzag line		B-border		N-border		B-edge		N-edge		B-border		N-border	
spin-α	spin-β	spin-α	spin-β	spin-α	spin-β	spin-α	spin-β	spin-α	spin-β	spin-α	spin-β	spin-α	spin-β	spin-α	spin-β
19.02	19.02	21.48	21.49	20.81	20.81	22.26	22.26	11.99	10.82	10.85	12.01	7.21	7.81	8.38	7.81
Charge transfer				-0.67	-0.67	+0.78	+0.78	+0.58	-0.59	-0.56	+0.6	-0.61	+0.01	+0.57	-0.002

small widths.

In BNQDs, substitution (both full-edge and partial-edge) decreases their H–L gaps. Surprisingly, H-L gap of C-full-ed-BNQDs is even below the H–L gap of GQDs, for all widths and lengths. Here also, it occurs solely because of the substituted edge carbon atoms, as shown in the pDOS plots (see Figures 3.3(e) and (f)).

From all the above results, we can conclude that, one can achieve a spin-polarized H–L gap in a rectangular GQD if any of the following conditions is satisfied:

1. Complete substitution of the zigzag edges of GQD with BN pairs, for widths greater than 1 nm.

2. Partial zigzag edge substitution (i.e., irrespective of number and position) of a GQD with BN pairs, in such a manner that, nitrogen atoms are at one zigzag edge and boron atoms are at the other.

Above conclusions have been verified up to a size of $\sim 4.2 \times 2.2$ nm^2 and we expect them to work for higher sizes (than what we have considered here) too.

Effect of external electric field on GQDs: As mentioned in the earlier sub-section, the reason for the spin-polarization in BN-partial-ed-GQDs, is not due to the intrinsic electric-field. To prove this, first we have to show that GQDs are spin-polarized when an external electric-field acts along the diagonal direction (because

charge-transfer effects are present along the diagonal direction in BN-partial-ed-GQDs) of the GQDs. Results of these calculations for (21, 4) GQD are given here. To ensure the stability of the system under the applied electric-field, first we have calculated the minimum force (when applied between the diagonal edges of GQD) at which the GQD structure starts destroying. The minimum force, F_{min}, is calculated as,

F_{min} = (C-C bond-energy of GQD)/(Distance between the diagonal edges).

For (21, 4)-GQD the distance between the diagonal edges is 27.49 Å and we took the C-C bond-energy to be 4.9 eV. [43] Substituting these values gives us $F_{min} \approx$ 0.18 eV/Å. Thus the minimum strength of the electric-field which can rupture the GQD structure is $E_{min} \approx 0.18$ V/Å. Considering this E_{min} value, we have applied an external electric field, only in the range of 0.01–0.05 V/Å, i.e., well below the E_{min} value, across the diagonal of the rectangular (21, 4) GQD. We find that, in the range of applied electric-field, the H–L gap of (21, 4)-GQD is always spin-dependent as shown in the inset of Figure 3.9(i). The spin-dependency in the H–L gap of GQDs can simply be explained from the fact that the applied electric field shifts the energy levels of the opposite spins in different directions, thus, breaking the localized edge-state spin-symmetry. A similar phenomenon was also observed when an external electric field was applied across the zigzag edges (though not along the diagonal direction) of a ZGQD. [37] To further understand the reason for such spin-polarized H–L gap, we have presented the individual shifts of the HOMOs and LUMOs for both the spins in Figure 3.9(i). From the figure it is clear that, energy of both the HOMOs (LUMOs) is increasing (decreasing) with an increase in the external electric-filed [as HOMO (LUMO) corresponds to electron (hole) occupied state]. These increments/decrements in the MO energies are consistent with the linear stark-effect, where the shift in the energy of a MO is given by $\Delta E = -\vec{P}.\vec{E}$, where $\vec{P}$ is the polarization and $\vec{E}$ is the applied electric-field.[69] From the equation,

it is clear that the shift in the MO energy is proportional to the polarization and the shift will be positive or destabilizing (negative or stabilizing) if the direction of the polarization is opposite (parallel) to the applied electric-field. Thus, the change in the energy of an MO due to the external electric-field can be understood by knowing the direction of polarization of that MO.
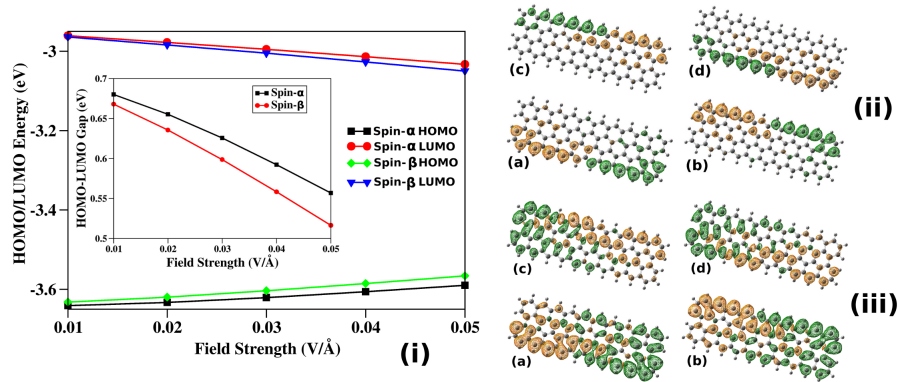
Figure 3.9: (i) Absolute energies of MOs of (21, 4)-GQD under the influence of an external electric-field. Inset shows the corresponding variation in the HOMO-LUMO gap. **(ii, iii)** Electron density difference maps (EDDMs) of (21, 4)-GQD. The two electric-fields considered for calculating EDDMs are 0.01 and 0.02 eV/Å for (ii) and 0.04 and 0.05 eV/Å for (iii) [see the text for details]. (a), (b), (c) and (d) in each sub-figure corresponds to spin-α-HOMO, spin-β-HOMO, spin-α-LUMO and spin-β-LUMO, respectively. For all the plots an isovalue of 0.002 e/(Å)^3 is considered. The direction of polarization is from the orange region to green region.

To get the direction of polarization of MOs, we have generated the cube files of each MO and took their squares to get the corresponding electron-densities of each MO. Then, we took the difference between the electron-densities of each MO at two different electric-fields. These electron-density difference maps (EDDMs) are given in Figure 3.9(ii, iii), where the green area shows the loss in the electron density and the orange area shows the gain in the electron density, and hence, the direction of polarization is always from orange to green. Now, from Figure 3.9(ii, iii), the reason for the shift in the MO energies is very obvious – a positive (negative) shift if the direction of polarization is opposite (parallel) to the applied electric-field direction. Thus, the shifts in the MO energies are consistent with the linear Stark-effect in the applied range of external electric-field. So, we conclude that, (i) similar to the ZGNRs, [25]H–L gap of GQDs can be tuned with an external electric-field (ii) these

changes in the H–L gap are consistent with the linear Stark-effect, (iii) such changes can be understood from the EDDMs plots, and importantly, (iv) although the H–L gap of GQDs can be spin-polarized under external electric-field, the spin-dependent H–L gap of BN-partial-ed-GQDs is not due to the internal electric-field, for the reasons discussed earlier.

3.3.2   Armchair QDs

Next, we have performed calculations on both substituted and pristine armchair QDs (AQDs). We have only considered the systems of medium size i.e., (33, 4) (see Figure 3.10) as changes in the electronic properties with the system size are found to be negligible for the case of ZQDs. Below the results of AQDs have been compared and contrasted with the results of ZQDs.

As shown in Table 3.4 and in Figure 3.11, we find that (a) DOS near the Fermi-level of AQDs is also mainly due to the carbon atoms (whenever carbon atoms are present in the system) and (b) their HOMO-LUMO gap (H–L gap) can be tuned through substitution similar to the case of ZQDs. One notable result is the huge decrement in the H–L gap for both the complete and partial edge substituted BNQDs when compared to the pristine BNQD. But, all the (33, 4) AQDs are semi-conducting and, unlike their ZQD counter parts, none of the AQDs are spin-polarized near the Fermi-level (even after substituting their edges with BN-pairs either partially or completely). Thus, AQDs' electronic properties can be considered as more rigid towards substitution compared to the ZQDs. As real QDs (experimentally obtained ones), can contain both zigzag and armchair edges/wings, we have also considered a mixture of armchair and zigzag wings in our study.

Figure 3.10: Optimized geometries of (i) AGQD, (ii) BN-partial-ed-AGQD, (iii) BN-full-ed-AGQD, (iv) ABNQD, (v) C-partial-ed-ABNQD and (vi) C-full-ed-ABNQD .

Figure 3.11: DOS and pDOS plots of (i) AGQD, (ii) BN-partial-ed-AGQD, (iii) BN-full-ed-AGQD, (iv) ABNQD, (v) C-partial-ed-ABNQD and (vi) C-full-ed-ABNQD

3.3.3   Hybrid QDs

There will be several possibilities while mixing the two types of wings. Here, we have considered a simple case, namely, the joining of a ZQD with an AQD to form a '+' shaped QD. In order to see the size effects of the wings on the calculated properties, we have considered 3 different sizes of the wings. At the same time, to avoid any confusion in understanding the new findings due to substitution (a) we kept the central/junction region of all the QDs as same (for all the 3 sizes) [which helped us to rule out (automatically) the width dependent electronic properties of AGQD (i.e., 3p, 3p+1 and 3p+2, where 'p' is an integer) [32]] and (b) in all the 3 sizes, we have maintained equal numbers of zigzag and armchair edges on both sides of the junction [which helped us to keep track on the important changes which will

Table 3.4: Formation energy and HLG values of all the AQDs.

System Name	Formation Energy(eV)	H–L Gap (eV)
AGQD	-0.555	1.62
BN-partial-ed-AGQD	-0.475	0.55
BN-full-ed-AGQD	-0.401	2.06
ABNQD	-0.498	4.41
C-partial-ed-ABNQD	-0.443	0.91
C-full-ed-ABNQD	-0.462	0.81

occur only because of the substitutional effects rather than the asymmetry across the junction]. The size of the QD is indicated by (A, Z), where 'A' and 'Z' are the lengths of the armchair and zigzag-edged-wings, respectively, in nm and the 3 sizes considered are (2.65, 2.67), (4.39, 4.16) and (6.12, 5.64). All the six systems of the medium size, (4.39, 4.16), are shown in Figure 3.12 and all of them have a total number of 240 atoms (308 atoms by including the hydrogen atoms), among which, 130 atoms are always at the edges of the QD and the remaining 110 atoms at the center, which makes these systems suitable for studying the edge effects. We believe that, our results will give the basic and fundamental understanding of these HQDs (hybrids of ZQDs and AQDs).

Stability

As HQDs have armchair and zigzag wings, all the 3 different spin-configurations, namely, ferromagnetic (FM), anti-ferromagnetic (AFM) and nonmagnetic (NM) configurations have been considered in this study. Both the formation energy and relative energy (with respect to the energy of the most stable spin-configuration) of all these configurations are given in the Table 3.5. As shown in the Table 3.5, all the systems are energetically stable (i.e., their formation energy values are negative), and hence, in principle, they should be experimentally realizable. Indeed, similar QDs (or more precisely, ribbons as lengths are of ~10 nm) have already been realized experimentally in the shapes of X (also can be seen as the HQDs of present study), Y
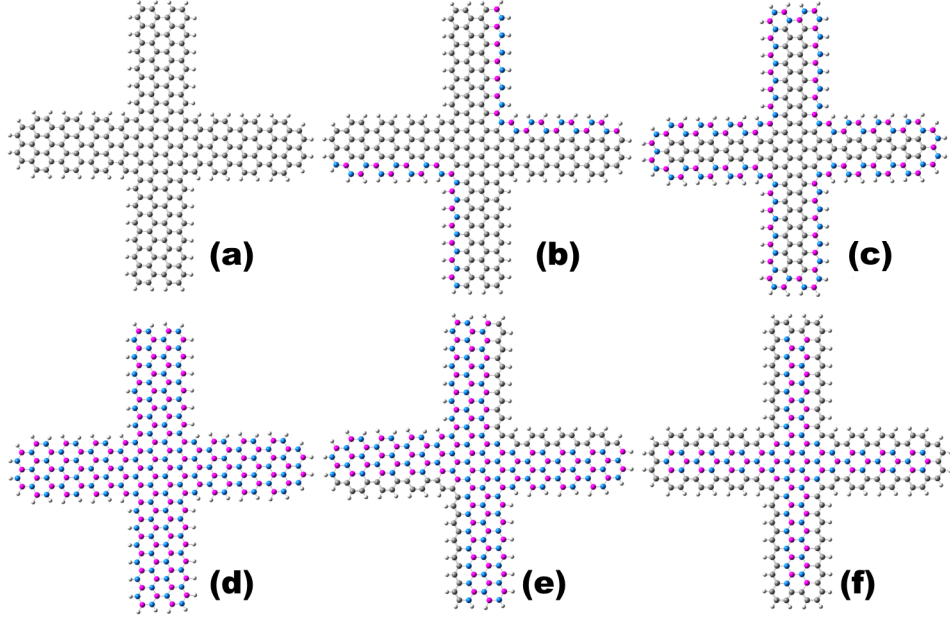
Figure 3.12: Optimized geometries of (a) HGQD, (b) BN-partial-ed-HGQD, (c) BN-full-ed-HGQD, (d) HBNQD, (e) C-partial-ed-HBNQD and (f) C-full-ed-HBNQD

and Z types. [15] Among all the QDs, we find that, only HGQD and BN-partial-ed-HGQD have an AFM ground state. For all other HQDs, the difference between the energies among different spin-configurations is either below the room-temperature or very near the room-temperature, and hence, we considered the ground states of these systems as non-magnetic only. Thus, our calculations suggest that all the HQDs can be synthesized experimentally and they will generally be non-magnetic. Next, we will discuss the electronic properties of these HQDs (in their ground states) and compare them with the electronic properties of the respective ZQDs and AQDs from which these HQDs are formed.

Table 3.5: Spin polarization, formation energy, relative energy and H-L gap values for all the systems in all the 3 spin configurations. First column describes the system names, where the last two indices represent the no.of atoms in that system and the spin configuration, respectively. Rest of the name represents the type of system as shown in Figure 3.12 (see figure caption).

System Name	Spin-polarization	Formation Energy (eV/atom)	Relative Energy (eV)	H-L gap	
				α-spin	β-spin
HGQD-176-AFM	0	-0.509	0	0.92	0.92
HGQD-176-FM	0	-0.509	0	0.92	0.92

HGQD-176-NM	0	-0.509	0.03	0.92	-NA-
HGQD-308-AFM	0	-0.490	0	0.64	0.64
HGQD-308-FM	4.0	-0.490	0.09	0.76	0.70
HGQD-308-NM	0	-0.490	0.4	0.12	-NA-
HGQD-440-AFM	0	-0.482	0	0.64	0.64
HGQD-440-FM	4.0	-0.481	0.27	0.43	0.34
HGQD-440-NM	0	-0.480	0.713	0.0041	-NA-
BN-partial-ed-HGQD-176-AFM	0	-0.424	0	0.60	0.09
BN-partial-ed-HGQD-176-FM	0.8	-0.424	0.01	0.27	0.30
BN-partial-ed-HGQD-176-NM	0	-0.424	0.028	0.12	-NA-
BN-partial-ed-HGQD-308-AFM	0	-0.408	0	0.42	0.02
BN-partial-ed-HGQD-308-FM	2.2	-0.407	0.051	0.1	0.08
BN-partial-ed-HGQD-308-NM	0	-0.407	0.114	0.05	-NA-
BN-partial-ed-HGQD-440-AFM	0	-0.399	0	0.3	0.03
BN-partial-ed-HGQD-440-FM	3.4	-0.399	0.027	0.14	0.15
BN-partial-ed-HGQD-440-NM	0	-0.399	0.205	0.05	-NA-
BN-full-ed-HGQD-176-AFM	0	-0.357	0.001	1.19	1.19
BN-full-ed-HGQD-176-FM	0	-0.357	0.005	1.19	1.19
BN-full-ed-HGQD-176-NM	0	-0.357	0	1.19	-NA-
BN-full-ed-HGQD-308-AFM	0	-0.340	0.027	0.73	0.73
BN-full-ed-HGQD-308-FM	0	-0.340	0	0.73	0.73
BN-full-ed-HGQD-308-NM	0	-0.340	0.012	0.73	-NA-
BN-full-ed-HGQD-440-AFM	0	-0.332	0.07	0.69	0.69
BN-full-ed-HGQD-440-FM	0	-0.332	0.07	0.69	0.69
BN-full-ed-HGQD-440-NM	0	-0.332	0	0.69	-NA-
HBNQD-176-AFM	0	-0.460	0	4.26	4.26
HBNQD-176-FM	0	-0.460	0.002	4.26	4.26
HBNQD-176-NM	0	-0.460	0.001	4.26	-NA-
HBNQD-308-AFM	0	-0.446	0.005	4.14	4.14
HBNQD-308-FM	0	-0.446	0	4.14	4.14
HBNQD-308-NM	0	-0.446	0.003	4.14	-NA-
HBNQD-440-AFM	0	-0.439	0.003	4.05	4.05
HBNQD-440-FM	0	-0.439	0.002	4.05	4.05
HBNQD-440-NM	0	-0.439	0	4.05	-NA-
C-partial-ed-HBNQD-176-AFM	0	-0.419	0.001	0.008	0.45
C-partial-ed-HBNQD-176-FM	1.1	-0.419	0	0.64	0.60

C-partial-ed-HBNQD-176-NM	0	-0.419	0.034	0.059	-NA-
C-partial-ed-HBNQD-308-AFM	0	-0.408	0.001	0.26	0.01
C-partial-ed-HBNQD-308-FM	0.9	-0.408	0	0.12	0.14
C-partial-ed-HBNQD-308-NM	0	-0.408	0.005	0.067	-NA-
C-partial-ed-HBNQD-440-AFM	0	-0.403	0.004	0.02	0.21
C-partial-ed-HBNQD-440-FM	0.8	-0.403	0.001	0.11	0.12
C-partial-ed-HBNQD-440-NM	0	-0.403	0	0.072	-NA-
C-full-ed-HBNQD-176-AFM	0	-0.408	0	0.80	0.80
C-full-ed-HBNQD-176-FM	0	-0.408	0.001	0.80	0.80
C-full-ed-HBNQD-176-NM	0	-0.408	0.002	0.80	-NA-
C-full-ed-HBNQD-308-AFM	0	-0.389	0	0.48	0.48
C-full-ed-HBNQD-308-FM	0	-0.389	0.006	0.48	0.48
C-full-ed-HBNQD-308-NM	0	-0.389	0.016	0.48	-NA-
C-full-ed-HBNQD-440-AFM	0	-0.379	0.002	0.25	0.25
C-full-ed-HBNQD-440-NM	0	-0.379	0	0.25	-NA-

Electronic properties

To understand the electronic properties of HQDs, we have calculated the HOMO-LUMO gaps (H–L gaps) of each of these systems as shown in Table 3.5. Here, we will discuss only the trends in the H–L gaps of the most stable spin-configurations of different HQDs. From the H–L gaps, we find that the electronic properties of HQDs are indeed a mixture of the electronic properties of ZQDs and AQDs. For example, from Table 3.5, we find that

1. H–L gap of both HGQD and HBNQD decrease with an increase in the system size as observed in the case of ZQDs. Reason for the decrement is due to both more bulk like behavior (with an increase in size) and extended conjugation (for carbon containing systems).

2. For a particular size of HQD, partial substitution at the edges show a drastic decrement in the H–L gap values for both HGQD and HBNQD. For the case of HGQD, the decrement in the H–L gap after partial substitution is always

> 0.2 eV and for HBNQD it is always > 4.0 eV (similar to both AQDs and ZQDs)

3. Complete edge substitution of HGQDs with BN pairs increased their H–L gap by a maximum amount of 0.15 eV (this is similar to AQDs, see Table 3.4 but, opposite of ZQDs), but for HBNQDs, complete edge substitution with carbon atoms decreases its H–L gap by, at least, 3.4 eV (similar to both AQDs and ZQDs). The reason for the latter is because of the extended conjugation obtained by 'C' atom substitutions.

4. BN-partial-ed-HGQDs show a spin-polarized H–L gap in their ground state spin-configuration (similar to ZQDs, but, opposite of AQDs).

Thus, substitution can help in tuning the H–L gap of HQDs and the change in HLG is huge when the edges are substituted partially and the changes are highly prominent when the systems are HBNQDs (than HGQDs). To further understand these changes in the H–L gaps, we have plotted both the density of states (DOS) and projected DOS (pDOS) for all the HQDs.

In Figure 3.13, we have given the DOS and pDOS of armchair and zigzag wings for all the HQDs of medium size [i.e., (4.39, 4.16)] in their respective ground states. Clearly, all the HQDs, except HBNQD and C-parital-ed-HBNQD, have greater zigzag edge contribution near the Fermi-level than the armchair edge. As the low-energy electronic properties are mainly dictated by the levels above and below (i.e., HOMO and LUMO) the Fermi-level, one should expect HBNQD and C-parital-ed-HBNQD (others) should have more AQD (ZQD) character than ZQD (AQD). Indeed, this is what we find in the DOS of the HQDs (compare Figure 3.13 and 3.11). An interesting example where one can appreciate that "the electronic nature of a HQD is directly governed by the wing nature of the A/ZQD" is the BN-partial-ed-HGQD.
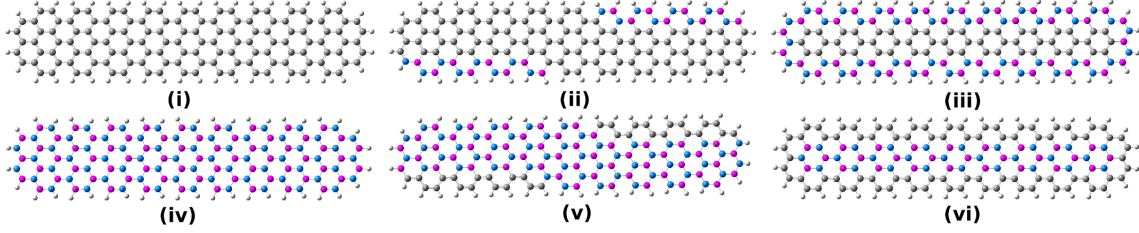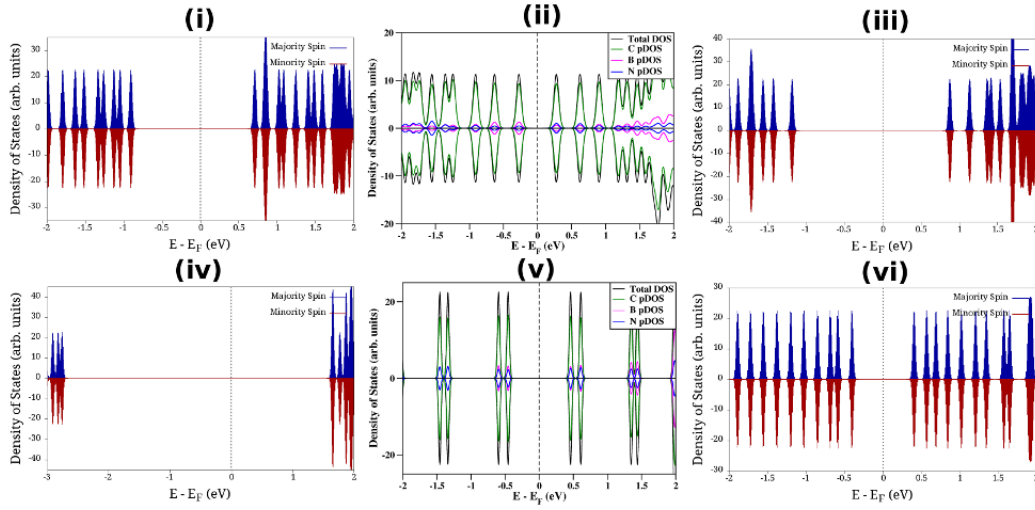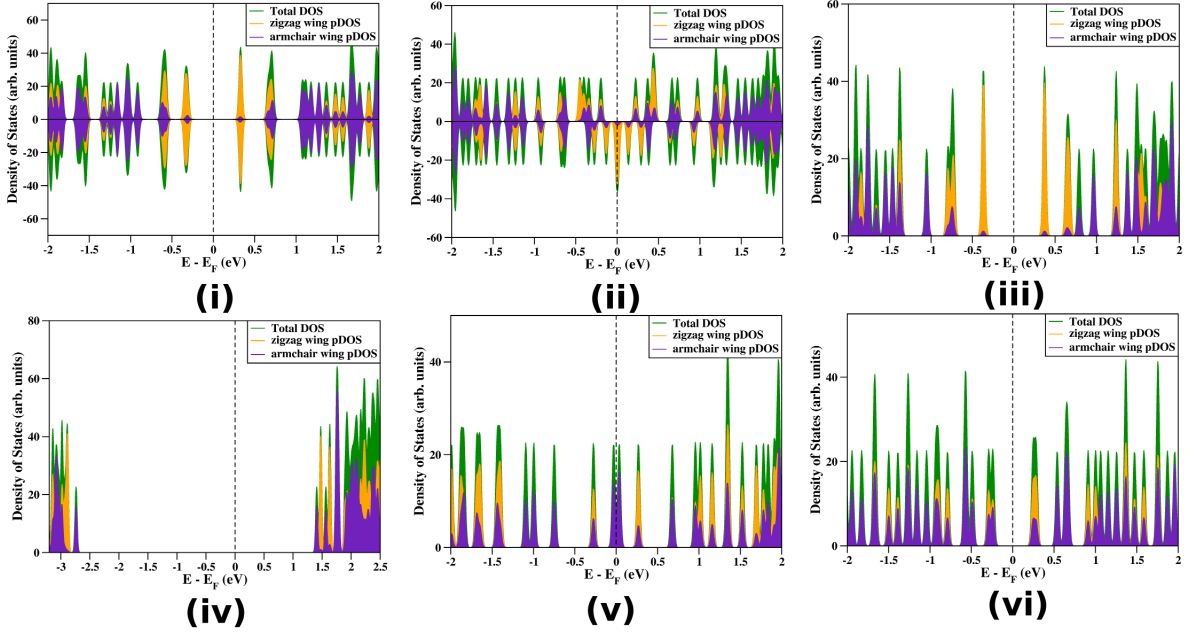
Figure 3.13: DOS and pDOS plots of (i) HGQD, (ii) BN-partial-ed-HGQD, (iii) BN-full-ed-HGQD, (iv) HBNQD, (v) C-partial-ed-HBNQD and (vi) C-full-ed-HBNQD. Green, orange and indigo colors indicate total DOS, zigzag wing pDOS and armchair wing pDOS, respectively.

As can be seen in Figure 3.13(ii), BN-partial-ed-HGQD is a spin-polarized semiconductor and the DOS and pDOS near the Fermi-level also compares exactly with that of BN-partial-ed-ZGQDs (see Figure 3.14(i)). Figure 3.14(ii-iv) shows the pDOS plots of the BN-partial-ed-HGQD of all sizes and all of them are spin-polarized semi-conductors, whose HOMOs and LUMOs are mainly composed of the states from zigzag wing C atoms. Similarly, C-partial-ed-BNQD's electronic structure is mainly dictated by the armchair wing C atoms as shown in Figure 3.13(e).

3.4   Conclusions

In conclusion, we have performed a series of calculations on ZQDs, AQDs and HQDs with and without substitutions. Also, changes in the properties of the quantum dots due to effects of size variation have been studied. Such calculations revealed that substitution can act as a powerful tool to determine the electronic properties of these QDs. All the systems were found to be thermodynamically stable. Increment in the
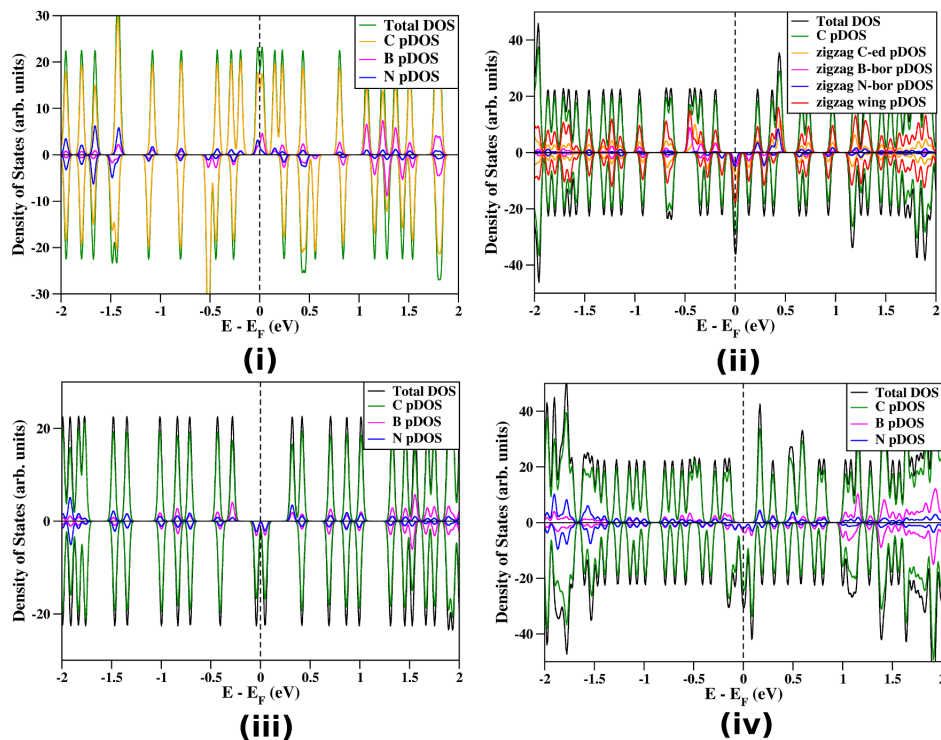
Figure 3.14: pDOS plots of BN-partial-ed (i) (33,4) -ZGQD, (ii) (4.39, 4.16) -HGQD, (iii) (2.65, 2.67) -HGQD and (iv) (6.12, 5.64)-HGQD

sizes of the QDs lead to the decrement of the H–L gap in all the systems except for C-full-ed-BNQDs (where, the increased delocalization of the π-electrons on the C atoms made this system's HOMO more stable leaving its LUMO energy unchanged). Substituting the pure QDs gave several interesting properties.

In ZQDs, above a critical width, BN-full-ed-GQDs were found to possess spin-polarized H–L gap due to the presence of an intrinsic electric-field in the system which can polarize the orbitals. Unlike BN-full-ed-GQDs, BN-partial-ed-GQDs have shown spin-polarized H–L gaps irrespective of the width of the system. We have clearly shown that electric-field is not the reason for the spin-polarized H-L gap in BN-partial-ed-GQDs, although it can create spin-polarized H–L gap in GQDs when applied along the diagonal direction of the QDs. After performing several studies by changing the position and the amount of substitution in GQDs, we found that the reason behind the spin polarized H–L gap in BN-partial-ed-GQDs is the spin

polarized charge transfer between the border carbon atoms by boron/nitrogen atoms. As this behaviour is not observed when only one type of edge or border atom is there in the system, we have concluded that to attain spin-polarized H–L gap in a system, we must have different types of edge and border C atoms. We also have shown that an external electric field can induce spin-polarized H–L gap in GQDs and we explained the energy shifts of the MOs under external electric-field by plotting the EDDMs proving that our results are consistent with linear Stark-effect.

Similar to ZQDs, in AQDs also we find that the H–L gap can be tuned by substituting the edge atoms. But, unlike ZQDs, AQDs didn't show any spin-polarization irrespective of the nature of the substitution (i.e., whether it is partial or full). On the other hand, similar to ZQDs, HQDs show spin-polarized DOS near the Fermi-level when the HGQDs edges are substituted partially with BN-pairs. Also, we find that, when a system has carbon atoms, then all the states near the Fermi-level has contribution from carbon atoms, and hence, the major electronic properties will be governed by the nature of these carbon states. Among HGQDs and HBNQDs, substitution has huge effects on HOMO-LUMO gap of HBNQDs compared to HGQDs. Finally, we found that the electronic properties of a HQD are mainly dictated by the electronic properties of either of its constituents i.e., ZQD or AQD.

Bibliography

[1] B. Huang, Q. Yan, G. Zhou, J. Wu, B.-L. Gu, W. Duan, and F. Liu, Appl. Phys. Lett. **91**, 253122 (2007).

[2] D. Jena, T. Fang, Q. Zhang, and H. Xing, Appl. Phys. Lett. **93**, 112106 (2008).

[3] T. B. Martins, A. J. da Silva, R. H. Miwa, and A. Fazzio, Nano Lett. **8**, 2293 (2008).

[4] X. Wang, Y. Ouyang, X. Li, H. Wang, J. Guo, and H. Dai, Phys. Rev. Lett. **100**, 206803 (2008).

[5] Y. P. Chen, Y. E. Xie, and X. H. Yan, J. Appl. Phys. **103**, 063711 (2008).

[6] F. OuYang, J. Xiao, R. Guo, H. Zhang, and H. Xu, Nanotechnology **20**, 055202 (2009).

[7] J. W. González, M. Pacheco, L. Rosales, and P. Orellana, Phys. Rev. B **83**, 155450 (2011).

[8] B. Wang, J. Wang, and H. Guo, Phys. Rev. B **79**, 165417 (2009).

[9] B. Zhou, W. Liao, B. Zhou, K.-Q. Chen, and G. Zhou, Eur. Phys. J. B **76**, 421 (2010).

[10] D. Zhang, L. Liu, Z. Bao, H. Xiao, and Y. Zhang, Physica E **53**, 110 (2013).

[11] Z. Wang, Q. Shi, Q. Li, X. Wang, J. Hou, H. Zheng, Y. Yao, and J. Chen, Appl. Phys. Lett. **91**, 053109 (2007).

[12] N. Xu, F.-J. Kong, and Y.-Z. Wang, Acta Phys. Chim. Sin. **27**, 559 (2011).

[13] H. Wan, B. Zhou, W. Liao, and G. Zhou, J. Chem. Phys. **138**, 034705 (2013).

[14] A. Rafael Botello-Méndez, E. Cruz-Silva, J. M. Romo-Herrera, F. Lopez-Urias, M. Terrones, B. G. Sumpter, H. Terrones, J.-C. Charlier, and V. Meunier, in *APS Meeting Abstracts* (2012), vol. 1, p. 11014.

[15] X. Wang and H. Dai, Nat. Chem. **2**, 661 (2010).

[16] S. Dutta, A. K. Manna, and S. K. Pati, Phys. Rev. Lett. **102**, 096601 (2009).

[17] S. Dutta and S. K. Pati, J. Phys. Chem. B **112**, 1333 (2008).

[18] E. A. Basheer, P. Parida, and S. K. Pati, New J. Phys. **13**, 053008 (2011).

[19] L. Ci, L. Song, C. Jin, D. Jariwala, D. Wu, Y. Li, A. Srivastava, Z. F. Wang, K. Storr, L. Balicas, et al., Nat. Mater. **9**, 430 (2010).

[20] D. J. Late, Y.-K. Huang, B. Liu, J. Acharya, S. N. Shirodkar, J. Luo, A. Yan, D. Charles, U. V. Waghmare, and V. P. Dravid, Acs Nano **7**, 4879 (2013).

[21] S. Neubeck, L. A. Ponomarenko, F. Freitag, A. Giesbers, U. Zeitler, S. V. Morozov, P. Blake, A. K. Geim, and K. S. Novoselov, Small **6**, 1469 (2010).

[22] S. S. Datta, D. R. Strachan, S. M. Khamis, and A. C. Johnson, Nano Lett. **8**, 1912 (2008).

[23] Q. Xu, M.-Y. Wu, G. F. Schneider, L. Houben, S. K. Malladi, C. Dekker, E. Yucelen, R. E. Dunin-Borkowski, and H. W. Zandbergen, ACS Nano **7**, 1566 (2013).

[24] N. Mohanty, D. Moore, Z. Xu, T. Sreeprasad, A. Nagaraja, A. Rodriguez, and V. Berry, Nat. Commun. **3**, 844 (2012).

[25] Y.-W. Son, M. L. Cohen, and S. G. Louie, Nature **444**, 347 (2006).

[26] . Girit, J. Meyer, R. Erni, M. Rossell, C. Kisielowski, L. Yang, C. Park, M. Crommie, M. Cohen, and S. Louie, Science **323**, 1705 (2009).

[27] P. Koskinen, S. Malola, and H. Häkkinen, Phys. Rev. Lett. **101**, 115502 (2008).

[28] M. S. José, A. Emilio, D. G. Julian, G. Alberto, J. Javier, O. Pablo, and S.-P. Daniel, J. Phys.: Condens. Matter **14**, 2745 (2002).

[29] K. Burke, J. P. Perdew, and M. Ernzerhof, Int. J. Quantum Chem **61**, 287 (1997).

[30] L. Kleinman and D. Bylander, Phys. Rev. Lett. **48**, 1425 (1982).

[31] J. Heyd, G. E. Scuseria, and M. Ernzerhof, J. Chem. Phys. **118**, 8207 (2003).

[32] S. Dutta and S. K. Pati, J. Mater. Chem. **20**, 8207 (2010).

[33] R. D. Gonçalves, S. Azevedo, and M. Machado, Solid State Commun. **175**, 132 (2013).

[34] A. K. Manna and S. K. Pati, J. Phys. Chem. C **115**, 10842 (2011).

[35] L. Yang, C.-H. Park, Y.-W. Son, M. L. Cohen, and S. G. Louie, Phys. Rev. Lett. **99**, 186801 (2007).

[36] P. Shemella, Y. Zhang, M. Mailman, P. M. Ajayan, and S. K. Nayak, Appl. Phys. Lett. **91**, 042101 (2007).

[37] O. Hod, V. Barone, and G. E. Scuseria, Phys. Rev. B **77**, 035411 (2008).

[38] X. H. Zheng, X. L. Wang, T. A. Abtew, and Z. Zeng, J. Phys. Chem. C **114**, 4190 (2010).

[39] H. Shi, A. Barnard, and I. Snook, Nanoscale (2012).

[40] B. Huang, H. Lee, B.-L. Gu, F. Liu, and W. Duan, Nano Research **5**, 62 (2012).

[41] V. Barone and J. E. Peralta, Nano Lett. **8**, 2210 (2008).

[42] S. R. K. C. S. Yamijala and S. K. Pati, J. Phys. Chem. C **117**, 3580 (2013).

[43] K. Erickson, R. Erni, Z. Lee, N. Alem, W. Gannett, and A. Zettl, Adv. Mater. **22**, 4467 (2010).

Chapter 4

Linear and Nonlinear Optical Properties of Graphene Quantum Dots: A Computational Study. *

4.1 Introduction

Materials with broadband absorption (BBA) and emission, that is, covering ultraviolet, visible, and near-infrared regions of the solar spectrum, have important applications in photodetectors, broadband modulators, bioimaging, solar cells etc. [1–6] Moreover, if the materials with the broadband absorption also shows optical nonlinearity, they can be very useful in applications involving optical parametric oscillation, high harmonic generation, [7, 8] Kerr effect [9, 10] and multiphoton imaging. [11] Thus, finding novel materials with both broadband absorption and optical nonlinear activity is of great interest.

Group IV-VI quantum dots like CdSe, PbSe, CdS, HgTe, ZnSe, etc. have already been there in variety of applications involving light emitting diodes, bio-imaging,

solar cells, because of their tunable absorption and specific optical nonlinear activity. [12–17] Materials prepared from high band gap semiconductors like ZnS, ZnSe, GaN, and AlN possess ultraviolet optical activity whereas CdS, rare earth doped GaN materials exhibit near IR activities. [18, 19] Although, tuning the size of a quantum dot can vary its active optical range, it cannot give the whole range altogether (i.e., simultaneously UV-VIS and IR range activity). To this end, GQDs and modified GQDs seems to be promising materials for such optical activities. [20–23] Together with their higher photostability, bio-compatibility and low cost preparation, GQDs may act as a substitute for the toxic IV-VI group quantum dots.

GQDs are the confined graphene materials available in various topologies [20–25] and graphene is a layered sp^2-bonded carbon material in honeycomb lattice. Graphene with its zero band gap has a limitation to its applications in optoelectronics due to its zero optical emission. On the other hand, GQDs exhibit a broadband absorption and they have emerged as attractive fluorescence materials in the ultraviolet, visible and even in infrared regions. [20–23, 26] During recent years, there has been a lot of research on the broadband activity of GQDs of different sizes, shapes and functionalities through both experiment and theory. [27–31] Also, there is a progress in identifying the shape and size dependent nonlinear activity of GQDs. [32–35]

Considering these studies into account, here, we have performed a systematic computational study on the linear and nonlinear optical (NLO) properties of hydrogen passivated GQDs (hence, may also be termed as polyaromatic hydrocarbons (PAHs)) of various sizes, shapes, edge structures and so forth. After careful analysis on these GQDs ($\sim$ 20) with simultaneous BBA and high NLO coefficients, we find that the necessary and sufficient condition for possessing such multi-functionality is due to the presence of inequivalent sublattice atoms. Also, we find that majority of the GQDs with only zigzag edges possess this multifunctionality. Additionally, we find that some of these GQDs show fascinating 1st hyperpolarizabilities ($\sim 10^3$-10^5
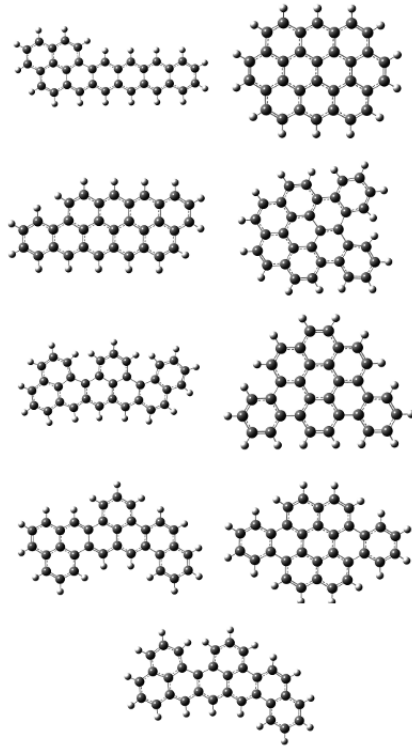
Figure 4.1: Some random shaped GQDs with 32 carbon atoms (C32)

times larger than the traditional NLO compounds [like p-nitroaniline etc]). In the following, first we have described how we have modeled our systems and then we have given the details of our computations. Next, we have compared the results from our semi-empirical calculations on structural stability and electronic properties with the earlier studies and then we have presented our results on linear and nonlinear optical properties. Finally, we have presented the results from first principles calculations on the systems, followed by the conclusions.

4.2 Modeling and Computational Details

As the number of varieties of GQDs which can be generated from graphene are huge, following Kuc et al. [25] we have considered ∼ 400 structures, based on their size, shape, edge etc. As the hydrogen passivated GQDs have been shown to be more stable than the GQDs with bare edges, we have only considered the former ones

throughout our study. As in ref [25], we have categorized our GQDs as circular (F) or triangular (T) or stripes (i.e., nanoribbons) (S) depending on their shape and zigzag (z) or armchair (a) depending on their edges. Thus, F_a (T_z) represents circular (triangular) GQDs with armchair (zigzag) edges. All other GQDs which don't fit in these categories mainly represent the different possible conformers of a GQD with particular number of carbon atoms and we refer them as random shaped GQDs. We identify these random shaped GQDs with their carbon atom numbers such as C22, C28, C74 etc. In Fig. 4.1, we have shown typical examples of random shaped GQDs.

All the structural optimizations have been performed using self-consistent charge (SCC) density functional tight-binding (DFTB) theory [36] within the third order expansion of the DFT energy functional (i.e., with DFTB3) [37] and with 3ob parameter set, [38] as implemented in DFTB+ package. [39] DFTB level of theory is used mainly due to the large number of systems (~ 400) considered in this study as well as its ability to give trends in band-gaps, energies etc. which are comparable to the ones given by DFT, especially for carbon related materials, even with different edges, defects etc. [40, 41] Geometry optimizations have been performed using conjugate gradient method and systems are considered to be optimized only when forces on all the atoms are less than 0.0001 Hartree/Bohr. For those systems whose energy levels near the Fermi-level are almost degenerate, we have increased the electronic temperature to 100 K to avoid any convergence issues.

It is important to notice that it is not a trivial task to either predict the exact ground state spin of PAHs, such as, linear polyacenes using single-determinant methods like HF, DFT and DFTB3 nor to perform *ab initio* many-body calculations with multi-determinants for all the considered GQDs. So, we got compromised ourselves to assume that the ground state spin for these PAHs is singlet (indeed, majority of the known PAHs are singlets) and performed optimizations. However,
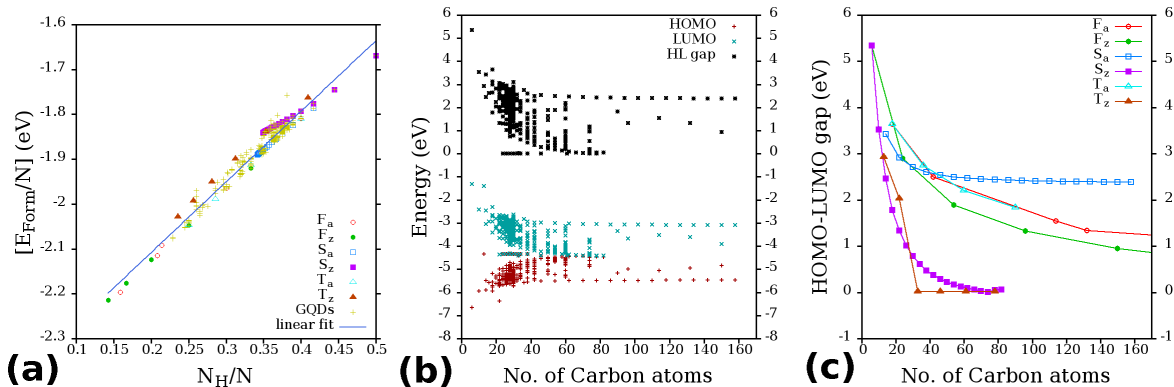
Figure 4.2: (a) A plot of E_{Form} per atom versus number of edge atoms to the total number of atoms (N) of all the GQDs. Straight line shows the linear fit. (b) Energies of HOMO, LUMO and the HOMO-LUMO gap (HLG) of all the GQDs and (c) Changes in the HLG with size for different shaped GQDs. Symbols T, F, S represents triangular, circular and striped GQDs. Subscripts a and z represents armchair and zigzag edges. See the "Modeling" for further details.

for few GQDs, we have performed semi-empirical many-body complete active space configuration interaction (CAS-CI) calculations, within the Hubbard model, to predict their ground state.

Linear optical properties of all the compounds have been computed at the semi-empirical ZINDO/S level of theory as implemented in g09 software package. [42] ZINDO/S has been proved to be very successful especially in predicting the optical properties of systems containing C, N, O, H atoms like polyaromatic hydrocarbon compounds, [43, 44] chlorophylls [45] etc. [46] At semi-empirical level, nonlinear optical (NLO) properties of all compounds have been calculated using MOPAC 2012 program package. [47, 48] All the first principles calculations for the linear (at time dependent density functional theory (TDDFT) level) and nonlinear optical properties have been performed using g09. Long range corrected (CAM-B3LYP) exchange correlation functional has been used in conjunction with 6-31+g(d) basis set for all the calculations. A minimum of first 12 lowest excited states have been considered in all the studies. GaussSum-2.2.6.1 [49] is used to plot the absorption spectra and a broadening of 0.333 eV has been used.

4.3   Results and discussion

4.3.1   Energetic stability and electronic properties

All the GQDs considered in this study are found to be energetically stable, that is, they have negative formation energy, $E_{Form} = E_{tot} - N_H{*}E_H - N_C{*}E_C$, where E_{tot}, E_H and E_C are the total energy of the system, energy of the hydrogen atom in a H_2 molecule (i.e., $E_{H2}/2$) and energy of the carbon atom in a graphene lattice (i.e., E_{Graph}/N_C), respectively. Here, N_C and N_H are the number of carbon and hydrogen atoms in the system. At DFTB3 level of theory, we find E_H and E_C to be -9.123 and -44.291 eV, respectively. A plot of formation energy per atom vs $N_H/(N_H+N_C)$ of all the systems is given in Fig. 4.2a. Clearly, there is a near linear relationship between the formation energy per atom and the number of edge atoms in all the systems (notice the linear fit in Fig. 4.2a), that is, system with lesser number of edge atoms is easier to form and vice-versa, as expected. [20, 50, 51] Similar results have been observed in some of the earlier studies on GQDs and PAHs. [25, 52] In agreement with these previous studies, we also find that among the different GQD shapes studied here, circular GQDs are the most stable ones and ribbon like GQDs are the least stable. All other GQDs' (triangular, random etc.) stability fall in between these two types of GQDs (see Fig. 4.2a). The reason for such a trend is again due to the less number of edge atoms in circular GQDs than in other GQDs considered in this study, as evident from the x-axis of Fig. 4.2a. Recent molecular dynamics simulations have also shown that among the different GQDs, circular and triangular GQDs with zigzag edges as the most stable ones till $\sim$ 4000 K. [24]

Next, the energies of HOMO, LUMO and their difference (i.e., HOMO-LUMO gap (HLG)) of all the GQDs are plotted in Fig. 4.2b as a function of number of carbon atoms. The calculated HLG values are mainly in the range of $\sim$ 0-3 eV. Also, from Fig. 4.2b and 4.2c, it can be observed that for a particular N_C, one can tune

the HLG from $\sim$ 0-3 eV depending on the shape and edges of the GQD. Indeed, tuneability of band-gap between $\sim$ 0-3 eV has already been reported for armchair graphene nanoribbons by varying their width [53, 54] and for the case of GQDs by varying their shape. [22, 23, 55, 56] Interestingly, we find that such tuning is possible even for the systems with N_C between 20 to 50. In fact, synthesis of GQDs (actually, PAHs) of different sizes have already been carried out. [21] From Fig. 4.2c, it can be noticed that HLG of the systems with zigzag edges converge rapidly to zero (reaching the semi-metallicity of graphene) than the armchair ones, irrespective of the shapes and the calculated trend of convergence is T_z-GQDs $>$ S_z-GQDs $>$ F_z-GQDs $>$ T_a-GQDs $\sim$ F_a-GQDs $>$ S_a-GQDs. As HLG reflects the kinetic stability of a system, the above trends suggest that kinetic stability will be highest for S_a-GQDs and least for T_z-GQDs and S_z-GQDs. As suggested by the Clar's rule, [21] higher kinetic stability of S_a-GQDs, compared to the other structures is due to the presence of larger number of resonant sextets in these structures. Similar reasons are also known for the lesser stability of zigzag edged structures compared to the armchair ones. [25] One may also notice that the HLG of "S_z and T_z", "T_a and F_a"-GQDs follows similar trend as N_C increases (for $N_C > 60$) as has also been observed in some of the recent studies. [24] Finally, as the HLG of these GQDs are tunable over a wide range and as HLG can be used as a rough estimate for the optical gap, [43] one may immediately expect that the optical properties of these GQDs can also be tuned over a wide range and the results of the respective calculations are given in the section 4.3.2.

Finally, we have studied three structural isomers of C28 (two kekulé isomers and one non-Kekulé isomer) using CAS-CI method, within the Hubbard model, using home developed code, to find their ground state. For the complete active space, we have considered total eight MOs (4 states above the HOMO and 4 states below the LUMO) and generated all possible CI configurations (i.e., 4900 (3136) determinants

for singlet (triplet) ground state) between them. In all our calculations the hopping parameter is considered as -2.4 eV and Hubbard parameter is considered to be 11.26 eV.
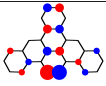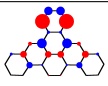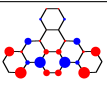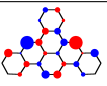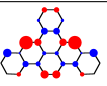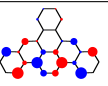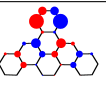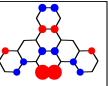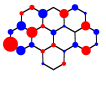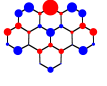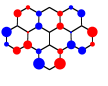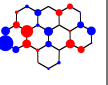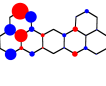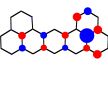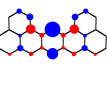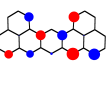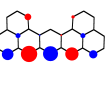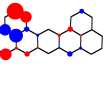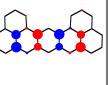
CAS-CI calculations have been performed in various charge states to predict the ground state and to verify Lieb's theorem on Hubbard model and Nagaoka theorem. We find that all the 3 GQDs obey the Lieb's theorem on Hubbard model but not the Nagaoka theorem as our Hubbard term is quite small (and not infinite). Lieb's theorem says that the ground state spin of a half-filled bipartite lattice is equal to half of the difference between sublattice atoms, i.e., $S = \frac{1}{2}|N_A - N_B|$. Here $N_{A/B}$ are the number of A or B sublattice atoms and S is the total spin of the ground state. As kekulé isomers have equal number of sublattice atoms (i.e., $|N_A - N_B| = 0$), they are expected to possess a singlet ground state and for non-kekulé isomers $|N_A - N_B| = 2$ and hence, a triplet state is expected. This is exactly what we have observed for all the GQDs at half-filling (charge-zero), where, C_{28}^{K1} and C_{28}^{K2} have singlet ground states and C_{28}^{NK} has triplet ground state (see Table 4.1). Structures, molecular orbitals and the nature of the ground state for all the three GQDs are given in the Table 4.2

Nagaoka theorem is a special case of the Hubbard model in which the on-site interaction U is infinite and there is exactly one hole. It says that the ground state of such system will have the maximum total spin, i.e., S=(N-1)/2, where N is total number of lattice sites (here, 28). Clearly, Nagoka theorem is not obeyed in these systems as the U value considered in our case is quite realistic and not infinite.

Table 4.1: Ground state spin of Kekulé and non-Kekulé PAHs.

Charge	C_{28}^{K1}	C_{28}^{K2}	C_{28}^{NK}
-1	$\frac{1}{2}$ (Doublet)	$\frac{1}{2}$ (Doublet)	$\frac{1}{2}$ (Doublet)
0	0 (Singlet)	0 (Singlet)	1 (Triplet)
1	$\frac{1}{2}$ (Doublet)	$\frac{1}{2}$ (Doublet)	$\frac{1}{2}$ (Doublet)

Table 4.2: Configurations with maximum contributions to the ground state are given for C_{28}^{K1}, C_{28}^{K2} and C_{28}^{NK} in their neutral charge states. Our CI configurations consist of eight molecular orbitals (MOs). Occupation of each of these MOs and the contribution of atomic-orbitals to each of them are shown for the ground state configuration (determinant).

	C_{28}^{K1}								
GS	4900 (84.4)	↑↓	↑↓	↑↓	↑↓	0	0	0	0
	C_{28}^{K2}								
GS	4900 (86.4)	↑↓	↑↓	↑↓	↑↓	0	0	0	0
	C_{28}^{NK}								
GS	3136 (78.0)	↑↓	↑↓	↑↓	↑	↑	0	0	0

4.3.2 Optical properties

First, we present the optical absorption of all the systems calculated at the ZINDO/S level of theory. Here, we have analyzed only the 20 low energy singlet excitations (i.e., within $Sz=0$ spin sector) from the ZINDO/S results. Absorption spectra of PAHs mainly consists of 3 bands, namely, alpha (α), beta (β) and para (p), out of which the most intense ones being β and p-bands (notations are according to Clar's rule [21], where $p(\beta)$-bands corresponds to the bands at higher (lower) wavelengths). Interestingly, in a very recent study, [43] it has been concluded that ZINDO/S is good at predicting the most intense p and β bands of all $C_{32}H_{16}$ benzenoid PAHs. Considering these facts, first we have plotted the histograms of "wavelengths corresponding to the most intense p-bands (p_{max}) and β-bands (β_{max})", respectively, in Figs. 4.3a and 4.3b and the corresponding oscillator strengths (OS) histograms in Figs. 4.4a and 4.4b. From these figures it can be noticed that, majority of the systems have their β_{max} and p_{max} in the UV-VIS region (200-760 nm) and the oscillator strength of β_{max} (p_{max}) is almost always (for majority of structures) >
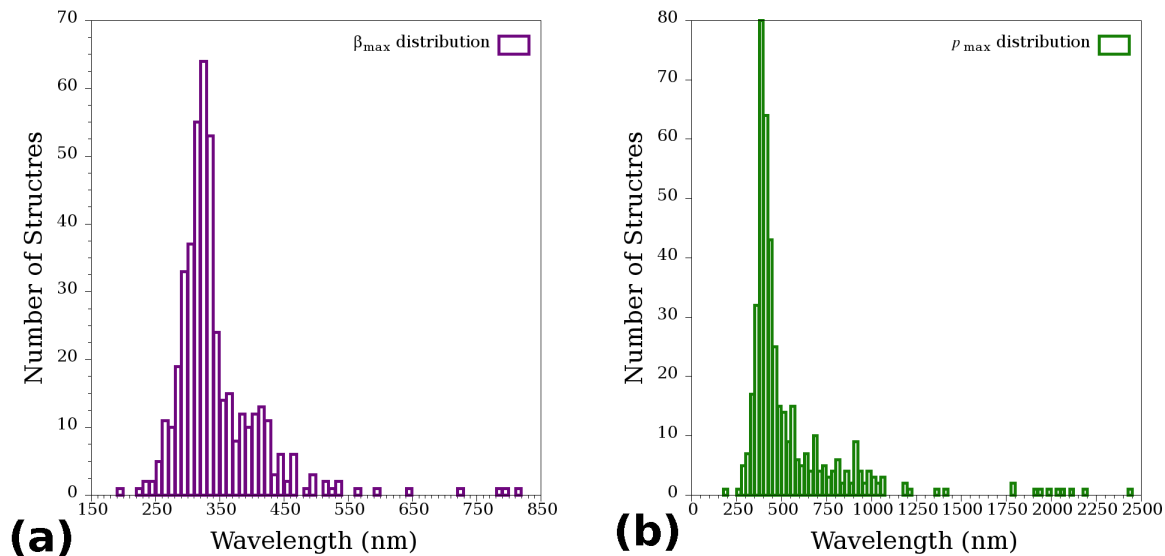
Figure 4.3: Histograms of wavelengths corresponding to (a) β_{max}, (b) p_{max} excitation in all GQDs. p_{max} excitations above 2500 nm have been omitted for clarity.

0.5 (0.1). Thus, majority of the GQDs considered in this study absorb strongly in the UV-VIS region (in particular, their β_{max} (p_{max}) is located in the region between 250-450 (300-700) nm).

However, interestingly, we find $\sim$ 70 GQDs whose p_{max} is in IR-region (> 760 nm). Materials absorbing in IR region are of great interest in the preparation of solar cells because half of the solar energy received by earth is in IR radiation range and most of the present day solar cells do not utilize this energy region. [20] Thus, knowing the reason for the IR-activity of these GQDs will be of great use and for this we have analyzed their p_{max} transition. We find that major contributions to p_{max} transition are always from excitations involving the frontier orbitals (that is, HOMO-1, HOMO, LUMO and LUMO+1), especially from HOMO and LUMO. Thus, the changes in these frontier MOs lead to changes in the p_{max} transition. Also, some of the earlier studies on PAHs have found that HLG of these systems is almost equal to the energy corresponding to the p_{max} transition (see Ref [43] and references there in).

For a few of these GQDs, we find HLG to be very small. In general, small HLGs
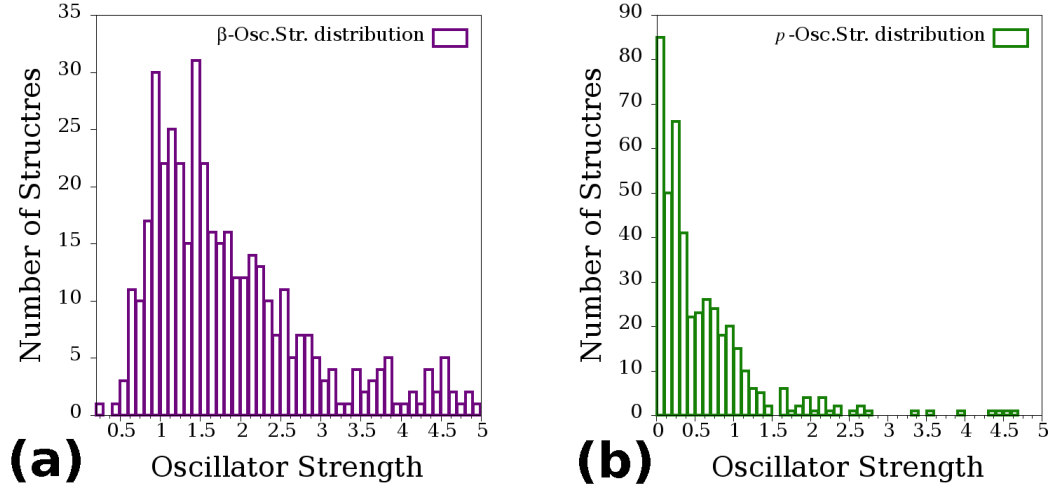
Figure 4.4: Histograms of oscillator strengths corresponding to (a) β_{max}, (b) p_{max} excitation in all GQDs.

occur either due to extended delocalization (as in conjugated carbon chains) or if there exists lesser number of resonant sextets (according to Clar's rule [21, 25, 43]). In our case, however, the very small HLGs are seen due to completely different reasons. If we look at the structures of these GQDs closely, we find that, they don't have same number of sublattice atoms (i.e., $N_A - N_B \neq 0$). In fact, in all the random shaped GQDs, we find there exists two additional sublattice atoms of one type (i.e., $| N_A - N_B | = 2$). p_z orbitals of these additional atoms remains as non-bonding orbitals and appear at the zero of energy (i.e., at the Fermi-level) in the energy level diagram. If there were no interactions (as in tight-binding calculations), both of these levels would be degenerate and would appear exactly at the zero of energy. (similar to what has been observed in triangular GQDs [22, 23, 57–59]). However, because of interaction terms in ZINDO/S Hamiltonian, we find the two levels to appear above and below the zero of energy with a very low energy gap (few meV). Interestingly, these two levels have opposite parity, due to which the transition dipole moment between the two become non-zero. Thus, these two levels give rise to optical transition with a finite oscillator strength (OS). Since, the energy gap between these two levels is too small, the optical absorption appears in IR-region.
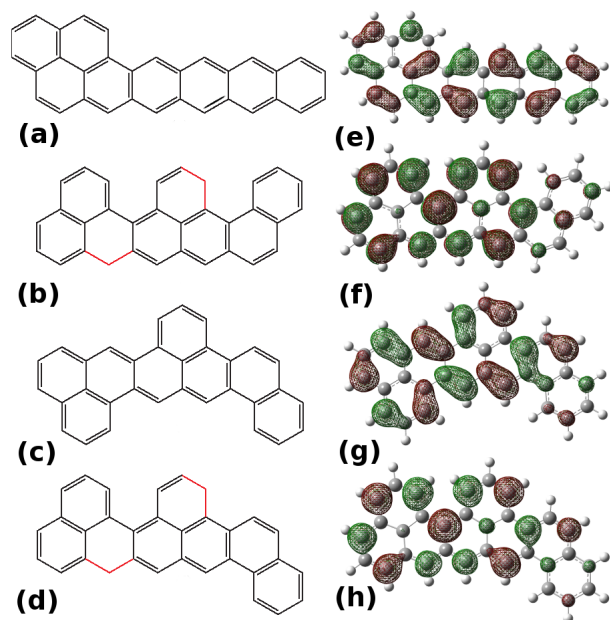
Figure 4.5: Schematic diagrams of four structural isomers of $C_{32}H_{18}$ GQD are given in (a)-(d) and their HOMO isosurfaces are given in (e)-(h), respectively. Iso-value of 0.02 e/Å^3 is used for all the plots.

As an example, in Figs. 4.5a–4.5d we have given four structural isomers (here after, addressed as 4.5a, 4.5b, 4.5c and 4.5d, respectively) of $C_{32}H_{18}$, where only 4.5b and 4.5d have the sublattice imbalance. As explained, only for 4.5b and 4.5d, we find p_{max} in IR-region (> 2000 nm) but not for 4.5a and 4.5c. In Fig. 4.5, we have also given the conjugation and isosurface plots of HOMO for these GQDs. As can be seen, because of sublattice imbalance, the conjugation in 4.5b and 4.5d GQDs is not continuous and there are "conjugation breaks", which are clear demonstration of solitonic structure (conjugated system), domain walls (seen in ferromagnetic metal blocks). The main point to notice is that, these defect states are intrinsic in these GQDs and these have not been externally induced.

IR-activity of GQDs which absorb below 2500 nm is mainly due to the zigzag edge nature of these GQDs, which invokes radical character (similar to edge states in ZGNRs) and lowers their HLG. For example, it is well known that the polyacenes have the lowest HLG among the various PAHs [21] and p_{max} of hexacene (6 fused benzne rings) itself is 750 nm. Also, Hod et al. [53, 54] have shown that rectangular
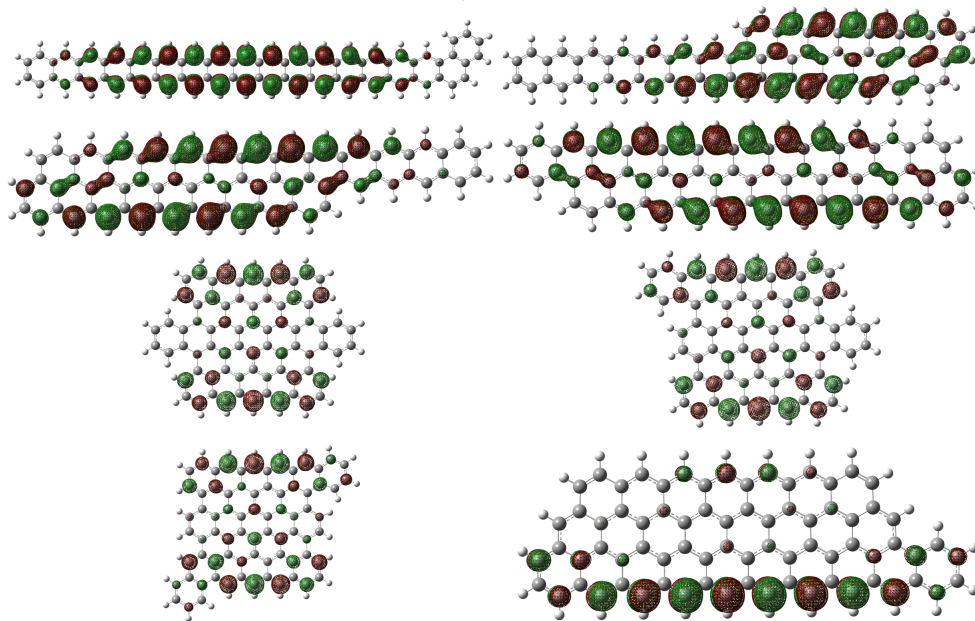
Figure 4.6: Isosurfaces of HOMO of some of the C74 GQDs considered in this study.

GQDs can possess low HLG and through TDDFT calculations, our group has also shown that p_{max} of rectangular GQDs is $\sim$ 1900 nm. [20] Inspecting the structures of GQDs which absorb in the region of 760-2500 nm, we find that all these GQDs have either polyacene type structure or rectangular type structure, with some of their edges being substituted with ethene, propene, cis-1,3-dibutene etc. Also, it is important to mention that HOMO of all the IR-active structures is different from that of the non-IR-active structures.

Frontier MOs of IR-active GQDs have larger number of nodes, and hence, look like the collection of p_z orbitals on individual carbon atoms without overlap (for example, see Figs. 4.5f and 4.5h). The reverse is true for the non-IR-active GQDs (see Figs. (4.5e, 4.5g)). Presence of large number of nodes destabilizes HOMO compared to its structural isomers with less number of nodes, and hence, lesser HLG and IR-activity. As an example of the above mentioned observations, we have given absorption spectra (see Fig. 4.7) and isosurfaces of HOMO (see Fig. 4.6) of C74 GQDs. Finally, as the OS of p_{max} peak for majority of these GQDs is > 0.5 and as OS of β_{max} peak is almost always found to > 0.5, we find that these GQDs can
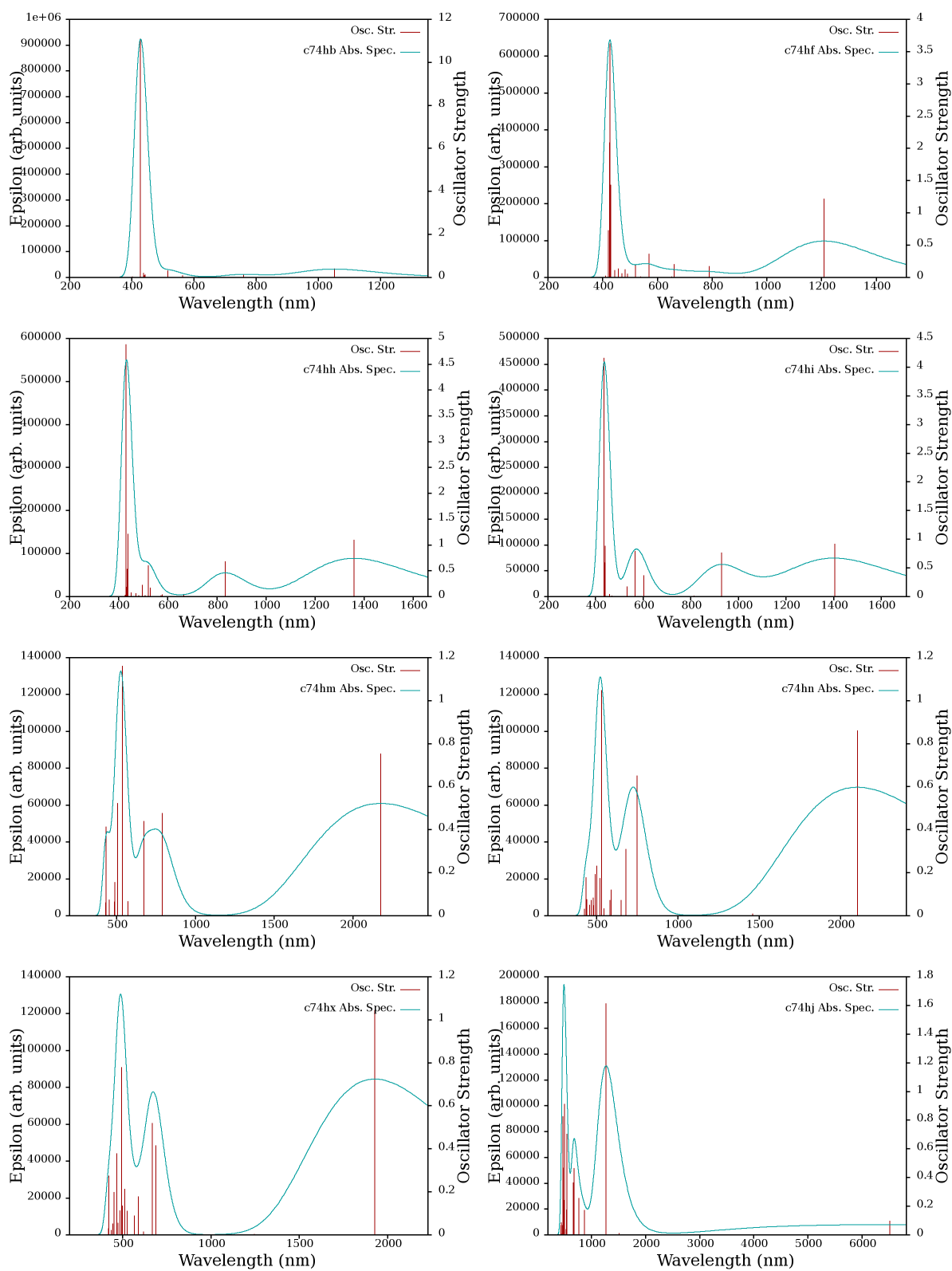
Figure 4.7: Absorption spectra corresponding to the GQDs given in the above figure (Fig. 4.5).

have broad band absorption (BBA), as predicted earlier for triangular GQDs [22, 23] and rectangular GQDs. [20] BBA of these GQDs can also be seen in Fig. 4.7. To conclude all the above results, we find that GQDs with inequivalent sublattice atoms or GQDs with rectangular or stripe shapes can absorb in IR-region and they may be suitable candidates for BBA.

Comparison of ZINDO/S and TDDFT results:

To put the results obtained from the ZINDO/S method at a solid footing, we have performed TDDFT calculations at CAMB3LYP/6-31+g(d) level of theory on a few GQDs. First, we will present our results on GQDs of various shapes. In Figs. 4.8a–4.8f, we have given the absorption spectra of S_a, S_z, F_a, F_z, T_a and T_z, respectively, calculated at both ZINDO/S and TDDFT levels of theory along with the iso-surfaces of their HOMO (only from TDDFT). Clearly, absorption profiles of both the methods compares farily well, although OS values predicted by ZINDO/S are higher than that of TDDFT. Also, λ_{max} predicted by ZINDO/S is consistently red-shifted compared to the TDDFT predicted values. Consistent with the previous arguments on the isosurface of HOMO (calculated using ZINDO/S), even with TDDFT we find larger number of nodes (see Fig. 4.8f) in the HOMO if the GQD has IR-activity and it has more overlapping character if the GQD is not IR-active (see Fig. 4.8a–4.8e). Also, we find that the character of the p_{max} excitation (i.e., MOs involved in the excitation) is predicted to be the same by both the methods. Importantly, we find that GQDs whose HOMO is mainly localized on the edge atoms (as in S_z and T_z) and whose p_{max} excitation has major contribution from HOMO to LUMO, are IR-active. From Fig. 4.8, one may also infer that the presence of zigzag edges is only a necessary, but not a sufficient condition (example being the F_z GQDs) for the IR-absorption. Finally, to see the effect of inequivalent sublattice atoms on the IR-activity, we have considered five C28-GQDs with $N_A - N_B = 2$, and we find all of them to be IR
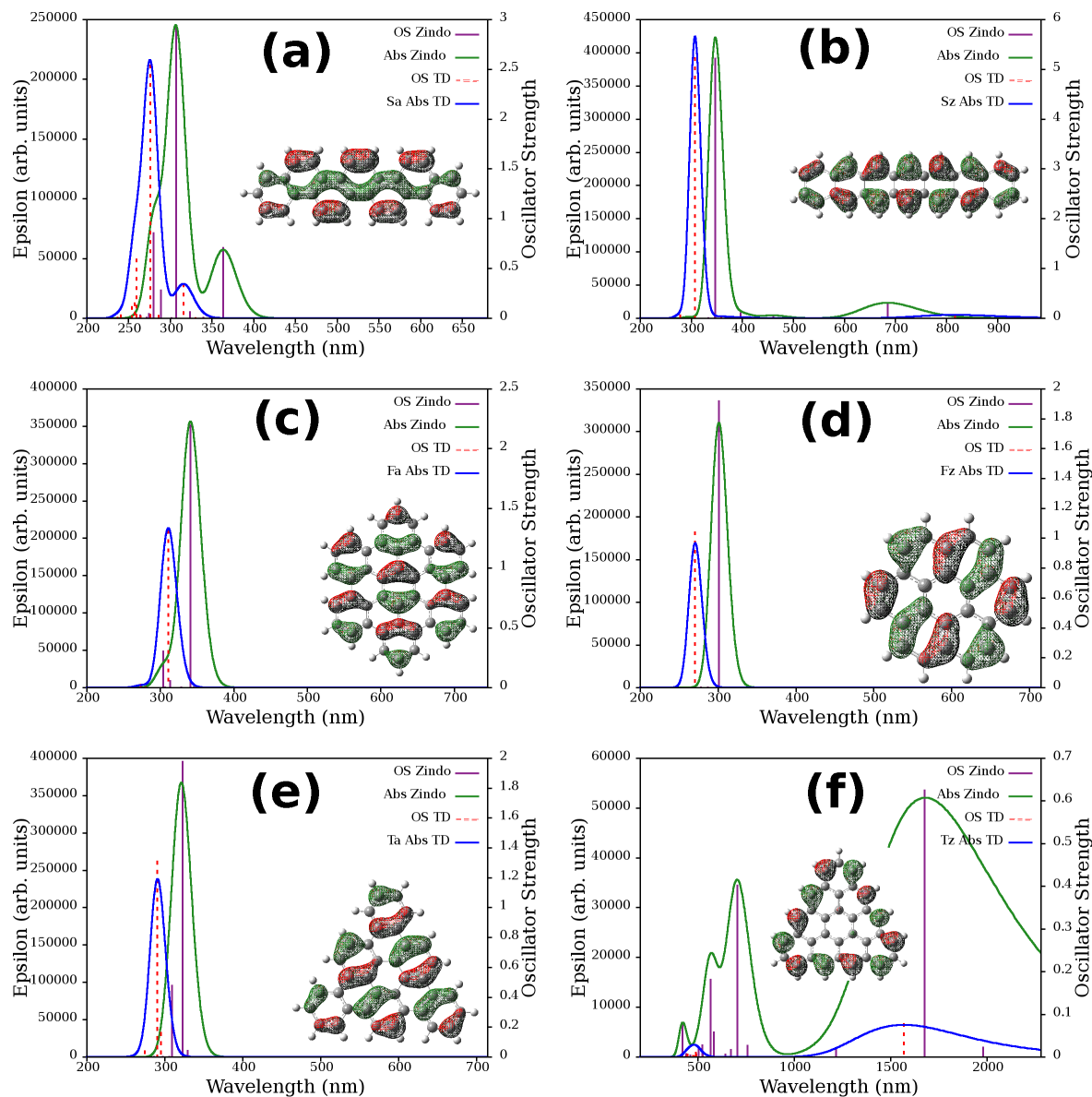
Figure 4.8: Absorption profiles of GQDs of various shapes calculated at both ZINDO/S level of theory and using TDDFT at CAMB3LYP/6-31+g(d) level of theory. Insets in each figure show the isosurface of the HOMO of that GQD calculated using TDDFT. (a)-(f) represents S_a, S_z, F_a, F_z, T_a and T_z GQDs, respectively. Iso-value of 0.02 e/Å^3 is used for all the plots.

Table 4.3: System names, wavelength corresponding to "p_{max}" and "β_{max}" excitations of all C28-GQDs whose p_{max} is in IR-region are given. Values inside the parenthesis are the ZINDO/S results and the ones which are outside are the CAM-B3LYP/6-31+g(d) results. Nomenclature is according to ref [25].

System	p_{max} (nm)	β_{max} (nm)
c28hcc	2966.1085 (3158.0065)	436.1311 (460.6820)
c28hj	4125.9014 (10818.7903)	346.5642 (429.1269)
c28hM	3035.8310 (4413.7891)	434.3282 (460.0666)
c28hR	3145.1887 (6156.0743)	393.7104 (454.2180)
c28hS	2896.1303 (4251.8291)	425.8401 (491.0231)
c28hss	3408.0082 (6687.3429)	397.7012 (448.3378)
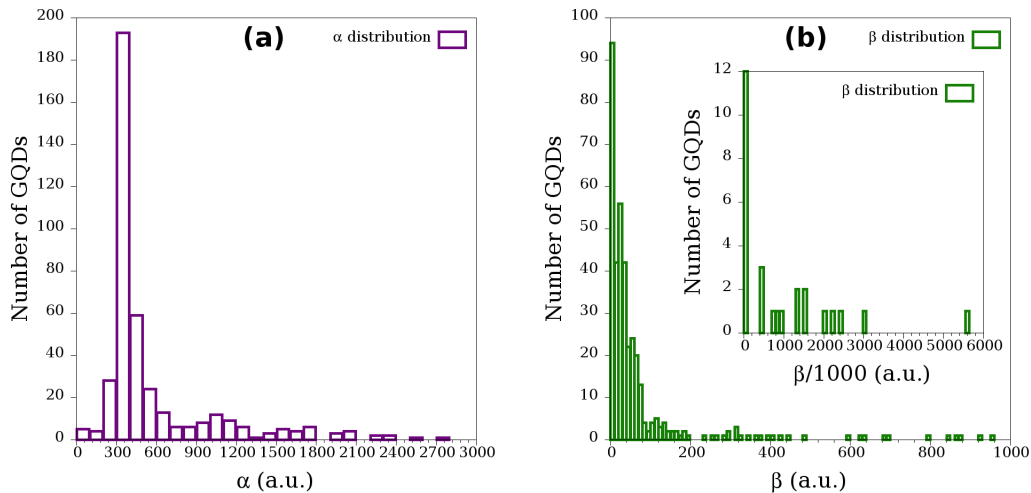
Figure 4.9: Histograms of isotropic average values of (a) polarizability, α and (b) first hyperpolarizability, β of all GQDs.

active, again consistent with the ZINDO/S results (see Table 4.3). Thus, we find that, results of ZINDO/S and TDDFT are consistent and compare well for the GQDs considered in this study.

4.3.3 Nonlinear optical properties

In this subsection, we present the linear polarizability (α) and first hyperpolarizability (β) of all the GQDs calculated using the finite field approach as implemented in the MOPAC and g09 packages. Expressions for the dipole moment and the energy of a

molecule interacting with an external electric field are given by Eqns. 1 and 2 [60].

$$\mu_i = \mu_{0i} + \alpha_{ij}F_j + \frac{1}{2}\beta_{ijk}F_jF_k + \frac{1}{6}\gamma_{ijkl}F_jF_kF_l + \dots \quad (4.1)$$

$$E(F) = E(0) - \mu_i F_i - \frac{1}{2!}\alpha_{ij}F_iF_j - \frac{1}{3!}\beta_{ijk}F_jF_k - \frac{1}{4!}\gamma_{ijkl}F_jF_kF_l - \dots \quad (4.2)$$

where, μ_0 is the permanent dipole moment, α_{ij}, β_{ijk} and γ_{ijkl} are the linear polar-izability, 1st and 2nd hyperpolarizability tensor elements, respectively. Also, for a molecule, the avergae values of above quantities (μ_{av} etc.) are defined as

$$\mu_{av} = (\mu_x^2 + \mu_y^2 + \mu_z^2)^{1/2} \quad (4.3)$$

$$\alpha_{av} = \frac{1}{3}(\alpha_{xx} + \alpha_{yy} + \alpha_{zz}) \quad (4.4)$$

$$\beta_{av} = (\beta_x^2 + \beta_y^2 + \beta_z^2)^{1/2} \quad (4.5)$$

where,

$$\beta_i = \frac{3}{5}(\beta_{iii} + \beta_{ijj} + \beta_{ikk}), i, j, k = x, y, z \quad (4.6)$$

In Figs. 4.9a and 4.9b, we have plotted the distribution of isotropic average α and β values for all the GQDs at static field. Similar to absorption profiles, majority of the GQDs' α and β values are confined to a small region. For these majority GQDs, we find that the α and β values are in the range of $250-700$ a.u. ($\sim 40-100$ Å^3) and $1-200$ a.u. ($10^{-32}-10^{-30}$ esu), respectively. Compared to the α and β values of para-nitroaniline (16.346 a.u. and 978.21 a.u., respectively), it is nice to notice that majority of the GQDs already have high polarizability and moderate hyperpolarizabilities. Importantly, we find that several GQDs possess α and β values which are orders of magnitude greater than that of para-nitroaniline (see Fig 4.9a and inset of Fig 4.9b).

In general, both linear polarizability and first order hyperpolarizabilities have

an inverse relationship with the energy gap between the states involved in the polarization, and are directly proportional to the transition moment. Thus, we can expect an increase in α and β if the ground and excited states are closely spaced or the transition moment between the states is high or both. From the above reasoning, one can also infer that GQDs with low HLG and whose 1st excited state has major contribution from HOMO to LUMO transition should give higher α and β values. Indeed, we find that all the GQDs which are IR-active also have high α and β (except the GQDs with inversion symmetry) values, that is, above the range of $250-700$ a.u. and $1-200$ a.u., respectively. Also, we find that some of the GQDs with zigzag edges, like F_z, which are not IR-active but have very high oscillator strength for the p_{max} (see Fig. 4.8d) excitation also show higher α values. However, due to the presence of inversion symmetry, such GQDs do not have higher β values. Based on all the above results, we conjecture that GQDs with very low HLGs can have both broad band absorption and nonlinear optical activity, and hence, are potential candidates for optoelectronic devices.

4.4   Conclusions

We have performed a systematic study on the GQDs of various sizes, shapes and edges to explore their linear and nonlinear optical properties. First, we find the formation energies of GQDs have a near linear dependence on their number of edge atoms and HOMO-LUMO gaps of a GQD with a particular number of carbon atoms can be tuned from $\sim$ 0-3 eV depending on its shape and edge nature. Trends in the HLG can be understood based on the Clar's rule of aromatic sextets for majority of the sytems. Extremely low HLGs of certain GQDs is due to the presence of unequal number of sublattice atoms in these GQDs, that is, $N_A - N_B \neq 0$. Tunability of HLG has also been reflected in the tunability of the absorption profiles in these GQDs. We find that majority of the GQDs absorb strongly in the UV-VIS region with their

β_{max} (p_{max}) being located in the region between 250-450 (300-700) nm) and their α and β values are in the range of $250-700$ a.u. and $1-200$ a.u., respectively. However, ~ 70 GQDs have their p_{max} in IR-region and have higher α (> 700 a.u.) and β (> 200 a.u.) values. A common feature which we find in all these IR-active GQDs is the existence of larger number of nodes in the isosurface of HOMO which leads to an increment in HOMO energy, and hence, decrement in the HLG. Due to their high oscillator strengths in both UV-VIS and IR-regions these GQDs can possess broad band absorption. With their high α and β values along with the BBA, we expect them to be potential candidates for optoelectronic devices.

Bibliography

[1] J. Zheng, R. a. Barton, and D. Englund, ACS Photonics **1**, 768 (2014).

[2] H. Sun and J. Autschbach, J. Chem. Theory Comput. **10**, 1035 (2014).

[3] J. T. Kim, Y.-J. Yu, H. Choi, and C.-G. Choi, Opt. Express **22**, 803 (2014).

[4] G. Sobon, J. Sotor, I. Pasternak, W. Strupinski, K. Krzempek, P. Kaczmarek, and K. M. Abramski, Laser Phys. Lett. **10**, 035104 (2013).

[5] A. Urich, K. Unterrainer, and T. Mueller, Nano Lett. **11**, 2804 (2011).

[6] Z. Sun, T. Hasan, F. Torrisi, D. Popa, G. Privitera, F. Wang, F. Bonaccorso, D. M. Basko, and A. C. Ferrari, ACS nano **4**, 803 (2010).

[7] S. A. Sø rngård, S. I. Simonsen, and J. P. Hansen, Phys. Rev. A **87**, 053803 (2013).

[8] S.-Y. Hong, J. I. Dadap, N. Petrone, P.-C. Yeh, J. Hone, and R. M. Osgood, Phys. Rev. X **3**, 021014 (2013).

[9] T.-Z. Shen, S.-H. Hong, and J.-K. Song, Nat. Mater. **13**, 394 (2014).

[10] R. Shimano, G. Yumoto, J. Y. Yoo, R. Matsunaga, S. Tanabe, H. Hibino, T. Morimoto, and H. Aoki, Nat. Commun. **4**, 1841 (2013).

[11] H. Yang, X. Feng, Q. Wang, H. Huang, W. Chen, A. T. S. Wee, and W. Ji, Nano Lett. **11**, 2622 (2011).

[12] B. S. Mashford, M. Stevenson, Z. Popovic, C. Hamilton, Z. Zhou, C. Breen, J. Steckel, V. Bulovic, M. Bawendi, S. Coe-Sullivan, et al., Nat. Photonics **7**, 407 (2013).

[13] V. Klimov, A. Mikhailovsky, and S. Xu, Science **290**, 314 (2000).

[14] H. Choi, J. G. Radich, and P. V. Kamat, J. Phys. Chem. C **118**, 206 (2014).

[15] J. Tian, R. Liu, Y. Zhao, Y. Peng, X. Hong, Q. Xu, and S. Zhao, Nanotechnology **21**, 305101 (2010).

[16] R. C. Somers, M. G. Bawendi, and D. G. Nocera, Chem. Soc. Rev. **36**, 579 (2007).

[17] A. D. Lad, P. Prem Kiran, G. Ravindra Kumar, and S. Mahamuni, Appl. Phys. Lett. **90**, 133113 (2007).

[18] A. Shavel, N. Gaponik, and A. Eychmu, pp. 5905–5908 (2004).

[19] A. M. Dennis, B. D. Mangum, A. Piryatinski, Y.-S. Park, D. C. Hannah, J. L. Casson, D. J. Williams, R. D. Schaller, H. Htoon, and J. a. Hollingsworth, Nano Lett. **12**, 5545 (2012).

[20] S. S. Yamijala, A. Bandyopadhyay, and S. K. Pati, J. Phys. Chem. C **117**, 23295 (2013).

[21] R. Rieger and K. Müllen, J. Phys. Org. Chem. **23**, 315 (2010).

[22] A. D. Güçlü, P. Potasz, M. Korkusinski, and P. Hawrylak, *Graphene Quantum Dots*, NanoScience and Technology (Springer Berlin Heidelberg, 2014).

[23] A. D. Güçlü, P. Potasz, and P. Hawrylak, Phys. Rev. B **82**, 155445 (2010).

[24] a. M. Silva, M. S. Pires, V. N. Freire, E. L. Albuquerque, D. L. Azevedo, and E. W. S. Caetano, J. Phys. Chem. C **114**, 17472 (2010).

[25] a. Kuc, T. Heine, and G. Seifert, Phys. Rev. B **81**, 085430 (2010).

[26] M. A. Sk, A. Ananthanarayanan, L. Huang, K. H. Lim, and P. Chen, J. Mat. Chem. C **2**, 6954 (2014).

[27] Z. Fang, Y. Wang, A. Schlather, and Z. Liu, Nano Lett. **14**, 299 (2013).

[28] X. Yan, B. Li, and L.-s. Li, Acc. Chem. Res. **46**, 2254 (2013).

[29] L. Tang, R. Ji, X. Li, G. Bai, C. P. Liu, J. Hao, J. Lin, H. Jiang, K. S. Teng, Z. Yang, et al., ACS nano **8**, 6312 (2014).

[30] H. Riesen, C. Wiebeler, and S. Schumacher, J. Phys. Chem. A **118**, 5189 (2014).

[31] I. Ozfidan, M. Korkusinski, a. D. Güçlü, J. a. McGuire, and P. Hawrylak, Phys. Rev. B **89**, 085310 (2014).

[32] Z. Zhou, Z. Liu, and Z. Li, J. Phys. Chem. C **115**, 16282 (2011).

[33] K. Yoneda, M. Nakano, R. Kishi, H. Takahashi, A. Shimizu, T. Kubo, K. Kamada, K. Ohta, B. Champagne, and E. Botek, Chem. Phys. Lett. **480**, 278 (2009).

[34] K. Yoneda, M. Nakano, K. Fukuda, and B. Champagne, J. Phys. Chem. Lett **3**, 3338 (2012).

[35] K. Yoneda, M. Nakano, and Y. Inoue, J. Phys. Chem. C **116**, 17787 (2012).

[36] M. Elstner, D. Porezag, G. Jungnickel, J. Elsner, M. Haugk, T. Frauenheim, S. Suhai, and G. Seifert, Phys. Rev. B **58**, 7260 (1998).

[37] Y. Yang, H. Yu, D. York, Q. Cui, and M. Elstner, J. Phys. Chem. A **111**, 10861 (2007).

[38] M. Gaus, A. Goez, and M. Elstner, J. Chem. Theory Comput. **9**, 338 (2013).

[39] B. Aradi, B. Hourahine, and T. Frauenheim, J. Phys. Chem. A **111**, 5678 (2007).

[40] A. Zobelli, V. Ivanovskaya, P. Wagner, I. Suarez-Martinez, A. Yaya, and C. P. Ewels, Phys. Status Solidi B **249**, 276 (2012).

[41] A. N. Enyashin and A. L. Ivanovskii, Phys. Status Solidi B **248**, 1879 (2011).

[42] M. J. Frisch, G. W. Trucks, H. B. Schlegel, G. E. Scuseria, M. A. Robb, J. R. Cheeseman, G. Scalmani, V. Barone, B. Mennucci, G. A. Petersson, et al., *Gaussian 09 Revision B.01*, gaussian Inc. Wallingford CT 2009.

[43] J. O. Oña Ruales and Y. Ruiz-Morales, J. Phys. Chem. A **118**, 5212 (2014).

[44] C. Cocchi, D. Prezzi, and A. Ruini, J. Phys. Chem. A **118**, 6507 (2014).

[45] J. Linnanto and J. Korppi-Tommola, Phys. Chem. Chem. Phys. **2**, 4962 (2000).

[46] A. a. Voityuk, WIREs Comput Mol Sci **3**, 515 (2013).

[47] *MOPAC2012, James J. P. Stewart, Stewart Computational Chemistry, Version 14.212L web: HTTP://OpenMOPAC.net.*

[48] J. D. C. Maia, G. A. Urquiza Carvalho, C. P. Mangueira, S. R. Santana, L. A. F. Cabral, and G. B. Rocha, J. Chem. Theory Comput. **8**, 3072 (2012).

[49] N. M. O'Boyle, A. L. Tenderholt, and K. M. Langner, J. Comput. Chem. **29**, 839 (2008).

[50] S. S. Yamijala, A. Bandyopadhyay, and S. K. Pati, Chem. Phys. Lett. **603**, 28 (2014).

[51] A. Bandyopadhyay, S. S. R. K. C. Yamijala, and S. K. Pati, Phys. Chem. Chem. Phys. **15**, 13881 (2013).

[52] Z. G. Fthenakis, Mol. Phys. **111**, 3289 (2013).

[53] V. Barone, O. Hod, J. E. Peralta, and G. E. Scuseria, Acc. Chem. Res. **44**, 269 (2011).

[54] O. Hod, V. Barone, and G. E. Scuseria, Phys. Rev. B **77**, 035411 (2008).

[55] D. P. Kosimov, a. a. Dzhurakhalov, and F. M. Peeters, Phys. Rev. B **81**, 195414 (2010).

[56] Z. Z. Zhang, K. Chang, and F. M. Peeters, Phys. Rev. B **77**, 235411 (2008).

[57] J. Fernández-Rossier and J. Palacios, Phys. Rev. Lett. **99**, 177204 (2007).

[58] A. D. Güçlü and P. Hawrylak, Phys. Rev. B **87**, 035425 (2013).

[59] O. Voznyy, a. D. Güçlü, P. Potasz, and P. Hawrylak, Phys. Rev. B **83**, 165417 (2011).

[60] H. A. Kurtz, J. J. P. Stewart, and K. M. Dieter, J. Comput. Chem. **11**, 82 (1990).

Chapter 5

Nitrogen doped graphene quantum dots as possible substrates to stabilize planar conformer of Au$_{20}$ over its tetrahedral conformer: A systematic dft study.*

5.1 Introduction

Properties of gold clusters, such as, stability, ionization potential, and catalytic activity, depend not only on their size but also on their shape and charge state.[1–4] Stabilizing a particular conformer among the others, to achieve the desired properties, is one of the active fields of research. [3, 5–13] When gold clusters are grown on a

substrate, the nature of the substrate highly dictates the stability and shape of the conformer. In the past few years, a large number of studies have been carried out on several substrates mainly to understand the substrate properties in stabilizing a particular conformer of the gold cluster. The main theme of majority of these studies is to stabilize the catalytically active planar conformer of Au_{20} cluster (P-Au_{20}) over the thermodynamically stable tetrahedral conformer (T-Au_{20}) [3, 5–12] on various metal oxides substrates, such as, MgO, [5–8, 10, 12] CaO [3, 11, 12] etc.

All the earlier experimental [14, 15] and theoretical studies [2, 9, 16] have shown that tetrahedral conformer is the most stable conformer in gas phase. Same trend in the stability has been found even when Au_{20} is on pristine MgO, CaO substrates.[3, 5–12] Also, T-Au_{20} also has a larger HOMO-LUMO gap (1.77 eV) compared to its other two-dimensional conformers. [2, 9] because of which T-Au_{20} is chemically more stable (or less reactive) and has limited applications in catalysis. Less reactivity of T-Au_{20} compared to P-Au_{20} has already been proven during the catalytic conversion of CO to CO_2 in the presence of O_2 on a Mo-doped MgO substrate.[7] Also, through theoretical calculations, it has been shown that both the electron accepting and donating capabilities of P-Au_{20} are more compared to that of T-Au_{20} and such trend has been found to be common for planar clusters of gold. [9] Thus, for catalytic applications, it is required to stabilize "less stable but catalytically more active" conformers of gold than the "less reactive and thermodynamically more stable" conformers.

Earlier studies have shown different ways to stabilize the planar conformer of Au_{20}, [3, 5–12], mainly using metal-oxide substrates. Some of the methods which were used to tune the morphology of Au_{20} include (i) depositing thin metal-oxide films on transition metals [3, 5–7] (ii) application of external field [8] when depositing bulk metal-oxides on transition metals and (iii) to add external dopants [3, 10–12] to bulk metal-oxides without depositing them on transition metals etc.

Unlike these studies, in this chapter we have considered graphene quantum dots (GQDs), [17–21] the zero-dimensional analogues of graphene, as the substrate. We have considered different possibilities like external doping by substituting the carbon atoms of GQD with nitrogen or boron atoms, increasing the doping concentration, introduction of defects, increasing the number of layers of GQDs etc., to see whether we can stabilize P-Au$_{20}$ over T-Au$_{20}$ on GQDs. We have considered GQDs as our substrates because of their easy synthesis and due to their ability to stabilize Pd nanoparticles (NPs) as reported by Li., *et al.* [22]. The same group (and also several other groups) has also shown the successful synthesis of N-doped GQDs (NGQDs) with precise control over the position of the dopant nitrogen. [23, 24] Though, both experimental and theoretical works exist on the interaction of Au clusters with N-doped graphene (not GQDs), they were not concentrated on tuning the morphology of Au clusters. In this chapter, we have shown that, NGQDs can act as alternative substrates to doped metal-oxide substrates in stabilizing the P-Au$_{20}$ over T-Au$_{20}$.

5.2   Computational Details

Previous studies on the interaction between graphene and transition metal clusters suggests that dispersion forces are important to exactly mimic the interaction between gold and graphene and these studies have also shown that the empirical dispersion correction i. e. DFT-D3 is sufficient to reproduce the results obtained with the best methods (EE+vdW for Au-graphene; EE+vdW, M06-2X and MP2 calculations for Au-coronene interactions) described in these works for graphene and gold interaction. [25] We have performed all the calculations using spin-unrestricted density functional theory with Becke–Lee–Yang–Parr (BLYP) GGA exchange-correlation functional, [26, 27] along with Grimme's DFT-D3 dispersion correction,[28] as implemented in the QUICKSTEP module of the CP2K package [29] (unless otherwise mentioned explicitly). We have used the norm-conserving Goedecker– Teter– Hutter (GTH)

pseudopotentials, [30–32] which are optimized in CP2K package to use them along with the BLYP functional. CP2K uses a hybrid Gaussian and plane wave method for the electronic representation.[33] In this work, Kohn-Sham valence orbitals have been expanded using double zeta valence polarized basis sets which are optimized for the GTH psuedopotentials (DZVP– MOLOPT– SR– GTH). Together with the NN50 smoothing method, a 320 Ry density cut-off is used for the auxiliary basis set of plane waves. To avoid any unwanted interaction with the periodic images, we have considered a $38 \times 38 \times 38$ Å cubic unit cell along with the poisson [34, 35] solver (to ensure the non existence of wave function after the edges of the simulation box). Geometry optimizations have been performed using BFGS method and systems are optimized till the force on each atom is less than 0.0001 Hartree/Bohr. G09 package [36] has been used to perform all the calculations on isolated gold clusters using different exchange-correlation functionals, namely, PBE, BLYP, B3LYP and M06-2X with LANL2DZ basis set and LANL2 pseudopotentials.

5.3   Results and Discussions

As mentioned clearly in all the earlier works, [5, 6, 8–11] the main reason for the stability of P-Au_{20} over T-Au_{20} on a doped metal-oxide substrate is due to the greater charge transfer from the substrate to P-Au_{20} than to T-Au_{20} (and also due to the greater charge accumulation at the cluster-substrate interface). However, there was no clear explanation regarding why there is a requirement of an oxide substrate if charge transfer is the sole reason for the stability of P-Au_{20}. To address this issue, first we have performed a series of calculations on isolated P and T-Au_{20} clusters (i.e. clusters without any substrate) with different charges and we find that the planar structure can be stabilized over tetrahedral structure when charge on the system is -2 or more. As shown in Figure 5.1, although the amount of charge required varies with E_{XC} used, it is clear that, above a particular charge dimensionality crossover will

surely occur. Also, in a previous work, [10] it has been shown that P-Au$_{20}$ can be stabilized over T-Au$_{20}$ on an Al-doped MgO substrate when substrate transfers ~ 0.9 e or more to the clusters. Thus, these results suggest that, even though a substrate is not necessary to stabilize P-Au$_{20}$ over T-Au$_{20}$, it will help to reduce the required amount of charge transfer in stabilizing P-Au$_{20}$. To further prove the non-necessity of an oxide-substrate to stabilize the planar conformer, we have considered a single layer graphene quantum dot (GQD) as our substrate and performed the calculations.
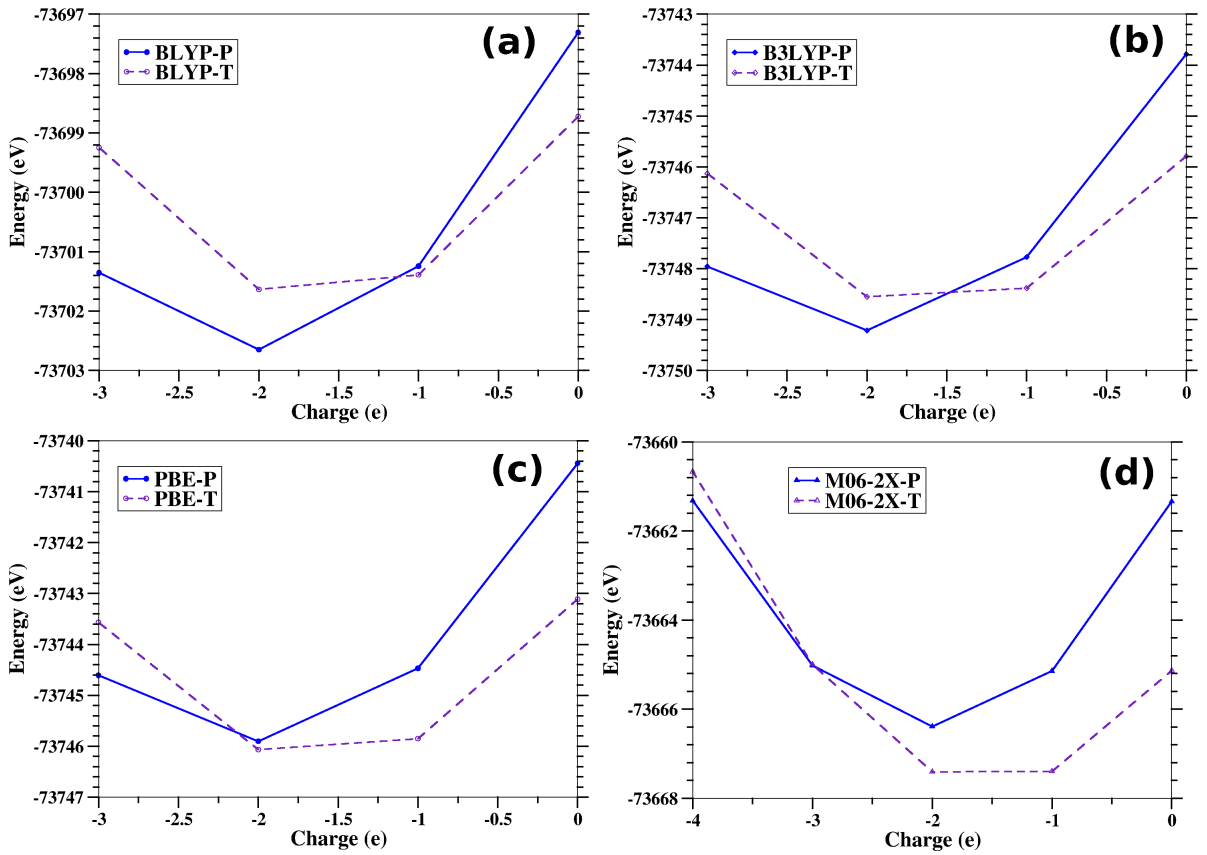
Figure 5.1: Energy of isolated Au$_{20}$ clusters as a function of charge and exchange-correlation functionals. (a) BLYP (b) B3LYP (c) PBE and (d) M06-2X functionals. P and T in the legends after the functional name denotes planar and tetra conformers, respectively, of Au$_{20}$.

In Table 5.1, we have given the energy difference ($E_{diff} = E_T - E_P$) between the T-Au$_{20}$ and P-Au$_{20}$ clusters when they are isolated and when they are on different substrates. Firstly, in accordance with several previous studies, we find that the tetra conformer is more stable (negative value of $E_T - E_P$) than the planar conformer

Table 5.1: Energy difference between P-Au$_{20}$ and T-Au$_{20}$ when they are isolated and when they are on different substrates along with the energy of substrate cluster interaction (E$_{SCI}$) is given for all the systems.

Systems	Energy (eV)	E$_T$ - E$_P$ (eV)	E$_{SCI}$ (eV)
P-Au$_{20}$	-17992.686		
T-Au$_{20}$	-17996.651	-3.965	
GQD	-35840.945		
P-Au$_{20}$@GQD	-53840.212		-6.582
T-Au$_{20}$@GQD	-53841.025	-0.813	-3.429
N-GQD	-35955.676		
P-Au$_{20}$@N-GQD	-53955.573		-7.211
T-Au$_{20}$@N-GQD	-53955.853	-0.280	-3.526
2N-GQD	-36070.362		
P-Au$_{20}$@2N-GQD	-54070.726		-7.679
T-Au$_{20}$@2N-GQD	-54070.701	0.025	-3.688
3N-GQD	-36185.150		
P-Au$_{20}$@3N-GQD	-54185.571		-7.736
T-Au$_{20}$@3N-GQD	-54185.454	0.117	-3.653
4N-GQD	-36299.796		
P-Au$_{20}$@4N-GQD	-54300.703		-8.222
T-Au$_{20}$@4N-GQD	-54300.194	0.509	-3.747
5N-GQD	-36414.411		
P-Au$_{20}$@5N-GQD	-54415.489		-8.392
T-Au$_{20}$@5N-GQD	-54414.844	0.645	-3.782
6N-GQD	-36529.330		
P-Au$_{20}$@6N-GQD	-54530.402		-8.386
T-Au$_{20}$@6N-GQD	-54529.753	0.649	-3.773
B-GQD	-35762.547		
P-Au$_{20}$@B-GQD	-53761.879		-6.646
T-Au$_{20}$@B-GQD	-53762.818	-0.939	-3.620
pyN-GQD	-36030.984		
P-Au$_{20}$@pyN-GQD	-54030.291		-6.621
T-Au$_{20}$@pyN-GQD	-54031.167	-0.876	-3.532

when the clusters are isolated. We find the same trend even when the clusters are on a GQD substrate, although the energy difference (E$_{diff}$) has reduced drastically (by $\sim$ 3 eV). In fact, the larger substrate-cluster interaction (SCI) for the case of P-Au$_{20}$ than for T-Au$_{20}$ is the reason for this reduced E$_{diff}$ and larger SCI in P-Au$_{20}$ is due to the shape of the P-Au$_{20}$ which allows all of its atoms to interact with the substrate. We have quantified the energy of SCI (E$_{SCI}$)as below: E$_{SCI}$ = E$_{tot}$

- E_{sub} - E_{Au}, where, E_{tot} is the total energy of the cluster on a substrate; E_{sub} and E_{Au} are the energies of the isolated substrate and the Au cluster, respectively, and the values are given in Table 5.1. Clearly, E_{SCI} for P-Au$_{20}$ is $\sim$ 3 eV greater than the T-Au$_{20}$, when these clusters are on a GQD substrate. Also, we find that (see Table 5.2) there is $\sim$ 1 e charge transfer (CT) to P-Au$_{20}$ from GQD, where as, it is only $\sim$ 0.2 e for T-Au$_{20}$. Thus, we find that, though T-Au$_{20}$ has acquired lesser amount of charge from GQD substrate and has lesser E_{SCI} compared with P-Au$_{20}$, its stability is still greater than that of P-Au$_{20}$. This higher stability of T-Au$_{20}$ on a GQD substrate is similar to what previously has been observed for the cases of MgO and CaO substrates [5, 6, 8–11] suggesting that our choice of substrate is correct and further necessary steps have to be taken in order to acquire the required stability of P-Au$_{20}$. Among the several previously implemented techniques, we find that one of the simple and successful technique for stabilizing P-Au$_{20}$ over T-Au$_{20}$ is doping the substrate with electron rich species [10–12]. Following these studies, we have doped our GQD substrates with nitrogen (N) atoms.

Doping GQDs with N atoms can be of several ways, for example, pyridinic, pyrrolic, substitutional [replacing C with N] etc. Experimental studies on gold clusters stabilized on N-doped graphene have shown that [24] (i) substitutional and pyrrolic (pyridinic) doping leads to n-type (p-type) graphene and (ii) dopant nitrogen sites in an n-type graphene serves as electron donors and gold clusters acts as electron acceptors. To verify these results, we have optimized the gold clusters on both substitutionally doped N-GQD and pyridinic N-GQD (pyN-GQD). In agreement with these results, we find a decrease (increase) in the negative "E_T - E_P" value (i.e., greater stabilization of planar clusters), compared to that of pristine GQD, when doping is substitutional (pyridinic). As our main aim is to stabilize P-Au$_{20}$, i.e. to attain a positive "E_T - E_P" value, we have performed all our further calculations only with substitutional doping. We have varied the doping concentration from

Table 5.2: Charges on the individual atoms (Mülliken charges) in the respective systems. Amount of the charge transferred to the gold clusters from the substrates can be directly identified by seeing column 3 (GOLD). Gain/loss of electron charge can be seen by comparing the respective systems with the isolated systems. For example, by comparing P-Au$_{20}$@GQD with GQD and P-Au$_{20}$, we can notice that, carbon has lost ~ 0.95 e charge and the same has been gained by gold.

Systems	CARBON	GOLD	NITROGEN	BORON	HYDROGEN
P-Au$_{20}$	0.00	0.00	0.00	0.00	0.00
T-Au$_{20}$	0.00	0.00	0.00	0.00	0.00
GQD	-1.75	0.00	0.00	0.00	1.75
P-Au$_{20}$@GQD	-0.83	-0.95	0.00	0.00	1.79
T-Au$_{20}$@GQD	-1.58	-0.18	0.00	0.00	1.76
N-GQD	-1.71	0.00	-0.03	0.00	1.74
P-Au$_{20}$@N-GQD	-0.75	-1.07	0.04	0.00	1.78
T-Au$_{20}$@N-GQD	-1.59	-0.20	0.04	0.00	1.75
2N-GQD	-1.69	0.00	-0.05	0.00	1.73
P-Au$_{20}$@2N-GQD	-0.42	-1.43	0.07	0.00	1.79
T-Au$_{20}$@2N-GQD	-1.45	-0.34	0.04	0.00	1.75
3N-GQD	-1.65	0.00	-0.08	0.00	1.73
P-Au$_{20}$@3N-GQD	-0.27	-1.62	0.10	0.00	1.79
T-Au$_{20}$@3N-GQD	-1.01	-0.79	0.05	0.00	1.76
4N-GQD	-1.62	0.00	-0.11	0.00	1.72
P-Au$_{20}$@4N-GQD	-0.29	-1.63	0.15	0.00	1.78
T-Au$_{20}$@4N-GQD	-0.99	-0.83	0.07	0.00	1.75
5N-GQD	-1.58	0.00	-0.13	0.00	1.71
P-Au$_{20}$@5N-GQD	-0.25	-1.66	0.15	0.00	1.77
T-Au$_{20}$@5N-GQD	-0.93	-0.87	0.05	0.00	1.75
6N-GQD	-1.53	0.00	-0.18	0.00	1.71
P-Au$_{20}$@6N-GQD	-0.20	-1.71	0.15	0.00	1.76
T-Au$_{20}$@6N-GQD	-0.90	-0.86	0.02	0.00	1.74
B-GQD	-1.63	0.00	0.00	-0.14	1.76
P-Au$_{20}$@B-GQD	-0.77	-0.98	0.00	-0.05	1.80
T-Au$_{20}$@B-GQD	-1.41	-0.35	0.00	-0.02	1.78
pyN-GQD	-1.27	0.00	-0.49	0.00	1.76
P-Au$_{20}$@pyN-GQD	-0.50	-1.02	-0.29	0.00	1.80
T-Au$_{20}$@pyN-GQD	-1.07	-0.42	-0.28	0.00	1.77

0.44 % (i. e. one N atom in 228 C atoms) to 2.63 % (6 N atoms in 228 C atoms) and while doping more than one nitrogen, we have considered the experimental results of N-doped graphene [37] and doped only the carbon atoms belonging to same sub-lattice.

In Table 5.1, we have given "E$_T$ - E$_P$" values for all the different concentrations

considered. Clearly, the most stable conformer of Au_{20} on a GQD substrate has changed from tetra to planar for all the nitrogen dopant concentrations greater than ~ 0.88 % (for the present level of theory). Also, we find an increase in the stability of P-Au_{20} with the increase in the dopant concentrations. This is an interesting result, because it proves the non-necessity of an oxide substrate for stabilizing catalytically active P-Au_{20} conformer. Many N-doped GQDs and graphene sheets have been synthesized. [22–24, 37] So, we checked the robustness of our result against (i) the dopant atoms position (ii) number of GQD layers and (iii) exchange-correlation functional. Firstly, for 2.63 % concentration, we find that P-Au_{20} is, at least, $\sim$ 0.26 eV more stable than T-Au_{20}, even when all the dopant atoms are in a single zigzag line of a GQD (which is not a favorable way of doping [37]). Next, as the experimentally synthesized GQDs generally contain more than one layer, we have also considered bi-layered GQDs. With an increase in the number of layers, we find that the stability of P-Au_{20} has further increased for the same number of dopant N-atoms. For example, when substituting with two nitrogen atoms stability of P-Au_{20} has increased from ~ 0.026 eV to ~ 0.1 eV when moved from monolayer GQD to bi-layer GQD. Similarly, when substituted with six nitrogen atoms, the stability has raised by ~ 0.3 eV for bi-layer GQD. Finally, we have changed the exchange correlation functional and found that the trend is still maintained, although the amount of gain in the stability is different. Thus, based on our results and on the available experimental methods for growing N-GQDs as well as gold clusters on N-doped graphene, we conjecture that experimentalists would find a dimensionality cross-over from T-Au_{20} to P-Au_{20} on N-GQDs.

Finally, to know the possible catalytically active sites of Au_{20} clusters, when supported on a N-GQD, we have plotted the iso-surfaces of charge transfer between N-GQD and Au_{20} clusters as shown in Figure 5.2. To plot the iso-surfaces of charge transfer, total electron density of the composite system (i.e. N-GQD + Au_{20}) has

been subtracted from the total electron density of the substrate and the cluster with the same geometry (i.e. without any further optimization). From these plots, it is clear that, major changes in the charge of the substrate occurred only for the atoms which are below the Au_{20} clusters. In the case of clusters, major changes have occurred for the corner atoms than for the atoms which are in the middle. Among T-Au_{20} and P-Au_{20} clusters, P-Au_{20} has large number of corner atoms and more number of atoms directly interacting with the substrate. Also, we notice that the amount of charge accumulated at the substrate cluster interface is more for P-Au_{20} than for T-Au_{20}. Finally, for T-Au_{20}, only those atoms which are directly above the N-GQD substrate have acquired more negative charge compared to the ones in the upper layers. Thus, based on all these results and earlier reports [5, 8, 10] we expect that corner atoms of both the clusters will act as active sites for catalytic applications and between P-Au_{20} and T-Au_{20}, the former with more active sites should be catalytically more active than T-Au_{20}.

5.4   Conclusions

In conclusion, motivated by the recent successful synthesis of colloidal GQDs and N-GQDs with precise control over the number of atoms, position of the dopants and their application in stabilizing Pd nanoparticles, we have investigated several possibilities of utilizing these doped/un-doped GQDs to stabilize the catalytically more useful P-Au_{20} compared to the thermodynamically more stable T-Au_{20}. Both single-layer and bi-layer GQDs, with and without nitrogen dopants, have been considered and we find that binding energy of P-Au_{20} towards GQD is more (~ 3 eV) compared to T-Au_{20} and it is much more when the GQDs are doped with nitrogen and is even more when the GQDs are bi-layered. Different concentrations of nitrogen doping have been considered and according to our findings, P-Au_{20} can be stabilized over T-Au_{20}, thermodynamically, by ~ 1 eV when the N-dopant concentration is
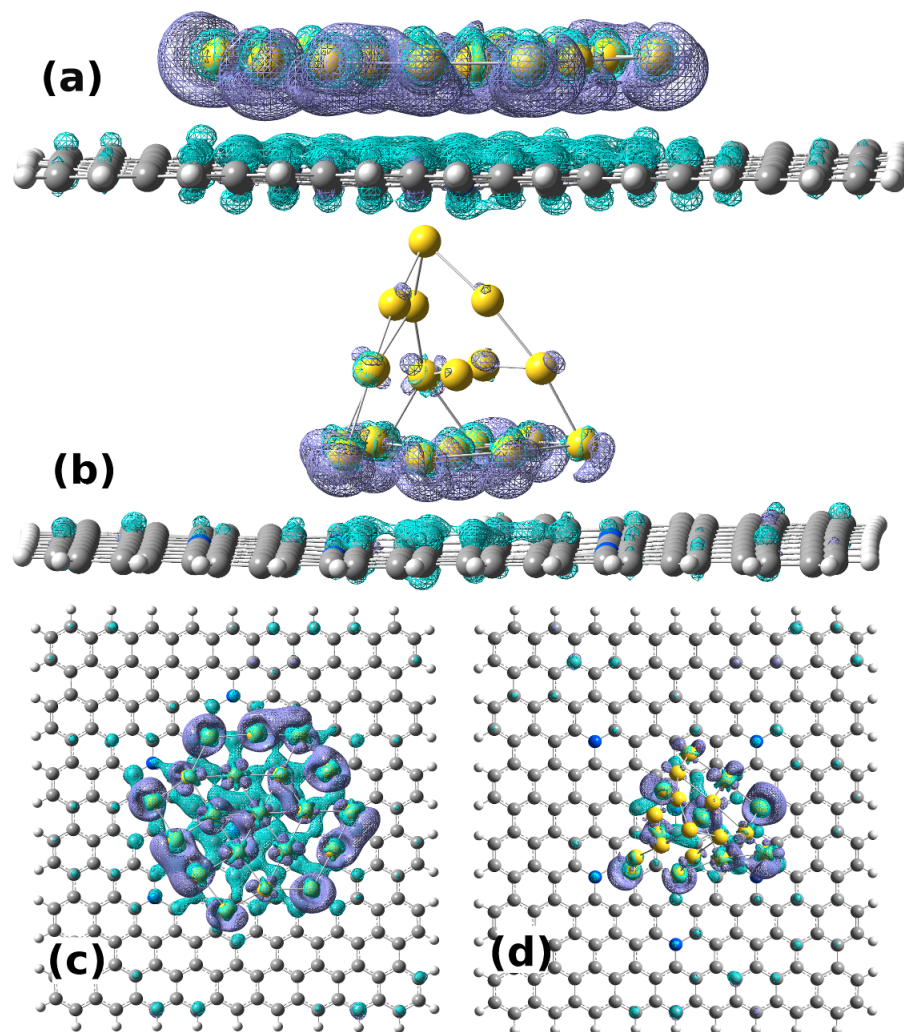
Figure 5.2: Isosurface contours depecting the charge transfer process from substrate to Au_{20} clusters. Top, bottom views of P-Au_{20} are shown in (a), (c) and of T-Au_{20} in (b), (d). Iso-value of 0.001 e/Å^3 is used for all the plots. Cyan color depicts loss in electron density.

~ 1.3 % (i.e. 1N-atom for every 76-C atoms) in bi-layer GQDs. Also, from charge transfer plots, we see that P-Au_{20} has more active sites for catalysis. Thus, mainly the stronger interaction of P-Au_{20} with N-GQD compared to T-Au_{20} is due to its larger contact area with N-GQD substrate and also its ability to accept more electrons.

Bibliography

[1] P. K. Jain, Angew. Chem. Int. Ed. **53**, 1197 (2014).

[2] E. S. Kryachko and F. Remacle, Int. J. Quantum Chem **107**, 2922 (2007).

[3] X. Shao, N. Nilius, and H.-J. Freund, Phys. Rev. B **85**, 115444 (2012).

[4] A. Nijamudheen and A. Datta, in *Nanoscience, Technology and Societal Implications (NSTSI)* (2011), pp. 1–5.

[5] D. Ricci, A. Bongiorno, G. Pacchioni, and U. Landman, Phys. Rev. Lett. **97**, 036106 (2006).

[6] M. Sterrer, T. Risse, M. Heyde, H.-P. Rust, and H.-J. Freund, Phys. Rev. Lett. **98**, 206103 (2007).

[7] C. Zhang, B. Yoon, and U. Landman, J. Amer. Chem. Soc. **129**, 2228 (2007).

[8] B. Yoon and U. Landman, Phys. Rev. Lett. **100**, 056102 (2008).

[9] A. Martinez, J. Phys. Chem. C **114**, 21240 (2010).

[10] N. Mammen, S. Narasimhan, and S. d. Gironcoli, J. Amer. Chem. Soc. **133**, 2801 (2011).

[11] X. Shao, S. Prada, L. Giordano, G. Pacchioni, N. Nilius, and H.-J. Freund, Angew. Chem. Int. Ed. **50**, 11525 (2011).

[12] F. Stavale, X. Shao, N. Nilius, H.-J. Freund, S. Prada, L. Giordano, and G. Pacchioni, J. Amer. Chem. Soc. **134**, 11380 (2012).

[13] A. Nijamudheen, D. Jose, and A. Datta, Comput. Theo. Chem. **966**, 133 (2011).

[14] J. Li, X. Li, H.-J. Zhai, and L.-S. Wang, Science **299**, 864 (2003).

[15] P. Gruene, D. M. Rayner, B. Redlich, A. F. G. van der Meer, J. T. Lyon, G. Meijer, and A. Fielicke, Science **321**, 674 (2008).

[16] B. Assadollahzadeh and P. Schwerdtfeger, J. Chem. Phys. **131**, 064306 (2009).

[17] S. S. Yamijala, A. Bandyopadhyay, and S. K. Pati, J. Phys. Chem. C **117**, 23295 (2013).

[18] A. Bandyopadhyay, S. S. R. K. C. Yamijala, and S. K. Pati, Phys. Chem. Chem. Phys **15**, 13881 (2013).

[19] S. S. Yamijala, A. Bandyopadhyay, and S. K. Pati, Chem. Phys. Lett. **603**, 28 (2014).

[20] O. Hod, V. Barone, and G. E. Scuseria, Phys. Rev. B **77**, 035411 (2008).

[21] O. Hod, J. E. Peralta, and G. E. Scuseria, Phys. Rev. B **76**, 233401 (2007).

[22] X. Yan, Q. Li, and L.-s. Li, J. Amer. Chem. Soc. **134**, 16095 (2012).

[23] X. Yan, B. Li, and L.-s. Li, Acc. Chem. Res. **46**, 2254 (2013).

[24] X. Xie, J. Long, J. Xu, L. Chen, Y. Wang, Z. Zhang, and X. Wang, RSC Adv. **2**, 12438 (2012).

[25] J. Granatier, P. Lazar, M. Otyepka, and P. Hobza, J. Chem. Theory Comput. **7**, 3743 (2011).

[26] A. D. Becke, Phys. Rev. A **38**, 3098 (1988).

[27] C. Lee, W. Yang, and R. G. Parr, Phys. Rev. B **37**, 785 (1988).

[28] S. Grimme, J. Antony, S. Ehrlich, and H. Krieg, J. Chem. Phys. **132**, 154104 (2010).

[29] J. VandeVondele, M. Krack, F. Mohamed, M. Parrinello, T. Chassaing, and J. Hutter, Comp. Phy. Comm. **167**, 103 (2005).

[30] C. Hartwigsen, S. Goedecker, and J. Hutter, Phys. Rev. B **58**, 3641 (1998).

[31] S. Goedecker, M. Teter, and J. Hutter, Phys. Rev. B **54**, 1703 (1996).

[32] M. Krack, Theor. Chem. Acc. **114**, 145 (2005).

[33] B. G. Lippert, J. Hutter, and M. Parrinello, Mol. Phys. **92**, 477 (1997).

[34] L. Genovese, T. Deutsch, A. Neelov, S. Goedecker, and G. Beylkin, J. Chem. Phys. **125**, 074105 (2006).

[35] L. Genovese, T. Deutsch, and S. Goedecker, J. Chem. Phys. **127**, 054704 (2007).

[36] M. Frisch, G. Trucks, H. Schlegel, G. Scuseria, M. Robb, J. Cheeseman, G. Scalmani, V. Barone, B. Mennucci, G. Petersson, et al., Gaussian, Inc., Wallingford, CT (2010).

[37] L. Zhao, R. He, K. T. Rim, T. Schiros, K. S. Kim, H. Zhou, C. Gutirrez, S. P. Chockalingam, C. J. Arguello, L. Plov, et al., Science **333**, 999 (2011).

Chapter 6

Electronic and Magnetic Properties of Zigzag Boron–Nitride Nanoribbons with Even and Odd–Line Stone–Wales (5–7 Pair) Defects *

6.1 Introduction

Nanoribbons, in particular graphene nanoribbons (GNRs), boron-nitride nanoribbons (BNNRs) and their hybrids, have attracted huge attention in recent years, because of their exciting applications in several fields like optics, electronics, opto-electronics, spintronics etc. [1–8] Applications of these nanoribbons (NRs) are dictated by their edges and depending on their edge nature, they are mainly divided into two types, namely, armchair and zigzag. [5]

---

*Work reported in this chapter is published in: Sharma S. R. K. C. Yamijala and Swapan K Pati, J. Phys. Chem. C, **117**, 3580–3594 (2013); Indian. J. Phys. **88**, 1-8, 2014.

Between the zigzag (z) and armchair edged NRs, zigzag edged NRs got enormous interest due to the presence of localized electronic states at their edges. These edge states enhance local-density of states near the Fermi-level. [1] Also, as proved by the previous studies on zGNRs [5, 6, 9] and zBNNRs, [2, 10, 11] these edge-states can be tuned, using different methods like passivation, doping, substitution, and application of external electric-fields etc., to attain tunable electronic and magnetic properties in these ribbons. Even, half-metallicity has been predicted in both zGNRs [4, 6, 12] and zBNNRs [2, 7, 8, 13] under different conditions.

In fact, both GNRs and BNNRs have been successfully synthesized experimentally either by cutting the corresponding 2D structures viz., graphene [14] and BN sheets or by unzipping the corresponding nanotubes (NTs) viz., Carbon-NTs [15] and BN-NTs, [16] respectively. But getting perfect edges through experiments is a difficult task and researchers often observed the presence of 5–7 reconstructions at the edges. [17] Huang et al. [18] have shown the presence of 5–7-defect lines across the grain boundary in graphene. Recently, Pan et al. [19] have also proved the presence of reconstructed 5–7 edges based on both the theory and experiment, in chiral GNRs. Apart from the 5–7 edge reconstructions, researchers have also observed the dynamics of the 5–7 defects inside the graphene. [20, 21] Also, Auwärter et al. have shown the two h-BN domains can co-exist on Ni (111) surface and they have demonstrated that linear defects define the boundary between these two domains, which also suggests the possibility of the presence of the 5–7 defects at these grain boundaries.

All the above experiments suggest that 5–7 (pentagon-heptagon, PH) defects are ubiquitous in graphene and its BN-analogues, and that the edges are more prone to these defects. So, it is required to know how the properties of the graphene or GNRs or BNNRs will change in the presence of these edge reconstructions. Theoretical studies have been performed on graphene, [22, 23] GNRs [9] and also on BNNRs [11] to answer this question. The main result of all these studies states "A 5–7 edge

reconstruction on a nanoribbon with a zigzag-edge will bring stability to the system and it will destroy the magnetic property of the edge where the reconstruction has occurred". On the other hand, most of these studies have considered only one-line-PH-defect at one of the edges of a nanoribbon. Notable exceptions works exist by Jia et al., [24] who proposed the possibility of two-line-PH-defect, and a theoretical study by Sudipta et al., [9] who have considered both one-line and two-line-PH-defects at the edges of a GNR. In fact, to the best of our knowledge, there is no other study, in both GNRs and BNNRs, where the effect of the number of PH-line-defects in nanoribbons has been considered.

In this chapter, we have mainly investigated the structural, electronic and magnetic properties of zigzag boron-nitride nanoribbons (zBNNRs) with and without pentagon-heptagon (PH) line-defects. We have varied the PH-line-defect number from one to eight and we have shown that, it is possible to tune the properties of zBNNRs, from insulating to semiconducting to half-metallic, depending on the PH-line-defect number. We thus find that the behavior of the system is completely dependent on the nature of the line-defect (i.e. even or odd). Robustness of the observed properties has been verified by varying the width of the zBNNRs and also by varying the position of a PH-line-defect from one-edge to the other. The rest of this chapter is arranged as follows: In section 6.2, we have presented the computational details. In section 6.3, we describe the different kinds of systems considered in this study. Section 6.4 is devoted to the discussion of stability, electronic and magnetic properties of all the considered systems. Finally, in conclusions section , we summarize the main findings.

6.2   Computational details

Spin-polarized density functional theory (DFT) calculations have been performed, for all the considered systems, using the *ab initio* software package SIESTA. [25, 26]

Generalized-gradient-approximation (GGA) within the Perdew-Burke-Ernzerhof (PBE) [27, 28] form is chosen for the exchange-correlation functional. Interaction between the ionic cores and the valence electrons is accounted by the norm conserving pseudo-potentials [29] in the fully non-local Kleinman-Bylander form. [30] The pseudo-potentials are constructed from 1, 3 and 5 valence electrons for the H, B and N atoms, respectively. To expand the wave-functions, numerical combination of localized atomic orbitals with double-ζ basis sets are used. To represent the charge density, a reasonable mesh-cut-off of 300 Ry is used for the grid integration. Conjugate-gradient (CG) method has been used to optimize the structures. We have also optimized the lattice parameters by allowing them to change.

As the systems under consideration are quasi-one-dimensional nanoribbons, we have sampled the Brillouin-zone by $36 \times 1 \times 1$ k-points using the Monkhorst-Pack scheme, [31] for the full-relaxation of the geometry, and $96 \times 1 \times 1$ k-points, for all the electronic and magnetic properties calculations. Systems are considered to be optimized only when the forces acting on all the atoms are less than 0.04 eV/Å. Cubic unit-cells with the initial lattice vectors (4.932, 0, 0); (0, 35, 0) and (0, 0, 15) Å have been considered for all the systems with $\sim$ 2 nm width (here, X-direction is considered as periodic and the width of the ribbon is considered along the Y-direction). After optimization, all the systems remained flat and a change in the lattice-vectors along the X-direction from 4.932 to $\sim$ 5.01 Å has been found. For the width dependent studies, similar amount of vacuum (15 Å) has been considered in the non-periodic directions, as in the case of 2 nm ribbons, to avoid any spurious interactions between the nanoribbons and their periodic images. For all the Density of States (DOS) and projected-DOS (pDOS) plots, a broadening parameter of 0.05 eV has been used while plotting the energy levels.

6.3   Systems under consideration
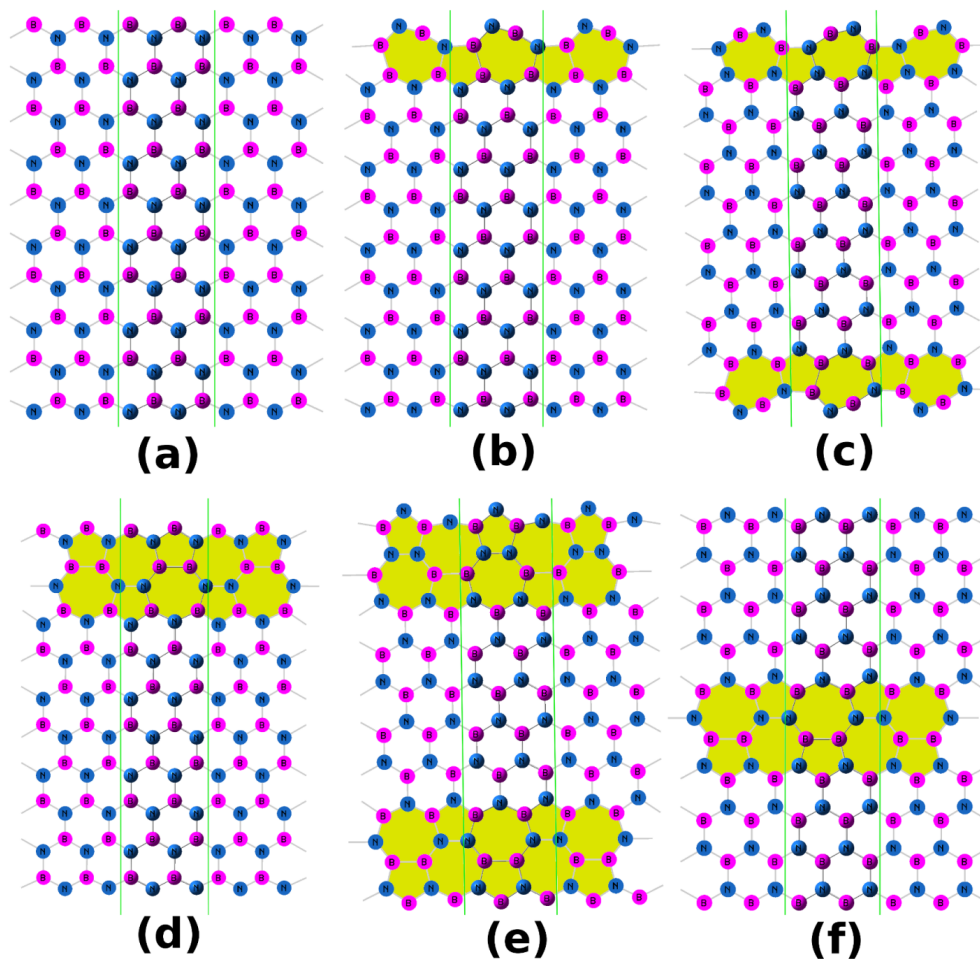
Figure 6.1: Structures of (a) perfect 10-zBNNR (b) De-ed-si-1_N (c) De-ed-bo-1 (d) De-ed-si-2_N (e) De-ed-bo-2 and (f) 4-D-3_De-mid-2. Shaded area represents the line-defect and the unit cell of a system is the area inside the two staright lines (green color).

Fig. 6.1 represents a few of various types of systems that we have considered in this study, where, we have named the systems with 5 indices. First index shows whether the ribbon is perfect (per) or it contains a defect (De). Second index dictates whether the defect is at the edge (ed) or at the middle (mid) of the ribbon. Third index tells whether the defect is at single-edge (si) or at both the edges (bo). Fourth index informs the number of the PH-line-defect introduced. Fifth index specially represents those systems which have defect at one edge and are perfect at the other edge (see, for example, Figs. 6.1(b) and 6.1(d)) and this index distinguishes boron (B) and

nitrogen (N) atoms at the perfect edge. The other two important types of systems (not shown in Fig. 6.1) are De-ed-si-1_B and De-ed-si-2_B, and they can be visualized by swapping the boron and nitrogen atoms of the systems in Figs. 6.1(b) and 6.1(d), respectively. It is required to mention, here, some *important and non-obvious points* regarding the PH-line-defects, which will be very much helpful to understand the results of the present work.

To generate an n-line-PH-defect, 'n' being an odd integer, we need 'n' number of zigzag and 'n' number of armchair chains (for example, 1-line-PH-defect can be visualized as a combination of 1-zigazag and 1-armchair chain. See shaded area in Fig. 6.1(b)). Importantly, any odd-line-PH-defect will have one edge as armchair-edge and the other edge will be zigzag (see the shaded area of Fig. 6.1(b)). On the other hand, an even-line-defect always possesses the same type of edges (either armchair or zigzag) and generating an n-line-PH-defect, 'n' being an even integer, is divided into two cases: (i) If both-edges of the defect have to be armchair, then, we have to take (n-1)-zigzag and n-armchair chains and (ii) if both-edges of the defect have to be zigzag, then, we have to take n-zigzag and (n-1)-armchair chains (see the shaded area of Fig. 6.1(d) for an example of 2-line-PH-defect with both the edges being zigzag).

Notably, adding a single odd-line-defect at the edge of a nanoribbon will change the nanoribbon's edge nature, i.e. the edge will be changed from zigzag to armchair [compare Figs. 6.1(a) and 6.1(b)] and vice-versa. In contrast, introduction of a single even-line-PH-defect at the edge will not change the nanoribbon's edge nature [compare Figs. 6.1(a) and 6.1(d)]. Hence, we cannot (can) introduce a single odd-line-PH-defect (even-line-PH-defect) in a ribbon, by keeping both the edges of same kind. Finally, it should be noted that, any n-line-PH-defect can only be prepared from a ribbon with (n+1)-chains.

Keeping these facts in mind, we aimed at understanding how even and odd-line-PH-defects will affect the electronic and magnetic properties of a ribbon. For all

the width independent studies, we have considered the zigzag-edged Boron-Nitride-nanoribbons of width ~ 2 nm, which according to the conventional notation [5] are equivalent to 10-zBNNRs (see Fig. 6.1(a)). In the 10-zBNNRs, we have varied the *number* of the PH-line-defect from one to eight. Also, as the *position* of a PH-line-defect can be either at an edge (single-edge or both-edge) or inside the ribbon, we considered the two-line-PH-defect as a representative system and we have varied its position in a 10-zBNNR from one edge of the ribbon to the other. Finally, to know how the width of a nanoribbon will change the defect's effect on electronic properties, we have varied the width from ~ 1.1 nm (6-zBBNR) to ~ 3.3 nm (16-zBNNR) with a 2-line-PH-defect. Spin-polarized DFT calculations, with different spin-configurations, have been performed for all these systems. Each spin-configuration is represented with an ordered pair, in which, the first element represents the spin-configuration at boron edge and the second element at the nitrogen edge. U and D represents the up and down-spins, respectively.

It is important to note that, we haven't considered the systems, where 1-line-PH-defect is in the middle of the ribbon as similar studies have already been performed for GNRs [32, 33] and also for BNNRs. [34] Also, systems with different types of defects at two edges (for example, 3-line at one-edge and 2-line at the other) are not considered. But, we strongly believe that one can easily expect the corresponding changes in the properties based on the present work.

6.4   Results and discussions

6.4.1   Perfect, 1-line-PH-defect and 2-line-PH-defect ribbons

Formation-energy (E_{Form}) of all the systems is calculated as:

$$E_{Form} = E_{tot} - [nB * E_B + nN * E_N + nH * E_H] \tag{6.1}$$

where, E_{tot} is the total energy of the system, E_B, E_N and E_H are the total-energies per atom of α-boron, N_2-molecule and H_2-molecule, respectively. nB, nN and nH are the number of boron, nitrogen and hydrogen atoms in the system, respectively. E_{Form} value of every system for each spin-configuration is given with respect to (i) the stable spin-configuration of that particular system and (ii) the perfect 10-zBNNR [in (UD, UU) spin-configuration], respectively, in columns 3 and 4 of Table 6.1. The negative formation energy for all the systems found in this work indicates that all are indeed stable.

Table 6.1: Spin-polarization (S_{pol}) of a system in different spin-configurations is given in column two. Columns 3 and 4 show the formation-energy of a system with respect to their corresponding stable spin-configuration and with respect to the perfect 10-zBNNR in (UD, UU) spin-configuration, respectively. Each spin-configuration is represented with an ordered pair, where, the first element of the ordered pair represents the spin-configuration at the boron-edge and the second element at the nitrogen edge. U and D represents up and down-spins, respectively. Energy of the most stable spin-configuration is scaled to zero.

System name and Spin-configuration	S_{pol}	Energy with respect to the most stable conformer (meV)	Energy of the system with respect to the perfect 10-zBNNR in (UD, UU) spin-configuration (eV)
Perfect 10-zBNNR, (UD, UU) (see Fig. 6.1(a))	1.926	0	0.000
Perfect 10-zBNNR, (UU, DD)	0.000	+ 16	0.016
Perfect 10-zBNNR, (UU, UU)	3.836	+ 16	0.016
De-ed-si-1_B, (UD, UU)	0.000	0	-0.148
De-ed-si-1_B, (UU, DD)	2.000	+ 35	-0.113
De-ed-si-1_B, (UU, UU)	2.000	+ 36	-0.112
De-ed-si-1_N, (UD, UU)	0.000	0	0.283
De-ed-si-1_N, (UU, DD)	1.982	+ 21	-0.262
De-ed-si-1_N, (UU, UU)	1.982	+ 21	-0.262
De-ed-bo-1, [(UD, UU), (UU, UU) and (UU, DD)] (see Fig. 6.1(c))	0.000	0	-0.489
De-ed-si-2_B, (UD, UU)	1.921	0	3.911

De-ed-si-2_B, (UU, DD)	0.000	+ 13	3.924
De-ed-si-2_B, (UU, UU)	3.820	+ 13	3.924
De-ed-si-2_N, (DU, UU) (see Fig. 6.1(d))	2.000	0	4.416
De-ed-si-2_N, (DD, UU)	0.000	+ 28	4.444
De-ed-si-2_N, (UU, UU)	3.764	+ 28	4.444
De-ed-bo-2, (UD, UU) (see Fig. 6.1(e))	2.000	0	8.303
De-ed-bo-2, (UU, DD)	0.000	+ 39	8.341
De-ed-bo-2, (UU, UU)	3.745	+ 42	8.345
4-D-3_De-mid-2, (DU, UU) (see Fig. 6.1(f))	1.918	0	4.470
4-D-3_De-mid-2, (DD, UU)	0.000	+ 22	4.492
4-D-3_De-mid-2, (UU, UU)	3.818	+ 17	4.487

From Table 6.1, one can find several interesting things. Firstly, in agreement with several previous studies on perfect zBNNRs, the spin-configuration with an anti-ferromagnetic ordering of the spins at the boron-edge and with a ferromagnetic ordering at the nitrogen edge, (UD, UU), was found to be the most stable spin-configuration. And, interestingly we find that, the same (UD, UU) spin-configuration is the most stable one for all the systems which have at least one zigzag edge with boron-atoms (i.e. irrespective of whether this zigzag edge arises because of a defect or not). Secondly, we find that the ground-state energy difference between the (UU, DD) and (UU, UU) spin-configurations, for all the systems, is always less than 5 meV and the energy difference between the (UD, UU) and (UU, DD)/ (UU, UU) is always large (in the range of 13 – 42 meV). The primary reason for these differences is the difference in the interaction between the spins of edge atoms. In the former case, although the edge spin-configuration has been changed from (UU, DD) to (UU, UU), the interaction between the spins on that edge didn't change (i.e. in both the cases the interaction is ferromagnetic), and hence, the change in energy is negligible. However, in the latter case, the spin-spin interaction at the edge has been

changed from anti-ferromagnetic to ferromagnetic, and hence, the difference in the energy between the systems is appreciable. From these results, we can infer that, change in the system's energy will be largely dictated by the spin-spin interaction at the same-edge atoms, (rather than by the spin-spin interaction between different edge atoms) when the distance between the edges is large (here, ~ 2 nm), as shown previously for the case of z-BNNRs. [2, 7]

Thirdly, the stability of the systems decrease in the order of: De-ed-bo-1 > De-ed-si-1_N > De-ed-si-1_B > perfect-10-zBNNR >> De-ed-si-2_B > De-ed-si-2_N > 4-D-3_De-mid-2 >> De-ed-bo-2. This order can be explained based on the changes in the edge nature in these systems. As shown in Fig. 6.1, system's edge nature changes from zigzag to armchair when we introduce a 1-line-PH-defect and it turns back to zigzag when we introduce a 2-line-PH-defect. Also, from the previous studies, it is known that the bare armchair edges are more stable than the bare zigzag edges, in both zGNRs,[35] and zBNNRs. [36] Combining these facts, we can see that, the higher stability of ribbons with 1-line-PH-defect is due to change in edge nature from zigzag to armchair. This is in agreement with the recent study by Bhowmick et al., where they have shown that edge formation energy of the 5–7-edge-reconstructed z-BNNRs is 0.08 eV/Å less than the perfect z-BNNRs. [11] On the other hand, as 2-line-PH-defect can not bring any change to the edge nature, and as some energy has to be spent to reconstruct an edge, 2-line-PH-defect ribbons are less stable than perfect ribbons. The same reason holds for the stability order: De-ed-bo-1 > De-ed-si-1, and De-ed-si-2 > De-ed-bo-2. In the former case, there are two armchair edges and hence, defect at both edges is more stable than the defect at a single edge. In the latter case, opposite is true because two reconstructed zigzag edges further decrease the stability of the system compared to one reconstructed zigzag edge and one pure zigzag edge. Also, the reason for 4-D-3_De-mid-2 to have similar energy as De-ed-si-2 is because both of them have a single-2-line-PH-defect. Next, we will

consider the spin-polarization of these systems.

Spin-polarization of a system is calculated as: $S_{pol} = Q_{up} - Q_{down}$, where, Q_{up} (Q_{down}) is the spin-up (spin-down) charge density. If S_{pol} is non-zero (zero), then the system is spin-polarized (spin-unpolarized) [with a spin magnetic moment, m = (S_{pol}) * μ_β, where μ_β is the Bohr-magneton [37]]. Values of the S_{pol} have been given in the Table 6.1. Based on these results, we propose that, the spin-polarization value of a BNNR for a particular spin-configuration can easily be estimated, if we know the edge nature (i.e. zigzag or armchair) of the BNNR. In general, (1) if both the edges are zigzag, then it will have a finite spin-polarization, only (a) when both the edges have ferromagnetic spin ordering and both the edges are coupled ferromagnetically or (b) when one edge have a ferromagnetic spin ordering and the other has anti-ferromagnetic spin-ordering. In the latter case, both the ferromagnetic and anti-ferromagnetic coupling across the edges will lead to a finite spin-polarization. (2) If one edge is armchair and the other edge is zigzag, then the system will have finite spin-polariztion when the spins are ordered ferromagnetically at the zigzag edge, irrespective of the spin-ordering at the armchair edge. Finally, (3) if both the edges are armchair, then the system will have zero-spin polarization, irrespective of the spin-ordering at the edges. For all the other cases, the systems will not be spin-polarized. All the above statements will be strictly valid for the bare BNNRs. Also, when the interaction between the two edges is negligible, the net spin-polarization of a system will be equivalent to the sum of the total amount of spin present at each edge. A similar type of conclusion has been drawn by Barone et al. regarding the formation energy, where they have shown that when the edges are less interacting, then the formation energy of a particular configuration can be approximated as the summation of the formation-energies of the other individual spin-configurations. [2] Finally, it is important to mention that, the above statements are highly dependent on the passivation, and we found that, the magnetic-moment which would arise from

a bare zigzag edge gets destroyed when the edge is passivated with hydrogen. Based on the above points, the calculated S_{pol} value for any system in Table 6.1 can be easily understood.

Next, we concentrate on the electronic and magnetic properties of these systems. Although the (UD, UU) is the most stable configuration for the bare z-BNNRs, a richer spectrum of electronic and magnetic behavior has been proved to be shown by the spin-configurations (UU, UU) and (UU, DD), both in the presence and absence of an external electric-field. [1, 2, 8] Following these studies, we have also plotted the projected-density-of-states (pDOS) for all the three different spin-configurations, as shown in Figs. 6.2 and 6.3. From both the Figs. 6.2 and 6.3, we find that, either a change in the spin-configuration or a change in the system leads to a change in the pDOS plots, primarily near the Fermi-level and these states near the Fermi-level have a major contribution from the edge-atoms of the nanoribbon. In the following, first we will describe the changes in the pDOS plots with a change in the spin-configuration for each system and then we will compare and contrast the pDOS plots of different systems.

Perfect ribbons

Fig. 6.2(a) shows the pDOS plots of the pristine 10-zBNNR in all the three different spin-configurations, which compares fairly well with the previous studies, [1, 2] where the minor changes are mainly due to the difference in the widths of the z-BNNRs considered. From Fig. 6.2(a), we can notice that, a change in the spin-configuration of a nanoribbon is clearly reflected in the pDOS plot. We find that, when the spin-configuration on the nitrogen edge (N-ed) of the ribbon is changed from UU to DD (i.e. from (UU, UU) to (UU, DD)) the pDOS of the N-ed atoms changes drastically. Moreover, if we take a mirror image of the N-ed pDOS of the (UU, UU) configuration across the zero of the Y-axis, the result is the N-ed pDOS of

the (UU, DD) configuration. This is because, the interaction between the spins at different edges is negligible, and hence, a change in the spin-configuration from UU to DD, at the N-ed, could only bring a change in the sign of the pDOS but not its magnitude. In contrast to the above, if we change the spin-configuration on a particular edge, we can expect a change also in the magnitude of the pDOS (this is because the distance between the spins on a single edge (~ 0.25 nm) is much less than the distance between the spins on two different edges (~ 2 nm)), and, this is what we have observed for the (UD, UU) spin-configuration of the perfect 10-zBNNR, as shown in the Fig. 6.2(a).

The major difference between the pDOS plots of (UU, UU) and (UD, UU) spin-configurations is the following (see Fig. 6.2(a)): B-ed pDOS which was spin-polarized and was broad near the Fermi-level in (UU, UU) configuration changes to non-spin-polarized and narrowed in (UD, UU) configuration. The change in the spin-polarization is because of the change in the spin-spin interaction between the edge-boron atoms [ferromagnetic (anti-ferromagnetic) in the former (latter) case]. The change in the width of the peaks of pDOS can be explained as follows: First, we should remember that the area under the B-ed pDOS for a particular energy range will give the number of B edge-states in that range and the number of edge-states of a system will be constant under any spin-configuration. Now, as we change the spin-configuration from (UU, DD) to (UD, UU) we bring in spin-symmetry at the B-edge, and this spin-symmetry urges equal contribution of the pDOS for both up and down spins. But, as the number of edge-states can't change with spin-configuration and as both-spins should have equal contribution, the broad peak has to narrow down without changing the area under the curve and this is what we have observed.

Finally, it is important to notice that, all the three magnetic-configurations are spin-polarized near the Fermi-level, and more importantly, among them the (UU, DD) shows half-metallic behavior, although its total spin-polarization is zero

Figure 6.2: pDOS plots of each system in three different spin-configurations. (a) Perfect 10-zBNNR (b) De-ed-si-1_B (c) De-ed-si-1_N (d) De-ed-bo-1. Spin-configuration of a system has been labeled inside the pDOS plots. Majority and minority spins have been labeled whenever it is applicable. Solid lines with dark-gray (green) and light-gray (orange) colors show the complete DOS and the pDOS of all the atoms except the edge atoms, respectively. Dotted light-gray (magenta) and dark-gray (blue) color lines represent the pDOS of the edge boron and nitrogen atoms, respectively.

(see Table 6.1 and Fig. 6.2(a)). Thus, 10-zBNNR in (UU, DD) spin-configuration behaves as an *anti-ferromagnetic half-metal (AFHMs)*. Previously, in 1995, Groot et al. have introduced this concept of AFHM [38] and later several compounds have been shown to possess this AF-half-metallicity as described by Wang et al. [39] Among the several applications of an AFHM, its usage as a tip in the spin-polarized scanning-tunneling-microscope is very interesting. [39, 40] So, AFHM materials are surely useful in the future spintronics devices and to attain this AFHM property in

a system without containing any element with d-orbitals, i.e. in 10-zBNNR, is very much interesting.

One-line-PH-defect ribbons

In the previous sub-section, we have shown the effect of spin-configuration on electronic and magnetic properties of a system. In this sub-section, we will show how the introduction of a line-defect can bring in changes to these properties. Figs. 6.2(b) and 6.2(c) show the pDOS plots of the systems De-ed-si-1_B and De-ed-si-1_N, respectively. From the pDOS plots, it is clear that systems have transformed from spin-polarized metals/half-metals to spin-polarized semi-conductors (for (UU, UU) and (UU, DD) configurations) after the introduction of a one-line-PH-defect at one-edge of a perfect ribbon. The spin-polarization in these systems is solely due to the spin alignment at the perfect edge. The zero-contribution of the defect-edge towards the spin-polarization of the system can be clearly understood by noticing the pDOS of the edge-atoms. For example, from Fig. 6.2(b), one can notice that, both the valence band maximum (VBM) and the conduction band minima (CBM) have a major contribution from the edge boron states which are present at the perfect edge. The fact that the spin-polarization is only due to the perfect-edge can be proved by comparing the pDOS plots of (UU, UU) and (UU, DD) configurations, where, we have changed the spin-configuration on a defect-edge from UU to DD and we couldn't find any change in the pDOS plots. Whereas, when we changed the spin-configuration on the perfect-edge from UU to UD, we can see that the system has lost its spin-polarization (which is because of the anti-ferromagnetic coupling between the spins at the perfect (boron)-edge). Finally, when one-line-PH-defect is introduced at the remaining perfect-edge (i.e. De-ed-bo-1), the system transforms from a spin-polarized semi-conductor to non-magnetic insulator. This result compares quite well with the results of Bhowmick et al., [11] where they have shown that 5–7

reconstruction at both the edges of a zBNNR is detrimental to the magnetic moment of the ribbon. From the above discussion, we can notice that, one can tune the system properties from metallic to semiconducting to insulating, by introducing a 1-line-PH-defect at the edge of a zBNNR.

Two-line-PH-defect ribbons

Although, we have proved, in the previous sub-section, that the introduction of a 1-line-PH-defect at a zigzag-edge destroys the magnetic moment, we didn't show whether this behavior is universal for any PH-line-defect or not. Indeed, in this sub-section we will prove that, a z-BNNR will lose (hold) its magnetic moment if the line-defect which is introduced has both armchair and zigzag-edges (only zigzag-edges), like 1-line-PH-defect (2-line-PH-defect). Figs. 6.1(d)– 6.1(e) show some example systems whose edge nature retains even after the introduction of a PH-line-defect.

Fig. 6.3 shows the pDOS plots of De-ed-si-2_B, De-ed-si-2_N, De-ed-bo-2 and 4-D-3-De-mid-2 systems. All these systems have finite spin-polarization near the Fermi-level and all of them are metallic at least for one spin, the other spin is varied depending on the system and spin-configuration. So, unlike 1-line-PH-defects, 2-line-PH-defects will preserve the magnetic nature of the systems. Similar to the perfect ribbons (see Fig. 6.2(a)), these systems also change their edge-pDOS near the Fermi-level depending on their spin configuration and the changes are quite similar to the perfect ribbons. For example, in Fig. 6.3a we find a mirror image behavior of the N-ed pDOS between the spin-configurations, (UU, UU) and (UU, DD), which is exactly what we have seen in Fig. 6.2(a). Similarly, if we compare the (UU, UU) and (UD, UU) configurations of Fig. 6.3(a), we can find the loss in spin-polarization for the B-ed pDOS in (UD, UU) spin-configuration because of the expected anti-ferromagnetic coupling between the boron-edge atoms. A similar

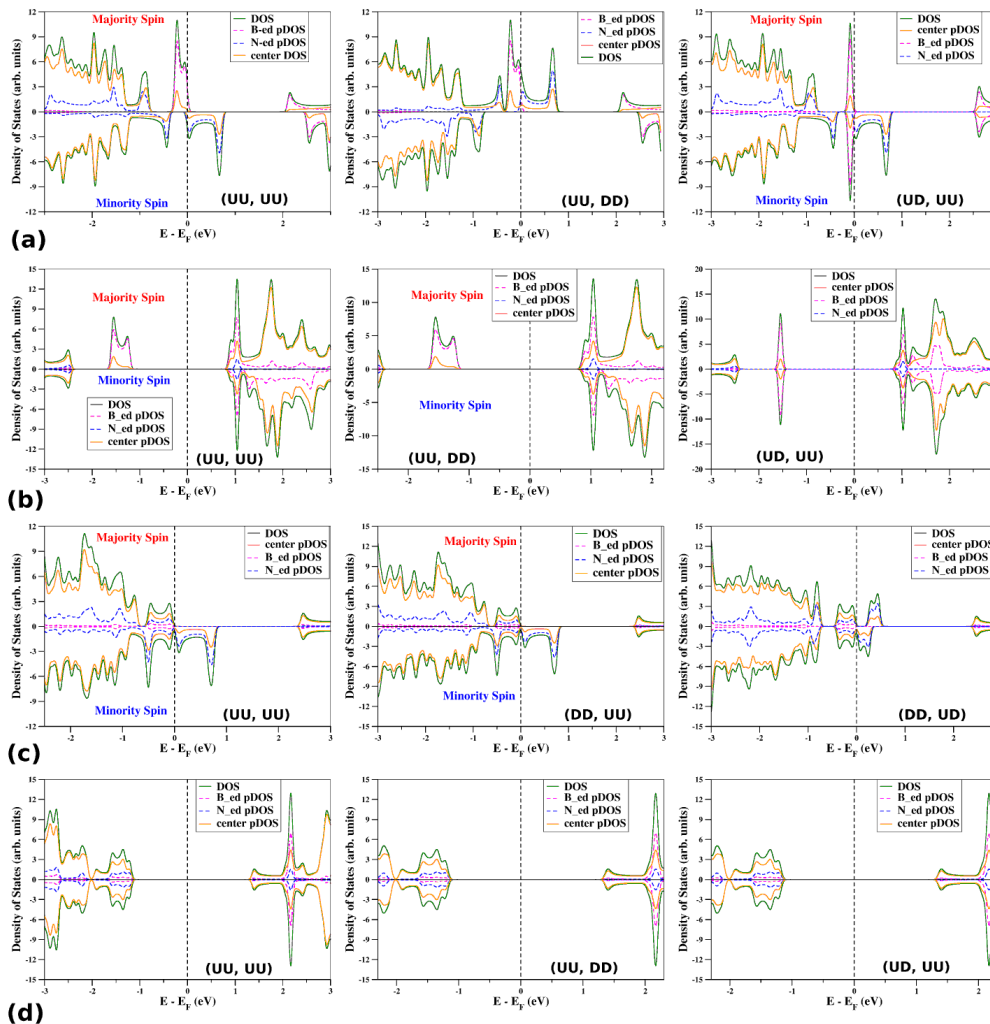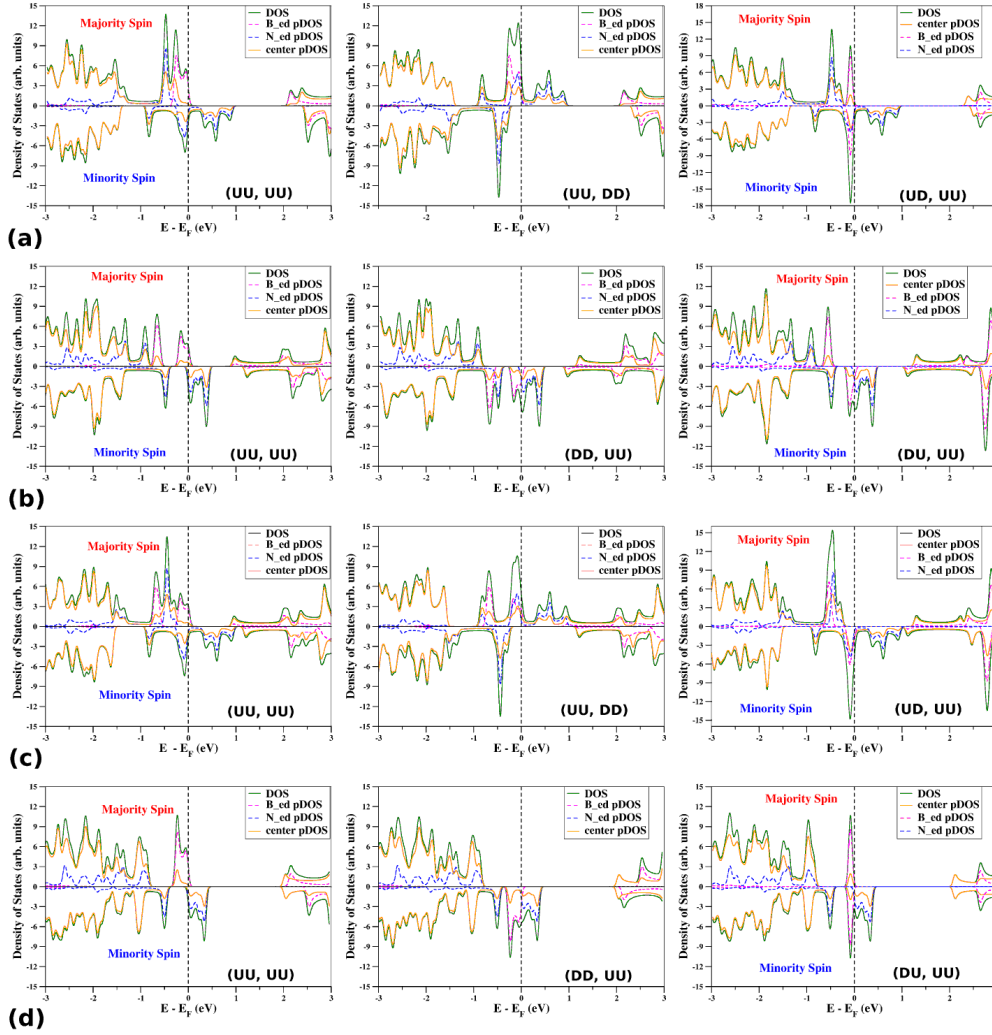**Figure 6.3:** pDOS plots of each system in three different spin-configurations. (a) De-ed-si-2_B (b) De-ed-si-2_N (c) De-ed-bo-2 (d) 4-D-3-De-mid-2. Spin-configuration of a system has been labeled inside the pDOS plots. Majority and minority spins have been labeled whenever it is applicable.

behavior in the pDOS plots has been found for the other systems (see Fig. 6.3).

An important finding which might not be very much obvious on the first look at Fig. 6.3 is: "Although the B-ed pDOS is non-spin-polarized in the (UD, UU) [or (DU, UU)] configuration for the systems, De-ed-si-2_B and 4-D-3-De-mid-2 [here after we call set-A], it remain spin-polarized for the De-ed-si-2_N and De-ed-bo-2 systems [here after we call set-B]". The main reason for the above finding is that boron atoms in the zigzag-edges of the systems in set-A and set-B are different from each other. Systems in set-A have a zigzag-edge which is made up of only hexagons
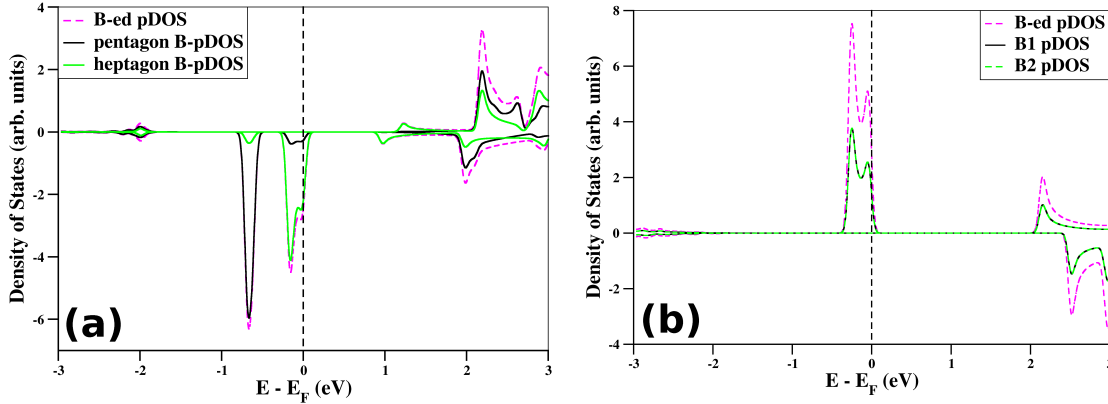
Figure 6.4: pDOS plots of each boron edge atom for the systems (a) De-ed-si-2_N and (b) De-ed-si-2_B in (UU, DD) spin-configuration. Pentagon [heptagon] B-pDOS means, pDOS of the edge boron atom which belong to the pentagon [heptagon] ring. B1, B2-pDOS indicates the pDOS from two different hexagon edge-boron atoms, which we numbered as 1 and 2.

i.e. a perfect-edge (see Fig. 6.1(f)), whereas, systems in set-B have a zigzag edge which is formed by alternating fused heptagons and pentagons i.e. a defect-edge (see Figs. 6.1(d) and 6.1(e)). So, in the former case, both edge-boron atoms belong to hexagon rings of the zigzag-edge, whereas in the latter case, one edge-boron atom belongs to a pentagon-ring and the other belongs to a heptagon-ring. This structural difference in the edge-boron atoms between the two sets is the reason for the difference in the spin-polarization found in the two cases. To prove this further, we have plotted the pDOS for each boron edge-atom for the systems De-ed-si-2_N and De-ed-si-2_B in (DD, UU)/ (UU, DD) configuration, as representative candidates for the defect and perfect edge systems, in Figs. 6.4(a) and 6.4(b), respectively.

Fig. 6.4(b) shows the individual pDOS contributions of each edge-boron atom to the total B-ed pDOS for De-ed-si-2_B system (a system which has boron atoms at the perfect-edge) and from the figure, we can notice that all the B-ed pDOS peaks have equal contribution from both the edge atoms. Firstly, as all the peaks have a contribution from each edge atom, a change in the spin on any edge-atom will have an effect on all the peaks. This is the reason to get a change in the peak width when we change the spin on the boron-edge atoms from UU to UD. Next, as the

contribution to each peak from each edge atom is same, peaks will have a zero-spin-polarization (finite spin-polarization) if spin on one edge atom is different (same) from the spin on the other atom. This is the reason to find a zero-spin-polarization (finite spin-polarization) for B-ed pDOS in the UD (UU) configuration. Contrary to the perfect edge systems, each peak in the B-ed pDOS (see Fig. 6.4(a)) of the defect edge-systems (here, De-ed-si-2_N) has a major contribution either from a pentagon or from a heptagon edge-boron atom. Now, as all the peaks have contributions from both the edge atoms (although differ in magnitude), here also, all peaks will change with a change in spin on an edge atom. This explains the reason for the changes in the peak widths for a change in spin-configuration from UU to UD. Next, as the contribution from both the edge-atoms is not same for any peak, each peak will have a finite spin-polarization, irrespective of the spin on the each edge-boron atom. This is the reason for the spin-polarization found even after a change in the spin-configuration on the B-ed atoms from UU to UD in the defect edge system. This is also the reason for the non-equivalent changes in the peak widths for the up and down spins of B-ed pDOS.

From all the above discussions, we can conclude that (i) System's spin-configuration can change its electronic and magnetic properties (ii) Among the several possible spin-configurations, perfect zBNNRs in (UU, DD) spin-configuration can act as potential candidates for anti-ferromagnetic half-metals, and hence, might be useful in the preparation of spin-polarized STM tips. Also, after comparing Figs. 6.2 and 6.3 we find that, whenever a system's edges are zigzag (both edges) then the system shows half-metallicity, only in the (UU, DD) spin-configuration. (iii) Introduction of a 1-line-PH-defect at an edge would destroy that edge's magnetic moment, and it is due to the armchair-edge generated by the 1-line-PH-defect, (iv) Unlike the 1-line-PH-defect, a 2-line-PH-defect would retain the edge magnetism and spin-polarization of a zBNNR due to its zigzag edge nature and changes in the electronic and magnetic

properties of a defective zigzag-edge system. And, (v) By knowing the pDOS of one spin-configuration, we can easily guess the pDOS of any other spin-configuration, provided (a) the spin-spin coupling between the atoms at two different edges of the ribbon is negligible and (b) we know the edge nature of the system (i. e. perfect edge or defect edge).

To find whether the above conclusions regarding the 1-line and 2-line-PH-defects are true for all cases, we have varied the number of line-defect from 3 to 8 in a 10-zBNNR. Here after, we will present the results only for the (UU, DD) spin-configuration as this configuration shows promising properties. The results are presented below.

6.4.2   Odd and even-line-defect ribbons

Table 6.2 shows the spin-polarization of the 10-zBNNRs with different line-defects in (UU, DD) spin-configuration. Clearly, all the odd-line-defects are spin-polarized and all the even-line-defects are not spin-polarized. As explained earlier, the reason for the finite spin-polarization for all the odd-line-defect ribbons is the presence of a single zigzag-edge which has spin-polarization, and the reason for zero total spin-polarization of the even-line-defects is because of the presence of two such zigzag edges, which carry exactly the same amount of magnetization value but with opposite sign. Thus, from the results presented in Table 6.2 we infer that the S_{pol} of the system is mainly due to the zigzag-edge of the system (irrespective of whether it is a perfect or a defect edge).

Table 6.2 also shows the stability of all these systems [with respect to the perfect-10-zBNNR in its (UU, DD) spin-configuration]. E_{Form} values of all these systems prove that, (i) not only the nature of the defect (i.e. odd or even-line) but also the size of the defect (i.e. 4-line or 8-line) will change the system stability and (ii) *for a ribbon with constant width, greater the number of the line-defect, lesser is its stability.*

We have also verified our statement regarding the gain in stability due to the presence of an armchair-edge in 1-line-PH-defect ribbon, by comparing the E_{Form} values of every odd-line-defect ribbon with its immediate lower even-line-defect ribbon [i.e. for example, we have compared the E_{Form} of 7-line-defect ribbon with the E_{Form} of the 6-line-defect ribbon] and we find that the E_{Form} values of these systems are nearly equal (with in the order of an eV). (Note that, comparing a 7-line-defect with 8-line-defect will not give any new understanding on the armchair-edge nature, because, 7-line-defect will obviously be more stable than 8-line-defect for its lesser size. On the other hand, 6-line-defect is expected to be more stable than 7-line-defect just based on its lesser size. So, a comparable E_{Form} value of 7-line-defect with a 6-line-defect indicates the armchair-edge's ability to stabilize the system). But, the amount of the stability acquired by a system through a change in the edge nature from zigzag to armchair might not be equal to the required amount of energy for the edge-reconstruction. If the former energy dominates, then the system attains stability and if latter energy dominates, the system will be unstable. The domination of the latter energy is the reason for the lesser stability of higher odd-line-defect (i.e. from 3-line) systems compared to the 1-line-PH-defect systems, even though they possess an armchair edge.

Table 6.2: Spin-polarization (S_{pol}) of each system is given in column two. Column 3 shows the stability of a system with respect to the perfect 10-zBNNR in (UU, DD) spin-configuration and is represented as E_{form}.

System-name	S_{pol}	E_{Form} (eV)
Perfect-10-zBNNR	0.000	0.000
Odd-line-PH-defects		
De-ed-si-1_B	2.000	-0.129
De-ed-si-1_N	2.000	-0.278
De-ed-si-3_B	2.000	4.261

De-ed-si-3_N	1.988	4.607
De-ed-si-5_B	2.000	9.350
De-ed-si-5_N	1.978	8.664
De-ed-si-7_B	2.000	13.426
De-ed-si-7_N	1.992	13.193
Even-line-PH-defects		
De-ed-si-2_B	0.000	3.908
De-ed-si-2_N	0.000	4.428
De-ed-si-4_B	0.000	8.292
De-ed-si-4_N	0.000	8.836
De-ed-si-6_B	0.000	12.627
De-ed-si-6_N	0.000	13.174
De-ed-si-8_B	0.000	16.933
De-ed-si-8_N	0.000	17.408
Variation in the defect position		
0-D-7_De-mid-2	0.000	3.908
1-D-6_De-mid-2	0.000	4.411
2-D-5_De-mid-2	0.000	4.476
3-D-4_De-mid-2	0.000	4.473
4-D-3_De-mid-2	0.000	4.476
5-D-2_De-mid-2	0.000	4.478
6-D-1_De-mid-2	0.000	4.467
7-D-0_De-mid-2	0.000	4.428

Along with the stability and spin-polarization, we have also calculated the changes

in the band-structure with a change in the defect line-number (n). Figs. 6.5 and 6.6 show the band-structure of all the odd and even-line-defects in (UU, DD) spin-configuration, respectively. From the band-structure plots, we find that all the systems with boron atoms at perfect-edge behave in one-kind and with nitrogen atoms at perfect-edge behave in another kind. This finding is valid for both even and odd-line-defect systems. For example, near the Fermi-level, all the odd-line-defect systems with boron atoms at the perfect-edge have nearly similar behaviors in dispersion, band-gap etc. (see Fig. 6.5). Similar behavior can also be seen for even-line-defects (see Fig. 6.6). These findings prove that, "*it is the edge nature of the defect which mainly dictates the electronic properties of the system than the number of the defect-line (n)*".

Variation of the defect-position

In this sub-section, we will discuss how the variation in the position of a defect affects the system's property. For this, we have chosen 2-line-PH-defect as our representative candidate and we have varied its position. We have chosen "2-line-PH-defect" because: 1) 2-line-PH-defect is an even-line-defect, and hence, irrespective of its position in the ribbon, it will not change the edge nature of the system, and also 2) according to our studies, 10-zBNNR with 2-line-PH-defect shows half-metallicity and we want to find whether this half-metallicity is retained even after a change of the defect position. As we already know that, a 2-line-defect will have 3 zigzag chains and as the ribbon considered has 10-zigzag chains, we are left with only 7-perfect zigzag chains after the introduction of a 2-line-PH-defect. These 7 chains can be arranged across the defect in 8 ways, and hence, there are 8 systems to study. The nomenclature of these systems is n-D-m_De-mid-2, where n, m represents the number of zigzag chains the defect (D) is away from the nitrogen and boron edge, respectively. For example, 2-D-5_De-mid-2 means, the defect is 2-chains away from the nitrogen
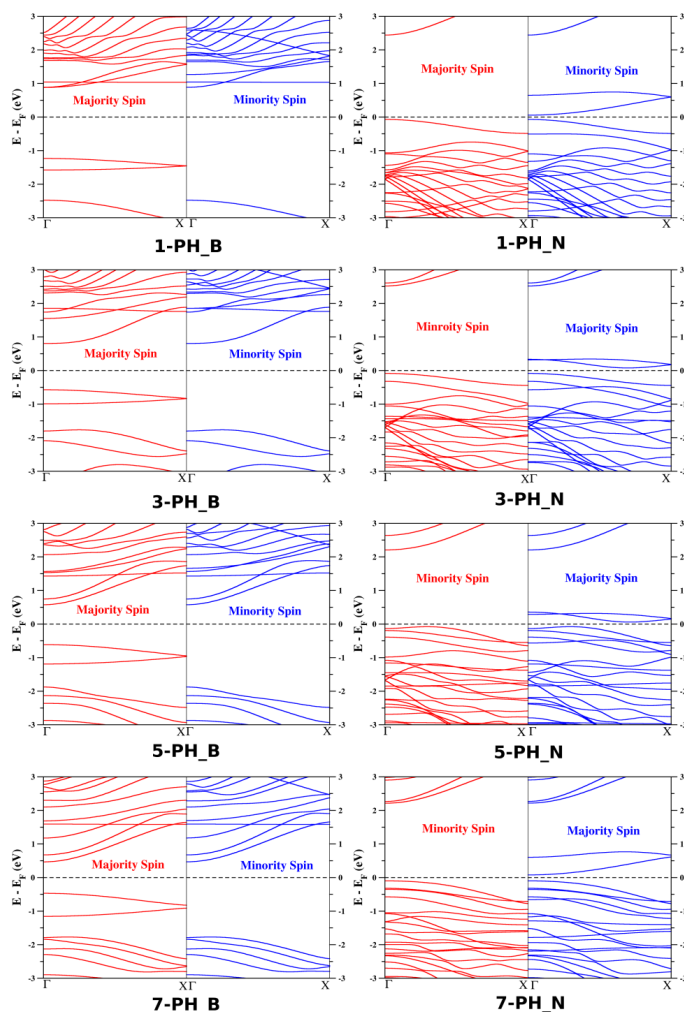
Figure 6.5: Band-structure plots of all odd-line-defect ribbons. The number of the line-defect (n) and atoms at the perfect edge (either B or N) are indicated below each plot, as n-PH_B/N. In each plot up-spin (down-spin) is given on the left-side (right-side). Majority and minority spins have been labeled whenever it is applicable.

edge and 5-chains away from the boron-edge.

E_{Form} values of all the eight systems are given in the Table 6.2 and except for the case of 0-D-7_De-mid-si-2-pr *there is hardly any change in the formation energy with change in the defect position.* This shows that, unlike the defect nature (i.e. odd-line or even-line), defect position has less effect on the formation energy, unless it changes the edge nature. The reason for the "0-D-7" system to be different from others is because of its nitrogen edge. In 0-D-7, the zigzag-edge with nitrogen atoms has the defect, whereas, for all the other systems, the nitrogen edge is perfectly zigzag-edged.
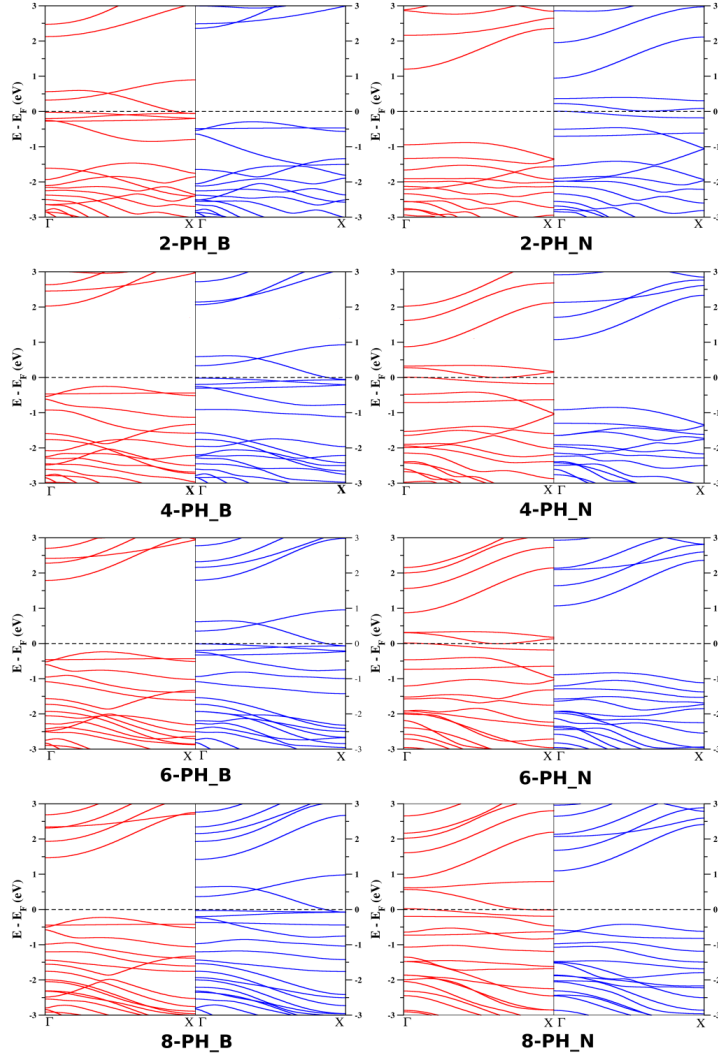
Figure 6.6: Band-structure plots of all even-line-defect ribbons. The number of the line-defect (n) and atoms at the perfect edge (either B or N) are indicated below each plot, as n-PH_B/N.

One interesting point to notice here is that, while translating the defect from B-ed to N-ed, the maximum energy was consumed only when the edge has changed from perfect zigzag-N-edge to defect zigzag-N-edge (i.e. from 1-D-6_De-mid-si-2-pr to 0-D-7_De-mid-si-2-pr), which again proves the importance of the edge nature in stabilizing a structure. As both the edges are zigzag and as the spin-configuration is (UU, DD), all these systems show zero S_{pol}. Fig. 6.7 shows the band-structure plots of all the eight systems. Clearly, all the systems are half-metallic irrespective of the defect position, which again proves that, the reason for the half-metallicity is the

zigzag-edge nature of these ribbons (which is preserved in all of them even though the defect is moving from one-end to the other-end of the ribbon).
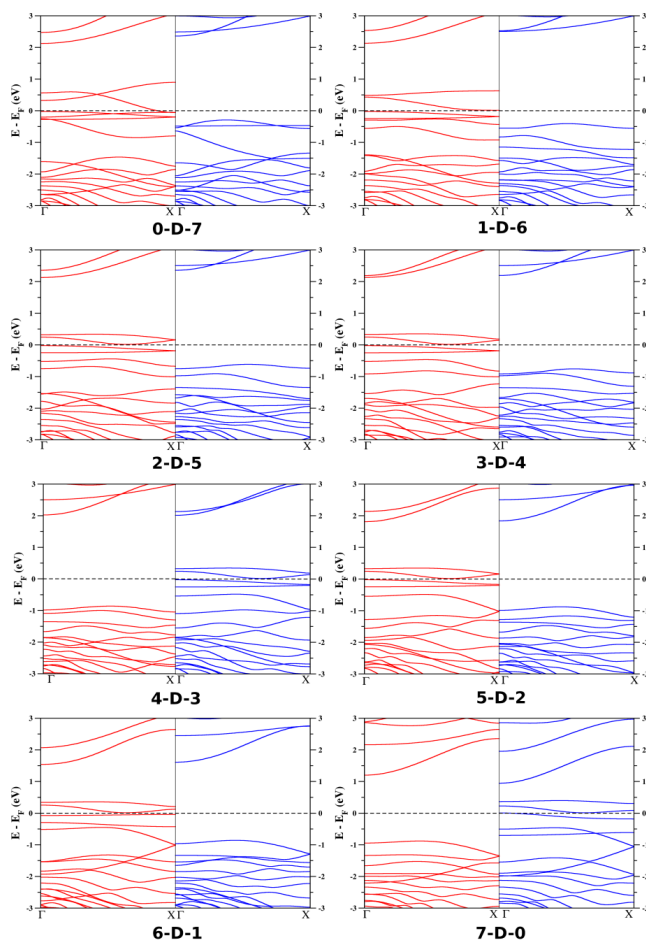
Figure 6.7: Band-structure plots of 10-zBNNR with a 2-line-PH-defect at different positions inside the ribbon. The position of the defect is indicated using the index n-D-m (see the text for nomenclature).

Varying the width of the ribbon:

Next, we have varied the width of the ribbon from 6-zBNNR to 16-zBNNR with a 2-line-PH-defect to check the robustness of our results. Again, S_{pol} value for all the systems is zero (and hence, not shown) because of their zigzag edge nature. Table 6.3 shows the formation energy for all the widths, which we have considered. As the number of atoms in each system varies, we have given the formation-energy values per atom, (E_{Form}), for each one of these systems. These values show that,

Table 6.3: Variation in the formation energy, E_{Form} (eV/ atom), with a variation in the number of zigzag chains, n, of De-ed-si-2_N systems is given.

n	6	7	8	9	10	11	12	13	14	15	16
E_{Form}	-0.962	-1.061	-1.136	-1.195	-1.241	-1.280	-1.311	-1.338	-1.362	-1.382	-1.399

formation of a defect is energetically more favorable in a bigger ribbon than in a smaller ribbon. Importantly, the change in the E_{Form} energy decreases and reaches almost a *saturation value* (less than room-temperature), once the system has more than 15-chains (> 3.1 nm). For example, the difference in the E_{Form} values between the ribbons with '6 and 7' or '7 and 8' chains is ∼ 0.1 eV, whereas, between '14 and 15' or '15 and 16' chains is just 0.02 eV.
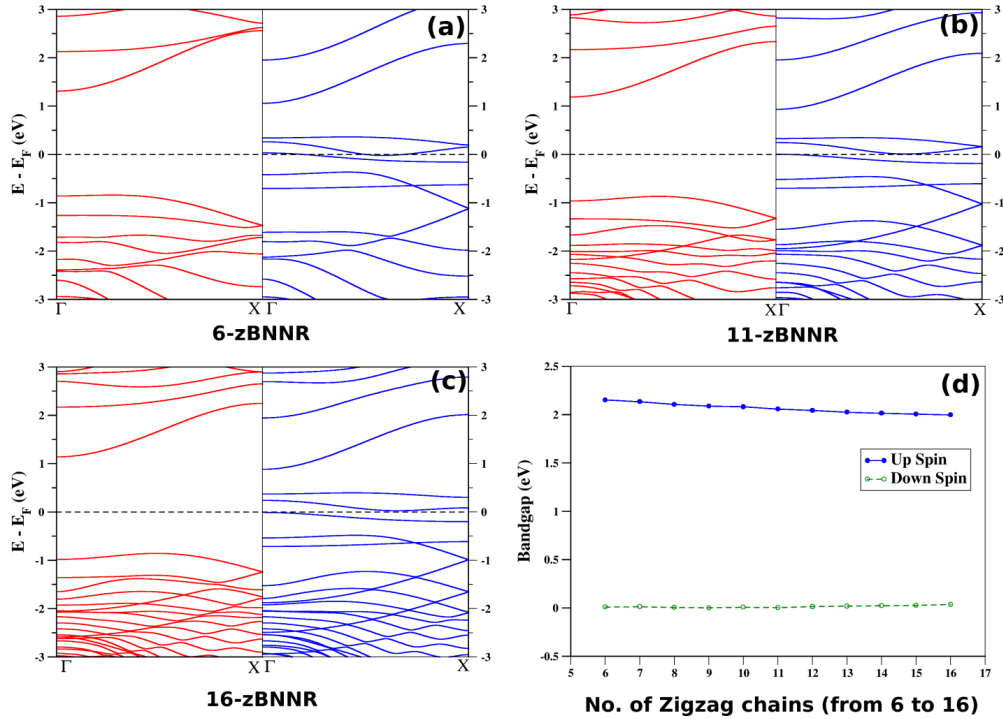
Figure 6.8: Band-structure plots of (a) 6-zBNNR (b) 11-zBNNR and (c) 16-zBNNR. (d) Variation of the band-gap with width, for both up and down-spins.

In Figs. 6.8(a)– 6.8(c), we have shown the band-structure plots for three representative widths, viz., 6, 11 and 16-zBNNRs, respectively. Note that, the band-structure plots for all the other widths considered in this study show exactly the similar behavior. From Figs. 6.8(a)– 6.8(c), we find that the half-metallicity in 10-zBNNR

is in fact robust against the ribbon width. These plots also show that, the dispersive nature of the states near the Fermi-level hasn't changed much with the ribbon width. Finally, in Fig. 6.8(d), we have presented the band-gap variation with a change in the ribbon width. As shown, with an increase in the width of the ribbon, there is very small change in the band-gap of the system's for both up and down-spins. Thus, this plot also proves the robustness of half-metallicity in 2-line-PH-defect systems.

Effect of passivation

Finally, we have also studied the effect of passivation on the electronic and magnetic properties of all these systems. For brevity, only the important results are mentioned. We find that, for (UU, DD) spin-configuration, a system with, (i) both of its edges as armchair will behave as non-magnetic insulator, irrespective of the passivation, (ii) one edge as zigzag and other one as armchair will behave as spin-polarized semiconductor either when both the edges are bare or when the defect-edge is passivated, and as non-magnetic insulator either when both the edges are passivated or when the perfect-edge is passivated, (iii) both of its edges as zigzag will behave as an anti-ferromagnetic half-metal when both the edges are bare; spin-polarized semiconductor when a single-edge is passivated; and non-magnetic insulator when both the edges are passivated. Thus, these findings, once again prove the importance of edge states in predicting the properties of BNNRs. Also, these findings show that edge states from bare zigzag edge are the reason for the metallic/semiconducting nature of an otherwise insulating BNNRs.

6.5   Conclusions

In conclusion, we have shown that all the properties of the systems presented in this work, are dependent mainly on the edge-nature of the ribbon, and we have also shown that the edge nature of a ribbon can be tuned using PH-line-defect number.

Among the several spin-configurations which we have considered, we find (UD, UU) configuration to be the most stable one, and the (UU, DD) configuration to be interesting one because it displays anti-ferromagnetic half-metallic behavior. We also find that, in contrast to the presence of a pair of hexagons at the perfect-zigzag-edge, a defect-zigzag-edge consisting of a pentagon and heptagon pair can cause large differences in their DOS, when the spin-configuration at these edges are changed.

Within the (UU, DD) spin-configuration, we have shown that, a system with, (i) one-edge as zigzag and other edge as armchair (odd-line-defects) will behave as spin-polarized semi-conductor, and (ii) both edges being zigzag (perfect ribbons or even-line-defect ribbons) will behave as anti-ferromagnetic half-metal. We have proved the robustness of the half-metallicity of the zigzag-edged systems against the defect line number, position of the defect and width of the ribbon. We have also discussed the stability of the ribbons and we have shown that, introduction of an n-line-defect is energetically more favorable for smaller 'n' than for larger 'n' and for a particular 'n', larger the size of the ribbon, it is energetically easier to introduce the defect. Finally, we conjecture that, half-metallic nature which we find for (UU, DD) spin-configuration is quite robust and would be observed for all the systems (with/without impurities, defects etc.) which have bare zigzag-edge at both the edges.

Bibliography

[1] M. Acik and Y. J. Chabal, Japanese J. App. Phys. **50**, 0101 (2011).

[2] V. Barone and J. E. Peralta, Nano Lett. **8**, 2210 (2008).

[3] W. Chen, Y. Li, G. Yu, Z. Zhou, and Z. Chen, J. Chem. Theory Comput. **5**, 3088 (2009).

[4] S. Dutta, A. K. Manna, and S. K. Pati, Phys. Rev. Lett. **102**, 096601 (2009).

[5] S. Dutta and S. K. Pati, J. Mater. Chem. **20**, 8207 (2010).

[6] S. Dutta and S. K. Pati, J. Phys. Chem. B **112**, 1333 (2008).

[7] L. Lai, J. Lu, L. Wang, G. Luo, J. Zhou, R. Qin, Z. Gao, and W. N. Mei, J. Phys. Chem. C **113**, 2273 (2009).

[8] F. Zheng, G. Zhou, Z. Liu, J. Wu, W. Duan, B.-L. Gu, and S. B. Zhang, Phys. Rev. B **78**, 205415 (2008).

[9] S. Dutta and S. K. Pati, Carbon **48**, 4409 (2010).

[10] E. A. Basheer, P. Parida, and S. K. Pati, New J. Phys. **13**, 053008 (2011).

[11] R. Mukherjee and S. Bhowmick, J. Chem. Theory Comput. **7**, 720 (2011).

[12] Y.-W. Son, M. L. Cohen, and S. G. Louie, Nature **444**, 347 (2006).

[13] E. Kan, F. Wu, H. Xiang, J. Yang, and M.-H. Whangbo, J. Phys. Chem. C **115**, 17252 (2011).

[14] X. Li, X. Wang, L. Zhang, S. Lee, and H. Dai, Science **319**, 1229 (2008).

[15] D. V. Kosynkin, A. L. Higginbotham, A. Sinitskii, J. R. Lomeda, A. Dimiev, B. K. Price, and J. M. Tour, Nature **458**, 872 (2009).

[16] H. Zeng, C. Zhi, Z. Zhang, X. Wei, X. Wang, W. Guo, Y. Bando, and D. Golberg, Nano Lett. **10**, 5049 (2010).

[17] P. Koskinen, S. Malola, and H. Hkkinen, Phys. Rev. B **80**, 073401 (2009).

[18] P. Y. Huang, C. S. Ruiz-Vargas, A. M. van der Zande, W. S. Whitney, M. P. Levendorf, J. W. Kevek, S. Garg, J. S. Alden, C. J. Hustedt, and Y. Zhu, Nature **469**, 389 (2011).

[19] M. Pan, E. C. Giro, X. Jia, S. Bhaviripudi, Q. Li, J. Kong, V. Meunier, and M. S. Dresselhaus, Nano Lett. **12**, 1928 (2012).

[20] J. C. Meyer, C. Kisielowski, R. Erni, M. D. Rossell, M. F. Crommie, and A. Zettl, Nano Lett. **8**, 3582 (2008).

[21] J. H. Warner, E. R. Margine, M. Mukai, A. W. Robertson, F. Giustino, and A. I. Kirkland, Science **337**, 209 (2012).

[22] B. W. Jeong, J. Ihm, and G.-D. Lee, Phys. Rev. B **78**, 165403 (2008).

[23] J. Kotakoski, J. C. Meyer, S. Kurasch, D. Santos-Cottin, U. Kaiser, and A. V. Krasheninnikov, Phys. Rev. B **83**, 245420 (2011).

[24] L. Li, S. Reich, and J. Robertson, Phys. Rev. B **72**, 184109 (2005).

[25] P. Ordejón, E. Artacho, and J. M. Soler, Phys. Rev. B **53**, R10441 (1996).

[26] J. M. Soler, E. Artacho, J. D. Gale, A. Garca, J. Junquera, P. Ordejn, and D. Snchez-Portal, J. Phys.: Condens. Matter **14**, 2745 (2002).

[27] K. Burke, J. P. Perdew, and M. Ernzerhof, Int. J. Quantum Chem **61**, 287 (1997).

[28] J. P. Perdew, K. Burke, and M. Ernzerhof, Phys. Rev. Lett. **77**, 3865 (1996).

[29] N. Troullier and J. L. Martins, Phys. Rev. B **43**, 1993 (1991).

[30] L. Kleinman and D. M. Bylander, Phys. Rev. Lett. **48**, 1425 (1982).

[31] H. J. Monkhorst and J. D. Pack, Phys. Rev. B **13**, 5188 (1976).

[32] A. R. Botello-Méndez, E. Cruz-Silva, F. Lopez-Urias, B. G. Sumpter, V. Meunier, M. Terrones, and H. Terrones, ACS Nano **3**, 3606 (2009).

[33] J. Zhou, T. Hu, J. Dong, and Y. Kawazoe, Phys. Rev. B **86**, 035434 (2012).

[34] P. Tang, X. Zou, S. Wang, J. Wu, H. Liu, and W. Duan, RSC Adv. **2**, 6192 (2012).

[35] P. Koskinen, S. Malola, and H. Hkkinen, Phys. Rev. Lett. **101**, 115502 (2008).

[36] B. Huang, H. Lee, B.-L. Gu, F. Liu, and W. Duan, Nano Research **5**, 62 (2012).

[37] A. S. Mahajan and A. A. Rangwala, *Electricity and Magnetism* (McGraw-Hil, 1989).

[38] R. A. de Groot, F. M. Mueller, P. G. v. Engen, and K. H. J. Buschow, Phys. Rev. Lett. **50**, 2024 (1983).

[39] Y. K. Wang, P. H. Lee, and G. Y. Guo, Phys. Rev. B **80**, 224418 (2009).

[40] H. Van Leuken and R. A. De Groot, Phys. Rev. Lett. **74**, 1171 (1995).

Chapter 7

Computational Investigations on the Laser-Induced Unzipping of MoS$_2$ and Carbon Nanotubes in Dimethylformamide *

7.1 Introduction

One of the major hurdles in replacing graphene with silicon in electronics industry is its zero bandgap. However, its low-dimensional analogue, namely, graphene nanoribbon (GNR) exhibits finite band gap. [1–3] These 1D nano-structures offer many attributes such as semiconducting nature, [4] high magnetoresostance, [5, 6] and half-metallicity in the presence of external electric-fields. [7] Moreover, due to their sp^2 carbon lattice and edges states, [8, 9] GNRs find applications in electronic devices, [10–14] magnetic field sensors, [15] transparent conducting electrodes [6]

etc. Also, from the last 2-3 years, there has been great interest in the properties of transition metal dichalcogenides (TMD) nanosheets. Thus, nanoribbons of TMDs are the obvious candidates for study, since quantum confinement and edge states are expected to give rise to new electronic and magnetic properties. Nanoribbons of MoS_2 and WS_2 with zigzag edges are expected to be ferromagnetic and metallic, whereas armchair nanoribbons would be nonmagnetic and semiconducting. [16–19]

GNRs have been prepared by unzipping of carbon nanotubes (CNTs) through chemical oxidation, a method that has been commonly used by many workers. [9, 20–22] On the other hand, WS_2NRs have been synthesized by means of chemical unzipping of WS_2 nanotubes using lithium intercalation followed by exfoliation in organic solvents. [23] There are some limitations to these procedures. CNT unzipping through chemical oxidation often gives rise to oxygen functionalities on the surface of GNRs and WS_2NT has the limitation that diffusivity of solvent molecules controls the unzipping process. Furthermore, chemical manipulation may not altogether avoid surface functionalities.

In order to avoid these limitations and to produce clean graphene and TMD nanoribbons, our experimental collaborators have carried out laser-induced unzipping of the carbon, MoS_2 and WS_2 nanotubes dispersed in dimethylformamide (DMF) medium. Earlier, a few of them have used laser-induced unzipping of CNTs to avoid surface oxygen functionalities and to produce pure GNRs, [24] but, in that study CNTs were in solid medium. Soon they have realized that laser-induced unzipping in solid form requires a quartz substrate for CNT coating (as other substrate materials would evaporate upon laser irradiation) and transferring the unzipped CNTs (i.e., GNRs) onto arbitrary functional substrates (to achieve any functional device) involve in loss of material. So, they expected to minimize material loss upon transfer by unzipping NTs in liquid medium and thus they have conducted the experiments in solvent medium using laser pulse.

Employing the above procedure, the experimental studies have observed that laser irradiation unzips carbon, WS_2 and MoS_2-NTs along the longitudinal axis, yielding GNRs, WS_2NRs and MoS_2NRs after 200 laser pulses. [25] Unlike other methods, [23, 26] laser unzipping is found to be a versatile method for the production of high-quality NRs with controllable width, edge states, and defects. As laser unzipping of CNTs in liquid media does not require any additional chemical treatment with or without external heating, this method turns into a green synthetic approach. Therefore, it is imperative to understand this emerging procedure and in this chapter we have tried to present our efforts to understand the mechanism of unzipping in these NTs.

7.2   Computational Details

To understand the mechanism of unzipping, first we have performed a series of calculations on single-walled (SW) and multi-walled (MW) carbon nanotubes (NTs) and on single-walled MoS_2NTs. To know whether the unzipping is favored along the longitudinal or lateral directions of a NT, we have considered a line of vacancies along these directions. We have used both density functional tight-binding (DFTB) theory and density functional theory (DFT) in our calculations. For the case of MoS_2NTs, all the calculations are performed using DFT. On the other hand, majority of the calculations on CNTs have been performed using self-consistent charge DFTB (SCC-DFTB) [27] within third order expansion of the energy (DFTB3) [3] and with 3ob parameter set, as implemented in DFTB+ package. [28] DFTB level of theory is used mainly due to the large system sizes (> 1000 atoms) considered. We couldn't use DFTB for MoS_2NTs due to the unavailability of the Slater-Koster parameters.

While using DFTB, geometry optimizations have been performed using conjugate gradient method and systems are considered to be optimized only when forces on all the atoms are less than 0.0001 Hartree/Bohr. A $1 \times 1 \times 15$ k-point grid has been

considered within the Monkhorst-Pack scheme, for all the SWNTs. For MWNTs, we were able to afford only the Gamma point calculations. An electronic temperature of 100 K is kept for all the calculations, to avoid convergence issues for the systems. VMD [29] and CoNTub [30] are used to generate the coordinates for the single-walled and multi-walled nanotubes, respectively. VMD is also used to create a few images. To check the robustness of the results obtained from DFTB3 method, we have compared them with the results of DFT for (7,7) SW-CNT. The results are comparable (exact) in the trends and almost the same when the relative energies are considered (which are only the relevant ones for the present study) as can be seen from the Tables 7.2 and 7.3.

All the DFT calculations have been performed using Perdew–Burke–Enzerhof (PBE) [31] exchange and correlation functional and double-ζ-polarized basis set (DZP) for all atoms as implemented in the SIESTA package. [32] Norm conserving pseudo potentials in the fully non-local Kleinman-Bylander [33] form with 1, 4, 6 and 6 valence electrons have been considered for H, C, S and Mo atoms, respectively. A Monkhorst k-point grid of $1 \times 1 \times 5$ and a real space mesh cut off of 300 Ry has been used. Systems are considered to be relaxed only when the forces acting on all the atoms are less than 0.04 eV/Å.

7.3   Results and Discussions

In this section, first, we would like to emphasize the most important results from the experiments on both CNTs and MoS_2NTs. The results include: (i) Nanotubes unzip along longitudinal direction (observed for MoS_2NTs) (ii) Lesser laser fluence is required to unzip thinner nanotubes (observed for CNTs) (iii) Nanotubes unzip to form nanoribbons in DMF (observed for both CNTs and MoS_2NTs).
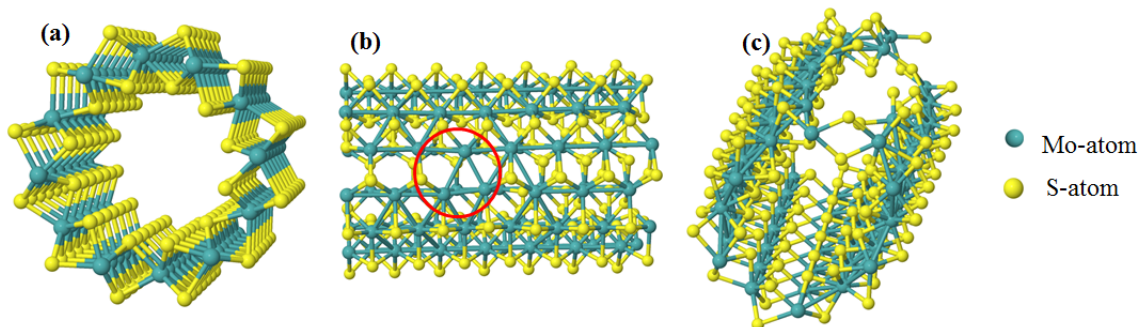
Figure 7.1: Optimized structures of (6, 6) MoS$_2$NT (a) with no vacancy (pristine) (b) with a 2-S vacancy and (c) with a 3-Mo longitudinal vacancy.

7.3.1   Energetics of defect formation

MoS$_2$ nanotubes

To get a microscopic understanding for the above results and to understand the laser-induced unzipping mechanism, first we have performed DFT calculations on MoS$_2$NTs. Since the experimental results show unzipping along the tube axis and zigzag edged nanoribbons, DFT calculations were performed on armchair MoS$_2$NT of chirality (6, 6) consisting of 36 atoms in the unit cell. We have studied the energetics of formation of various kinds of vacancies in the nanotubes as strong laser irradiation ruptures the nanotube. The structure of pristine MoS$_2$NT shown in Fig. 7.1a has been generated by considering a supercell consisting of 252 atoms. Six types of possible vacancies were examined, namely, (i) a single Mo-vacancy; (ii) a triple Mo-vacancy with (a) all vacancies along the longitudinal axis (tube axis), (b) two along the longitudinal axis and one along lateral axis, (c) all vacancies along the lateral axis; (iii) dual S-vacancy and (iv) hexa S-vacancy. In Table 7.1, we present the energetics of defect stability, formation energy, and the defect formation with respect to 1-Mo vacancy.

From the energetic studies, we see that the formation energy of a Mo-vacancy is almost equal to the formation energy of a S-vacancy in an armchair MoS$_2$NT. We find that creation of further Mo-vacancies is energetically feasible if they are created
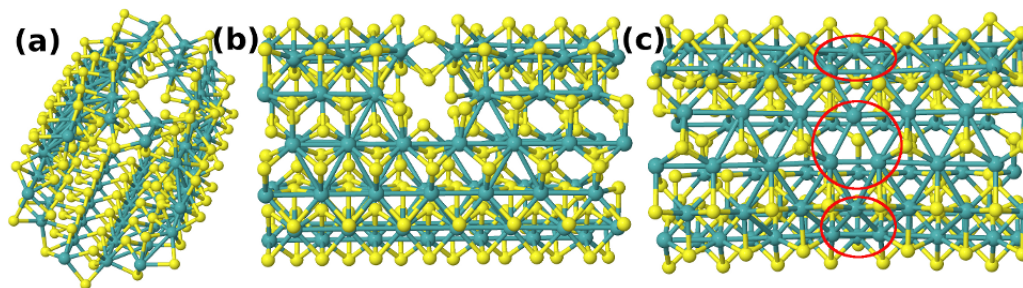
Figure 7.2: Optimized structures of $(6, 6)$ MoS_2 with (a) 3-Mo longitudinal and lateral vacancy (b) 3-Mo lateral vacancy and (c) hexa S-vacancy.

Table 7.1: Energetics of formation of different kinds of vacancies in MoS_2 nanotubes

System	E_{defect} - $E_{pristine}$ (eV)	$E_{Form} = E_{defect}$ - $E_{pristine}$ - n × $E_{Mo/S}$ (eV)	With respect to 1-Mo (eV)
1-Mo	221.922	2.806	0.000
3-Mo longitudinal	650.793	-6.554	-14.973
3-Mo longitudinal and lateral	664.184	6.837	-1.582
3-Mo lateral	667.268	9.921	1.502
2-S	559.105 (279.552/S)	5.016 (2.508/S)	–
6-S	1674.097	11.831	–

along the longitudinal axis than along the diameter of the tube. We also find that an already created vacancy decreases (increases) the amount of energy required to create the next vacancy if the new vacancy is along the longitudinal axis (lateral axis). Figs. 7.1b, 7.1c shows the optimized structures of MoS_2NT after creation of 2-S and 3-Mo longitudinal vacancies, respectively. Creation of a 2-S vacancy does not change the tube structure significantly except the formation of new bonds between Mo atoms (see circle in Fig. 7.1b). However, creation of 3-Mo longitudinal vacancies changes the tube structure drastically and initiates the unzipping process along the tube axis. Unzipping process is not initiated by creating other combinations of 3-Mo vacancies (namely, 3-Mo-longitudinal and lateral vacancy and 3-Mo-lateral vacancy. See Fig. 7.2). Thus, these results clearly suggest that longitudinal unzipping is energetically more favorable than other ways of unzipping the MoS_2 nanotubes, corroborating with the experimental observations.

Carbon nanotubes (single-walled and multi-walled)

We have performed similar calculations also with CNTs. Apart from considering various kinds of vacancies, we have also considered CNTs of various diameters and chiralities as it is well known that the properties of NTs depend on both of these parameters. [34] Also, multi-walled CNTs have been studied to identify any differences in the unzipping process compared to their single-walled counterparts. Accordingly, three CNTs with chiralities (7,7), (15, 15) and (21, 0) have been considered, where, (7, 7) and (15, 15) are armchair nanotubes (and hence, metallic) with diameters of approximately 1 nm and 2 nm, respectively and (21, 0) is a semiconducting zigzag NT with diameter similar to that of (15, 15). For modeling MW-CNT, we have considered a double walled nanotube, where the inner and outer tubes have the chirality (7, 7) and (16, 16), respectively and the inter-tube spacing has been kept as 6 Å.

To model defects created in SWNTs by laser pulse, similar to MoS_2 nanotubes, we have created vacancies (only along the direction of the tube axis [34]) by directly removing the carbon atoms from the hexagonal lattice. To know whether there is any cumulative effect during the formation of vacancies, we have gradually increased the vacancy number from 1 to 3 (represented as v1, v2 and v3). Also, to know the favorable positions of vacancies with respect to each other, in a multi-vacant SWNT, we have varied the position between the vacancies (See Fig. 7.3). Results of the calculations from both DFTB and DFT levels of theory are given in Tables 7.2 and 7.3, respectively.

From Table 7.2, we notice that formation of a di-vacancy is much easier than isolated mono-vacancies. Similarly, tri-vacancies would cost even less energy when compared to the energy required to form 3 isolated mono-vacancies. Our calculations on SWNTs and MWNTs establish that the energy required to create a multi-vacancy
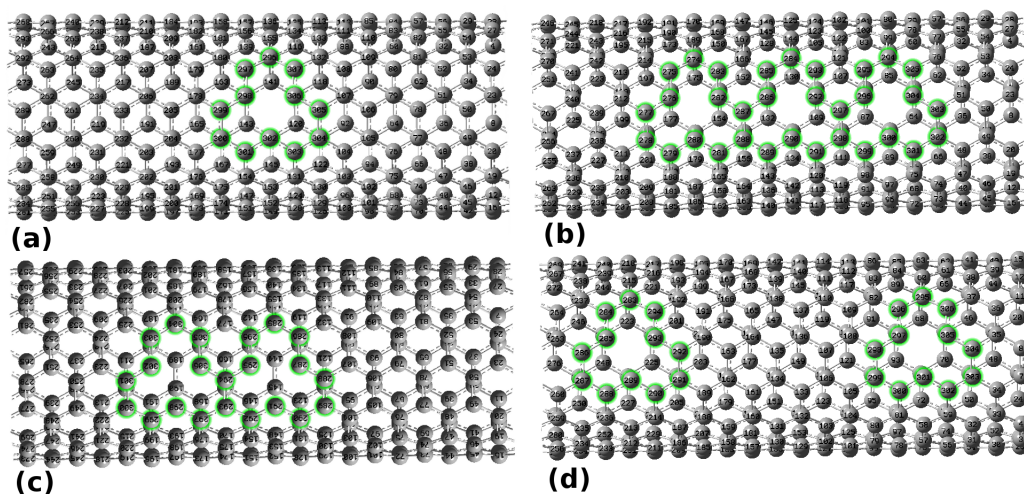
Figure 7.3: Structures of (7, 7) CNT with (a) single vacancy (v1) (b) three single vacancies (v3) (c) two single vacancies side-by-side (v2a) (d) two single vacancies apart from each other (v2b)

Table 7.2: Energetics of formation of different kinds of vacancies in CNT nanotubes (DFTB results). Symbols $E_{pristine}$ and E_{vn} denote the energy of a nanotube in its pristine state and when it has 'n' vacancies, respectively. E_C is the energy of the single carbon atom. E_{Form} and E_{cum} are the formation and cumulative energies.

System	$E_{Form} = E_{defect} - E_{pristine} - n \times E_C$ (eV)	E_{cum} (eV) $= E_{defect} - (n \times E_{v1})$
v1–(7,7)	16.947	0.000
v2a–(7,7)	30.537	-3.356
v2b–(7,7)	31.350	-2.543
v3–(7,7)	42.481	-8.359
v1–(15,15)	20.756	0.000
v2a–(15,15)	34.685	-6.827
v2b–(15,15)	36.655	-4.857
v3–(15,15)	47.087	-15.181
v1–(26,0)	25.592	0.000
v2a–(26,0)	39.966	-11.218
v2b–(26,0)	40.194	-10.990
v3–(26,0)	54.438	-22.339
v1–(7,7), (16,16)	15.614	0.000
v2–(7,7), (16,16)	29.641	-1.586
v3–(7,7), (16,16)	42.112	-4.729

Table 7.3: Energetics of formation of different kinds of vacancies in CNT nanotubes (DFT results). Symbols have similar meaning as in Table 7.2.

System	$E_{Form} = E_{defect} - E_{pristine} - n \times E_C$ (eV)	E_{cum} (eV) $= E_{defect} - (n \times E_{v1})$
v1–(7,7)	11.715	0.000
v2a–(7,7)	19.992	-3.438
v2b–(7,7)	20.649	-2.781
v3–(7,7)	26.316	-8.829

(E_{vn}) in a nanotube is not just equal to the energy required to create n such single-vacancies (E_{v1}); rather it is always less (i.e., $E_{vn} < n \times E_{v1}$). This is true even when the position of the defect changes; for example, see v1 versus v2a and v2b for any nanotube. Also, our study shows that creating vacancies side-by-side is more favorable than creating them away from each other. Thus, similar to MoS_2NTs, in CNTs also there is a cumulative effect while creating the vacancies. Even, we got similar conclusions from DFT results on CNTs (see Table 7.3) and we believe that this cumulative effect is manifested in the form of crack propagation under laser exposure.

Interestingly, we have also found that an increase in the nanotube diameter (for example, see(7,7) $\sim$ 1 nm and (15, 15) $\sim$ 2 nm) leads to the increment in the energy required to create a defect (E_{Form}), once again, corroborating with experimental results. In general, wider nanotubes have less curvature and greater overlap between the P_z-orbitals on the adjacent carbon atoms (maximum overlap occurs when the orbitals are parallel to each other, as in graphene sheet). Greater curvature (as presented in thinner NTs) leads to the formation of weaker-bonds locally, compared to a wider nanotube. Thus, compromised orbital overlap in thinner NTs seems to be the reason for their unzipping at lesser laser fluence.

7.3.2   Effects of defect annealing

Till now, based on our energetics calculations, we were able to show that (i) the laser irradiation leads to the unzipping of NTs through the formation of vacancies, (ii) their formation is favored along longitudinal direction and (iii) a thinner nanotube will require lesser laser affluence. At this point of discussion, it should be noted that for the case of a Mo-vacancy in MoS_2 nanotubes, the formed vacancy will be stable and it will also help the neighboring Mo-atoms to break their bonds leading to the unzipping of NT (see Fig. 7.1c). But, a mono-vacancy or bi-vacancy in a CNT (similarly, S-vacancy in MoS_2NTs) results into chemically active edges inside the sp^2 network. Such vacancy defects are vulnerable to reconfiguration and to form Stone-Wales like defects if annealed in an equilibrium manner in carbon networks (see Figs. 7.1b and 7.2c for S-vacancies in MoS_2NTs). These results have also been observed in our calculations, where we have observed the annealing of vacancies to form 5-9 rings, though not planar, as shown in Figs. 7.4c, 7.4d, 7.4e, for single, double, triple vacancies, respectively.

On the otherhand, it should be noted that laser irradiation with extreme intensity gives rise to non-equilibrium processes. Moreover, successive laser irradiation with each new pulse incident after 1/5 second (as the pulse rate of laser used in the experiment was 5 Hz), produces periodic local energy bursts that would locally break C-C bonds. In CNTs, the vacancy migration barrier is only 1 eV, suggesting the mobility of vacancy at relatively low temperatures. [35] Local heat accumulation in CNTs due to successive incident laser pulses during laser exposure would catalyze vacancy migration. Single defects would thus merge with each other and grow into larger voids, which align along the axial direction, as these are the locations with equivalent sets of physical and chemical conditions (Also, which is "the" energetically favorable option based on our calculations).

Also, even if the vacancies reconfigure to form 5-9 defects (though, it may not
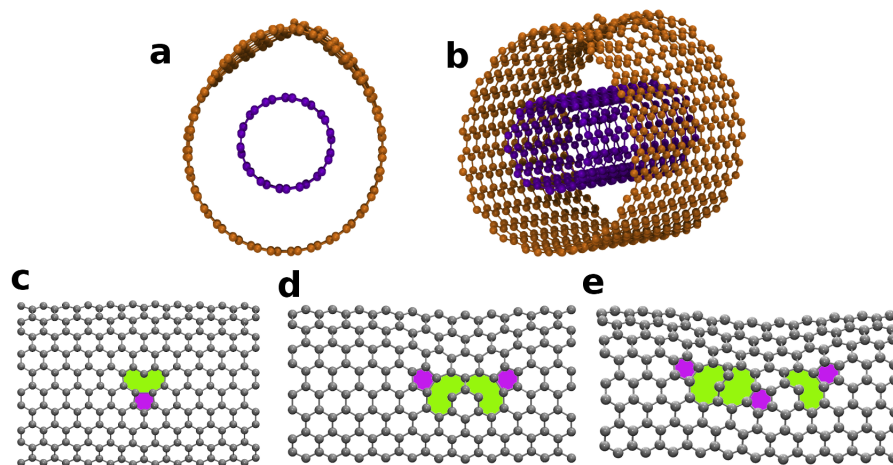
Figure 7.4: (a), (b) Front, side views of MWNT; (c), (d) and (e) top views of MWNT with asingle, double and triple vacancy, respectively. 5 and 9 membered rings have beenhighlighted with pink and light green, respectively.

occur due to the non-equilibrium conditions), as observed in our calculations on MWNTs as well as on SWNTs, they all will align linearly as shown in figures 7.4a, 7.4b and 7.4e. These figures contain front, side and top views, respectively, of the optimized structure of a MWNT with 3 vacancies. In figures 7.4a and 7.4b, one can see the formation of crest (out-of-plane structure of atoms to release in-built strain upon laser exposure) parallel to the axis of MWNT. Such crest formation along with the result that "energy will be minimal for aligned vacancies" suggests that the crack should propagate along the line joining the vacancies. Also, this result is in good agreement with a previous MD study on the unzipping of MWNTs under stress. [34] The same study also show that among various feasible ways of crack propagation, the most favorable one will involve the alignment of vacancies parallel to the tube axis. Combining all these results, we conclude that under favorable conditions, such linear alignment (of either the vacancies or the annealed defects) along the tube axis can result in longitudinal unzipping of CNTs to give GNRs.
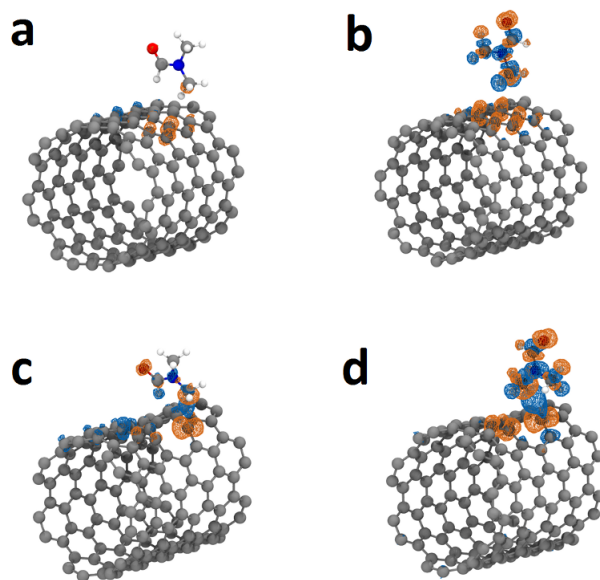
Figure 7.5: Charge density difference calculated for CNT+DMF system at (a) 10^{-5} V/Å and (b) 0.1 V/Å and for CNT+V1+DMF system at (c) 10^{-5} V/Å and (d) 0.1 V/Å.

7.3.3   Effect of solvent and external field

To gain better understanding of interaction of laser field (electric field) with CNT alone or CNT+DMF, we have optimized energetically favorable relative configurations of DMF molecule when adsorbed on CNT. In a system, at a constant field strength (E), the potential (= -eEr) due to electric field (of laser) will have more impact at the locations with more charge density than those with less charge density. We have calculated gains in energy when CNT or CNT+DMF are placed in electric field of gradually increasing strengths. Upto 10^{-5} V/Å, we did not observe much change in energetics. The calculated gains in energies are -1.3195 eV, -2.0489 eV and -2.4099 eV for a CNT, CNT+DMF and for CNT+v1+DMF respectively, when these systems are placed in extreme electric field considered in our study i.e., 0.1 V/Å.

Also, charge distribution itself changes under application of strong electric field (due to laser exposure). Charge density difference calculated for CNT+DMF upon application of electric fields are shown in Figs. 7.5(a) and (b) for 10^{-5} V/Å and 0.1 V/Å respectively. It is apparent that the influence of electric field is minimal upto

10^{-5} V/Å and one can visually observe the clear-cut changes in charge distribution at field as high as 0.1 V/Å. Thus, under laser exposure, DMF and CNT interact strongly. This strong interaction with laser (electric field) can create defects in the nanotubes at adsorbed sites. We further calculated charge density distribution for CNT+DMF+v1 at 10^{-5} V/Å and 0.1 V/Å fields (as shown in Fig 7.5(c) and (d) respectively). Clearly, there is a dramatic influence of just a single vacancy on charge distribution when CNT+DMF system is placed at 0.1 V/Å field. This enhanced charge density caused by the formation of a single vacancy visually demonstrates that formation of vacancies becomes more and more favorable as its number increases as the process of unzipping progresses. Further propagation of the defect is more favored along the longitudinal axis (than the lateral direction), as longitudinal unzipping will not change the alignment of the induced dipole (because of external electric-field) in the CNT, and hence, it is easy to create defects along longitudinal axis than along lateral axis.

Effect of DMF

The solvent, dimethylformamide (DMF), also plays a role in the unzipping of NTs. Since DMF molecules are dipolar, the positive side of their dipoles would be pointing at the defect sites. In the presence of a high external electric-field, the defect (and solvent molecules) induced dipoles in the nanotube would align along the direction of the electric-field to gain stability. Creation of vacancies along the longitudinal direction promotes induced dipoles to point along the same direction and hence minimizes their potential energy (which is not favorable in the lateral direction). Thus, longitudinal unzipping is more favorable and the unzipping occurs through the creation of vacancies.

7.4   Conclusions

In conclusion, we have demonstrated the laser-induced unzipping mechanism of NTs to achieve NRs. We find that thinner CNTs require less laser fluence for unzipping due to the formation of weaker π-bonding and there is always a cumulative effect while creating the defects in both MoS_2 and carbon NTs. Consistent with experiments, we find that longitudinal unzipping is always energetically favorable in both NTs.

The proposed mechanism of unzipping includes the formation of vacancies and the generation of induced dipole-moment across the nanotube under the influence of external electric-field due to the charge accumulation near the vacancies. DMF molecules align themselves along the tube axis near the vacancies with their dipoles being parallel to the induced dipoles to minimize the interaction with external field. This leads to the accumulation of further charge near the vacancies and supports longitudinal unzipping of nanotubes.

Bibliography

[1] M. Y. Han, B. Özyilmaz, Y. Zhang, and P. Kim, Phys. Rev. Lett. **98**, 206805 (2007).

[2] Y.-W. Son, M. L. Cohen, and S. G. Louie, Phys. Rev. Lett. **97**, 216803 (2006).

[3] Y. Yang, H. Yu, D. York, Q. Cui, and M. Elstner, J. Phys. Chem. A **111**, 10861 (2007).

[4] X. Li, X. Wang, L. Zhang, S. Lee, and H. Dai, Science **319**, 1229 (2008).

[5] J. Bai, R. Cheng, F. Xiu, L. Liao, M. Wang, A. Shailos, K. L. Wang, Y. Huang, and X. Duan, Nat. Nanotechnol. **5**, 655 (2010).

[6] W. Y. Kim and K. S. Kim, Nat. Nanotechnol. **3**, 408 (2008).

[7] Y.-W. Son, M. L. Cohen, and S. G. Louie, Nature **444**, 347 (2006).

[8] K. A. Ritter and J. W. Lyding, Nat. Mater. **8**, 235 (2009).

[9] C. Tao, L. Jiao, O. V. Yazyev, Y.-C. Chen, J. Feng, X. Zhang, R. B. Capaz, J. M. Tour, A. Zettl, S. G. Louie, et al., Nature Physics **7**, 616 (2011).

[10] B. Obradovic, R. Kotlyar, F. Heinz, P. Matagne, T. Rakshit, M. Giles, M. Stettler, and D. Nikonov, Appl. Phys. Lett. **88**, 142102 (2006).

[11] H. Santos, L. Chico, and L. Brey, Phys. Rev. Lett. **103**, 086801 (2009).

[12] A. Sinitskii, A. Dimiev, D. V. Kosynkin, and J. M. Tour, ACS nano **4**, 5405 (2010).

[13] A. Sinitskii, A. A. Fursina, D. V. Kosynkin, A. L. Higginbotham, D. Natelson, and J. M. Tour, Appl. Phys. Lett. **95**, 3108 (2009).

[14] B. Wang and J. Wang, Phys. Rev. B **81**, 045425 (2010).

[15] S. Costamagna, A. Schulz, L. Covaci, and F. Peeters, Appl. Phys. Lett. **100**, 232104 (2012).

[16] H. Zhang, X.-B. Li, and L.-M. Liu, J. Appl. Phys. **114**, 093710 (2013).

[17] H. Pan and Y.-W. Zhang, J. Mater. Chem. **22**, 7280 (2012).

[18] Y. Li, Z. Zhou, S. Zhang, and Z. Chen, J. Amer. Chem. Soc. **130**, 16739 (2008).

[19] F. López-Urías, A. L. Elías, N. Perea-López, H. R. Gutiérrez, M. Terrones, and H. Terrones, 2D Materials **2**, 015002 (2015).

[20] D. V. Kosynkin, W. Lu, A. Sinitskii, G. Pera, Z. Sun, and J. M. Tour, ACS nano **5**, 968 (2011).

[21] S. Rao, S. N. Jammalamadaka, A. Stesmans, V. Moshchalkov, J. v. Tol, D. Kosynkin, A. Higginbotham-Duque, and J. Tour, Nano Lett. **12**, 1210 (2012).

[22] S. Rao, A. Stesmans, D. Kosynkin, A. Higginbotham, and J. Tour, New J. Phys. **13**, 113004 (2011).

[23] C. Nethravathi, A. A. Jeffery, M. Rajamathi, N. Kawamoto, R. Tenne, D. Golberg, and Y. Bando, ACS nano **7**, 7311 (2013).

[24] P. Kumar, L. Panchakarla, and C. Rao, Nanoscale **3**, 2127 (2011).

[25] K. Vasu, S. S. R. K. C. Yamijala, A. Zak, K. Gopalakrishnan, S. K. Pati, and C. N. R. Rao, Small **11**, 3916 (2015).

[26] D. Kvashnin, L. Y. Antipina, P. Sorokin, R. Tenne, and D. Golberg, Nanoscale **6**, 8400 (2014).

[27] M. Elstner, D. Porezag, G. Jungnickel, J. Elsner, M. Haugk, T. Frauenheim, S. Suhai, and G. Seifert, Phys. Rev. B **58**, 7260 (1998).

[28] B. Aradi, B. Hourahine, and T. Frauenheim, J. Phys. Chem. A **111**, 5678 (2007).

[29] W. Humphrey, A. Dalke, and K. Schulten, J. Mol. Graph. **14**, 33 (1996).

[30] S. Melchor and J. A. Dobado, J. Chem. Inf. Comput. Sci. **44**, 1639 (2004).

[31] K. Burke, J. P. Perdew, and M. Ernzerhof, Int. J. Quantum Chem **61**, 287 (1997).

[32] M. S. José, A. Emilio, D. G. Julian, G. Alberto, J. Javier, O. Pablo, and S.-P. Daniel, J. Phys.: Condens. Matter **14**, 2745 (2002).

[33] L. Kleinman and D. Bylander, Phys. Rev. Lett. **48**, 1425 (1982).

[34] R. Dos Santos, E. Perim, P. Autreto, G. Brunetto, and D. Galvao, Nanotechnology **23**, 465702 (2012).

[35] A. Krasheninnikov, P. Lehtinen, A. Foster, and R. Nieminen, Chem. Phys. Lett. **418**, 132 (2006).